

Chen, Bo (2025) Thermal processing of agricultural waste-based biorefinery residues and plastics for producing sustainable fuels and end of life value. PhD thesis.

https://theses.gla.ac.uk/85634/

Copyright and moral rights for this work are retained by the author

A copy can be downloaded for personal non-commercial research or study, without prior permission or charge

This work cannot be reproduced or quoted extensively from without first obtaining permission from the author

The content must not be changed in any way or sold commercially in any format or medium without the formal permission of the author

When referring to this work, full bibliographic details including the author, title, awarding institution and date of the thesis must be given

Enlighten: Theses
<a href="https://theses.gla.ac.uk/">https://theses.gla.ac.uk/</a>
research-enlighten@glasgow.ac.uk

# Thermal processing of agricultural waste-based biorefinery residues and plastics for producing sustainable fuels and end of life value



## Bo Chen

Submitted in fulfilment of the requirements for the Degree of Doctor of Philosophy

School of Engineering
College of Science and Engineering
University of Glasgow
November 2025

i

#### **Abstract**

The depletion of fossil fuel reserves and escalating environmental concerns—such as greenhouse gas emissions and plastic pollution—have intensified the global pursuit of renewable and circular energy solutions. Thermochemical conversion technologies, particularly pyrolysis, offer effective pathways for valorising carbon-rich waste into fuels, chemicals, and functional materials. The co-pyrolysis of lignocellulosic biomass with plastic waste exploits synergistic effects between hydrogen-deficient and hydrogen-rich feedstocks, improving product yield and quality. However, feedstock heterogeneity, complex reaction mechanisms, and variability from environmental aging and industrial processing remain key challenges to optimizing and scaling pyrolysis systems. This dissertation presents a systematic research framework addressing these challenges through the investigation of co-pyrolysis behaviour, catalytic upgrading, and kinetic modelling of integrated bio-based and polymeric residues, with an emphasis on process circularity, feedstock interdependency, and environmental resilience.

The study began with thermogravimetric analysis (TGA) of various corn stalk tissues (stem, husk, ear, cob, and leaf), high-density polyethylene (HDPE), and their blends. Structural differences in the plant tissues strongly influenced decomposition behaviour and product distribution. The corn cob/HDPE blend achieved the highest yields of valuable chemicals (such as furan derivatives and aromatics) and exhibited the lowest activation energy (149.3 kJ/mol). Machine learning models, including random forest (RF) and gradient boost regression tree (GBRT), were applied to predict mass loss, with RF showing superior performance. Building upon these findings, downstream ethanol processing residue (EPR) from a corn cob-based biorefinery was co-pyrolyzed with HDPE. In situ catalysis with bottom ash (BA) from the same biorefinery reduced activation energy and promoted deoxygenation and aromatic hydrocarbon formation. Pyrolysis-gas chromatography/mass spectrometry (Py-GC/MS) confirmed catalytic improvements in product distribution. To further enhance circularity, wood-plastic composites (WPCs) were examined. TGA and TG-FTIR revealed synergistic effects between EPR and plastic, lowering activation energies and facilitating a one-dimensional diffusion pyrolysis mechanism. Additionally, artificial weathering of WPCs altered plastic crystallinity and pyrolysis behaviour, informing post-consumer management strategies.

Overall, this research advances a comprehensive approach to the circular pyrolytic valorisation of biorefinery residues and plastics. Through integrated thermal analysis, catalytic enhancement, kinetic modelling, and machine learning, the findings contribute to the

development of efficient, low-emission thermochemical processes for sustainable waste management and renewable energy production.

#### **Abbreviations**

WPC: Wood-plastic composite;

PP: Polypropylene

HDPE: High density polyethylene

TGA: Thermogravimetric analysis

DTG: Derivative thermogravimetry

FTIR: Fourier transform infrared spectroscopy

Py-GC/MS: Pyrolysis—gas chromatography/mass spectrometry

TG-FTIR: Thermogravimetric analysis coupled with Fourier transform infrared spectroscopy

MSW: Municipal solid waste;

PVC: Polyvinyl chloride

PLA: Polylactic acid

BA: Bottom ash

EPR: Ethanol processing residue

KAS: Kissinger-Akahira-Sunose

FWO: Flynn-Wall-Ozawa

DAEM: Distributed activation energy models

AI: Artificial intelligence

ML: Machine learning

ANN: Artificial neural network

GBR: Gradient boosting regression

RF: Random forest

MSE: Mean squared error

R<sup>2</sup>: Regression coefficient

FESEM: Field emission scanning electron microscopy

EDS: Energy-dispersive X-ray spectroscopy

XRF: X-ray Fluorescence Spectroscopy

BET: Brunauer–Emmett–Teller Theory

DFT: Density functional theory

RSPR: Reed straw processing residual

MA-HDPE: Maleic anhydride grafted HDPE

XRD: X-Ray diffractometer

### **Contents**

Abstract	ii
Acknowledgement	viii
Declaration and Contributing Papers	
1. Introduction	. 11
1.1 Thermal processing technology for sustainable fuel production	. 11
1.1.1 Pyrolysis	
1.1.2 Gasification	.14
1.1.3 Hydrothermal liquefaction	.14
1.2 Feedstocks	.15
1.2.1 Biomass	.15
1.2.2 Plastics	.16
1.2.3 Other waste feedstocks	.16
1.2.4 Wood plastic composite	.17
1.3 Catalyst used in thermal processing technology.	.19
1.3.1 Over Commercial catalysts	
1.3.2 Over non-commercial catalysts	
1.3.3 Operation mode of catalytic pyrolysis	.26
1.4 Pyrolysis kinetics	
1.5 Pyrolysis mechanism	.29
1.5.1 Pyrolysis mechanism of biomass	.29
1.5.2 Pyrolysis mechanism of plastic	.30
1.5.3 Pyrolysis mechanism of WPC	
1.6 The background of the project	.34
1.7 Project aims	.36
1.8 Thesis plan	.37
1.9 Identified knowledge gaps	.38
2. Co-pyrolysis corn stalk and high-density polyethylene: emphasized on the differences	of
fibrous tissues on thermal behaviour and kinetics	.41
2.1 Introduction	.41
2.2 Materials and methods	.43
2.2.1 Materials	.44
2.2.2 Characterization of corn stalk tissues and HDPE	.44
2.2.3 Thermal test	
2.2.4 Py-GC/MS	.45
2.2.5 Kinetics	.46
2.2.6 Machine learning	.49
2.3 Result and discussion	
2.3.1 Thermogravimetric analysis of different corn stalk tissues and HDPE	.51
2.3.2 Thermogravimetric analysis of corn stalk tissues and HDPE blends	.53
2.3.3 Py-GC/MS analysis	.55
2.3.4 Kinetic analysis	
2.3.4 Weight loss prediction via machine learning methods	.68
2.4 Conclusion	
3. Catalytic Co-pyrolysis of cellulosic ethanol processing residue with high-dens	sity
polyethylene over biomass bottom ash catalyst	.72

3.1 Introduction	72
3.2 Materials and methods	
3.2.1 Materials	74
3.2.2 Characteristics of EPR and Bottom ash	75
3.2.3 Thermal analysis	76
3.2.4 Kinetics	77
3.3 Results and discussion	
3.3.1 EPR and BA characterization	
3.3.2 Co-pyrolysis of EPR and HDPE	
3.3.3 Py-GC-MS analysis	
3.3.4 Kinetic analysis	
3.4 Conclusion	
4. Pyrolysis behaviour and kinetic analysis of waste polylactic acid composite reinforce	ed with
reed straw processing residue	93
4.1 Introduction	93
4.2 Materials and methods	
4.2.1 Materials and preparation of RSPR/PLA composite	
4.2.2 Characteristics of RSPR/PLA composite	
4.2.3 Thermogravimetric and pyrolysis products analysis	
4.2.4 Kinetics analysis	
4.3 Results and discussion	
4.3.1 Thermogravimetric analysis	100
4.3.2 Volatile products analysis by TG-FTIR and Py-GC/MS	
4.3.3 Kinetic analysis	
4.4 Conclusion	
5. Pyrolytic valorisation of post-consumed wood-plastic composites: emphasis of	on the
weathering as a variable to the thermal behaviour, kinetics and pyrolytic products distri	bution
	119
	_
5.1 Introduction	
5.2 Materials and methods	
5.2.1 Materials	
5.2.2 Preparation of wood-plastic composite and Xenon lamp weathering	
5.2.3 Characterization of wood-plastic composite	
5.2.4 Pyrolysis of the weathered wood-plastic composites	
5.2.5 Kinetics analysis	
5.3 Results and discussions.	
5.3.1 Physicochemical and surface properties of the weathered wood-	_
composites.	
5.3.2 Thermogravimetric analysis of the weathered wood-plastic composites.	
5.3.3 Pyrolysis kinetics of the weathered wood-plastic composites	
5.3.4 Valorisation products from the pyrolysis of the weathered wood-	_
composites	
5.4 Conclusion	
6. Conclusion and future work	144
6.1 Conclusion	144
6.2 Future perspectives and outlook	
6.3 Implications of the current work	

Appendix 1. Proximate Analysis	153
Appendix 2. Ultimate analysis	155
Appendix 3. Biochemical analyses	156
Appendix 4. The pyrolytic products from the co-pyrolysis of corn stalk tis	ssues and HDPE.
(Chapter 2)	158
Reference	167

#### Acknowledgement

First and foremost, I would like to express my deepest gratitude to my supervisor, Dr. Ian Watson, for his invaluable guidance, continuous support, and encouragement throughout my PhD journey. His insightful advice, patience, and expertise have been instrumental in shaping the direction and quality of this research.

I would also like to extend my sincere thanks to Di Cai, my senior from Beijing University of Chemical Technology (BUCT), whose generous help and technical advice have greatly contributed to the successful completion of this work. His mentorship and willingness to share his experience have made a significant difference in both my research and personal development.

I gratefully acknowledge the financial support provided by the China Scholarship Council (CSC), without which this research would not have been possible.

Finally, I would like to express my heartfelt thanks to my parents for their unconditional love, constant support, and encouragement throughout this journey. Their belief in me has been a source of strength and motivation at every stage of my academic life.

To everyone who has supported me—academically, professionally, and personally—throughout this journey, thank you.

#### **Declaration and Contributing Papers**

The work contained in this thesis, submitted for the degree of Doctor of Philosophy, is my own original work, except where due reference is made to other authors. No material within has been previously submitted for a degree at this or any other university.

Part of Chapter 1 have been published at ACS books *Depolymerization: Concepts*, *Progress, and Challenges Volume 1: Core Concepts and Fundamentals*: Bo Chen, Ian Watson, Zhitong Yao, Di Cai. 2025. Pyrolysis Depolymerization of Waste Macromolecules. 1498, 197-210. https://doi.org/10.1021/bk-2025-1498.ch010

Results of Chapter 2 have been published at *Science of The Total Environment*: Bo Chen, Deyin Xie, Yongjie Jiang, Yankun Wang, Changsheng Su, Zhitong Yao, Di Cai, Hu i Cao, Ian Watson. 2024. Co-pyrolysis of corn stalk and high-density polyethylene with emphasis on the fibrous tissue difference on thermal behavior and kinetics. 957, 177847. https://doi.org/10.1016/j.scitotenv.2024.177847

Results of Chapter 3 have been published at *Biomass Conversion and Biorefinery*: Bo Chen, Zhitong Yao, Changwei Zhang, Shikun Cheng, Mengying Zhu, Yankun Wang, Yilu Wu, Hui Cao, Ian Watson, Di Cai. 2023. Catalytic co-pyrolysis of cellulosic ethanol–processing residue with high-density polyethylene over biomass bottom ash catalyst. 14(15), 18031-18040. https://doi.org/10.1007/s13399-023-03915-5

Results of Chapter 4 have been published at *Carbon Resources Conversion*: Bo Chen, Sen Ma, Sachin Kumar, Zhitong Yao, Wanqi Feng, Jianbo Zhao, Xu Zhang, Di Cai, Hui Cao, Ian Watson. 2024. Pyrolysis behaviour and kinetic analysis of waste polylactic acid composite reinforced with reed straw processing residue. 7(3), 100226. https://doi.org/10.1016/j.crcon.2024.100226

# **Chapter 1**

Introduction and literature review

#### 1. Introduction

Traditional energy sources—primarily fossil fuels such as coal, oil, and natural gas—have long served as the backbone of industrial energy consumption. However, their finite nature, along with growing environmental concerns over greenhouse gas emissions and climate change, has spurred the global pursuit of renewable and sustainable energy alternatives [1]. However, the over-reliance on fossil fuels makes it difficult to eliminate their use in the futuer[2]. Sustainable fuels, which are derived from biomass and waste plastics, can either be blended with traditional fossil fuels or used as an alternative to change the petroleum-based energy infrastructures to renewable infrastructures. The production of sustainable fuels utilizes a variety of raw materials including crops like corn and sugarcane for ethanol [3,4], and soybeans and palm oil for biodiesel [5,6]. Waste materials, such as plastic, animal fats and vegetable oils, are also employed in the production process [7,8]. The methods of sustainable fuels production vary depending on the type of feedstock and the desired fuel. In general, these methods can be categorized into biochemical processes, which include fermentation to produce ethanol [9], and thermochemical processes like gasification, hydrothermal liquefaction and pyrolysis to produce bio-oils and syngas [10]. Each method yields different products, including bio-oils, syngas, and biochar, which can be further processed into fuels comparable to conventional gasoline, diesel, and other petrochemical derivatives. Moreover, each method has its unique set of technological challenges and economic considerations. Among these methods, thermal processing stands out due to its ability to handle a wide range of biomass types, including agricultural residues, forest waste, and even municipal solid waste, turning waste into valuable energy carriers [10]. However, the crude oil obtained from the thermal (non-catalytic) process can not directly replace the traditional fossil fuels due to the high oxygenate content such as aldehydes, ketones and alcohol, acidity, and corrosiveness [11]. Introducing catalysts into the thermal process enhances the breakdown of complex molecules, facilitating dehydration, decarboxylation, and decarbonylation reactions, which consequently refines the bio-oil's quality, resulting in an improved product with potentially higher energy content and stability [12].

#### 1.1 Thermal processing technology for sustainable fuel production

Thermal processing technology for sustainable fuel production have emerged as a crucial component in the renewable energy sector, which mainly included pyrolysis, gasification, and hydrothermal liquefaction [13]. Fig.1.1 shows the conversion routes of different thermal

processing methods. These techniques convert biomass, plastics and other organic waste materials into sustainable fuels such as bio-oil, syngas, and biochar through the application of high temperatures and controlled environments, which break down complex materials into simpler chemical structures, thereby transforming waste and non-fossil resources into viable energy sources [14].

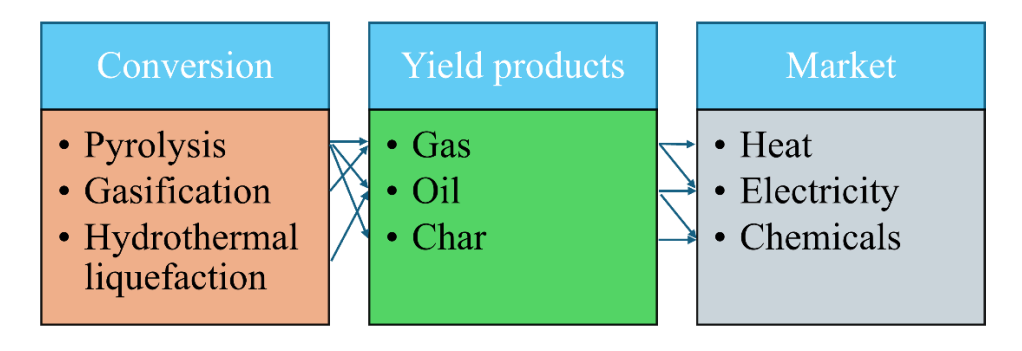


Fig 1.1 Conversion route of different thermal processing methods

#### 1.1.1 Pyrolysis

Pyrolysis is the thermal decomposition of feedstocks at high temperatures in the absence of oxygen, which can effectively decompose feedstock into liquid bio-oil, syngas and char [15]. According to the retention time and heating rate, the pyrolysis process is categorized into slow, fast, and flash pyrolysis, affecting the yield and composition of the output (liquid, gas, and char) [16]. Table 1.1 summarizes the difference among three pyrolysis techniques. Slow pyrolysis applies heat slowly in an oxygen-free setting to break down the feedstocks. It's a controlled process that aims to maximize the yield of char or biochar. The process operates at lower temperatures, typically ranging from 300 °C to 500 °C, with a much longer residence time that can vary from several minutes to hours, depending on the desired output and the characteristics of the feedstock [17]. Conversely, fast pyrolysis aims to optimize liquid product yield through higher heating rates and shorter residence times [17]. The versatility of pyrolysis allows production of various biofuels, including bio-oil, syngas, and biochar. Bio-oil can be further refined to generate transport fuels, while syngas—a mixture of hydrogen, carbon monoxide, and other hydrocarbons—can be utilized for energy generation or as a building block for synthetic fuels. Biochar, the carbon-rich byproduct, serves as a soil amendment, closing the loop in the carbon cycle and contributing to soil fertility and carbon sequestration [18]. A large amount of related work has been done in the pyrolysis of different feedstocks. For instance, Wu et al. [19] investigated the products' composition of the fast and slow pyrolysis of WPC made from waste automotive plastic and sugarcane skin. The gaseous products from WPC

pyrolysis are mainly consists of alkanes, aromatics and a small amount of CO<sub>2</sub>. Olefins are the main products in pyrolysis oil. Lin *et al.* [20] conducted a comprehensive study on the interactions between the primary wood components (cellulose, hemicellulose, and lignin) and polypropylene (PP) during the pyrolysis process. Their TGA results revealed that the decomposition of cellulose and hemicellulose was hindered by the presence of PP, while lignin decomposition was enhanced. Py-GC/MS analysis indicated that H-transfer reactions from PP played a pivotal role in facilitating the breaking of glucosidic bonds and stabilizing the primary radicals in cellulose pyrolysis, leading to the favourable formation of levoglucosan. Regarding the interactions between hemicellulose and PP, the presence of PP facilitated the generation of ketones, particularly cyclopentenones, owing to glycosidic break, dehydration, and recyclization reactions. Additionally, lignin depolymerization was enhanced through the abstraction of hydrogen from PP. These biomass-derived components also promoted the β-scission of PP and facilitated the formation of light hydrocarbons with a carbon number of 3n.

Table 1.1 The comparison of different pyrolysis techniques

Pyrolysis	Temperature	Residence	Heating	Advantages	Disadvantages	Reference
type	range (°C)	time (s)	rate			
			(°C/min)			
Slow	300-600	5 mins - few	~5 to 10	Favoured for	Long	[18]
pyrolysis		hours		biochar	processing	
				production	time	
Fast	400-700	~2 mins	~200	Short reaction	Expensive	[21]
pyrolysis				time	setup for heat	
				High liquid	insulation and	
				products	rapid cooling	
				Low solid	system	
				products	Feedstock	
					require proper	
					pre-treatment	
Flash	500-850	~2 s	~1000 -	Short reaction	Expensive	[22]
			3000	time	setup for heat	
				High liquid	insulation and	
				products	rapid cooling	
				Low solid	system	
				products		

#### 1.1.2 Gasification

Gasification is considered as the cleanest and the most efficient thermochemical process employed in H<sub>2</sub> production due to its capability to recover nearly the entire energy content of the feedstock while mitigating the production of harmful substances [23,24]. During gasification, feedstock is subjected to high temperatures and a controlled supply of oxygen or steam in a gasifier [25]. This process chemically converts the feedstock into a mixture of carbon monoxide (CO), hydrogen (H<sub>2</sub>), and other gaseous compounds [26]. Syngas, the resulting product, is a versatile fuel that can be further processed and used for a variety of applications, including electricity generation, heat production, or the synthesis of biofuels like ethanol or biodiesel [27,28]. During the gasification process, gasifying agents like CO<sub>2</sub>, air or steam, and high temperatures (700-1000 °C) are needed [29-31]. Among different gasifying agents, air is favourable over other agents because of its easier operational capacity and generation of high-quality syngas [32]. This process converts biomass or other feedstocks into a combustible gas mixture, mainly composed of hydrogen, carbon monoxide, and methane, which can be used for energy supply for electricity generation, heating, and synthesis of liquid biofuels and chemicals. Gasification's robustness and efficiency make it particularly suitable for large-scale biofuel production, capable of handling diverse feedstocks ranging from agricultural residues to municipal waste. Seo et al. [24] and Jeon et al. [33] studied the air gasification of WPCs over different catalysts for achieving higher H<sub>2</sub> generation. The results from both works showed that air gasification technology is a promising way to process discarded WPCs to produce valuable H<sub>2</sub>. Furthermore, both works pointed out that high tar content is a crucial obstacle of gasification, which results in reducing H<sub>2</sub> and CO selectivity, clogging and corrosion inside the reactors, and alleviating the overall efficiency of syngas production [34].

#### 1.1.3 Hydrothermal liquefaction

Hydrothermal liquefaction (HTL) offers another thermal pathway to produce sustainable fuels, simulating the natural geological processes that produce fossil fuels. HTL process converts feedstocks into liquid fuels by exposing them to high temperatures and pressures within a watery environment [35]. Compared with pyrolysis and gasification, HTL operates under milder conditions, with temperatures usually ranging from 250 to 374°C and at lower

heating rates. One of HTL's significant advantages is its efficiency in processing wet materials, such as algae and food waste. Eliminating the need to pre-dry the material not only saves energy, but also reduces operating costs, making HTL a promising technique for converting feedstocks especially wet feedstocks into valuable liquid fuels [36]. Derek *et al.* [36] studied the chemical properties of bio-oil produced from the hydrothermal liquefaction of *Spirulina* algae, swine manure and digested anaerobic sludge. The results indicated that the composition of feedstocks has great influence on the chemical characteristics of biocrude oil from the HTL process.

Each thermal processing technology brings its unique advantages and challenges. Pyrolysis is favoured for its simplicity and potential for decentralized biofuel production. In contrast, gasification's ability to process a broad range of waste materials offers an attractive pathway for waste-to-energy conversion. Hydrothermal liquefaction's compatibility with wet feedstocks provides a pathway for utilizing resources that would otherwise be considered waste.

#### 1.2 Feedstocks

#### 1.2.1 Biomass

Biomass is the most abundant sustainable resource in the world, and it is composed of chemical elements including carbon, hydrogen, nitrogen, oxygen, and sulfur. Historically, humans have utilized various natural materials such as crop husks to produce energy by combustion. However, the direct combustion of these materials was not ideal as it produced significant amounts of smoke, carcinogenic substances, and ash [14]. The emergence of thermal processing technologies has changed the situation, making biomass one of the primary feedstocks for sustainable fuel production. These advanced technologies allow for more efficient conversion of biomass into clean energy, reducing the environmental issues associated with its direct combustion [37]. Biomass encompasses a wide variety of organic materials derived from plants and animals, which store sunlight in the form of chemical energy. Common types of biomasses include forestry waste such as wood chips, sawdust, agricultural residues like straw and husks, grassy and woody plants, algae, and the organic components of municipal and industrial wastes.

Agricultural residues, which includes straw, husk, bagasse, and other by-products of farming activities, are abundant and typically considered waste, making them an inexpensive and sustainable option for fuel production [38,39]. Similar to agricultural residues, forestry wastes such as wood chips, sawdust, and bark are significant feedstocks. These materials are by-products of the timber industry and are used to produce a high yield of biochar and bio-oil

through slow or fast pyrolysis [40]. The use of forestry residues not only helps in managing waste from wood processing but also in producing energy that can potentially replace fossil fuels in many applications. Special crops grown specifically for energy production, such as miscanthus, switchgrass, and willow, are known as energy crops [41,42]. These crops are particularly engineered to have a high biomass yield and are typically grown on land not suitable for food crops, thus not competing with food production. Energy crops are a renewable feedstock that can be continually replanted and harvested for energy production, providing a sustainable and reliable source of biomass for thermal processing. Recently, Algae has emerged as a promising feedstock due to its high oil content, which can be efficiently converted into biodiesel. It grows rapidly, has a high per-acre yield compared to terrestrial crops, and can be cultivated in ponds or bioreactors that do not compete with arable land. Algae can also help in carbon capture, as it absorbs CO<sub>2</sub> during photosynthesis [43].

#### 1.2.2 Plastics

Plastics have recently been recognized as a potential feedstock for thermal processing, especially given the global push towards reducing plastic waste. Plastics are primarily composed of polymers that can be converted back into monomers or other useful chemicals through processes such as pyrolysis. The main categories of plastics used in thermal processing include:

- 1) Post-consumer plastics: Everyday plastic waste collected from residential and commercial locations, often contaminated and mixed, which presents challenges in processing [44].
- 2) Industrial plastics: Clean, often single-type plastic wastes from industrial or commercial processes, which are easier to process due to their uniformity [21].
- 3) Ocean plastics: Plastics collected from marine environments, which are gaining attention due to the environmental damage they cause [45].

The thermal decomposition of plastics can help alleviate the problem of plastic waste, converting what would otherwise be a pollutant into a valuable resource. However, the process needs to be carefully managed to minimize the production of toxic by-products.

#### 1.2.3 Other waste feedstocks

In addition to traditional biomass and plastics, other waste feedstocks, such as municipal solid waste (MSW), industrial by-products and sewage sludge, are being explored for their

potential in sustainable fuel production. MSW includes a wide range of materials, including plastics, which can be converted into synthetic crude oil through pyrolysis. This process not only reduces landfill use but also recovers valuable resources from waste [46]. Various industrial by-products can also serve as feedstock for thermal processing. For instance, the residues from paper and pulp industries, slaughterhouses, and beverage production can be processed to produce fuels. These wastes, which would otherwise pose a disposal problem, can be converted into energy, helping industries reduce their environmental footprint [47,48]. In addition, an often-overlooked feedstock is sewage sludge, the by-product of wastewater treatment. Rich in organic matter, sludge can be processed to produce bio-oil and syngas. Utilizing sludge helps in waste management and produces energy from a resource that is otherwise a disposal problem [49]. Food waste which contains large energy content is another promising feedstock for sustainable fuel. As global food waste continues to be a major concern, with significant amounts wasted at consumer and retail levels, converting this waste into bioenergy offers a dual benefit: reducing the environmental impact of organic waste and creating renewable energy resources [50]. Many researchers have demonstrated that food waste is rich in carbon and hydrogen content and showed good potential for thermal processing [51,52].

#### 1.2.4 Wood plastic composite

Wood plastic composite (WPC) is a hybrid material made by combining plant (including wood or non-wood) fibres or particles with plastic polymers, typically polyethylene (PE), polypropylene (PP), or polyvinyl chloride (PVC) [53,54]. WPC first emerged in the early 1990s as a relatively new class of materials and gained commercial attention and began to be used in various applications in the early to mid-1990s [55]. The WPC industry has experienced substantial growth with the development of global construction and manufacturing sectors. According to a report by Grand View Research, Inc., the global WPC market size was estimated at \$6.41 billion in 2022 and is expected to grow at a compound annual growth rate (CAGR) of 11.6 % from 2023 to 2030 [56].

Compared with pure plastics, WPC reduces the demand for virgin plastics and incorporates renewable wood fibres, making it more environmentally friendly [57]. It also maintains the natural appearance of wood while benefiting from the durability, low maintenance, fungi and insect resistance properties of plastic [58,59]. In addition, the presence of wood fibre enhances the stiffness, thermal stability and creep behaviour of WPC [60]. Due to the desirable

properties of WPC, it has been widely used in construction and building materials, furniture, automotive industry and environmental applications such as park benches [61].

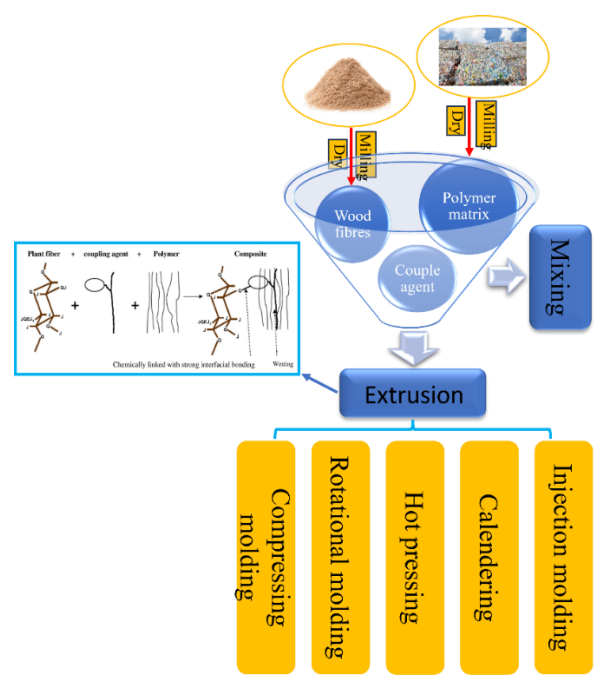


Fig 1.2 The manufacturing process of WPC

The manufacturing process of WPC was shown in Fig 1.2. Typically, the materials used in WPC production include wood fibres and thermoplastic polymers [62]. In order to improve compatibility between the wood fibres and polymers, enhance performance properties, and protect WPC against degradation, coupling agents such as like compatibilizers, lubricants and stabilizers are often introduced to WPC production [63]. These materials are mixed and then fed into an extrusion machine, where it is heated and forced through a die to form the desired shape. According to the intended application, the extruded WPC material may undergo additional shaping processes such as injection molding [63], calendaring [64], hot pressing [65], rotational molding [66] and compressing moulding [67] to achieve the final product's shape and size. The sustainable and customizable nature of WPCs has made them a popular choice in industries such as construction, automotive manufacturing, and furniture production. Additionally, advancements in WPC technology continue to expand the possibilities and improve the efficiency of these manufacturing processes.

Although WPC is considered as a "Green Composite", the end life disposing of WPC also presents several challenges due to their heterogeneous composition, which includes both wood fibres and thermoplastic polymers [68]. Conventional disposal methods such as landfilling and incineration do harm to the environment, because the thermoplastic polymers are non-biodegradable waste and can leach harmful chemicals into the environment over time [20]. In

addition, incineration can release greenhouse gases and toxic emissions [69]. Hence, a sustainable approach is required for the proper disposal of WPCs without harming the environment. Recycling is considered as a "Green" method for WPCs disposal [57]. But there are two obstacles for the application of recycling WPC. One is wood component starts to degrade and emit volatiles on repeated processing at temperatures around 220 °C [70]. The other is reprocessing induces thermal and oxidative degradation of polymer [71,72]. Another sustainable method for WPC disposal is thermochemical conversion processes.

#### 1.3 Catalyst used in thermal processing technology.

The bio-oil obtained from non-catalytic pyrolysis contains lots of oxygenates (acids, ketones, furans, aldehydes and phenols) and aliphatic compounds, which made it difficult to use directly [73,74]. Several methods including catalytic cracking, hydrotreating and other chemical and physical process have been used to upgrade the bio-oil[75–77]. Among these upgrading technologies, catalytic pyrolysis is more favoured due to its high efficiency in deoxygenation and cracking [78]. To improve the quality of bio-oil and increase the yield and selectivity of target products, different catalysts are introduced to the pyrolysis process, including commercial catalyst like zeolites (e.g., HZSM-5, HBeta, HY, etc.) and metal oxides (e.g., MgO, Al<sub>2</sub>O<sub>3</sub>, Fe<sub>2</sub>O<sub>3</sub>, CaO, ZnO, etc.), and non-commercial catalyst such as fly ash and bottom ash. Table 1.2 summarized some commercial and non-commercial catalysts used in the thermal processing technology.

#### 1.3.1 Over Commercial catalysts

Commercial catalysts, such as zeolites and metal oxides, are those that are readily available on the market and are manufactured at a large scale for specific industrial applications. They are typically well-characterized, with standardized properties that ensure consistent performance across various processes.

Zeolites are crystalline aluminosilicate sieves with open pores and ion exchange capabilities[79,80]. The structural features of zeolites, including high surface area, pore channel systems, ion-exchange sites, adjustable acidity, and high thermal stability, make them valuable catalysts which are widely employed in recent research [81]. Park *et al.* studied the effect of different kinds of microporous zeolites including HZSM-5, HBeta and HY on the thermal behaviour of WPC pyrolysis and products distribution [82]. The TG results showed no matter which catalyst was used in the pyrolysis process; the decomposition temperatures of

WPCs were shifted to the lower temperature. The same finding was obtained in another work of theirs [78]. In addition, Due to the small pore size of HZSM-5 and the large amount of coke inside the HY pore, the diffusion hindering effect of the reactants was obvious in both groups, which leading to the lower yield of aromatics than over HBeta. Lin *et al.* using different zeolite catalyst including HZSM-5, HBeta, HY and HUSY in the catalytic pyrolysis of poplar wood/HDPE composite, they found that the catalyst with high acidity and large pose size favoured the formation of aromatics, but the large pore size also promoted the formation of coke, which in agreement with Park *et al.* [82]. Sun *et al.* [83] studied the effect of USY and HUSY in catalytic pyrolysis of WPCs on pyrolysis products distribution. They found that the yield of olefins and aromatics increased sharply and the yield of oxygenates (aldehydes, acetic acid and ketones) reduced significantly with the presence of both catalysts, this is due to the high activity of USY and HUSY in the decarboxylation and decarbonylation of pyrolysis products, and USY has a better performance than HUSY.

Metal oxides is another type of widely used commercial catalyst in bio-oil upgrading, owing to its low cost and accessibility. In addition, it has been reported metal oxides could efficiently remove the oxygenates in pyrolysis products. Lin et al. [84] investigated the effects of different metal oxides including ZnO, CaO, MgO and Fe<sub>2</sub>O<sub>3</sub> on the distribution of products in catalytic fast pyrolysis of poplar wood/HDPE composite. Because of the strong basicity of CaO, it effectively reduced the yield of oxygenates in pyrolytic products through ketonization of acids and aldol condensations of linear carbonyl compounds. MgO has similar catalytic activity with CaO, because they are both basic. Because the basicity of MgO is lower than Cao, the deoxygenation effect of MgO is lower than CaO. In addition, they also found the strong basicity of CaO promoted the coke formation during the pyrolysis process. There is no noticeable change in the pyrolysis products using ZnO compared with uncatalyzed pyrolysis, which indicates the catalytic activity of ZnO is weaker than MgO and CaO. But the yield of Alkene is the highest among four catalysts by using ZnO. The catalytic performance of Fe<sub>2</sub>O<sub>3</sub> is between that of CaO and ZnO. In Heo et al.'s work [85], several low-cost catalysts including natural zeolite, spent fluid catalytic cracking (FCC) catalyst and γ-Al<sub>2</sub>O<sub>3</sub> were introduced to the fast pyrolysis of WPC to decrease the cost of aromatics production. Similar with other catalysts, the presence of these low-cost catalysts decreased the decomposition temperature of WPC, leading to the decrease of activation energy of the catalytic pyrolysis. Zeolites provided the highest aromatics yield among three low-cost catalysts, followed by FCC catalyst and  $\gamma$ -Al<sub>2</sub>O<sub>3</sub>, owing to its high acidity. However, because of the small pore size of zeolite, the

pyrolysis products catalysed over natural zeolite contained wide carbon number distribution and oxygenates compared to that over FCC catalyst and  $\gamma$ -Al<sub>2</sub>O<sub>3</sub>.

#### 1.3.2 Over non-commercial catalysts.

Ash, particularly biomass ash, has been explored as a catalyst in the pyrolysis process due to its intrinsic chemical properties and availability as a by-product of combustion processes [86]. Using ash as a catalyst in pyrolysis can enhance the breakdown of organic materials into valuable chemical products and fuels, offering an economically viable and environmentally friendly option for waste valorization.

Ash predominantly consists of metal oxides such as calcium oxide (CaO), magnesium oxide (MgO), potassium oxide (K<sub>2</sub>O), and sodium oxide (Na<sub>2</sub>O). These oxides can exhibit basic properties that make ash a potential catalyst in thermochemical conversions like pyrolysis [11]. The basic sites on ash particles can facilitate the cracking of large molecules and enhance the reforming of tar into smaller, more valuable gaseous products [87]. The catalytic activity of ash is primarily attributed to its alkaline metal content, which can influence the reaction pathways and product distribution during pyrolysis. The advantages of using Ash in pyrolysis process were concluded below [88]:

- 1) Cost-Effectiveness: Ash is a low-cost catalyst option since it is a waste product from biomass combustion and other industrial processes. This reduces the need for purchasing commercial catalysts and lowers the overall cost of the pyrolysis operation.
- 2) Availability: Given that ash is a by-product of numerous industrial processes, especially in power generation and biomass combustion facilities, it is readily available in large quantities.
- 3) Environmental Impact: Utilizing ash as a catalyst helps in waste management by repurposing an industrial by-product, thus contributing to environmental sustainability and reducing landfill use.
- 4) Enhanced Gas Production: Ash catalysis in pyrolysis has been shown to increase the yield of combustible gases like hydrogen and carbon monoxide by facilitating tar cracking and reforming processes.

Currently, many researchers have explored the potential of ash as the catalyst in the pyrolysis process. For instance, Loy *et al.* [89] used industrial waste coal bottom ash as a catalyst in the catalytic pyrolysis of rice husk; the results illustrated that using coal bottom ash as catalyst could increase the syngas production and decrease coke formation, and the hydrogen was increased by 8.4%. In another work, Wu *et al.* [90] used incineration bottom ash as catalyst

in the catalytic pyrolysis of biogas residue. The results suggested that incineration bottom ash had a negative effect on biogas residue pyrolysis. Similar to the aforementioned research, the bottom ash (BA), which is from the combustion of EPR to generate heat or electricity to power the biorefinery process, also exhibited great potential to be reused as a catalyst to upgrade bio-oil and decrease the activation energy of pyrolysis reactions [86,91]. This is because it contains high silica content and mesoporous surface area, which could improve the pyrolysis performance [88]. In addition, other impurities such as lime, alkalis, iron oxide, and alumina are also contained in BA to ensure good pyrolysis performance [86].

While ash shows potential as a catalyst in pyrolysis, several challenges and considerations need addressing. The chemical composition of ash can vary significantly depending on the source of the biomass and the combustion conditions. This variability can affect the consistency and predictability of catalytic performance in pyrolysis. Ash also can suffer from deactivation due to the sintering of active components at high pyrolysis temperatures or from fouling due to the deposition of heavy tars and metals [88]. In addition, there is a risk of metal leaching from ash into the product oil or gas, which can complicate downstream processing and pose environmental risks. In conclusion, while ash holds promise as a catalyst in pyrolysis for sustainable fuel production, maximizing its potential requires addressing its variability, enhancing its stability and activity, and ensuring environmental compliance in its handling and disposal.

Table 1.2 Commercial and non-commercial catalysts used in thermal processing techniques

	Thermochemical		Feedstocks: catalyst		
Feedstocks	conversion method	Catalyst	(mass ratio)	Observation	References
Poplar wood- polypropylene composite	Pyrolysis	ZnO, CaO, Fe <sub>2</sub> O <sub>3</sub> and MgO	(mass ratio)	CaO enhances the elimination of oxygen; MgO enhances the yield of alkene; The yield of alkene is the highest among the four catalyst and the yield of ketone and phenol are increased by using ZnO as catalyst; $Fe_2O_3 \ facilitated \ the \ yield \ of \ aromatics.$	[84]
Commercial WPC (PP, PE, woody sawdust, CaCO <sub>3</sub> )	Pyrolysis	HY (5.1), HBeta (25) and HZSM-5 (23)	1:2/1:5	The yield of aromatics by in-situ catalytic pyrolysis is higher than that by ex-situ catalytic pyrolysis; The yield of aromatics is following the order:  HBeta>HZSM-5>HY.	[82]
Commercial WPC (PP, PE, woody sawdust, CaCO <sub>3</sub> )	Pyrolysis	ZSM-5, HBeta, HDMZSM-5 and HDMBeta	In-situ: 1:1/1:0.25;1:0.5; 1:1; 1:2; 1:4;(Testing the effect of HDMZSM-5). Ex-situ: 1:3	The decomposition temperature of WPC is the lowest by using HDMBeta, followed by HDMZSM-5 and ZSM-5; HDMZSM-5 has the highest yield of aromatics, followed by ZSM-5, HDMBeta and Beta;	[78]
Corn stalk/HDPE composite	Pyrolysis	Activated carbon	1:1	The selectivity of aromatics was facilitated by increasing the H <sub>3</sub> PO <sub>4</sub> impregnation ratio (0-2.0) and carbonization temperature (600-750 °C) in activated carbon synthesized process, in which the highest yield of aromatics occurred when the impregnation ratio is 1:1 and carbonization temperature is 700 °C (64.01%).	[92]

Poplar wood/ HDPE composite	Pyrolysis	USY zeolite and HUSY zeolite	1:1	Both USY and HUSY have good performance in the decarboxylation and decarbonylation of the pyrolytic products, and USY has better performance than HUSY.	[83]
Poplar wood/ HDPE composite	Pyrolysis	HZSM-5, P-HZSM-5 with different P loading (0-10 wt.%)	1:1/2/4/8/16	Parent HZSM-5 enhanced the yield of aromatics and P-HZSM-5 facilitated the formation of light aliphatic hydrocarbons (C <sub>4</sub> -C <sub>12</sub> ); The selectivity of aromatics increased when catalyst to WPC ratio increased; P-HZSM-5 with 3.5 wt.% P loading has the highest yield	[93]
Ethanol processing residue/HDPE	Pyrolysis	Bottom ash	1:0.1	of light hydrocarbons (C <sub>4</sub> -C <sub>12</sub> ).  The addition of bottom ash could increase the yield of hydrocarbons and lower the activation energy.	[11]
Bio-oil produced from pyrolysis of rice hush	Pyrolysis	Rice hush ash	1:0.04	Rice husk ash can decrease the density and acidity of bio-oil and increase the heat value and the yield of easter compounds in the bio-oil.	[91]
Biogas residue	Pyrolysis	Biomass incineration bottom ash	4:1 / 9:1	The addition of bottom ash hindered the pyrolysis of biogas residue and increased the activation energy of pyrolysis process, while it favoured the biochar formation and stability.	[90]
Rice husk	Pyrolysis	Coal bottom ash and commercial catalysts	1:0.1	Compared with commercial catalyst, the pyrolysis process using coal bottom ash as catalyst has the lowest coke formation (3.65 wt.%) and high syngas	[89]

		(nickel and natural		(68.3 vol%). Furthermore, the hydrogen concentration	
		zeolite)		had increased 8.4 vol% in catalytic pyrolysis of rice	
				husk using coal bottom ash catalyst compared to non-	
				catalytic pyrolysis.	
Rice husk	D l	Rice hull ash	1.0.1	The addition of rice hull ash can lower the activation	F0.6
Rice nusk	Pyrolysis	Rice null ash	1:0.1	energy compared to non-catalytic pyrolysis process.	[86]
				HZSM-5 promoted the yield of monomethyl aromatics,	
				while HBeta and HY promoted the formation of	
Poplar wood/ PP	Dec 1 c '	HZSM-5, HBeta, HY		polyaromatics; The synergistic effect over HZSM-5 on	FO 4
composite	Pyrolysis	and HUSY	1:4	WPC pyrolysis enhanced of selectivity of	[94]
				polyaromatics while HBeta and HY favoured the	
				formation of mono aromatics.	
				The addition of fly ash lowered the reaction	
				temperature and favoured the conversion of biomass.	
XX/1	D 1 '	El 1	20.1	In addition, the by-product in pyrolysis process,	50.5
Wheat straw	Pyrolysis	Fly ash	20:1	heterogeneous wheat straw-fly ash bio-char, can	[95
				efficiently remove methylene blue, a model organic	
				pollutant, from water, than biochar alone.	

#### 1.3.3 Operation mode of catalytic pyrolysis

In general, catalytic pyrolysis process can be divided into two operation modes based on the location of the catalyst in the process, which are in-situ catalytic pyrolysis and ex-situ catalytic pyrolysis [96]. In the in-situ operation mode, the feedstock and catalyst are physically mixed, and the catalytic pyrolysis process takes place within a single reactor, where the catalyst can immediately interact with the volatiles released from the feedstock. Conversely, in the exsitu operation mode, the feedstock and catalyst are placed in two separate reactors. The pyrolysis vapor generated in the first non-catalytic reactor is carried to a secondary catalyst reactor, enabling the vapor to contact with the catalyst [97]. Park et al. [82] compared the effect of two operation mode on the products distribution in catalytic pyrolysis of WPC. They suggested that the ex-situ operation mode hindered the diffusion effect of reactants molecules into the catalyst pores, because the pyrolysis vapor produced in the first reactor was carried through the secondary reactor in a short time, thereby the diffusion of reactants molecules into catalyst pores was severely hindered. In addition, Yildiz et al. [97] pointed out the increasing residence time causing by adding the secondary catalytic reactor before condenser facilitated the thermal cracking and a loss in condensable compounds. In the in-situ operation mode, the reactor and catalyst can act as a fluidized bed and bubbling bed, which can enhance the mass transfer between the reactant and catalyst. But the accumulation ash content in the in-situ catalytic process was a problem need to be prevented for the long-term use of catalyst [98].

#### 1.4 Pyrolysis kinetics

The kinetic analysis of pyrolysis involves examining the rates of thermal degradation reactions and how these rates are influenced by temperature, the composition of the feedstocks, and the pyrolysis environment. Kinetics analysis is crucial for optimizing pyrolysis processes, designing reactors, and predicting the yield and composition of pyrolysis products [99]. Kinetic studies typically employ thermogravimetric analysis (TGA) to monitor the weight loss of samples as a function of temperature and time, providing data that can be modeled to extract kinetic parameters like activation energy ( $E_a$ ), pre-exponential factor (A), and reaction order (n). The pyrolysis process of solid materials can be described as the solid-state decomposition reaction [100]:

Solid feedstocks 
$$\rightarrow$$
 Gases + Volatiles + Char

Solid-state decomposition is a complex process which involves a multifaceted set of phenomena, making the precise prediction of the reaction mechanism challenging. In the

pyrolysis of WPCs, researchers employ two principal approaches to study the pyrolysis kinetics and reaction mechanism: model-free (iso-conversional) methods and model-fitting methods [101–104]. The expressions and parameters of different model free methods used in the research was listed in Table 1.3 and Table 1.4. Choudhary *et al.* [104] investigated the kinetic of biomass epoxy bio-composites by four kinds of model free methods including Friedman, KAS, FWO and Starink, they suggest that these iso-conversional methods could reveal changes in activation energy with the degree of conversion, thereby offering clues about the complexity of the reaction mechanism.

The presence of both wood fibers and plastic polymers in WPCs, each with its distinct thermal degradation pathway, introduces complexity into kinetic modeling. Traditional models that assume a single-step degradation mechanism are often inadequate for describing the multistep degradation behaviours of WPCs [105]. Consequently, researchers have turned to more sophisticated models, such as distributed activation energy models (DAEM), to better understand the reaction mechanism of WPC thermal degradation. In the work by Sun *et al.* [101], DAEM was employed to study the kinetics of WF (wood fiber)/PLA (polylactic acid) composites pyrolysis. In the DAEM model, it proposed an infinite number of irreversible, first-order parallel reactions, each characterized by different activation energies, occur simultaneously. To describe the range of these activation energies, a distribution function, denoted as  $f(E_a)$ , is employed. According to this model, both the  $E_a$  and the pre-exponential factor (A) can be determined experimentally through thermogravimetric analysis (TGA), as demonstrated in equations (1.1) and (1.2) [1].

$$\ln\left(\frac{\beta}{T^{2}}\right) = \ln\left(\frac{AR}{E_{a}}\right) + 0.6075 - \frac{E_{a}}{RT} (1.1)$$

$$\frac{V}{V^{*}} = 1 - \int_{E_{s}}^{\infty} f(E_{a}) dE_{a} = \int_{0}^{E_{s}} f(E_{a}) dE_{a} (1.2)$$

Where  $V^*$  represents the total volatile content of WPCs and V is the volatile produced as a function of time.

Table 1.3 Model free methods for activation energy assessment in the research

Method	Expressions	Plots	Reference
Friedman	$\ln\left(\frac{d\alpha}{dt}\right) = \ln[Af(\alpha)] - \frac{E_a}{RT}$	$\ln\left(\frac{d\alpha}{dt}\right)$ vs. $1/T$	[102–104]
Kissinger-	$\ln\left(\frac{\beta}{T^2}\right) = \ln\left(\frac{AR}{E_a g(\alpha y)}\right) - \frac{-E_a}{RT}$	$\ln\left(\frac{\beta}{T^2}\right)$ vs. $1/T$	[104]
Akahira-Sunose	$m(T^2) = m(E_a g(\alpha y))$ RT	$m_{T^2}$ vs. 1/1	[104]
Flynn-Wall-	$\ln \beta = \left(\frac{\ln AE_a}{Rg\alpha}\right) - 5.335 - \frac{1.0516E_a}{RT}$	$\ln \beta$ vs. $1/T$	[101,102,104]
Ozawa	$RT = \binom{Rg\alpha}{}$ RT	πρ νδ. 1/1	[101,102,104]

Starink 
$$\ln\left(\frac{\beta}{T^{1.92}}\right) = \ln\left(\frac{AR^{0.92}}{g(\alpha)E^{0.92}}\right) - 0.312 - \frac{1.0008E_a}{RT}$$
  $\ln\left(\frac{\beta}{T^{1.92}}\right) \text{ vs. } 1/T$  [101,104]

Coats-Redfern (modified)  $\ln\left[\frac{\beta}{T^2\left(1-2\frac{RT}{E_a}\right)}\right] = \ln\left[\frac{AR\left(1-\frac{2RT}{E_a}\right)}{\beta E_a}\right] - \frac{E_a}{RT}$   $\ln\left(\frac{\beta}{T^2}\right) \text{ vs. } 1/T$  [102]

Vyazovkin  $\Phi(E_a) = \sum_{i=1}^n \sum_{j\neq 1}^n \frac{J[E_a, T_i(t_\alpha)]}{J[E_a, T_j(t_\alpha)]}$  - [103]

Kissinger  $\ln\left(\frac{\beta}{T_m^2}\right) = \ln\left(\frac{AR}{E_a}\right) - \frac{E_a}{RT}$   $\ln\left(\frac{\beta}{T_m^2}\right) \text{ vs. } 1/T$  [102]

Table 1.4 All parameters used in the listed formulas and their units.

Parameters	Definition	value		
α	Conversion rate			
β	Heating rate			
T	Temperature (K)			
$\boldsymbol{E}_{\boldsymbol{a}}$	Activation energy (kJ mol <sup>-1</sup> )			
$\boldsymbol{A}$	Pre-exponential factor (S <sup>-1</sup> )			
R	Gas constant ( $J \text{ mol}^{-1} K^{-1}$ )	8.314		
$J[E_a,T_i(t_\alpha)]$	$J[E_a, T_i(t_\alpha)] = \int_{t_\alpha - \Delta_\alpha}^{t_\alpha} e^{-E_\alpha/RT_i(t)} dt$			

Model-fitting methods are commonly employed in pyrolysis kinetics to identify the most suitable reaction mechanism by fitting experimental data to predefined kinetic models [106]. These methods utilize the integral or differential forms of reaction rate equations to optimize kinetic parameters—such as  $E_a$ , A, and reaction order (n)—by minimizing the deviation between experimental and theoretical conversion curves. Typical models include first-order, diffusion-controlled, and nucleation-growth mechanisms. While model-fitting offers valuable mechanistic insights, it requires the assumption of a specific reaction model.

Among these approaches, the master-plot method provides a straightforward way to determine the reaction mechanism in solid-state decomposition [107]. It involves normalizing experimental conversion data and comparing it with theoretical curves derived from various kinetic models. By matching the experimental curve shape to these standardized plots, the most appropriate model can be identified, often without the need for prior knowledge of kinetic parameters such as  $E_a$  or A.

#### 1.5 Pyrolysis mechanism

#### 1.5.1 Pyrolysis mechanism of biomass

Due to the different composition of biomass component, the pyrolysis mechanism of lignocellulosic biomass involves complex thermochemical processes that occur in the absence of oxygen, leading to the decomposition of organic materials into various products such as biochar, bio-oil, and syngas [22]. Understanding the mechanism of biomass pyrolysis is crucial for optimizing process conditions and product yields.

The pyrolysis mechanism of biomass was shown in Fig 1.3. During biomass pyrolysis, a series of reactions occur parallel and sequentially, including dehydration, depolymerization, isomerization, aromatization, decarboxylation, and charring [108]. In general, the pyrolysis of biomass can be divided into four main stages: (i) Moisture removal, (ii) Devoltalization, (iii) Secondary reactions, (iv) Tar formation and cracking [109]. The first step in biomass pyrolysis is the removal of moisture from the biomass. As the temperature increases, water molecules evaporate from the biomass, requiring energy input but not contributing to the pyrolysis reactions. Devoltalization is the primary pyrolysis stage, where volatile components in the biomass are released as gases. This stage occurs at relatively low temperatures (typically between 200°C to 500°C). In this stage, biomass components such as cellulose, hemicellulose, and lignin undergo thermal decomposition, breaking down into smaller molecules. These smaller molecules undergo further decomposition and rearrangement, leading to the formation of various volatile compounds such as hydrocarbons, oxygenates, and aromatics. As volatile components are released, a solid residue called char or biochar is formed, consisting mainly of carbon-rich materials [110]. After devolatilization, secondary reactions take place in the remaining char. Char reacts with oxygen or steam to produce syngas (a mixture of hydrogen and carbon monoxide) through gasification reactions. In addition, char can also undergo partial oxidation reactions with oxygen, leading to the formation of carbon dioxide and water vapor [111]. The last stage is tar formation and cracking. During devolatilization, some of the volatile compounds condense to form tar, which is a complex mixture of organic compounds. Tar can undergo further decomposition through cracking reactions, producing lighter hydrocarbons, gases, and char [108].

The pyrolysis process of biomass is influenced by several factors such as temperature, heating rate, biomass composition, particle size and reactor design. Higher temperature and heating rate generally lead to faster pyrolysis rates and increase gas and liquid yield. The chemical composition of biomass, including the proportions of cellulose, hemicellulose, lignin,

and ash, influences the pyrolysis products and reaction pathways. The size of biomass particles and the design of the pyrolysis reactor can affect heat transfer rates and residence times, influencing the pyrolysis kinetics and product distribution [22,108].

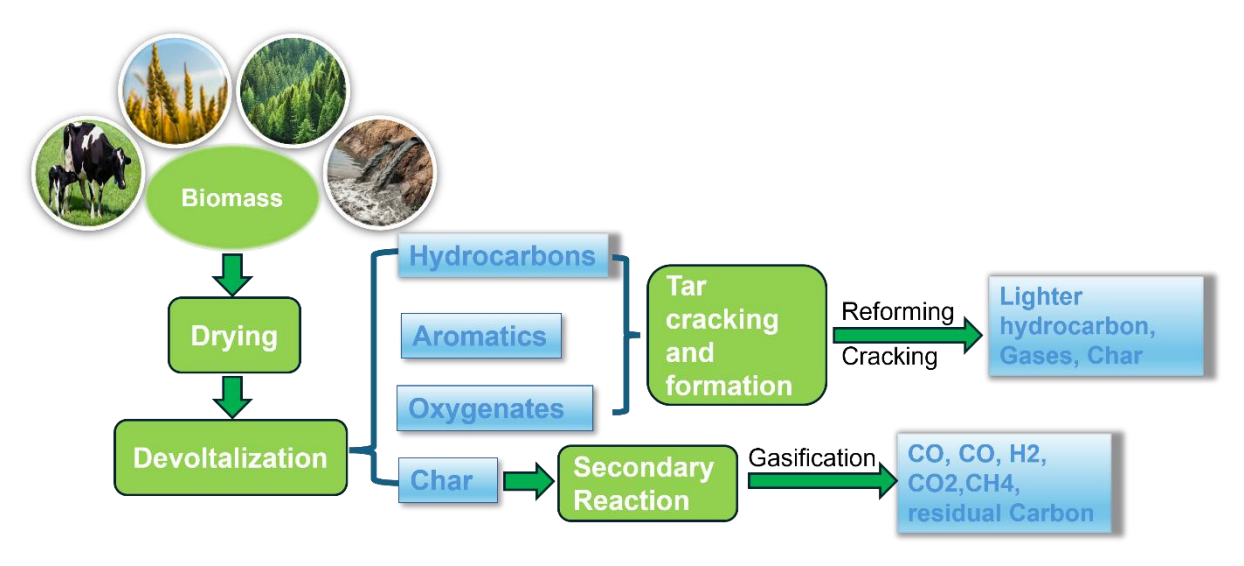


Fig 1.3 The pyrolysis mechanism of biomass

#### 1.5.2 Pyrolysis mechanism of plastic

During the pyrolysis process of plastic, the long polymer chain of plastics was thermally degraded into smaller molecules in the absence of oxygen, typically yielding liquid oil, gases, and a small amount of char [79]. This process is used to recycle plastics into usable fuels and chemicals. In general, different type of plastics have different composition, so the specific mechanism and products can vary depending on the type of plastic being processed.

Fig 1.4 illustrated the pyrolysis mechanism of plastics. Typically, at the start of pyrolysis, the plastic is heated to high temperatures (between 300 °C and 900 °C). This heating must be controlled to prevent combustion, as the presence of oxygen can lead to burning rather than pyrolysis. As the temperature increases, the long polymer chains in plastics start breaking down into smaller hydrocarbon chains. This process is known as cracking. The type of plastic determines the bonds that break and the temperature at which these breaks occur. In the resulted products, lighter and shorter hydrocarbon chains often form gases such as methane, ethane, propane, and butane. Medium-length chains condense into a liquid oil that can be further refined and used as a fuel similar to diesel or gasoline. Longer chains and aromatic compounds can form waxy residues or solid char, depending on the specific conditions of the pyrolysis process [112]. The various hydrocarbons are then distilled and collected. The gases can be captured and used as fuel or for energy generation. The oil can be refined and used directly as

a fuel or as a feedstock for producing new plastics or other chemicals. Any solid residues, such as char, are usually processed further or disposed. Char can sometimes be used for carbon black production or as a soil amendment. The efficiency and selectivity of pyrolysis in producing desirable products (like liquid oil vs. gas) can be influenced by factors such as the type of plastic, the temperature profile, the heating rate, and the reactor design [69].

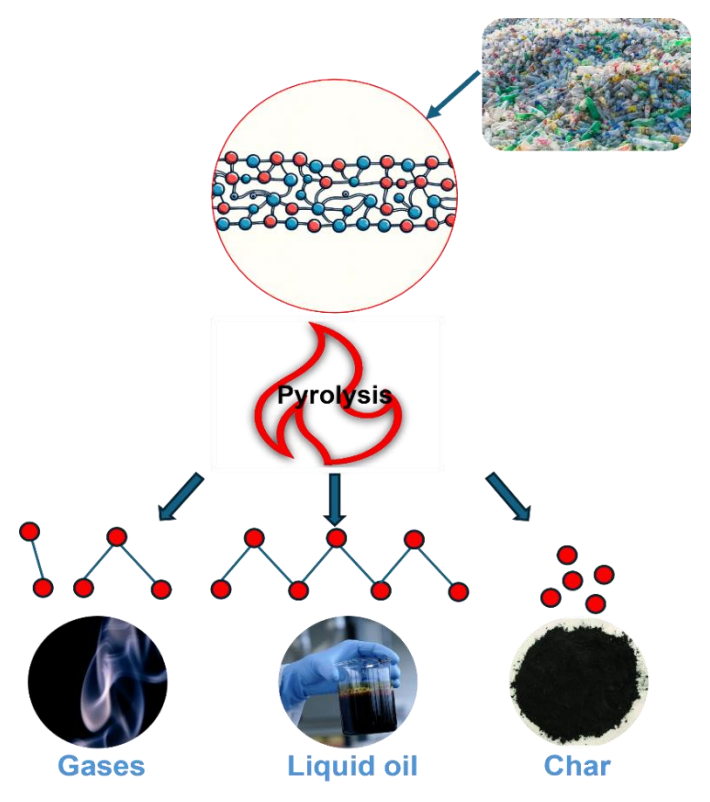


Fig 1.4 The pyrolysis mechanism of plastics

#### 1.5.3 Pyrolysis mechanism of WPC

As mentioned before, WPCs are made by combining wood fibres or wood flour with plastics, often including additives that enhance their properties. The thermoplastic component in WPCs is mainly polyethylene (PE), polypropylene (PP), or polyvinyl chloride (PVC), which lack oxygen in their molecular structure and are rich in carbon and hydrogen [113]. The other main component in WPCs is wood fibres, which is a hydrogen-deficient feedstock [114]. The bio-oil produced from solo pyrolysis of wood fibres usually has several limiting factors, including a high concentration of oxygenated compounds, significant viscosity, high water content, and a relatively low heating value [115]. The integration of hydrogen-rich thermoplastics within WPCs for pyrolysis introduces an appropriate approach to overcoming these limitations. During the pyrolysis process, the thermoplastic components can act as hydrogen donors, facilitating hydrogenation reactions that reduce the oxygen content in the

bio-oil. This reduction in oxygenates directly contributes to lowering the viscosity, decreasing the water content, and enhancing the heating value of the bio-oil [116–118]. Furthermore, the pyrolysis of wood components within WPCs generates free radicals, which can significantly influence the decomposition of the thermoplastic materials present in the composite [119]. Specifically, they can promote the breakdown of plastic polymers, thereby increasing the availability of hydrogen for hydrogenation reactions and enhancing the overall efficiency of the pyrolysis process [120]. This synergistic interaction between the decomposition of wood fibres and plastics not only improves the yield and quality of the bio-oil but also contributes to a more efficient conversion of WPCs into valuable products [121]. Thus, WPCs, being a blend of biomass and plastic, present a balanced feedstock that can generate a spectrum of chemicals and fuels upon pyrolysis [122]. Moreover, WPCs are often made from recycled plastics and wood waste, making their pyrolysis a promising recycling route. This aligns with circular economy principles by diverting waste from landfills and reducing the demand for virgin resources [123]. Compared with co-pyrolysis of wood fibres and thermoplastics, WPCs provide a more intimate and uniform mixing of wood fibres and plastics at the molecular level than is typically achievable by simply co-feeding wood and plastics into a pyrolysis reactor. This close interaction facilitates synergistic effects that can lead to more efficient thermal degradation of both components [124]. In addition, the uniform mixture of wood and plastic in WPCs also can lead to a more controlled and consistent pyrolysis process, resulting in a higher yield of desirable pyrolysis products. Co-pyrolysis of separate wood fibres and plastics may require significant pre-processing to achieve optimal mixing and size reduction to ensure efficient heat transfer and chemical interaction during pyrolysis [125]. In contrast, WPCs are already a homogenized material, reducing the need for extensive pre-processing and potentially lowering overall processing costs. Pyrolyzing WPCs allows for the optimization of process conditions (such as temperature, heating rate, and residence time) tailored to the specific composition of the composite material. This optimization can improve the efficiency and selectivity of the pyrolysis process, enabling better control over the production of specific chemicals or fuels [126]. In co-pyrolysis, achieving such optimized conditions for both wood and plastics simultaneously can be more challenging due to their differing thermal degradation behaviours. Utilizing WPCs, which often contain recycled plastics and wood waste, presents an environmentally friendly solution for managing WPC waste, which might otherwise end up in landfills. Compared to co-pyrolysis, which might involve the use of virgin or separately collected materials, pyrolysis of WPCs directly aligns with sustainability goals by reducing waste and promoting the recycling of composite materials [127].

The pyrolysis mechanism of WPCs involves the thermal decomposition of both wood fibres and plastics. Initially, wood components undergo dehydration, releasing water and volatile compounds. This is followed by the breakdown of cellulose, hemicellulose, and lignin into smaller molecules. Cellulose and hemicellulose decompose at lower temperatures, producing a range of oxygenated compounds, while lignin decomposes over a wider temperature range, contributing to the formation of aromatic hydrocarbons [128]. Simultaneously, the plastic components undergo a different set of reactions, typically starting with chain scission, which breaks the long polymer chains into shorter fragments. Depending on the type of plastic, various hydrocarbons and hydrocarbon gases are released. For example, polyethylene and polypropylene yield waxes and oils rich in aliphatic hydrocarbons, while polyvinyl chloride produces hydrochloric acid along with a variety of hydrocarbons [79]. The interaction between decomposing wood and plastic components can influence the pyrolysis process and the product distribution. Sun et al. study the pyrolytic behaviour of WPC made from poplar wood and HDPE [129]. It was observed from the study that due to the lower decomposition temperature of wood fibre compared to HDPE, the free radical formed during the pyrolysis of wood fibre participate in the decomposition reactions of HDPE, yielding light olefins. Sun et al. examined the interactions between wood fibre and polylactic acid (PLA). The study suggested that acidic substances released during wood fibre pyrolysis could catalyse the breaking of alkoxy and acyloxy bonds on PLA chains [101]. Lin et al. [20] provided additional insights into the interactions among hemicellulose, cellulose, lignin, and polypropylene (PP) during WPC pyrolysis. Their findings indicate that cellulose could hinder the intermolecular hydrogen transfer reaction while PP can stabilize the levoglucosan radicals by hydrogen abstraction from the hydrogen-rich PP, leading to the increase in anhydrosugars and aliphatic hydrocarbons [130,131]. Further studies explored the synergistic effect between hemicellulose and plastics, and they found they found plastic could promote the dehydration and recyclization reactions of hemicellulose-derived oxygenates, favouring the formation of cyclopentenones [132,133]. Plastics were found to alter the pathways for removing oxygencontaining functional groups in lignin, favouring gas and water formation through decarboxylation, decarbonylation, and dehydration reactions [134]. Additionally, the presence of PP was shown to promote lignin pyrolysis by abstracting hydrogen, which competes with the intermolecular hydrogen transfer reaction of polymers. All these biomass-derived components promoted the β-scission of PP and facilitated the formation of light hydrocarbons [8].

WPCs represent a promising feedstock for pyrolysis, offering a sustainable way to recycle mixed waste materials while producing valuable chemicals and fuels. The advantages of WPC pyrolysis over the co-pyrolysis of separate plastics and wood.

#### 1.6 The background of the project

As globalization progresses and energy demands increase, the environmental issues and supply limitations of traditional fossil fuels become increasingly prominent. Biomass energy, due to its renewable and environmentally friendly characteristics, is considered an important alternative to fossil fuels [135,136]. The development and utilization of biomass energy, especially in the field of thermochemical conversion, are crucial for alleviating the energy crisis and reducing environmental pollution.

Corn stover, the leftover plant material after harvesting the corn grain, represents a significant portion of agricultural waste globally [137]. Traditionally viewed as a byproduct with limited utility beyond animal feed and bedding, recent advances in biomass utilization have paved the way for more sophisticated applications such as biofuel production, biogas generation, and even as a matrix for material science applications. One such novel application is the development of WPCs where corn stover is integrated with plastic materials to produce composites with enhanced physical properties suitable for various construction and manufacturing uses [63].

The focus of this doctoral thesis is on the pyrolysis behaviour of corn stover, specifically examining the thermal degradation properties of different parts of the stover. Pyrolysis, the thermal decomposition of materials at elevated temperatures in an inert atmosphere, is a critical process for converting biomass into biochar, bio-oil, and syngas, which are valuable as fuels and chemical feedstocks. However, no matter which biomass material is used for pyrolytic production of biofuels, a common technical bottleneck is the high oxygen content and elevated acidity in the resulting bio-oil [138]. To solve this problem, the co-pyrolysis of biomass and hydrogen sufficient feedstock, such as rubber [138], polypropylene [130], polyethylene [139], polyvinyl chloride [140] and polystyrene [141] was introduced to increase the carbon and hydrogen content, which further increased the higher heating value of the resulting fuel [142]. With co-pyrolysis of biomass in the presence of a polymer, the oxygenate content in the produced bio-oil decreases, while the yields of aromatic hydrocarbons increase. Nevertheless, research on the characteristics of co-pyrolysis of different corn stem tissues and plastic is still limited; hence, the effect of different corn stem tissues on co-pyrolysis with plastic calls for

deeper evaluation to identify the role of utilizing waste plastic and agricultural products for improved product quality.

Further, this research explores the pyrolysis of the residual biomass left after the biorefining process of corn stover. Compared to the direct use of lignocellulosic biomass for biofuels production, utilizing the solid residual from second-generation bioethanol plant can significantly improve the economic feasibility of biorefineries and simplify the downstream solid waste management [63]. In a typical second-generation bioethanol plant using corn cob as the feedstock, the ethanol-processing residue (EPR) is remained as a solid waste after saccharification and fermentation. Due to the high content of lignin and non-hydrolysable holocellulose in EPR, it also can be considered as an ideal feedstock for biofuel production [143]. By studying the thermal behaviour of this residue, it is possible to tailor pyrolysis processes to maximize the yield and quality of the desired products. In order to further improve the quality of bio-oil, catalytic co-pyrolysis of biomass and waste plastic is advocated. The bottom ash (BA), which is from the combustion of EPR to generate heat or electricity to power the biorefinery process, also exhibited great potential to be reused as a catalyst to upgrade biooil and decrease the activation energy of pyrolysis reactions [86]. This is because it contains high silica content and mesoporous surface area, which could improve the pyrolysis performance. In addition, other impurities such as lime, alkalis, iron oxide, and alumina are also contained in BA to ensure good pyrolysis performance [86]. Hence, the BA was introduced to the catalytic co-pyrolysis of EPR and HDPE to investigate the catalytic performance of BA.

The thesis also investigates the pyrolytic behaviour of WPCs which was made from biorefinery residues. Compared to directly employing lignocellulosic biomass as reinforcement in WPCs production, using the solid residue from biorefinery plant can markedly enhance the economic feasibility and streamline the management of solid waste in subsequent stages. WPCs made from biorefinery residues not only help in adding value to what would otherwise be waste materials but also contribute to the sustainability of plastic products by partially replacing the petrochemical components with renewable biomass. The pyrolysis behaviour of these composites is crucial for understanding their stability and decomposition profiles, which are important for both their processing and end-of-life scenarios.

Lastly, the impact of aging on the pyrolysis behaviour of wood-plastic composites is examined. Aging of WPCs can occur due to environmental factors such as exposure to UV radiation, moisture, and thermal cycles, leading to changes in their physical and chemical properties. These changes could significantly influence the pyrolysis behaviour of aged WPCs, affecting their decomposition temperature, the rate of weight loss, and the composition of the

pyrolysis products. By understanding these aspects, it is possible to predict the lifecycle impacts of WPCs and optimize their formulation for better performance and durability.

This comprehensive study on the pyrolysis behaviour of corn stover and its derived materials contributes to the broader field of biomass utilization and sustainable materials science. By advancing knowledge in these areas, this research supports the development of technologies and materials that are environmentally friendly and economically viable, addressing some of the critical challenges in managing agricultural waste and creating value-added products.

# 1.7 Project aims and objectives

The overarching aim of this research is to develop an integrated thermochemical framework for the circular valorisation of biomass—plastic hybrid residues, progressing from raw lignocellulosic feedstocks to aged bio-composites. By systematically investigating the pyrolytic behaviour, catalytic enhancement, and kinetic mechanisms at each transformation stage, this study aims to provide scientific and technological insights for sustainable waste-to-resource conversion. The specific objectives for the work are described below.

# **Objective 1: Raw biomass co-pyrolysis (Chapter 2)**

To investigate the thermal decomposition and co-pyrolysis behaviour of various corn stalk tissues (stem, husk, ear, cob, and leaf) blended with HDPE under different heating rates using TGA. To determine how tissue structure influences decomposition kinetics and synergistic interactions with HDPE by applying iso-conversional kinetic methods (FWO, KAS) and machine-learning models (RF, GBRT) for predictive analysis.

Expected measurable outcomes: activation energies for each blend, correlation coefficients (R<sup>2</sup>) of ML predictions, and product profiles from Py-GC/MS identifying products distribution.

# **Objective 2: Catalytic valorisation of biorefinery residue (Chapter 3)**

To evaluate the catalytic co-pyrolysis of EPR and HDPE using BA recovered from the same biorefinery as a circular catalyst. To quantify the influence of BA on thermal decomposition, activation energy, and product yield using TGA, kinetics analysis, and Py-GC/MS.

Expected outcomes: reduction of activation energy, enhanced deoxygenation and aromatic selectivity, and demonstration of a closed-loop valorisation of biorefinery waste.

# **Objective 3: Pyrolysis of bio-based composite (Chapter 4)**

To analyse RSPR/PLA composite's pyrolysis behaviour and kinetics under nitrogen atmosphere. To identify the synergistic effects between RSPR and PLA during decomposition via TG–FTIR, Py–GC/MS, and kinetic modelling (FWO, KAS, master-plot).

Expected results: lower average activation energy, confirmation of the reaction mechanism model and synergistic effect between RSPR and PLA.

# **Objective 4: Aging effects on WPCs (Chapter 5)**

To examine the impact of weathering on the pyrolysis and kinetic behaviour of WPCs prepared from EPR and HDPE. To determine how UV aging alters crystallinity, decomposition rate, and product distribution using TGA, TG-FTIR, and Py-GC/MS.

Expected measurable indicators: increase in residue yield,  $E_{\alpha}$  reduction, and product shifts toward short-chain hydrocarbons with decreased oxygenates.

# 1.8 Thesis plan

This thesis is organized into six chapters, forming a coherent research framework that progressively advances from the pyrolysis of raw biomass to the circular valorisation of its derivative composites. Each chapter builds upon the previous one, integrating material evolution, catalytic enhancement, and environmental durability to establish a comprehensive understanding of biomass–plastic hybrid conversion.

Chapter 1 provides a general introduction to the background and significance of biomass and plastic co-pyrolysis for sustainable fuel and material production. It reviews recent advances in thermochemical conversion, catalytic upgrading, and AI-assisted kinetic modelling, and defines the research objectives and scope of the study.

Chapter 2 investigates the co-pyrolysis of raw corn stalk tissues (stem, husk, ear, cob, and leaf) with HDPE. This chapter establishes the fundamental thermal behaviour, decomposition kinetics, and synergistic interactions between unprocessed lignocellulosic biomass and plastics, laying the groundwork for subsequent studies on processed residues.

Chapter 3 extends the investigation to the EPR obtained from the same corn-based biorefinery. Building on Chapter 2, this study examines how biorefinery treatment alters the structural and chemical characteristics of the biomass, influencing its co-pyrolysis behaviour with HDPE. The use of in-situ BA as a catalyst exemplifies a closed-loop valorisation of industrial waste within the biorefinery system.

Chapter 4 further develops the concept of circular utilisation by employing EPR-derived residues as reinforcement to fabricate a RSPR/PLA composite. The chapter explores its thermal degradation, gas evolution, and products distribution during pyrolysis, linking biorefinery residues to functional bio-based plastics and demonstrating a step toward sustainable composite design.

Chapter 5 continues this material lifecycle by investigating the artificially weathered WPCs derived from EPR and HDPE. Through thermogravimetric and kinetic analyses, this chapter reveals how aging-induced physicochemical changes affect decomposition mechanisms and product distributions, providing insights into end-of-life management and recycling of WPCs.

Finally, Chapter 6 summarises the main findings, highlights the novelty of the integrated circular approach—from raw biomass to aged composite—and proposes future perspectives for process optimisation, catalyst development, and AI-driven predictive modelling in biomass—plastic hybrid pyrolysis.

# 1.9 Identified knowledge gaps

Although extensive work has been conducted on biomass and plastic pyrolysis, several key knowledge gaps remain unresolved, limiting the translation of laboratory findings into practical, circular-economy applications. This thesis identifies the following gaps as critical scientific and technological barriers:

#### 1. Feedstock structural effects

Current studies seldom distinguish the tissue-specific structural differences within lignocellulosic feedstocks. The lack of understanding of how stem, husk, cob, or leaf microstructures affect thermal decomposition kinetics and product distribution restricts optimisation of feedstock preparation and process control.

# 2. Catalytic upgrading with industrial byproducts

Most catalytic pyrolysis research relies on expensive or synthetic catalysts. The potential of industrial byproducts, such as bottom ash from biorefineries, remains underexplored. This gap hampers the development of low-cost, circular catalytic systems that could enhance both economic feasibility and environmental performance.

# 3. Composite and residue valorisation

Existing literature primarily focuses on pure biomass or plastics, with limited attention to hybrid and residual feedstocks (e.g., ethanol-processing residue, RSPR/PLA composites, WPCs). These complex materials dominate real-world waste streams, yet their synergistic pyrolysis behaviour and kinetic interactions are poorly understood.

# 4. Aging and environmental resilience

Few studies have examined how weathering and environmental exposure alter the physicochemical properties of lignocellulose–plastic composites. The absence of such data limits the ability to design realistic end-of-life pyrolysis strategies and conduct comprehensive lifecycle assessments.

# 5. Data-driven process understanding

Traditional kinetic models depend heavily on experimental datasets and manual fitting. The limited adoption of machine-learning approaches constrains predictive accuracy and scalability in modelling pyrolysis kinetics, leaving a gap in data-driven process optimisation.

# **Chapter 2**

Co-pyrolysis corn stalk and high-density polyethylene: emphasized on the differences of fibrous tissues on thermal behaviour and kinetics

# 2. Co-pyrolysis corn stalk and high-density polyethylene: emphasized on the differences of fibrous tissues on thermal behaviour and kinetics

This chapter investigates the thermal behaviour and co-pyrolysis performance of individual corn stalk tissues (stem, husk, ear, cob, and leaf) blended with high-density polyethylene (HDPE) under a nitrogen atmosphere using TGA. The study highlights the influence of tissue-specific structural differences on thermal decomposition, product distribution, and reaction kinetics. Furthermore, machine learning models, including random forest and gradient boosting regression, were applied to predict mass loss behaviour, demonstrating the potential of data-driven tools in pyrolysis process modelling. The results underscore the importance of tissue-level feedstock separation to optimize co-pyrolysis outcomes.

#### 2.1 Introduction

In a typical biomass pyrolysis process, biomass will break down into bio-oil, gaseous products, and solid fraction [144]. Among them, the bio-oil production is always rich in aromatic compounds, which are highly valued for their use in various chemical industries. To date, a wide variety of biomass materials, such as wood, protein [145], microalgae [138], sewage sludge [146], and lignocellulosic agricultural residuals [100] have been recognized as potential sources for bio-oil production due to their low-cost and abundant supply [147].

In previous work [148], because of the differences in chemical compositions and various types of cells and interior structures, the pyrolysis kinetics and thermal behaviour of different types of lignocellulosic fibres were proved to be distinctively different. For example, Biswas et al. [149] studied the pyrolysis features of 4 common agricultural biomass residues namely: corn cob, wheat straw, rice straw and rice husk, and found that the bio-oil yields from each different type of biomass residue were different due to the different composition of the agricultural biomass. Similar results were also obtained in Çepelioğullar and Pütün's study [150], in which another 4 biomass materials (Cotton stem, hazelnut shell, sunflower residue, and arid land plant Euphorbia rigida) were co-pyrolyzed with polyvinyl chloride and polyethylene terephthalate, respectively. The Phenolic compound contents and aliphatic functional groups in the bio-oils production also varied widely. Zhou et al. [151] compared the pyrolysis characteristics of lignin with softwood, herbaceous and hardwood in absence and presence of zeolite catalyst. The results indicate herbaceous produce higher yields of phenolic

compounds (16.26 %) and aromatic hydrocarbons (8.67 %) in the final products than softwood and hardwood; this can be attributed to their highly branched polymer structure.

No matter which biomass material is used for pyrolytic production of biofuels, a common technical bottleneck is the high oxygen content and elevated acidity in the resulting bio-oil [138]. To solve this problem, the co-pyrolysis of biomass and hydrogen sufficient feedstock, such as rubber [138], polypropylene [152], polyethylene [139], polyvinyl chloride [140] and polystyrene [141] was suggested to increase the carbon and hydrogen content, which further increased the higher heating value of the resulting fuels [142]. With co-pyrolysis of biomass in the presence of a polymer, the oxygenate content in the produced bio-oil decreases, while the yields of aromatic hydrocarbons increase [82]. Kai *et al.* [153] identified the superiority of using plastics in co-pyrolysis with corn stem, for example, HDPE, which causes white pollution if it is not properly managed, offers improved biofuel composition in co-pyrolysis through deoxygenation.

Corn stalk, always treated as agriculture waste, is one of the most abundant lignocellulosic biomass resources to produce renewable energy and chemicals [3,154]. Corn stalk pyrolysis has been extensively studied, including the effects of pretreatments on corn stalk pyrolysis and the investigation of volatile reactions during corn stalk pyrolysis [155,156]. Because of the diverse function of the plant organs and tissues, the chemical composition and cell structures are also different in the same plant, leading to complex chemical pathways during thermochemical treatment [157]. For instance, previous researchers have demonstrated that the different corn stalk tissues showed differences in depolymerization, scarification and biological conversion abilities [3,158]. The composite materials reinforced by different corn stalk tissues also showed differences in physical and mechanical properties [137]. Wang et al. [159] investigated the corn stalk pyrolysis fraction, the results indicated that the different chemical inhomogeneity was the main reason for the behaviour differences. Nevertheless, to our best knowledge, research on the characteristics of co-pyrolysis of different corn stalk tissues and plastic is still rarely reported. Actually, characterizing the thermal behaviour differences of various corn stalk tissues is highly significant. The upstream harvesting and supply chain of the raw biomass material can be easily categorized into different tissues, allowing for more efficient processing and utilization [3,137,158]. The investigation towards the tissue's differences could guide to the intensification of the co-pyrolysis processes target to enhanced valorisation potentials and environmental benefits of the low-valuable corn stalk and recycled plastic. Therefore, a deeper evaluation of the effects of different corn stalk tissues on copyrolysis with plastic is necessary to understand the role of utilizing waste plastic and agricultural products in enhancing product quality.

In this chapter, TGA, the commonly applied thermo-analytical technique for thermal study, is used to evaluate the thermal behaviours of co-pyrolysis of the blends consisted of different corn stalk tissues with HDPE. In addition, Py-GC/MS test was conducted to identify the effect of different corn stalk tissues on the pyrolytic products distributions. The model free methods including Kissinger-Akahira-Sunose (KAS) [160], Flynn-Wall-Ozawa (FWO) [152] and master-plot method were used to investigate the kinetics of the co-pyrolysis. Moreover, machine learning methods were adopted to predict the TG curves via the temperature, heating rates, and the chemical compositions of the corn stalk tissues.

# **Novelty statement**

This chapter introduces a novel comparative approach to elucidate tissue-specific effects on the co-pyrolysis behaviour of lignocellulosic biomass and plastic. By isolating and analysing different corn stalk tissues (stem, husk, ear, cob, and leaf), the study reveals how physicochemical composition influence thermal decomposition kinetics, product selectivity, and synergistic interactions with HDPE. The incorporation of machine learning models (RF, GBRT) for weight-loss prediction provides an additional data-driven dimension, offering a predictive and scalable framework for pyrolysis analysis. This chapter establishes the fundamental basis for understanding feedstock heterogeneity, upon which the subsequent residue and composite studies are built.

#### 2.2 Materials and methods

This section outlines the experimental procedures, materials, and analytical techniques employed in this study. It includes detailed descriptions of the feedstock preparation, characterization methods, pyrolysis and co-pyrolysis experiments, and the analytical tools used to evaluate thermal behaviour, reaction kinetics, and product distribution. Both conventional thermogravimetric analysis and advanced spectroscopic techniques were utilized, alongside machine learning algorithms and kinetic modelling approaches, to ensure a comprehensive understanding of the thermal decomposition processes and interactions between biomass and polymeric materials. The following subsections present these methodologies in detail.

#### 2.2.1 Materials

The corn stalk was kindly provided by China Agricultural University and was harvested in an experimental field in City Zhuozhou, China. The corn stalk tissues including stem, husk, ear, cob, and leaf were separated and dried at 105 °C overnight. Then, the dried corn stalk tissues were milled into > 60 meshes and stored at -20 °C before use. HDPE 600 (density of 0.956 g/cm³, melting point of 136 °C, size of > 60 meshes, and a melt flow index (MFI) of 1.8 g/min) was purchased from Beijing Jinma Plastic Co. Ltd., China. The corn stalk tissues/HDPE blends were mixed by a laboratory mortar with a mass ratio of 1: 1.

#### 2.2.2 Characterization of corn stalk tissues and HDPE

The chemical compositions of the corn stalk tissues were determined by the method of the National Renewable Energy Laboratory of USA (NREL) [161], and the detailed experimental protocols are provided in the Appendix 3. Water content, volatiles matter, fixed carbon and ash content in the tissues were determined following the national standard of China (GB/T 212-2008 and GB/T 28731-2012) [146]. In addition, ultimate analysis was employed to determine the elemental composition of corn stalk tissues and HDPE using an element analyser. The detailed experimental procedure are described in the Appendix 1 and 2. All measurements were performed in triplicate (n = 3) to ensure reproducibility, and the mean values are reported.. The proximate analysis and ultimate analysis results of corn stalk tissues and HDPE are listed in Table 2.1, and the biochemical compositions of the corn stalk tissues are listed in Table 2.2.

#### 2.2.3 Thermal test

The pyrolysis behaviours of corn stalk tissues, HDPE, and their mixtures, were analysed by a thermogravimetric analyser (Q500, TA, USA) under a nitrogen atmosphere at a flow rate of 60 mL/min. The materials were heated from room temperature (~25 °C) to 650 °C with heating rates of 10 °C/min, 20 °C/min and 40 °C/min. Three replicates were conducted in each test.

Table 2.1 Proximate and ultimate analysis of corn stalk tissues and HDPE.

Samples		HDPE	Stem	Husk	Ear	Cob	Leaf
	Water	ND	4.55±0.20	7.12±0.02	5.69±0.10	5.9±0.0	6.12±0.0
Proximate analysis <sup>a</sup>	water	ND		7.12±0.02	J.09±0.10	8	3
	Volatiles	100±0.	85.34±0.15	75.35±0.78	76.81±0.95	74.1±0.	$74.74\pm0$ .
		05			70.81±0.93	88	65

	Fixed	ND	7.79±0.30	13.81±0.35	12.51±0.19	17.86±0	10.62±0.
	carbon	ND	7.79±0.50	13.01±0.33	12.31±0.19	.40	33
	Ash	NID	2 22 + 0 12	2.72+0.22	4.00+0.10	2.14±0.	$8.52 \pm 0.1$
		ND	2.32±0.13	3.72±0.22	4.99±0.10	05	1
	С	85.55±	44.50+0.20	42.35±0.22	43.86±0.12	44.74±0	41.75±0.
	C	0.12	44.59±0.20	42.33±0.22	43.80±0.12	.08	13
	Н	$14.31 \pm$	5.06+0.15	( 04+0 25	7.06+0.10	5.85±0.	$5.82 \pm 0.1$
		0.05	5.86±0.15	6.04±0.25	5.86±0.10	10	4
Ultimate	O*	$0.00\pm0.$	40.46+0.14	49.9±0.33	40.50.015	48.56±0	50.59±0.
analysis <sup>a,b</sup>	$O^*$	02	48.46±0.14		48.50±0.15	.22	17
	3.7	$0.06\pm0.$	0.72 : 0.00	1 22 : 0 10	1.50.0.15	$0.58\pm0.$	1.51±0.1
	N	02	$0.72\pm0.09$	1.32±0.10	1.58±0.15	11	0
	~	$0.08\pm0.$	0.25.0.00	0.20.002	0.20.005	$0.27 \pm 0.$	$0.33 \pm 0.0$
	S	01	$0.37\pm0.09$	$0.39\pm0.02$	$0.20\pm0.05$	10	3

<sup>&</sup>lt;sup>a</sup> On dry mass fraction basis (wt%), <sup>b</sup> On dry and ash-free basis (wt%), \* Calculated by difference.

Table 2.2 The chemical composition of different corn stalk tissues<sup>a</sup>.

Samples	Cellulose (wt%)	Hemicellulose (wt%)	Lignin (wt%)	Ash (wt%)	Soluble constituents (wt%)
Stem	25.56±2.22	34.59±1.90	20.51±1.10	1.89±0.33	17.47±0.50
Husk	24.11±2.15	45.74±2.15	$11.05 \pm 0.95$	$1.50\pm0.11$	$17.60 \pm 0.45$
Ear	$17.00\pm1.25$	$36.44 \pm 2.50$	$20.28 \pm 0.88$	$4.49 \pm 0.15$	$21.79 \pm 0.95$
Cob	$18.00\pm2.31$	33.53±2.25	21.60±1.01	$3.65 \pm 0.20$	$23.21 \pm 0.99$
Leaf	$18.92 \pm 1.33$	40.24±1.96	$13.10\pm0.59$	$1.89\pm0.28$	$23.32 \pm 1.00$

<sup>&</sup>lt;sup>a</sup> On dry mass fraction basis (wt%)

# **2.2.4 Py-GC/MS**

The volatile products from the co-pyrolysis of different corn stalk tissue/HDPE blends were analysed using Py-GC/MS (Frontier-EGA/PY3030D-JP, Thermo Fisher TRACE 1310, ISQ LT, USA). Approximately  $0.8 \pm 0.1$  mg of each dried and ground sample (<0.2 mm) was loaded into a deactivated stainless-steel sample cup and subjected to pyrolysis at 600 °C with a heating rate of 20 °C/ms and a holding time of 20 s. The transfer line between the pyrolyzer and the GC/MS was maintained at 300 °C to prevent condensation of volatile components. The GC/MS injector temperature was set to 300 °C with a split ratio of 80:1, and helium was used as the carrier gas at a constant flow rate of 1 mL/min. Chromatographic separation of the

pyrolysis vapours was achieved on a VF-17MS capillary column (30 m  $\times$  0.25 mm i.d.  $\times$  0.25  $\mu$ m film thickness). The initial column temperature was maintained at 40 °C for 12 s, then increased to 200 °C at 5 °C/min, and subsequently to 300 °C at 20 °C/min, where it was held for 5 min.

The mass spectrometer was operated in electron ionization (EI) mode at 70 eV, scanning from m/z 35 to 500. The MS ion source and quadrupole temperatures were 230 °C and 150 °C, respectively. Compound identification was performed by comparing the obtained spectra with the NIST 17 mass spectral database. The relative peak areas in the total ion chromatogram (TIC) were used for semi-quantitative estimation of product distribution among different chemical families (e.g., furans, phenolics, ketones, esters, hydrocarbons). Method blanks were analysed between runs to confirm the absence of carryover.

#### 2.2.5 Kinetics

Most of the solid-state pyrolysis reactions involve several intermediate stages and a series of reaction mechanisms [109]. Consequently, it is difficult to develop a kinetic model to fully understand the mechanisms. Therefore, some assumptions are made to simplify the kinetic model [162]. In general, the rate of non-isothermal solid degradation is described by the following equation [147]:

$$\frac{d\alpha}{dt} = kf(\alpha) \tag{2.1}$$

where  $\alpha$  is the conversion rate, and can be calculated by:

$$\alpha = \frac{m_0 - m_t}{m_0 - m_f} \tag{2.2}$$

where  $m_0$  is the initial sample mass,  $m_t$  is the mass sample at time t, and  $m_f$  is the final mass of sample. In Eq. (2.1) the rate of degradation,  $\frac{d\alpha}{dt}$ , is a function of, k the reaction rate constant which is a function of T and  $f(\alpha)$ . k can be expressed by the Arrhenius formula, given by:

$$k(T) = Aexp(\frac{-E_a}{pT}) \tag{2.3}$$

where A is the pre-exponential factor, E is the activation energy (kJ/mol), R is the gas constant (8.314 J mol· K<sup>-1</sup>) and T is the absolute temperature (K).  $f(\alpha)$  can be written as:

$$f(\alpha) = (1 - \alpha)^n \tag{2.4}$$

where n is the order of reaction. Substituting equations (2.3) and (2.4) into Eq. (2.1), yields the following equation:

$$\frac{d\alpha}{dt} = Aexp\left(\frac{-E_a}{RT}\right)(1-\alpha)^n \tag{2.5}$$

For non-isothermal TGA analysis, the heating rate  $\beta$ , defined as  $\beta = \frac{dT}{dt}$ , is substituted into Eq. (2.5), giving:

$$\frac{d\alpha}{dT} = \frac{1}{\beta} A exp\left(\frac{-E_a}{RT}\right) (1 - \alpha)^n \tag{2.6}$$

By separating variables, the integrated form of Eq. (6) can be expressed as:

$$g(\alpha) = \int_0^\alpha \frac{d\alpha}{f(\alpha)} = \frac{A}{\beta} \int_{T_0}^T exp\left(-\frac{E_a}{RT}\right) dT$$
 (2.7)

where  $g(\alpha)$  is defined as this integrated form of  $f(\alpha)$ . Based on the above equations, the following methods are employed to determine E.

#### 2.2.5.1 Iso-conversional method

The iso-conversional method is a typical technique to estimate the apparent activation energy regardless of the reaction mechanism. Two kinds of iso-conversional methods, KAS and FWO, are applied to evaluate the activation energy in this work.

The KAS method uses the following equation [163]:

$$ln\left(\frac{\beta}{T^2}\right) = ln\frac{AR}{Eg(\alpha)} - \frac{E_a}{RT}$$
 (2.8)

where the activation energy, E, can be calculated from the slope obtained from the linear least square plot of  $ln\left(\frac{\beta}{T^2}\right)$  vs  $\frac{1}{T}$ .

The FWO method uses the following equation [164]:

$$ln(\beta) = ln \frac{0.0048 A E_a}{Rg(\alpha)} - \frac{1.0516 E_a}{RT}$$
 (2.9)

where E can be determined from the linear correlation of  $ln(\beta)$  vs  $\frac{1}{T}$  as well.

# 2.2.5.2 Master-plot method

To better understand the reaction mechanisms of co-pyrolysis process, the master-plot method was adopted to determine the reaction model. This approach involves the generation of both experimental and theoretical master plots based on Eq. (2.10) [165]:

$$\frac{g(\alpha)}{g(0.5)} = \frac{E_a A P(u_\alpha) / \beta R}{E_a A P(u_{0.5}) / \beta R} = \frac{P(u_\alpha)}{P(u_{0.5})}$$
(2.10)

where, experimental plots of  $P(u_{\alpha})/P$   $(u_{0.5})$  versus  $\alpha$  were generated using kinetic parameters obtained in section 2.2.5.1. Theoretical plots of  $g(\alpha)/g$  (0.5) versus  $\alpha$  were derived from various solid-state reaction models (Table 2.3).

The alignment or overlap of experimental master plot curves with theoretical master plot curves indicates the most suitable reaction mechanism model for the pyrolysis process.

Table 2.3 presents a collection of mathematical models commonly applied in the kinetic analysis of solid-state thermal decomposition reactions—such as pyrolysis, combustion, or gassolid reactions. These models describe how the reaction rate evolves as a function of conversion  $(\alpha)$  under various mechanistic assumptions.

Table 2.3 Most frequently used solid-state reaction models [106].

•	•		
Mechanisms	Symbol	$f(\alpha)$	$G(\alpha)$
Order of reaction			
First-order	$F_{I}$	1-α	$-\ln(1-\alpha)$
Second-order	$F_2$	$(1-\alpha)^2$	$(1-\alpha)^{-1}-1$
Third-order	$F_3$	$(1-\alpha)^3$	$[(1-\alpha)^{-2}-1]/2$
Diffusion			
One-way transport	$D_I$	$0.5\alpha$	$\alpha^2$
Two-way transport	$D_2$	$[-\ln(1-\alpha)]^{-1}$	$(1-\alpha) \ln(1-\alpha) + \alpha$
Three-way transport	$D_3$	1. $5(1-\alpha)^{2/3} [1-(1-\alpha)^{1/3}]^{-1}$	$[1-(1-\alpha)^{1/3}]^2$
Ginstling-Brounshtein equation	$D_4$	1.5 [ $(1-\alpha)^{-1/3}-1$ ] <sup>-1</sup>	$(1-2\alpha/3)$ - $(1-\alpha)^{2/3}$
Limiting surface reaction between both	h		
phase			
One dimension	$R_{I}$	1	α
Two dimensions	$R_2$	$2(1-\alpha)^{1/2}$	$1-(1-\alpha)^{1/2}$
Three dimensions	$R_3$	$3(1-\alpha)^{2/3}$	$1-(1-\alpha)^{1/3}$
Random nucleation and nuclei growth			
Two-dimensional	$A_2$	$2(1-\alpha) \left[-\ln(1-\alpha)\right]^{1/2}$	$[-\ln(1-\alpha)]^{1/2}$
Three-dimensional	$A_3$	$3(1-\alpha) \left[-\ln(1-\alpha)\right]^{2/3}$	$[-\ln(1-\alpha)]^{1/3}$
Exponential nucleation			
Power law, n=1/2	$P_2$	$2\alpha^{1/2}$	$lpha^{1/2}$
Power law, n=1/3	$P_3$	$3\alpha^{2/3}$	$lpha^{1/3}$
Power law, n=1/4	$P_4$	$4\alpha^{3/4}$	$lpha^{1/4}$

# 2.2.5.3 Thermodynamic parameters

The thermodynamic parameters including the pre-exponential factor A (s<sup>-1</sup>), enthalpy change  $\Delta H$  (kJ/mol), Gibbs free energy  $\Delta G$  (kJ/mol), and changes in entropy  $\Delta S$  (kJ/mol·K) play a crucial role in optimizing the pyrolysis process and designing pyrolysis reactors. A reflects the frequency of successful molecular collisions leading to decomposition; it is closely associated with the reaction rate and molecular orientation during pyrolysis.  $\Delta H$  represents the amount of heat absorbed or released

during the decomposition process, indicating whether the reaction is endothermic or exothermic.  $\Delta G$  indicates the spontaneity of the pyrolysis reaction under given conditions; a negative  $\Delta G$  suggests that the reaction is thermodynamically favourable.  $\Delta S$  provides insights into the degree of molecular disorder or randomness introduced during pyrolysis, with positive values typically signifying increased freedom of movement in the transition state. These parameters can be calculated by using the equations below:

$$A = -\frac{\beta E_a}{RT_m^2 f'(a_m)} \exp\left(\frac{E_a}{RT_m}\right)$$
 (2.11)

$$\Delta H = \mathbf{E}_a - RT \tag{2.12}$$

$$\Delta G = E_a + RT_m \ln \left( K_B T_m / hA \right) \tag{2.13}$$

$$\Delta S = (\Delta H - \Delta G)/T_m \tag{2.14}$$

where  $f'(\alpha)$  is the first derivative of reaction model  $f(\alpha)$ , which is determined by master-plot method.  $K_B$  is the Boltzmann constant (1.3819 ×10<sup>-23</sup> J/K), h is the Planck constant (6.626 ×10<sup>-34</sup> J/s),  $T_m$  is the DTG peak temperature and  $\alpha_m$  is the conversion rate at peak temperature.

#### 2.2.6 Machine learning

To predict the derivative weight in TG analysis, the machine learning models were developed. The database was collected from the TGA experiments of corn fibers/HDPE blends with a heating rate of 10 °C/min. The datasets from corn stem/HDPE, corn leaf/HDPE and corn husk/HDPE were selected as training set for establishing the prediction model, the data set of corn ear/HDPE was selected as validating set for model optimization, and the data set of corn cob/HDPE blend was selected as testing set to evaluate the performance of the prediction model. Based on the structure and property of the database, RF and GBRT algorithms were used to establish the model in this study. The hyperparameters tuning was performed by random search method via scikit-learn library.

#### 2.2.6.1 Random Forest

RF is a versatile ensemble learning method that can handle both regression and classification tasks. It is robust to overfitting and can deal with non-linear relationships [166]. Table 2.4 displays the optimized range of RF parameters, while the remaining

parameters used the default configuration provided by the scikit-learn library for implementing the algorithm.

Table 2.4 Optimized range of RF parameters in RF algorithm.

Parameters	Optimized Range
'n_estimators' (estimators)	100-1000
'max_depth' (depth)	3-50
'min_samples_split' (split)	2-11
'min_samples_leaf' (leaf)	1-11

# 2.2.6.2 Gradient Boosting Regression Tree

GBRT algorithms is an ensemble technique that builds models sequentially, each new model correcting errors made by previous models. It is highly effective for regression tasks with complex datasets [167]. To enhance the prediction model's performance, hyperparameters including the total number of trees, learning rate, and maximum depth of individual regression trees were tuned using the random search method. Meanwhile, the remaining parameters were set to their default configurations provided by the scikit-learn library.

# 2.2.6.3 Evaluation of model performance

The model's performance was assessed using Mean Squared Error (MSE) and Regression Coefficient ( $R^2$ ). MSE represents the average squared difference between predictions and experimental results and the  $R^2$  is the correlation between predictions and experimental results. MSE and  $R^2$  can be calculated by Eq. (2.15) and Eq. (2.16), respectively.

$$R^{2} = 1 - \frac{\sum_{i=1}^{N} (Y_{i}^{exp} - \widehat{Y}_{i})^{2}}{\sum_{i=1}^{N} (Y_{i}^{exp} - Y_{exp}^{exp})^{2}}$$
(2.15)

$$MSE = \frac{1}{N} \sum_{i=1}^{N} (Y_i^{exp} - \widehat{Y}_i)^2$$
 (2.16)

where N is the number of the database,  $Y_i^{exp}$  represent the actual value,  $Y_{ave}^{exp}$  is the average actual values, and  $\widehat{Y}_i$  is the predicted value. A higher  $R^2$  and a lower MSE suggest superior prediction performance of the prediction model. All the algorithms employed were implemented using the scikit-learn library.

#### 2.3 Result and discussion

In this section, the experimental results are presented through tables and figures. The findings are compared with existing literature, and potential mechanisms are discussed to explain the observed outcomes.

# 2.3.1 Thermogravimetric analysis of different corn stalk tissues and HDPE

TGA and DTG curves of pure HDPE and corn stalk tissues (stem, husk, ear, cob, and leaf) are shown in Fig 2.1. The characteristics of thermal degradation are summarized in Table 2.5. When the temperature was lower than 200 °C, the thermal decomposition rate of all the corn stalk tissues were also low, typically < 10 % (Fig.1a), which was mainly attributed to decomposition of bound water and light volatile compounds in the fibrous structures. In addition, because of the poor stability of the hemicellulose, a small part of the corn stalk tissues were slowly decomposed in this stage [168].

Table 2.5 TG and DTG characteristics of corn stalk tissues and HDPE.

Samples	$T_{in}^a$	$T_m^b$ $T_f^c$ Weight los		Weight loss d	Total weight loss
	(°C)	(°C)	(°C)	(wt%)	(wt%)
HDPE	420	474	520	93.7	99.1
Stem	150	331.4	500	73.8	77.9
Husk	150	331.8	500	74.9	79.1
Ear	150	352.9	500	73.0	78.0
Cob	150	335.0	500	73.6	77.8
Leaf	150	345.9	500	69.4	74.7

<sup>&</sup>lt;sup>a</sup> Initial decomposition temperature. <sup>b</sup> Temperature of maximum decomposition rate.

<sup>&</sup>lt;sup>c</sup> Final temperature. <sup>d</sup> Weight loss at 450 °C.

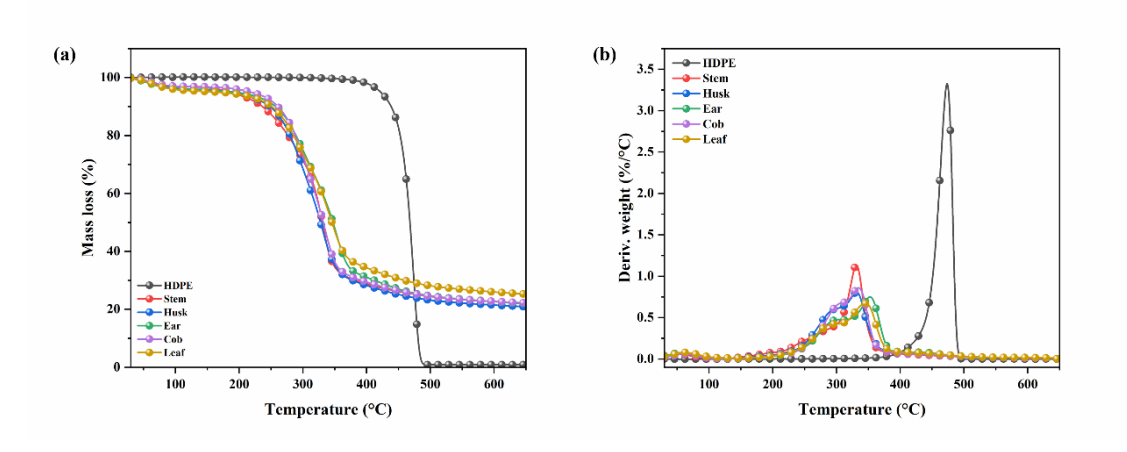


Fig 2.1 TG (a) and DTG (b) profiles of HDPE and different corn stalk tissues at heating rate of 10 °C/min

The weight loss in all of the corn stalk tissue specimens sharply increased at around 200 °C, as depicted in the DTG curves (Fig 2.1b), which was the onset temperature of hemicellulose decomposition. The main decomposition stage of all corn stalk tissues was spanning from 200 °C to 460 °C, where primary organic components such as cellulose, hemicellulose, and lignin undergo significant breakdown, concurrently generating a large amount of non-condensable gases and volatiles [169]. Additionally, the DTG curves exhibited several peaks, attributed to the thermal degradation of hemicellulose, cellulose, and lignin, occurring within the temperature ranges of 275-350 °C, 180-350 °C, and 250-500 °C, respectively [63]. Due to the overlapping temperature ranges for the decomposition of hemicellulose and cellulose, a shoulder peak is observable in the DTG curve [170]. In comparison with other tissues, the shoulder peak in the corn stem was less obvious (Fig. 1b). This difference can be attributed to the higher content of cellulose (25.56±2.22 %) and lignin (20.51±1.10 %), and a lower content of hemicellulose (34.59±1.90 %) of corn stem in contrast to other tissues. Additionally, Table 4 shows that the maximum decomposition rates for corn ear and corn leaf occurred at 352.9 °C and 345.9 °C, respectively, which were higher than those for the stem (331.4 °C), husk (331.8 °C), and cob (335.0 °C). Furthermore, a minimal weight loss was observed in the final stage of the TG curve, linked to the slow decomposition of carbonaceous residues [171].

Contrary to lignocellulosic fibres, only one peak was observed in the HDPE DTG curve, indicating a single-stage decomposition of HDPE occurring in range of 410-520 °C (Fig 2.1). The peak was strong and narrow, reflective of the simple structure and

composition of HDPE [172]. As the temperature increased, the weight of HDPE decreased gradually with the release of volatiles. According to Table 2.5, a total weight loss of 99.1 % was achieved at 520 °C, suggesting nearly complete decomposition of HDPE at this temperature.

#### 2.3.2 Thermogravimetric analysis of corn stalk tissues and HDPE blends

Fig 2.2 presents the TG and DTG curves of various corn stalk tissues and HDPE blends, and the characteristic parameters of their thermal degradation processes detailed in Table 2.6. According to TGA results, the degradation of corn stalk tissues and HDPE mixtures generally occurs in two stages. Similar with the results observed in Fig 2.1 for pure materials, minimal weight loss was recorded in the blends when heated below 150°C, which was attributed to the evaporation of bound water and the release of small volatile molecules.

The first degradation stage of blends aligns with the thermal degradation of the pure corn stalk tissues, predominantly occurring between 150 °C and 400 °C. The weight losses for the mixtures during this stage were as follows: 32.0 % for stem, 33.5 % for husk, 32.6 % for ear, 31.3 % for cob, and 30.3 % for leaf. During this phase, the chemical components such as cellulose, hemicellulose, and a portion of lignin in the corn stalk decomposed across all tissue types. The second degradation stage, occurring between 400 °C and 640 °C, predominantly involved HDPE degradation. The weight losses for the mixtures in this stage were as follows: 55.6 % for stem, 53.2 % for husk, 53.8 % for ear, 56.5 % for cob, and 54.9 % for leaf. Notably, the maximum temperature of the decomposition rates for the five blends in the first stage were consistently slightly lower than those of pure corn stalk tissues, suggesting that the presence of HDPE promoted the pyrolysis process of the fibres [150]. Furthermore, the temperatures for maximum decomposition rates in the second stage were slightly higher than those seen in the pyrolysis of HDPE alone (474.0 °C). This is attributed to the coking phenomenon and char formation of corn stalk tissues at temperatures above 400 °C, which in turn inhibits the thermal decomposition of HDPE [73].

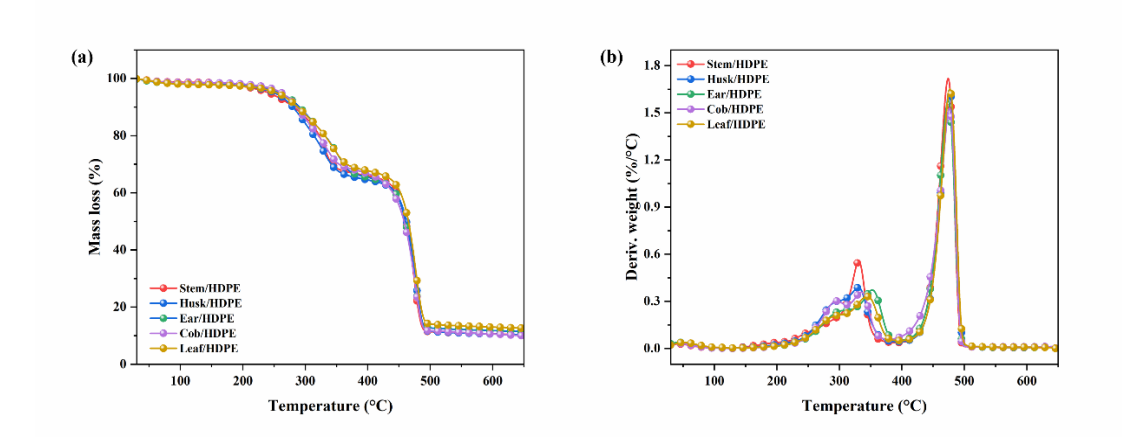


Fig 2.2 TG (a) and DTG (b) profile of HDPE and different corn stalk tissues blends at heating rate of 10 °C/min.

Table 2.6 TG and DTG characteristics of corn stalk tissues and HDPE blends.

Samples	First stage		Second sta	ige	_ Total weight
	Peak temp.	Weight loss	Peak	Weight loss	loss
	(°C)	(wt%)	temp.	(wt%)	(wt%)
			(°C)		()
Stem/HDPE	330.9	32.0	474.0	55.6	89.6
Husk/HDPE	330.1	33.5	476.4	53.2	89.7
Ear/HDPE	352.6	32.6	474.2	53.8	88.4
Cob/HDPE	334.8	31.3	476.1	56.5	89.8
Leaf/HDPE	344.3	30.3	476.8	54.9	87.2

The TGA and DTG curves of corn stalk tissues and HDPE blends at different heating rates (10 °C/min, 20 °C/min, and 40 °C/min) are investigated (Fig 2.3 and Fig 2.4), respectively. Generally, an increase in the heating rate resulted in the equivalent weight loss occurring at lower heating rate [171]. Therefore, the total weight loss from all the mixtures remained unchanged, indicating that variations in the heating rate do not influence the overall mass loss during co-pyrolysis. The DTG profiles (Fig.2.4) illustrate two distinct groups of peaks corresponding to the decomposition of corn stalk tissues and HDPE. As the heating rate increased, the DTG peaks shifted towards higher temperatures, indicating a delay in the thermal decomposition process of the corn stalk tissue/HDPE mixtures, as also observed in Fig 2.4. The delay is likely due to the poor thermal conductivity of biomass and the resulting temperature gradient through the depth of the biomass, leading to a non-uniform temperature distribution within the lignocellulosic particles [173].

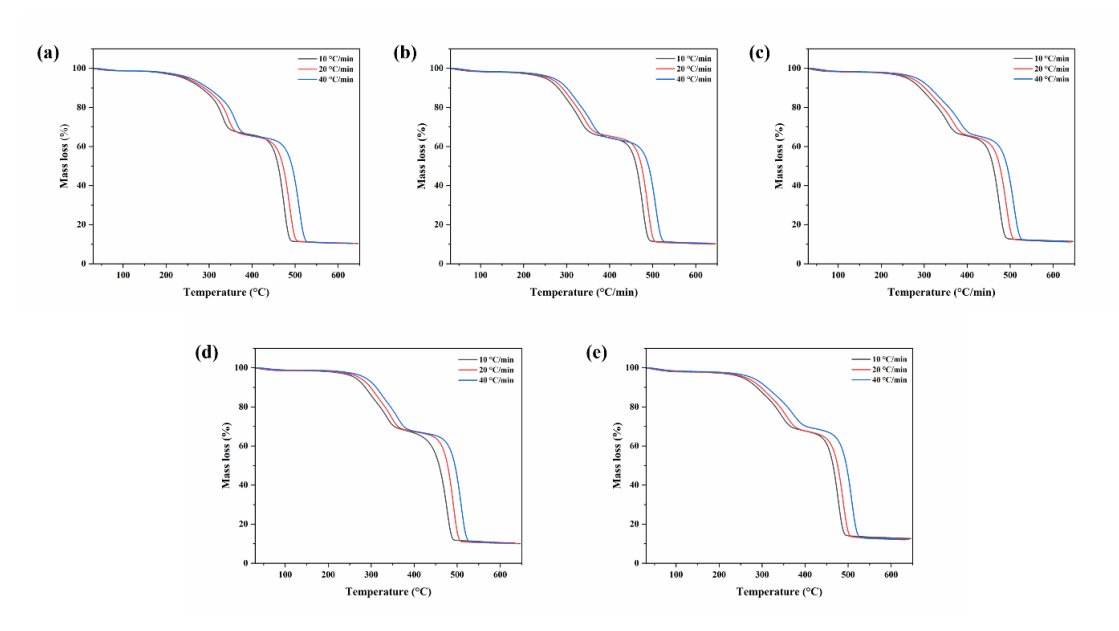


Fig.2.3 TG profiles of corn stalk tissues and HDPE blends at heating rate of 10 °C/min, 20 °C/min, and 40 °C/min. (a) Corn stem/HDPE; (b) husk/HDPE; (c) ear/HDPE; (d) cob/HDPE; and (e) leaf/HDPE.

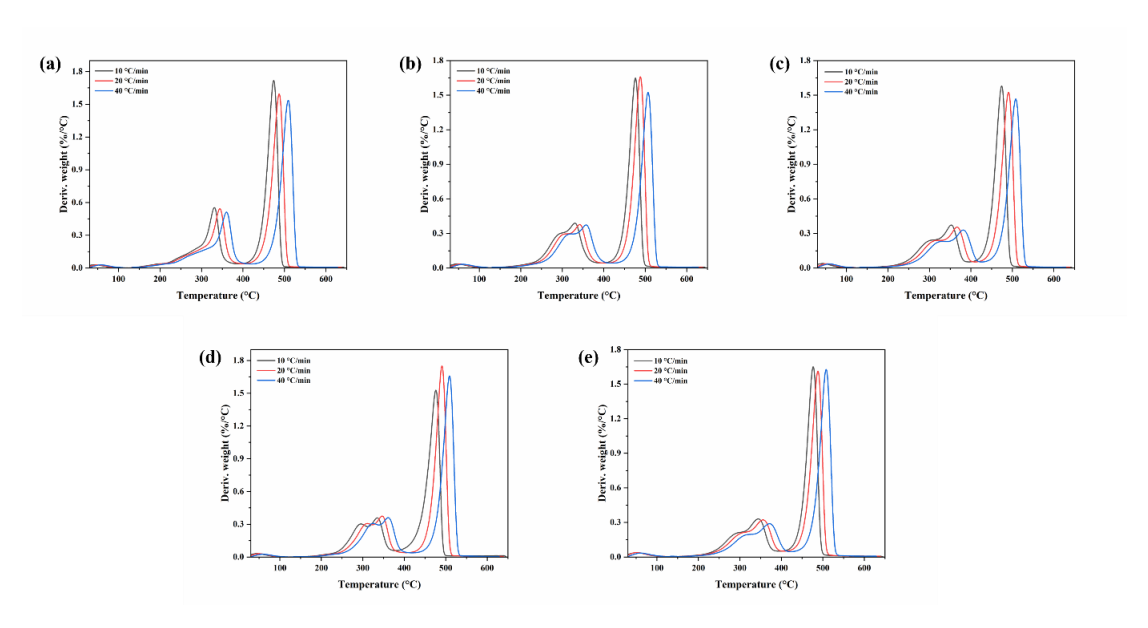


Fig 2.4 DTG profiles of corn stalk tissues and HDPE blends at heating rate of 10 °C /min, 20 °C /min, and 40 °C /min. (a) Corn stem/HDPE; (b) husk/HDPE; (c) ear/HDPE; (d) cob/HDPE; and (e) leaf/HDPE.

# 2.3.3 Py-GC/MS analysis

Table S1 listed the pyrolytic products from co-pyrolysis of HDPE and different tissues of corn stalk at 600 °C. Each mixture has a unique profile of compounds, including hydrocarbons, ketones, acids, alcohols, furans, aromatic hydrocarbons, esters,

and others. Notably, typical pyrolytic products of woody biomass components (cellulose, hemicellulose, lignin) and HDPE were identified. For instance, aldehydes (e.g., benzaldehyde) and ketones (e.g., 2-butanone, 2-propanone 1-(acetyloxy)-) are formed through further fragmentation and rearrangement of cellulose-derived intermediates [128]. Furans (e.g., tetrahydrofuran) resulted from the dehydration and rearrangement of the sugar unit within the cellulose and hemicellulose. Alcohols (e.g., 3-hexyn-2-ol) emerged during the breakdown of cellulose and hemicellulose, although the yields of these compared were relatively lower than other products. Acetic acid, a typical byproduct of hemicellulose pyrolysis, originated from the acetyl groups present in hemicellulose [82]. The phenolic compounds (e.g., phenol) and benzene are the products from the decomposition of lignin fractions in lignocelluloses matrixes [174]. Alkenes and alkanes across a broad carbon number range indicate cracking reactions, where larger hydrocarbon molecules in HDPE break down into smaller, unsaturated ones [175]. Additionally, esters (e.g., propanoic acid 2-oxo- methyl ester) reflect esterification reactions occurring during the pyrolysis or present in the biomass [176].

Fig 2.5 illustrated the pyrolytic products distribution from co-pyrolysis of HDPE and different tissues of corn stalk. Among these products, alcohol, hydrocarbons, phenol, furan, and aromatics are valuable organic compounds for biofuel production [177]. In contrast, oxygenated compounds such as acids, esters, aldehydes, and ketones are undesirable products. Acids contribute to corrosiveness, while esters are associate with decreased heating value of pyrolysis oil. Ketones and aldehydes can cause instability in bio-oil during transport and storage, and other substances such as nitrogencontaining compounds pose environmental risks [175]. As can be seen in Fig 2.5, the corn cob/HDPE mixture has the highest content of aromatic hydrocarbons (13.68 %), which is attributed to the highest content of lignin in corn cob ( $21.6\pm1.01$  %). Meanwhile, due to the high content of lignin in corn ear (20.28±0.88 %), the phenolic compounds in pyrolytic products of corn ear/HDPE mixture are highest, because the phenolic compounds are mainly derived from the coniferyl and syringyl building blocks of lignin [178]. Furthermore, the acid compounds in pyrolytic products in corn leaf/HDPE (31.43 %) and corn husk/HDPE (27.17 %) groups are higher than other groups, attributed to the high content of hemicellulose in corn leaf (40.24±1.96 %) and corn husk (45.74±2.15 %). Acid compounds are mainly originated from the acetyl groups present in hemicellulose and the further breakdown of initial pyrolytic products of hemicellulose and cellulose [82]. Compared to other groups, the corn cob/HDPE mixture has a higher content of aromatic hydrocarbons and furan, which are favourable for biofuel production, while the acid and ester compounds are lower, making it more desirable for biofuel production.

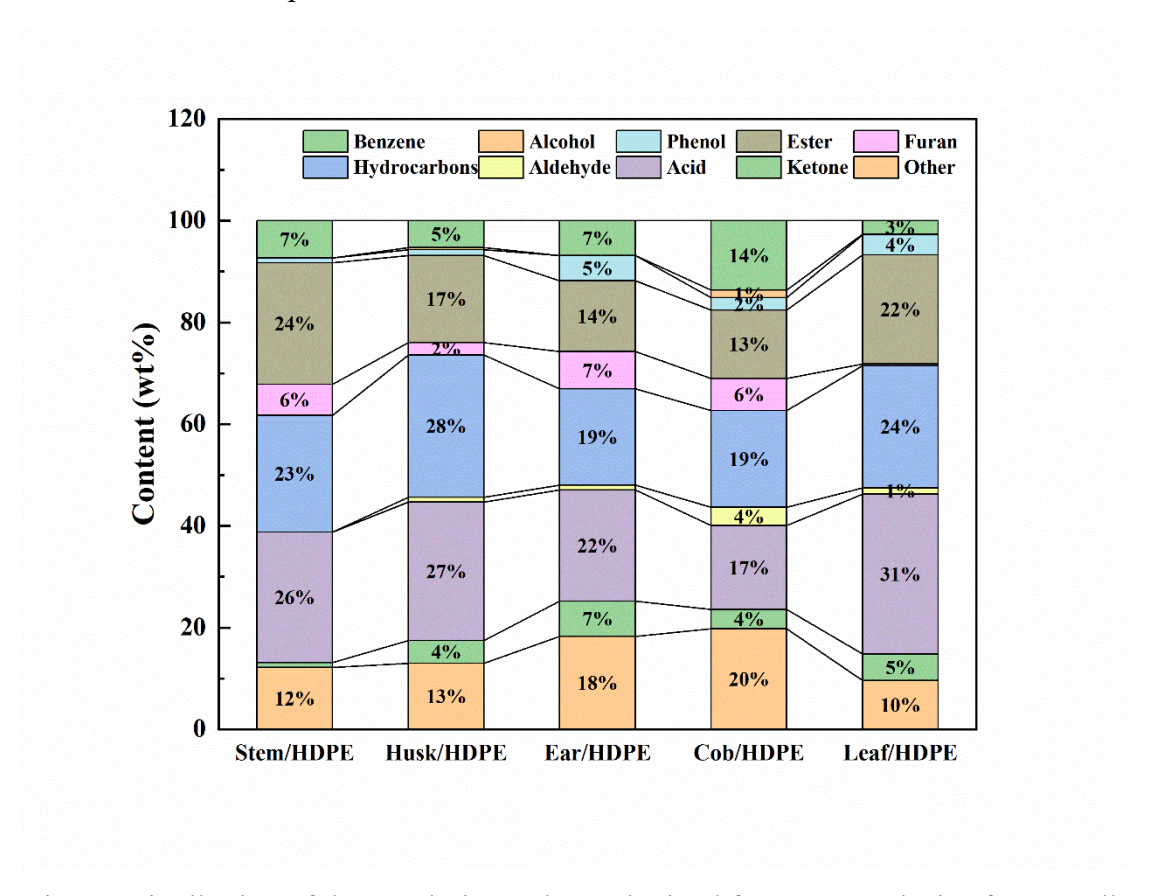


Fig 2.5 Distribution of the pyrolytic products obtained from co-pyrolysis of corn stalk tissues and HDPE.

#### 2.3.4 Kinetic analysis

# 2.3.4.1 Model free methods

Thermal decomposition reactions are extremely complex, which involve a series of complex pyrolysis mechanisms and hundreds of components and reactions [35]. Herein, two kinds of model free methods including FWO and KAS were adopted to estimate the activation energy ( $E_a$ ), in order to better understand the differences of copyrolysis kinetics of using the different corn stem tissues with HDPE. Fig 2.6 (a-e) and Fig 2.6 (f-j) showed the linear correlation between  $\frac{1}{T}$  and  $ln\left(\frac{\beta}{T^2}\right)$  (KAS),  $\frac{1}{T}$  and  $ln(\beta)$  (FWO) at different heating rates. The  $E_a$  values at conversion rate ( $\alpha$ ) from 0.2-0.8 calculated by KAS and FWO methods are listed in Table 2.7 and Table 2.9 along with the coefficient of correlation ( $R^2$ ). The average values of  $R^2$  are greater than 0.96 in all

groups, demonstrating that the results are precise and the two model free methods were suitable for the feedstock's kinetics calculations [127]. The average activation energy values based on KAS and FWO methods were very close. Therefore, the results were deemed acceptable. Furthermore, the results calculated from FWO were slightly higher than that of KAS method, which ascribed to the different derivation process and error range in two model free methods [179].

It has been reported before the  $E_a$  for HDPE pyrolysis is 329.93 kJ/mol, which is much higher than that of co-pyrolysis of HDPE with different corn stalk tissues. The results demonstrated a positive synergistic effect between the HDPE and biomass is obtained [180]. As can be seen from the Table 2.7 and Table 2.8, the average  $E_a$  of copyrolysis of HDPE and different corn stalk tissues was in the order: husk/HDPE> stem/HDPE> ear/HDPE> leaf/HDPE> cob/HDPE. The husk/HDPE group exhibited the highest  $E_a$  among five groups, owing to the highest cellulose content and lowest lignin content in corn husk compared to the other tissues. Due to the inherent structural stability of lignocellulose, cellulose needs a higher  $E_a$  than hemicellulose and lignin for decomposition. Consequently, a greater cellulose content in corn stalk requires higher  $E_a$  to initiate the decomposition reaction [181]. Moreover, in the co-pyrolysis process, lignin generates reactive free radicals that act as hydrogen acceptors [182]. Simultaneously, these free radicals can absorb the hydrogen donor produced from HDPE. This interaction promotes the decomposition of HDPE, leading to a lowered  $E_a$ for the co-pyrolysis process of lignocelluloses and HDPE [183]. Consequently, the corn husk, having the lowest lignin content, did not exhibit a pronounced synergistic effect with HDPE, leading to a higher  $E_a$  than other groups. In addition, cob/HDPE has the lowest  $E_a$ . This can be attributed to the low content of cellulose and high hemicellulose content. The  $E_a$  for hemicellulose decomposition is lower than lignin and cellulose because of the unstable structure [184]. Additionally, it is observed from Fig 2.6 that within the conversion range of 0.1 to 0.4, the  $E_a$  exhibited fluctuations with conversion. The fluctuations in  $E_a$  during the conversion range of 0.1–0.4 is attributed to the decomposition of corn stalk fibers present in the blend. In leaf/HDPE, ear/HDPE, husk/HDPE and stalk/HDPE groups, the  $E_a$  decreased at  $\alpha$ =0.3 and then increased. This phenomenon could be associated with the decomposition of active cellulose, which required lower energy [185]. Conversely, the  $E_a$  for corn cob increased at  $\alpha$ =0.3, this could be attributed to the high content of hemicellulose in corn cob, which mainly decomposed at the beginning of co-pyrolysis. The  $E_a$  of corn cob was decreased at

 $\alpha$ =0.4. During this stage, hemicellulose and most of the cellulose were decomposed, while lignin and soluble constituents experienced slow decomposition[186]. Thus, the decrease of  $E_a$  can be attributed to the low content of cellulose, lignin and soluble in corn cob. The activation energy remains stable in the conversion range of 0.5–0.8 in all the tested groups. This could be attributed to the dominance of HDPE degradation. A lower  $E_a$  corresponds to a lower energy demand for the pyrolysis reaction. Thus, the corn cob/HDPE group, which has the lowest  $E_a$  value, is favoured for the practical application in terms of energy consumption.

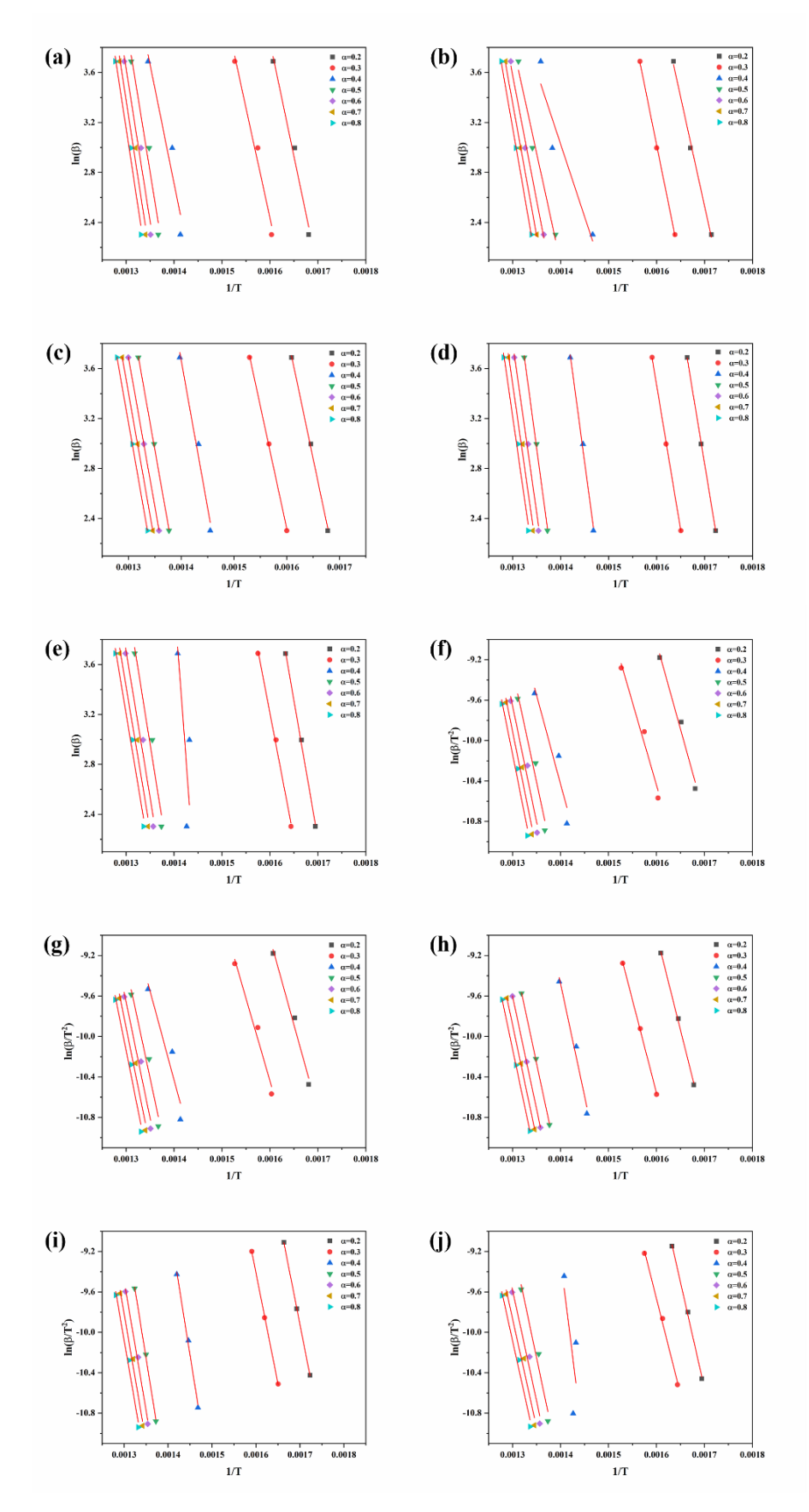


Fig 2.6 The linear relationship between  $\frac{1}{T}$  and  $ln\left(\frac{\beta}{T^2}\right)$  (KAS) (a-e), and  $\frac{1}{T}$  and  $ln(\beta)$  (FWO) (f-j).

Table 2.7 The activation energy  $(E_a)$  and correlation coefficient  $(R^2)$  calculated by FWO method.

~	Stem/HDPE		Cob/HDPE	Cob/HDPE		Ear/HDPE			Leaf/HDPE	
α	$E_a(kJ/mol)$	$R^2$	$E_a(kJ/mol)$	$R^2$	$E_a(kJ/mol)$	$R^2$	$E_a(kJ/mol)$	$R^2$	$E_a(kJ/mol)$	$R^2$
0.2	175.5	0.99	138.4	0.99	159.0	0.99	184.3	0.99	145.3	0.98
0.3	158.7	0.99	150.2	0.99	155.0	0.99	182.8	0.99	139.9	0.98
0.4	202.5	0.95	121.5	0.96	186.3	0.98	226.2	0.99	150.4	0.92
0.5	190.0	0.97	150.2	0.99	188.0	0.99	225.8	0.99	187.3	0.97
0.6	186.8	0.97	164.4	0.99	188.9	0.99	215.1	0.99	193.7	0.97
0.7	181.9	0.98	173.5	0.99	189.5	0.99	212.4	0.99	196.6	0.98
0.8	182.4	0.98	174.5	0.99	189.5	0.99	211.4	0.99	197.5	0.98
Average	182.5	0.98	153.2	0.99	179.5	0.99	208.3	0.99	173.0	0.97

Table 2.8 The activation energy  $(E_a)$  and correlation coefficient  $(R^2)$  calculated by KAS method.

α	Stem/HDPE		Cob/HDPE		Ear/HDPE	Ear/HDPE			Leaf/HDPE	
$\alpha$	$E_a(kJ/mol)$	$\mathbb{R}^2$								
0.2	174.6	0.99	135.6	0.99	157.0	0.99	184.0	0.99	142.7	0.98
0.3	156.6	0.99	147.6	0.99	152.4	0.99	182.0	0.99	136.4	0.97
0.4	200.8	0.94	115.6	0.95	184.3	0.99	226.4	0.99	146.1	0.91
0.5	187.4	0.96	145.6	0.99	185.4	0.99	225.1	0.99	184.5	0.96
0.6	184.0	0.97	160.1	0.99	186.1	0.99	213.7	0.99	191.1	0.97
0.7	178.7	0.98	169.8	0.99	186.6	0.99	210.7	0.99	195.0	0.97
0.8	179.1	0.98	170.7	0.99	186.6	0.99	209.5	0.99	197.3	0.98
Average	180.2	0.97	149.3	0.99	176.9	0.99	207.3	0.99	170.4	0.96

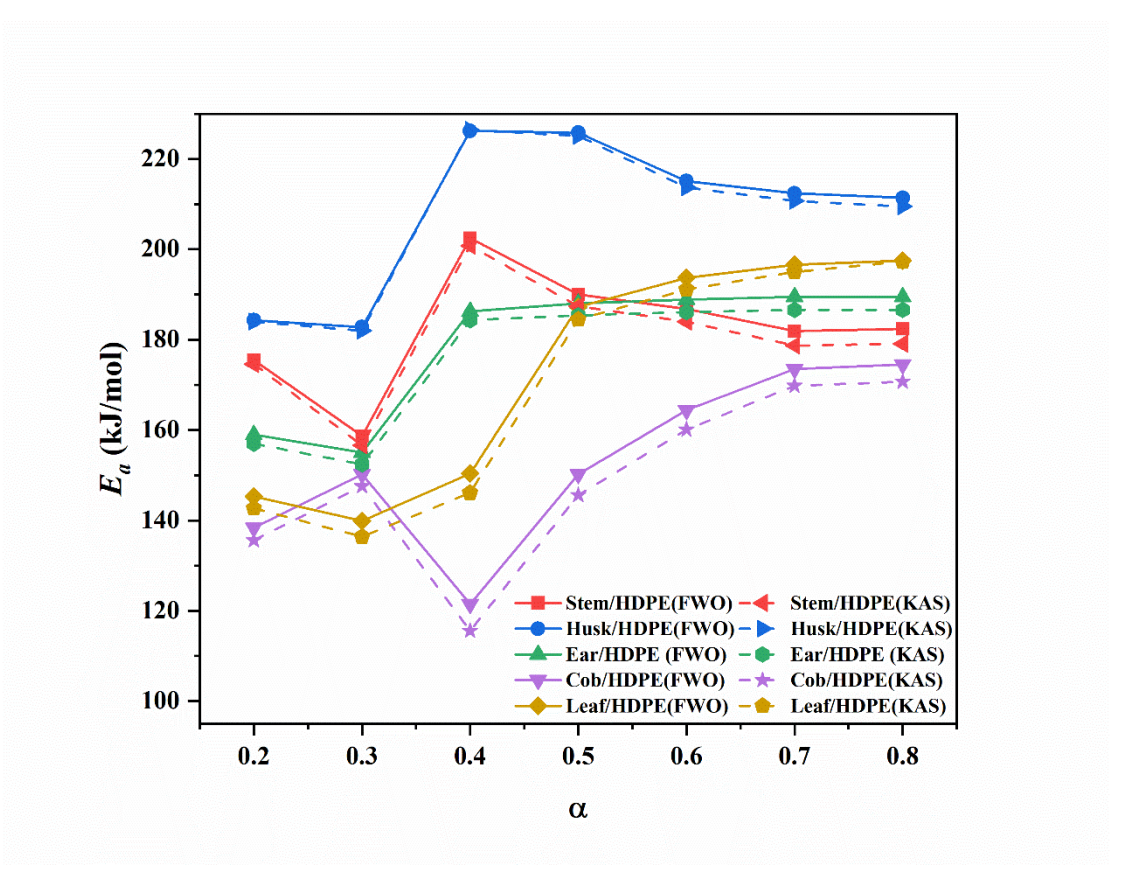


Fig 2.7 The activation energy of the co-pyrolysis of different corn stalk tissues and HDPE at different conversion rates.

#### 2.3.4.2 Master plot methods

Understanding the reaction model of the pyrolysis process is essential as it offers guidance for selecting or designing the pyrolysis reactor [127]. In this section, the reaction models for the co-pyrolysis of different corn stalk tissues and HDPE were determined using master plot methods. Fig 2.8 illustrates the relationships between  $\alpha$  and  $P(u)/P(u_{0.5})$  for all groups at different heating rates (10 °C/min, 20 °C/min, and 40 °C/min). Generally, the  $P(u)/P(u_{0.5})$  curves remained similar across different heating rates in all groups, suggesting that the co-pyrolysis process followed the same kinetics models under varying heating rates. Consequently, the  $P(u)/P(u_{0.5})$  curves at a heating rate of 10 °C/min were chosen to determine the kinetic models for all groups. Fig 2.9 illustrated the comparison of curves representing  $\alpha$  versus  $G(\alpha)/G(0.5)$  plotted by various theoretical kinetic functions (Table 2.3) and experimental master-plots  $P(u)/P(u_{0.5})$  for different corn fibers with HDPE at a heating rate of 10 °C/min. There is no matching kinetics model for the conversion range of 0.2-0.4 in all groups, which

corresponds to the main decomposition of corn stalk, indicating the pyrolytic reactions were complex during this stage [187]. Within the conversion range of 0.5-0.8, the copyrolysis of corn leaf/HDPE followed the first-order reaction model (F1), and the copyrolysis of corn ear/HDPE and corn stem/HDPE followed the diffusion one-way transport reaction model (D1), while the co-pyrolysis of corn husk/HDPE conformed to the diffusion two-way transport reaction model (D2). Additionally, the co-pyrolysis of corn cob and HDPE adhered to the diffusion two-way transport reaction model (D2) in the conversion range of 0.5-0.7 and transitioned to diffusion one-way transport reaction model (D1) in the range of 0.7-0.8. The diffusion reaction involves the heat transfer from an external source to solids, either preceding or concurrent with the reactions. This mechanism also contains the outward diffusive transport of the hot gases generated during the decomposition of lignocellulose [188]. These results demonstrate that the types of corn stalk tissue also influence the kinetics of the co-pyrolysis. Moreover, the transition of the reaction model from D2 to D1 in the co-pyrolysis process of corn stalk and HDPE suggests a slight simplification of the pyrolysis reaction in the later stage [189].

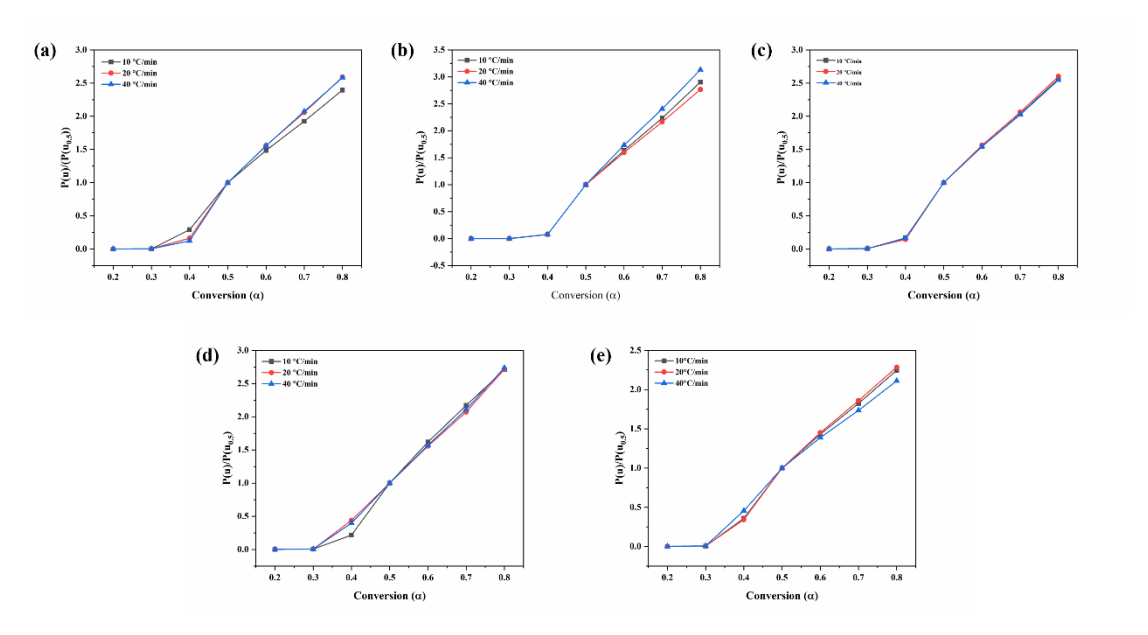


Fig.2.8 The curves of  $\alpha$  versus P(u)/P(u<sub>0.5</sub>): (a) stem/HDPE; (b) husk/HDPE; (c) ear/HDPE; (d) cob/HDPE; and (e) leaf/HDPE.

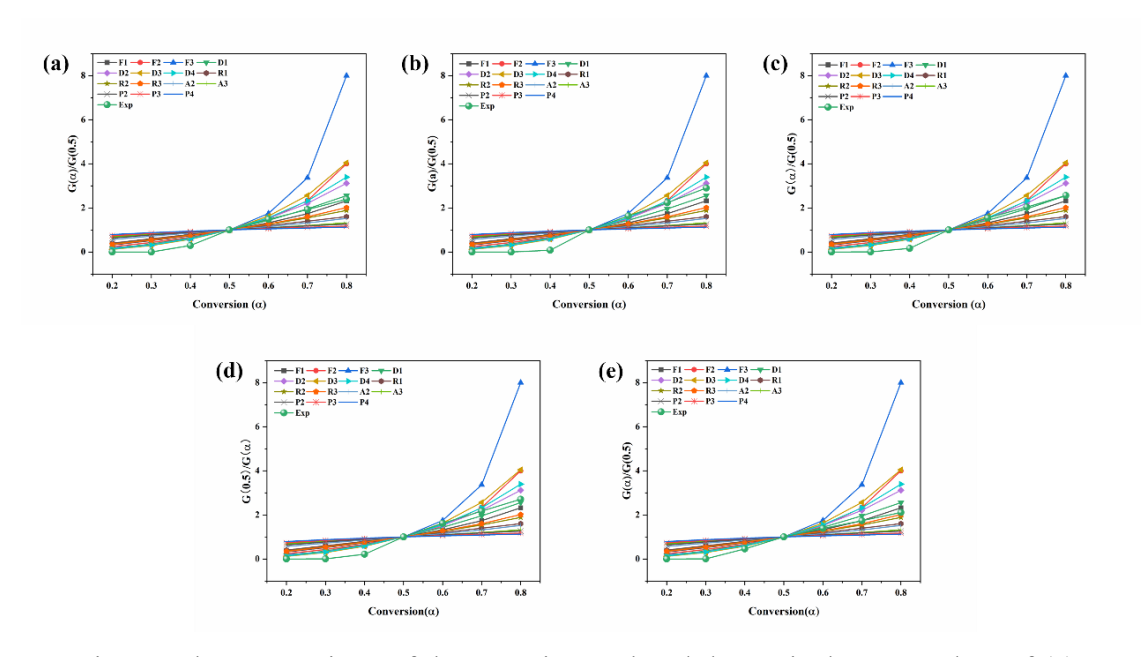


Fig 2.9 The comparison of the experimental and theoretical master plots of (a) stem/HDPE; (b) husk/HDPE; (c) ear/HDPE; (d) cob/HDPE; and (e) leaf/HDPE.

# 2.3.4.3 The evaluation of thermodynamic parameters

Based on the results obtained from the model free and master plot method, the thermodynamic parameters including the pre-exponential factor A (s<sup>-1</sup>), enthalpy change  $\Delta H$  (kJ/mol), Gibbs free energy  $\Delta G$  (kJ/mol), and changes in entropy  $\Delta S$  (kJ /mol·K) were calculated by Eqs. (2.11-14), as listed in Table 2.9. It can be observed that A varied across different groups. Notably, the corn husk/HDPE blend exhibited the highest A among the five groups, suggesting the co-pyrolysis process of corn husk/HDPE blends was highly reactive with complex and synergistic reactions occurring [188]. Additionally, the pre-exponential factors within each group differed with changes in conversion, suggesting the multifaceted nature of degradation during co-pyrolysis. The values of  $\Delta H$  in all the experimental groups were positive, indicating that the co-pyrolysis process of corn stalk tissues/HDPE is endothermic, involving the cleavage of polymer chains and the breakdown of the lignocellulosic matrixes. The highest  $\Delta H$  value was observed in the corn husk/HDPE groups, attributed to the higher content of thermally resistant components such as cellulose. Furthermore, the higher  $\Delta H$  in the corn husk/HDPE blend can be attributed to the lesser synergistic effect between corn husk and HDPE, as discussed in the activation section.  $\Delta G$  represents the overall energy changes of the pyrolysis system for the formation of the activated complex [190]. Therefore, the lowest value of  $\Delta G$  in corn cob/HDPE group is more favourable for the occurring of the pyrolytic reactions. The positive values of  $\Delta G$  in all groups indicate that the co-pyrolysis process of corn stalk tissues /HDPE was non-spontaneous and required an external heat supply [191]. In Table 2.9, it can be observed that the values of  $\Delta S$  were negative in all groups, indicating that the reactivity of the original materials was low, leading to a longer time for the formation of the activated complex[99]. Furthermore, the values of  $\Delta S$  within the conversion range of 0.5-0.8 are higher compared to those within the range of 0.2-0.4 in all groups, demonstrating the reactions occurring at  $\alpha$ =0.5-0.8 were more difficult to initiate than those at  $\alpha$ =0.2-0.4.

Table 2.9 Thermodynamic parameters of co-pyrolysis of different corn stalk tissues and HDPE.

	Stem/HDPI	Ξ			Husk/HDPI	Ξ			Ear/HDPE				Cob/HDPE				Leaf/HDPE			
α		ΔΗ	ΔG	ΔS		ΔΗ	ΔG	ΔS		ΔΗ	ΔG	ΔS		ΔΗ	ΔG	ΔS		ΔΗ	ΔG	ΔS
ū.	A (s-1)	(kJ/mol	(kJ/mol	(J/mol·K)	A (s-1)	(kJ/mol	(kJ/mol)	$(J/mol\cdot K$	A (s-1)	(kJ/mol	(kJ/mol	$(J/mol\cdot K$	A (s-1)	(kJ/mol	(kJ/mol	(J/mol·	A (s-1)	(kJ/mol	(kJ/mol	(J/mo
		)	)	(3/11101 K)		)	(KJ/IIIOI)	)		)	)	)		)	)	K)		)	)	1·K)
0.2	6.03×10 <sup>11</sup>	237.7	168.3	-92.7	2.62×10 <sup>12</sup>	238.1	177.7	-80.6	3.18×10 <sup>10</sup>	238.4	150.7	-117.2	8.25×10 <sup>8</sup>	196.9	129.4	-90.1	2.65×10 <sup>9</sup>	196.8	137.7	-78.7
0.3	$2.98 \times 10^{12}$	238.3	150.3	-117.7	$1.88 \times 10^{12}$	238.2	175.7	-83.3	1.47×10 <sup>10</sup>	238.5	146.1	-123.6	6.17×10 <sup>9</sup>	196.4	141.4	-73.4	9.24×10 <sup>8</sup>	197.1	131.2	-87.8
0.4	$4.70 \times 10^{13}$	236.8	194.5	-56.5	$2.91 \times 10^{15}$	236.8	220.1	-22.3	3.03×10 <sup>12</sup>	237.4	178.1	-79.3	2.84×10 <sup>7</sup>	197.9	109.4	-118.2	4.69×10 <sup>9</sup>	196.6	140.2	-75.2
0.5	$5.08 \times 10^{12}$	237.2	181.1	-75.0	$2.35 \times 10^{15}$	236.8	218.8	-24.1	3.63×10 <sup>12</sup>	237.3	179.1	-77.8	4.41×10 <sup>9</sup>	196.5	139.4	-76.2	2.80×10 <sup>12</sup>	195.2	178.4	-22.4
0.6	$2.88 \times 10^{12}$	237.3	177.7	-79.7	$3.58 \times 10^{14}$	237.2	207.4	-39.7	4.08×10 <sup>12</sup>	237.3	179.8	-76.8	4.97×10 <sup>10</sup>	195.9	153.9	-56.1	8.36×10 <sup>12</sup>	195.0	184.9	-13.4
0.7	$1.19 \times 10^{12}$	237.5	172.4	-87.1	$2.18 \times 10^{14}$	237.3	204.4	-43.8	4.44×10 <sup>12</sup>	237.3	180.3	-76.1	2.50×10 <sup>11</sup>	195.5	163.6	-42.6	1.59×10 <sup>13</sup>	194.8	188.7	-8.1
0.8	$1.27 \times 10^{12}$	237.5	172.8	-86.5	$1.79 \times 10^{14}$	237.3	203.2	-45.5	4.44×10 <sup>12</sup>	237.3	180.3	-76.1	2.91×10 <sup>11</sup>	195.5	164.5	-41.4	2.33×10 <sup>13</sup>	194.8	191.0	-5.0
Ave	8.30×10 <sup>12</sup>	237.5	173.9	-85.1	8.61×10 <sup>14</sup>	237.4	201.1	-48.4	2.81×10 <sup>12</sup>	237.6	170.7	-89.6	8.60×10 <sup>10</sup>	196.4	143.0	-71.1	7.20×10 <sup>12</sup>	195.7	164.6	-41.5
rage	0.50^10	201.0	173.9	-03.1	0.01^10	237.7	201.1	-10.1	2.01^10	257.0	170.7	-07.0	0.00^10	170.4	175.0	-/1.1	7.20^10	173,7	107.0	-41.5

# 2.3.4 Weight loss prediction via machine learning methods

The intersection of machine learning and thermal analysis is a burgeoning field with immense potential for prediction of the pyrolysis behaviours [192,193]. Sensitive analysis was conducted to identify the importance of the inputs on the influence of output. Fig 2.10 reveals the input variables importance in the models, with temperature overwhelmingly dominating at 78.13 %, followed by heating rate at 21.12 %. This suggests that temperature is the primary driver of the weight loss phenomenon being modelled. Other variables, such as cellulose, hemicellulose, lignin, ash, and soluble constituent, have negligible importance, indicating that their roles in predicting weight loss are minimal compared to temperature and heating rate.

The comparison between the RF and GBRT models was presented in Fig 2.11 and Table 2.10. The RF model demonstrates outstanding predictive ability, with an  $R^2$  score of 0.9925, signifying that the model can explain over 99 % of the variance in the dependent variable. This is coincidence with a low MSE of 0.0029, indicating precise predictions. The RF's hyperparameters show a balanced approach between complexity and computational cost, with 100 trees and a depth of 10, ensuring that the model captures sufficient complexity without undue computational burden. In contrast, the GBRT model achieves an even higher  $R^2$  score of 0.9994 and an impressively low MSE of 0.0008. Such statistics reflect a model that is almost perfectly in sync with the observed data. The GBRT achieves this with 383 estimators at a maximum depth of 4, pointing towards a focused approach that leverages boosting to minimize errors sequentially. It is apparent that both RF and GBRT models are highly effective in predicting the weight loss of the blends. However, the GBRT model's marginally superior performance metrics suggest that when computational resources permit, it may be the more advantageous choice. Moreover, the sensitive analysis highlights the critical influence of temperature and heating rate in thermal decomposition processes.

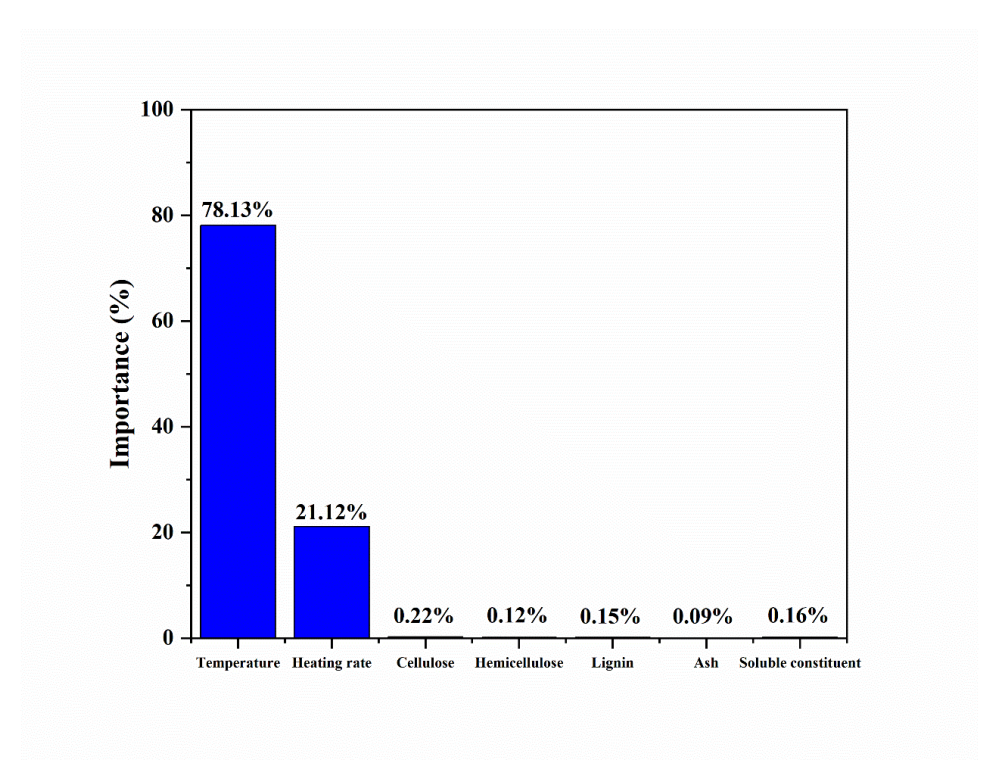


Fig 2.10 Importance of input variables in machine learning models.

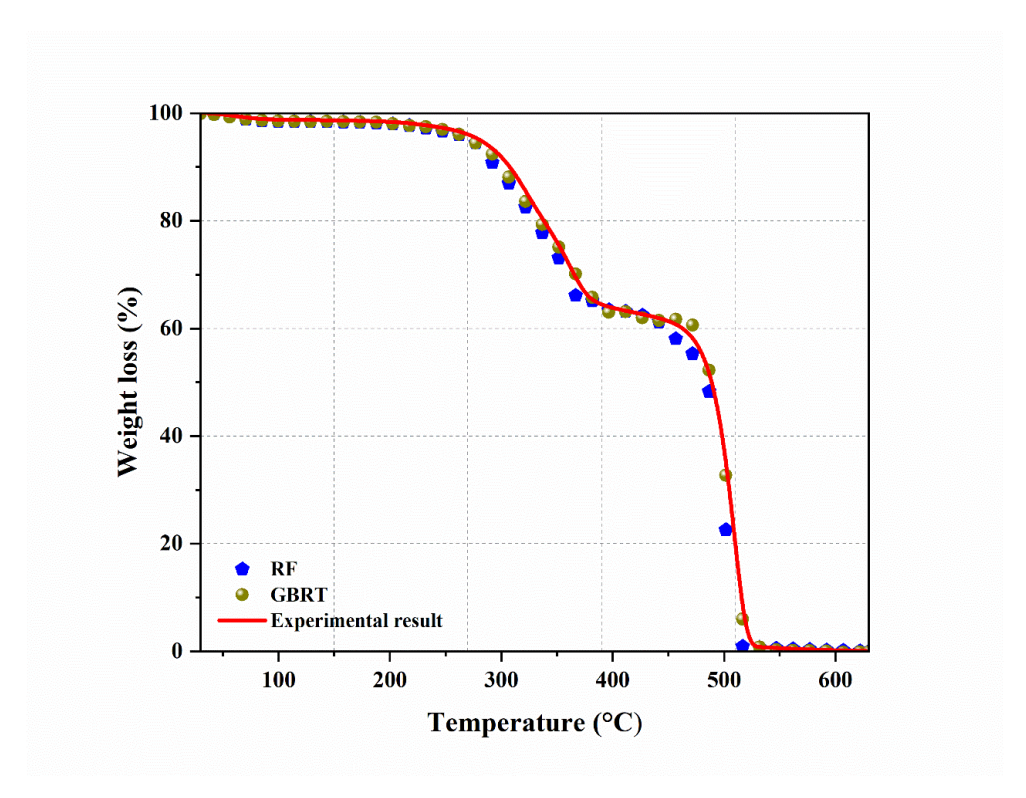


Fig 2.11 Comparison of predicted and actual stem/HDPE weight loss values from RF and GBRT models

Table 2.10 The best  $R^2$  and MSE scores of different models based on best hyperparameter choice.

Model	$R^2$	MSE	Optimized hy	Optimized hyperparameters					
	K	WISE	Estimators	Split	Leaf	Depth			
RF	0.9925	0.0029	100	2	2	10			
GBRT	0.9994	0.00008	383	2	5	4			

#### 2.4 Conclusion

The thermal behaviours, products distribution, and kinetics of co-pyrolysis of corn stalk and HDPE blends towards different fibrous tissues were investigated. It was observed that the DTG peak temperatures were lower in the co-pyrolysis processes for all groups compared to that of pure materials, suggesting that the presence of HDPE promotes the decomposition of corn stalk. Py-GC/MS analysis revealed that the pyrolytic products from corn cob/HDPE blends contained a higher concentration of aromatic hydrocarbons and furans, which are beneficial for biofuel production. Kinetic analyses, performed using the KAS and FWO methods, showed variations in activation energy values among the testing blends, reflecting the influence of corn stalk tissues on the kinetics of co-pyrolysis performance. The cob/HDPE group exhibited the lowest activation energy (149.3 kJ/mol), suggesting cob is the most effective corn stalk tissue for energy-efficient co-pyrolysis applications. Additionally, the RF and GBRT algorithms successfully predicted the TG profiles of corn stalk tissues/HDPE mixtures, with the GBRT algorithm demonstrating superior performance compared to the RF algorithm. Therefore, corn stalk tissues, particularly corn cob, can serve as a viable, costeffective feedstock for the co-pyrolysis of biomass and plastic, offering a sustainable approach to managing agricultural wastes.

# **Chapter 3**

Catalytic Co-pyrolysis of cellulosic ethanol processing residue with high-density polyethylene over biomass bottom ash catalyst

# 3. Catalytic Co-pyrolysis of cellulosic ethanol processing residue with high-density polyethylene over biomass bottom ash catalyst

In this chapter, a comprehensive approach was undertaken to enhance the utilization of lignocellulosic biomass by focusing on the co-pyrolysis of biorefinery residues and plastic waste. Specifically, the solid residue generated from a biorefinery plant processing corn cobs was selected as feedstock. To explore synergistic effects and improve product quality, this residue was co-pyrolyzed with plastic, aiming to promote waste valorisation and energy recovery. Furthermore, the bottom ash derived from the same biorefinery process was examined for its potential as a low-cost, sustainable catalyst in the co-pyrolysis of corn cob residue and plastic. The catalytic performance of the bottom ash was evaluated in terms of its influence on pyrolysis behaviour. This integrated strategy not only seeks to maximize resource recovery from agricultural and plastic wastes but also explores circular economy opportunities within the biorefinery framework.

### 3.1 Introduction

Compared to direct use of lignocellulosic biomass for biofuels production, utilizing the solid residual from second-generation bioethanol plant can significantly improve the economic feasibility of biorefineries and simplify the downstream solid waste management [63,194,195]. In a typical second-generation bioethanol plant using corn cob as the feedstock, the ethanol-processing residue (EPR) is remained as a solid waste after saccharification and fermentation. Due to the high content of lignin and non-hydrolysable holocellulose in EPR, it also can be considered as an ideal feedstock for biofuels production [143]. As talked in previous chapters, in the co-pyrolysis process biomass and plastic, plastic could provide hydrogen during the co-pyrolysis process and prohibits the coke formation because of the appropriate H/C<sub>eff</sub> ratio [152,196,197]. In addition, co-pyrolysis of biomass and waste plastics is also environmentally friendly as it reduces carbon emissions and offers innovative ideas for end-of-life strategies and energy extraction for waste plastics [13].

In order to further improve the quality of bio-oil, catalytic co-pyrolysis of biomass and waste plastic is advocated [86,198]. Various commercial catalysts, e.g. zeolites [199], dolomite [200] and Ni-based catalysts [201] have been used to upgrade bio-oil by co-pyrolysis. However, the economic feasibility of catalytic co-pyrolysis has long been criticized by the high cost and low recyclable catalysts. Currently, many researchers focus on using solid waste. For instance, Loy *et al.* [89] used industrial waste coal bottom ash as a catalyst in catalytic pyrolysis of rice

husk, the results illustrated that the using coal bottom ash as catalyst could increase the syngas production and decrease coke formation, and the hydrogen was increased by 8.4 %. In another work, Wu *et al.* [90] used incineration bottom ash as catalyst in catalytic pyrolysis of biogas residue. The results suggested incineration bottom ash had negative effect on biogas residue pyrolysis. Similar to the aforementioned research, the bottom ash (BA), which is from the combustion of EPR to generate heat or electricity to power the biorefinery process, also exhibited great potential to be reused as a catalyst to upgrade bio-oil and decrease the activation energy of pyrolysis reactions [86,91]. This is because it contains high silica content and mesoporous surface area, which could improve the pyrolysis performance [88]. In addition, other impurities such as lime, alkalis, iron oxide, alumina are also contained in BA to ensure the good pyrolysis performance [86].

In fact, benefits from the EPR pyrolysis are obvious. For instance, part of the EPR obtained in the biorefinery process can be used as a pyrolysis feedstock, while another part can be burned to supply heat to the upstream processes, and the combustion product BA can be reused as a catalyst in the pyrolysis process. On this basis, combining the pyrolytic bio-oil production with conventional biorefinery process, solid residues produced in the typical second-generation biorefinery process, including the EPR and BA, can be utilized as feedstock and catalyst, respectively, so as to realize 'zero emission' of solid waste.

To better investigate pyrolysis behaviours of EPR, TGA is the simplest and quickest method to gain the complete profile of non-isothermal thermal decomposition process [202]. The kinetic parameters such as activation energy, pre-exponential factor and order of reaction can be determined from TGA experiments whether using model-free or model-fitting models.

In this section, aiming to extend the entire second-generation bio-ethanol process, the EPR and HDPE are utilized as feedstocks for pyrolytic bio-oil production. During the process, BA was recycled and further reused as catalyst for the co-pyrolysis of EPR/HDPE blends (Fig 3.1). To better understand the chemical and physical properties of EPR and BA, the chemical composition was characterised by Brunauer–Emmett–Teller analysis (BET), Fourier transform infrared spectroscopy (FT-IR), X-ray fluorescence (XRF), Field emission scanning electron microscope (FESEM), and Energy disperse X-ray analysis (EDX). Thermogravimetric analysis (TGA) was conducted to investigate the pyrolysis characteristics of catalytic co-pyrolysis and non-catalytic co-pyrolysis of EPR/HDPE. Two model-free methods (KAS and FWO) are used to calculate the activation energy of pyrolysis process. The product distribution from the pyrolysis process was characterized by Py-GC/MS.

# **Novelty statement**

This chapter advances the concept of circular catalytic valorisation by employing BA, a byproduct from the ethanol biorefinery process, as a low-cost in-situ catalyst for the copyrolysis of EPR and HDPE. Unlike conventional studies that rely on synthetic catalysts, this work demonstrates the dual valorisation of both organic residues and inorganic wastes within the same system. Through TGA–kinetic modelling (FWO, KAS) and Py–GC/MS, it elucidates how BA catalysis reduces activation energy, enhances aromatic formation, and promotes deoxygenation, providing a sustainable and economically feasible catalytic route for industrial biorefineries.

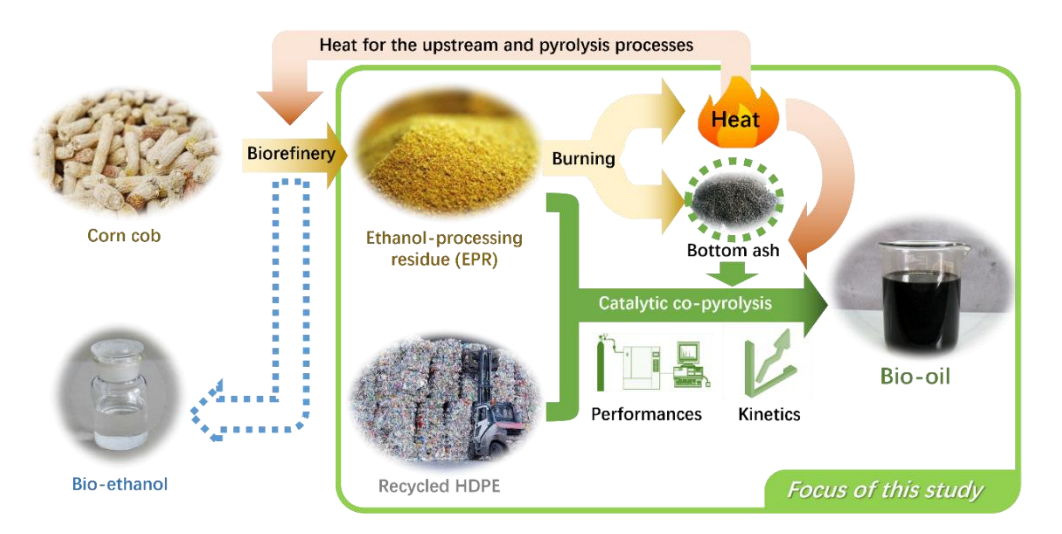


Fig 3.1 Diagram for the co-pyrolysis of EPR and HDPE by BA.

# 3.2 Materials and methods

This section outlines the experimental procedures, materials, and analytical techniques employed in this study.

### 3.2.1 Materials

The EPR from the corn cob biorefinery process and BA were obtained from Longlive Biotech Co., Ltd., China. The BA was collected after the burning of EPR for heat. The high-density polyethylene (HDPE 600) was purchased from Beijing Jinma Plastic Co. Ltd., China. Density and melting point of HDPE were 0.956 g cm<sup>-3</sup> and 136 °C, respectively. The EPR and BA were first dried at 105 °C for 24 h, followed by milling into particles with average size of less than 20 µm.

### 3.2.2 Characteristics of EPR and Bottom ash

The ultimate and proximate analyses of the ethanol-processing residue (EPR), including moisture, volatile matter, fixed carbon, and ash contents, were conducted using the same procedures described in Chapter 2. The elemental composition was determined by an elemental analyser, and the biochemical components of EPR were analysed following the National Renewable Energy Laboratory (NREL, USA) protocol (detailed method in Appendix 3). All analyses were performed in triplicate for reproducibility, and detailed experimental procedures are provided in the Appendix 1 and 2 [26]. The functional groups of EPR were evaluated by Fourier-transform infrared spectrometer (FT-IR) (Nicolet 6700, Thermo Fisher, USA) in the range of 500 cm<sup>-1</sup> to 4000 cm<sup>-1</sup> with a resolution of 4 cm<sup>-1</sup>. N<sub>2</sub> adsorption measurements were conducted by a gas sorption system (Autosorb-iQ, Quantachrome, USA).

The surface morphology and elemental composition of the EPR and BA were characterized using field emission scanning electron microscopy (FESEM, Hitachi SU8020, Japan) equipped with an energy-dispersive X-ray spectroscopy (EDS, IXRF 550i, USA) detector. Prior to observation, all samples were dried at 105 °C for 12 h and then mounted on aluminium stubs using conductive carbon tape. A thin layer of gold (~5 nm) was sputter-coated on the surface using a Quorum Q150T coater to enhance conductivity and reduce charging effects. The FESEM was operated at an accelerating voltage of 5–10 kV, with a working distance of 8–10 mm, and secondary electron (SE) imaging was used to capture fine surface structures. EDS spectra and elemental maps were acquired under the same conditions with a live time of 60 s to ensure quantitative accuracy. The elemental composition was averaged from at least five random regions of each sample to minimize local heterogeneity.

The inorganic elemental composition of the bottom ash (BA) was determined using a wavelength-dispersive X-ray fluorescence spectrometer (WDXRF, Rigaku ZSX Primus III+, Japan). Prior to analysis, the BA samples were oven-dried at 105 °C for 12 h, finely ground to below 75 µm, and pressed into pellets under 20 MPa pressure to ensure uniform surface texture and analytical stability. Measurements were carried out under vacuum conditions using a Rh anode X-ray tube operated at 50 kV and 50 mA. The instrument was equipped with a LiF(200) crystal for wavelength dispersion, and both a flow proportional counter and a scintillation counter were employed for light and heavy element detection, respectively. Calibration was performed using oxide-type certified reference materials of similar matrix composition to ensure analytical accuracy. The data were processed using Rigaku ZSX software for semi-

quantitative "Fundamental Parameters" analysis, which automatically corrects for matrix effects and spectral overlaps. Each sample was measured in triplicate (n = 3), and the averaged concentrations of major oxides (e.g., SiO<sub>2</sub>, CaO, Fe<sub>2</sub>O<sub>3</sub>, Al<sub>2</sub>O<sub>3</sub>, MgO, K<sub>2</sub>O, Na<sub>2</sub>O, TiO<sub>2</sub>) and minor elements were reported as oxide weight percentages (wt%) on a dry basis.

The specific surface area, pore volume, and pore size distribution of BA were determined using nitrogen ( $N_2$ ) adsorption—desorption isotherms at 77 K with a gas sorption analyzer (Autosorb-iQ, Quantachrome, USA). Prior to measurement, samples were degassed at 150 °C for 6 h under vacuum (<  $10^{-3}$  mbar) to remove adsorbed moisture and gases. The BET (Brunauer–Emmett–Teller) method was used to calculate the specific surface area in the relative pressure range  $P/P_0 = 0.05-0.30$ . The total pore volume was determined from the adsorbed nitrogen volume at  $P/P_0 \approx 0.99$ , assuming complete pore filling. The micropore volume was obtained by the t-plot method, while the pore size distribution was derived from the adsorption branch of the isotherm using the density functional theory (DFT) model. All analyses were performed in triplicate to ensure reproducibility, and representative isotherms and surface micrographs are presented in the results section.

# 3.2.3 Thermal analysis

TGA (LECO TGA701) was carried out to evaluate the thermal decomposition behavior of EPR/HDPE blend and EPR/HDPE/BA blend. The EPR/HDPE blend was mixed in the ratio of 1:1 meanwhile the EPR/HDPE/BA blend was mixed in the ratio of 1:1:0.1. The samples were heated from room temperature to 700 °C at three different heating rates (10, 20, 40 K/min) in N<sub>2</sub> atmosphere. Each experiment was carried out in triplicate.

The pyrolysis products were analysed by Py-GC/MS to identify and characterise the volatile compounds generated during thermal decomposition. The analyses were conducted using a CDS 5000 pyrolyser (Chemical Data Systems, USA) coupled to a GC/MS system (Thermo Fisher TRACE 1310 GC and ISQ LT MS, USA). Approximately  $0.80 \pm 0.10$  mg of finely ground and oven-dried sample (< 0.20 mm) was placed in a deactivated stainless-steel sample cup and introduced into the microfurnace of the pyrolyser. The initial furnace temperature was set at 300 °C, then increased to 600 °C at a heating rate of 1 °C/ms, and held for 20 s to ensure complete volatilisation of the organic components. The interface and transfer line temperatures between the pyrolyser and the GC/MS were maintained at 300 °C to prevent condensation of pyrolysates. Chromatographic separation of the evolved volatiles was achieved using a VF-17MS capillary column (30 m × 0.25 mm i.d. × 0.25 µm film thickness).

The injector temperature was maintained at 300 °C with a split ratio of 80:1, and helium (99.999 %) was used as the carrier gas at a constant flow rate of 1 mL min<sup>-1</sup>. The column temperature program was as follows: the initial oven temperature was held at 40 °C for 12 s, ramped to 200 °C at 5 °C min<sup>-1</sup>, then to 300 °C at 20 °C min<sup>-1</sup>, and maintained at the final temperature for 5 min. The mass spectrometer was operated in electron ionisation (EI) mode at an energy of 70 eV, scanning over a mass-to-charge (m/z) range of 35–500 u. The ion source and quadrupole were maintained at 230 °C and 150 °C, respectively. Compound identification was performed by matching the acquired spectra with the NIST 17 mass spectral library, applying a minimum match quality threshold of 800. Semi-quantitative analysis of the pyrolysis products was carried out based on the relative peak areas in the total ion chromatogram (TIC), assuming equal response factors for all detected compounds.

### 3.2.4 Kinetics

The pyrolysis process of solid-state feedstocks such as biomass and plastic waste can be assumed to be treated as a single reaction: Biomass and/or plastic  $\rightarrow$  volatiles + char. The kinetic theory was discussed in Chapter 2.

#### 3.3 Results and discussion

### 3.3.1 EPR and BA characterization

The chemical compositions of EPR are listed in Table 3.1. It contains 58.8±2.30 wt% of cellulose, 5.4±0.10 wt% of hemicellulose, and 22.5±0.90 wt% of lignin. The high cellulose content and low hemicellulose could be attributed to the hydrolysis of hemicellulose during the acid pretreatment and delignification during the alkali pretreatment before simultaneous saccharification fermentation [63]. Because of the resistant corn cob structure, the raw material, the inaccessible holocellulose by cellulase remains in the EPR. Compared with the negligible ash content in the raw corn cob, the ash content in EPR was relatively high, owing to the residual yeast cells and salts [63].

According to the proximate analysis, EPR has a high volatile matter content ( $59.76\pm1.00$  wt%), which would be leading to an elevated amount of pyrolysis products and decrease the yield of solid products [198,203]. Moreover, even though the EPR theoretically contains proteins and cells debris, the N and S contents were extremely low ( $1.80\pm0.23$  wt% and  $0.51\pm0.02$  wt%, respectively), indicating there would be low emission of NO<sub>x</sub> and SO<sub>2</sub> in the pyrolysis progress.

Table 3.1 Physical and chemical properties of EPR.

Index	Values	Unit	
Chemical composition a			
Cellulose	58.8±2.30	%	
Hemicellulose	$5.4 \pm 0.10$	%	
Lignin	22.5±0.90	%	
Soluble substances	5.1±0.20	%	
Ash	$8.2 \pm 0.10$	%	
Proximate analysis <sup>a</sup>			
Moisture	$7.05 \pm 0.25$	%	
Volatile matter	$59.76 \pm 1.00$	%	
Fixed carbon	15.61±0.65	%	
Ash	$17.58 \pm 0.45$	%	
Ultimate analysis <sup>b</sup>			
C	$48.70 \pm 0.92$	%	
Н	4.97±0.15	%	
$O^*$	$19.39 \pm 0.89$	%	
N	$1.80 \pm 0.23$	%	
S	$0.51 \pm 0.02$	%	

<sup>&</sup>lt;sup>a</sup> On dry mass fraction basis (wt%), <sup>b</sup> On dry and ash-free basis (wt%), <sup>\*</sup> Calculated by difference.

The FT-IR spectrum of EPR was also analyzed (Fig 3.2). The large band between 3000 cm<sup>-1</sup> and 3750 cm<sup>-1</sup> belongs to the O-H stretching vibration of hydroxyl of cellulose and hemicellulose [204]. The peak located at 2920.88 cm<sup>-1</sup> is attributed to C-H stretching vibration of methyl or methylene group [205]. In addition, the peak around 1648.24 cm<sup>-1</sup> is the C=O stretching which indicated the aromatic groups of lignin, and the peak at 1512.03 cm<sup>-1</sup> is evidence of benzene skeletal vibration of lignin [63]. The peak arising from 1061.89 cm<sup>-1</sup> belongs to the C-O stretching vibration of cellulose and hemicellulose [205]. Therefore, EPR had a large amount of aromatic and oxygenated functional groups.

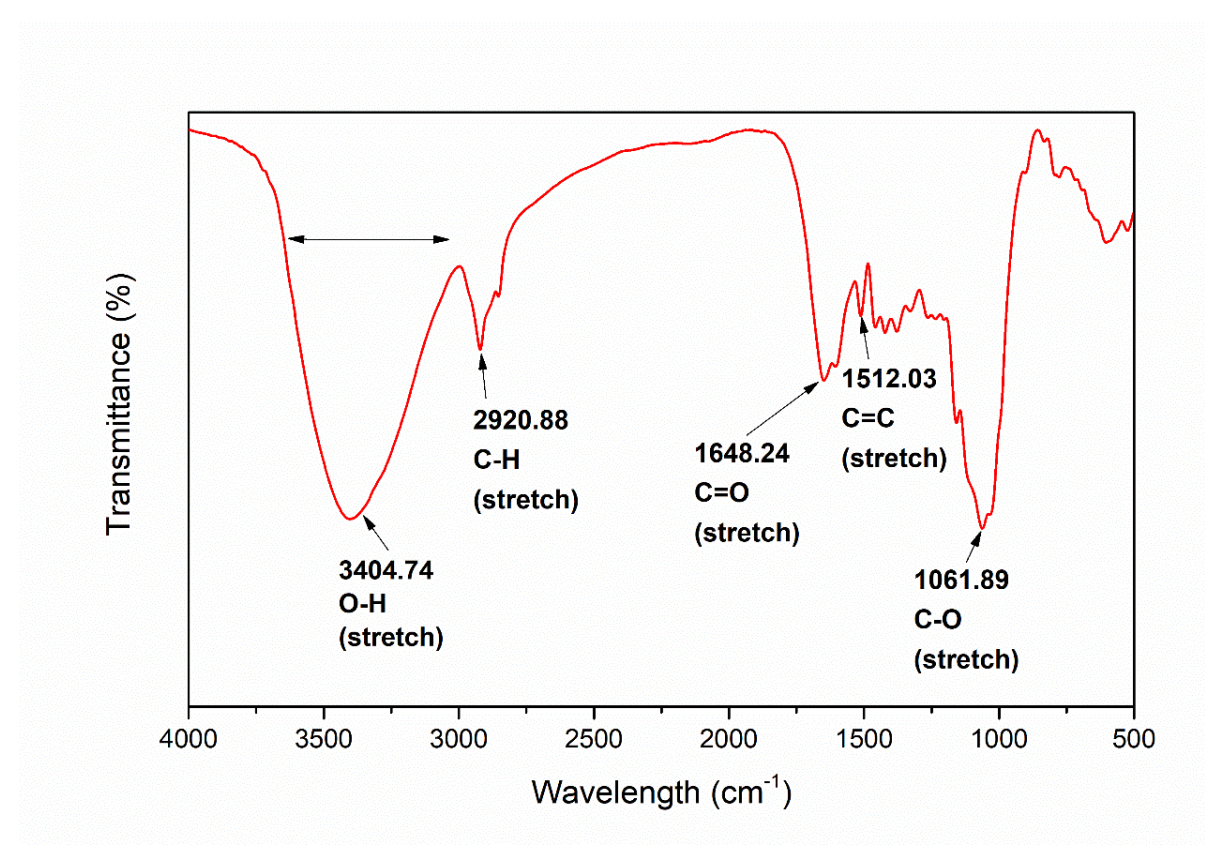


Fig 3.2 The FTIR spectra of EPR

The surface morphology and elemental composition of EPR were shown in Fig 3.3, and the EDS results were listed in Table 3.2. It exhibited a rough surface after acid pretreatment and enzymatic hydrolysis process, and there are many different sizes of cracks and pore cavities afforded to the adhesion of BA with feedstock. The EDS analysis illustrated that the EPR is mainly containing C (56.67 wt%) and O (32.29 wt%) elements. Furthermore, a small amount of alkali metals such as Na (3.60 wt%) was also measured, which could be assigned to the residual salts after fermentation.

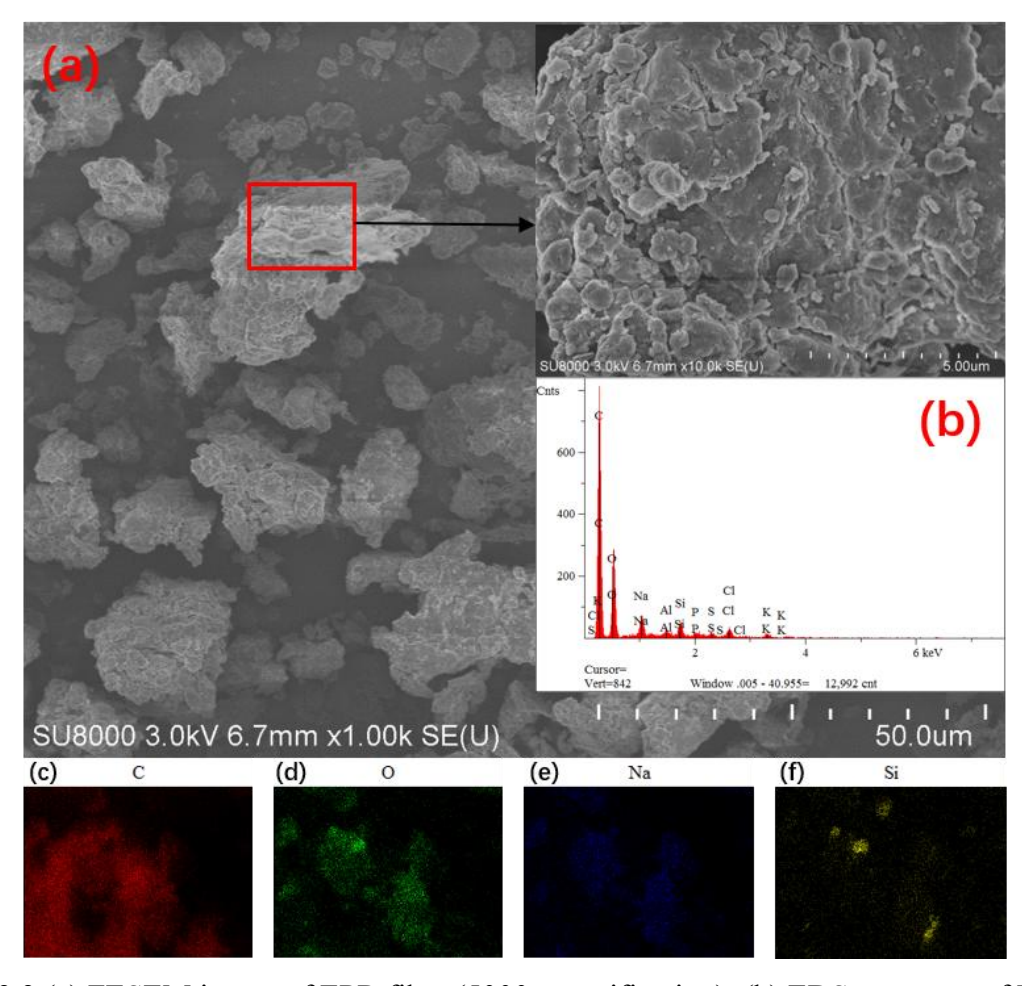


Fig 3.3 (a) FESEM image of EPR fiber (5000 magnification); (b) EDS spectrum of EPR fiber; (c-f) EDS element distribution of C, O, Na and Si, respectively.

Table 3.2 EDS analysis result of EPR fibre<sup>a</sup>

Element	Content (wt.%)
C	56.67±2.33
O	32.29±1.12
Na	3.60±0.94
Si	$1.79 \pm 0.46$

<sup>&</sup>lt;sup>a</sup> Analysis on dry mass fraction basis.

Table 3.3 illustrated the XRF analysis results, which indicated that BA is mainly composed of SiO<sub>2</sub> (52.95 wt%). Moreover, high content of alkali metal oxides such as CaO (10.32 wt%), K<sub>2</sub>O (10.11 wt%), MgO (3.11 wt%) and Na<sub>2</sub>O (2.24 wt%) were also detected, along with transition metal oxides (e.g., Fe<sub>2</sub>O<sub>3</sub>) and amphoteric metal oxides (e.g., Al<sub>2</sub>O<sub>3</sub>). Alkali metal oxides always prohibited coke formation on catalyst [206], whilst the Fe<sub>2</sub>O<sub>3</sub> and Al<sub>2</sub>O<sub>3</sub> could

enhance the syngas production [86], therefore, the BA can be potentially used as catalyst to improve the pyrolysis behaviour of EPR [95].

Table 3.3 XRF analysis result of BA<sup>a</sup>

Content (wt.%)
52.95±2.13
$10.32 \pm 0.95$
$10.11 \pm 0.92$
$7.89 \pm 0.53$
4.77±0.71
3.73±0.12
3.11±0.22
2.24±0.08
$1.86 \pm 0.05$
$1.58 \pm 0.02$
1.44±0.09

<sup>&</sup>lt;sup>a</sup> Analysis on dry mass fraction basis,

Fig 3.4 demonstrated the FESEM image of BA (Fig 3.4a), EDS spectrum of BA (Fig 3.4b) and EDS element distribution of C, O, Na, Mg, Al, Si, Cl, K, Ca and Fe, respectively (Fig 3.4c-i). The SEM analysis indicated that the BA exhibits a porous structure, and there are many small particles disperse on the surface. The porous and agglomerated structure of BA increases the contact area with biomass [87]. The elemental compositions of BA are shown in Table 3.4, which showed the C and O contents are 32.23 wt% and 25.62 wt%, respectively, whereas the content of Si is 13.76 wt%. The BET surface area, pore volume and diameter of BA are further determined (Table 3.5). The average pore diameter of BA is 3.710 nm, indicating that BA mainly consisted of mesoporous material [207]. The cumulative pore volume of BA is 0.101 cc g<sup>-1</sup>, which is much higher than that from traditional catalysis such as Ni (0.019) and CaO (0.0016) [207]. Furthermore, the surface area of BA is 11.038 m²/g, it is also higher than fresh nickel (4.68 m²/g) and natural zeolite (1.25 m²/g) [89]. According to Loy *et al.*'s work [89], the higher BET surface area of BA would provide more active sites for the co-pyrolysis of EPR and HDPE, which driven us to further investigate the co-catalytic performances of the EPR/HDPE/BA blend.

<sup>&</sup>lt;sup>b</sup> Calculated by difference.

Table 3.4 EDS analysis of BA<sup>a</sup>

Element	Content (wt%)
С	32.23±1.33
O	25.62±2.13
Si	13.76±1.11
Fe	5.33±0.33
Ca	5.18±0.25
Al	4.48±0.02
K	4.23±0.56
Cl	3.31±0.25
Na	3.08±0.12
Mg	2.78±0.34
<sup>a</sup> On dry mass fraction basis	
Table 3.5 BE	T analysis of BA <sup>a</sup>

Table 3.5 BET analysis of BA

Surface area	11.038±0.33	$m^2/g$
Cumulative pore volume	$0.101 \pm 0.01$	cc/g
Average pore diameter	3.710±0.21	nm

<sup>&</sup>lt;sup>a</sup> BJH absorption.

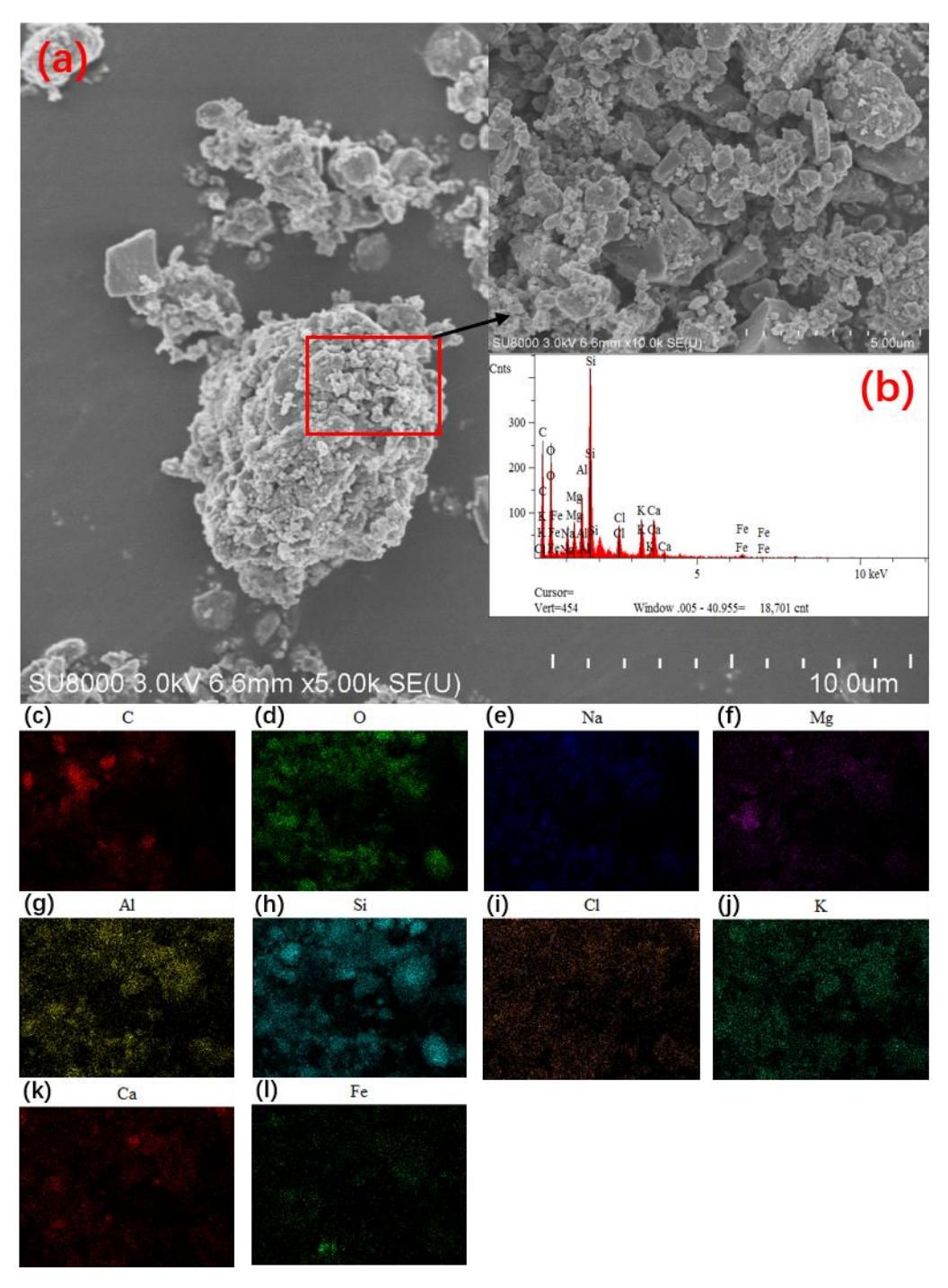
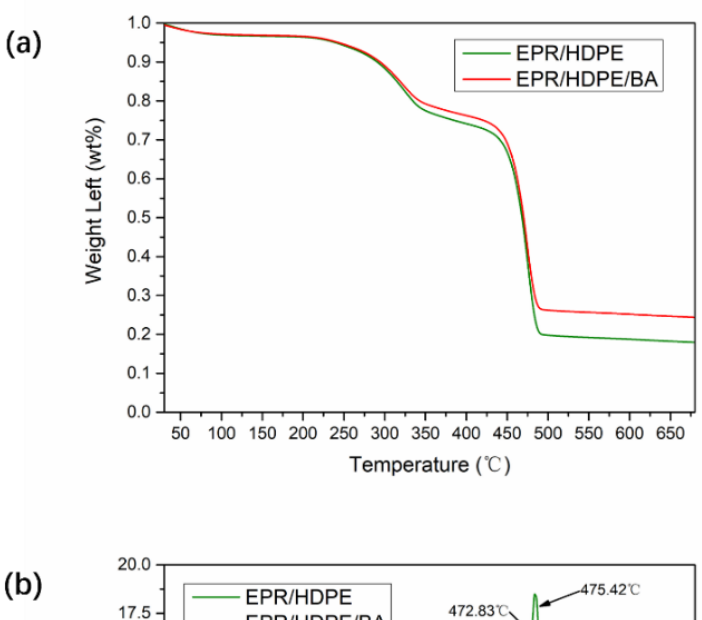


Fig 3.4 (a) FESEM image of PA (5000 magnification); (b) EDS spectrum of BA; (c-i) EDS element distribution of C, O, Na, Mg, Al, Si, Cl, K, Ca and Fe, respectively.

# 3.3.2 Co-pyrolysis of EPR and HDPE

Fig. 3.5 shows the TGA and DTG patterns of the EPR/HDPE/BA blends. The BA-free process is treated as the control (refers to the non-catalytic pyrolysis process). As it can be observed in Fig 3.5a, both the non-catalytic and catalytic pyrolysis processes present similar degradation trends. Generally, the thermal degradation of EPR/HDPE in both two groups that are with and without BA can be divided into four stages. In the temperature range of room temperature (~25 °C) to 150 °C, the weight loss is mainly attributed to thermally driving off the moisture and light volatile compounds in EPR. In addition, hemicellulose begins to decompose at this stage because of its loose structure [63]. The second stage occurs in the temperature range of 200-380 °C. In this stage, cellulose and hemicellulose decomposed rapidly. Hemicellulose has a relatively loose structure, because it consists of saccharides such as glucose and xylose, and exhibited an amorphous structure that can be easily degraded [208]. Whereas, cellulose consists of long-chain polymers, glucose, which exhibit a more stable structure than other components. Hence, the decomposition temperature of cellulose is higher than hemicellulose [209]. The strong and sharp peak located at 472 °C belongs to the degradation of HDPE [172]. The slow degradation of lignin almost exists in the whole pyrolysis process, since lignin has a stable structure with aromatic rings [86]. It has been reported that the decomposition of lignin releases much CH<sub>4</sub> and H<sub>2</sub> due to the presence of aromatic ring and O-CH<sub>3</sub> functional group [210].



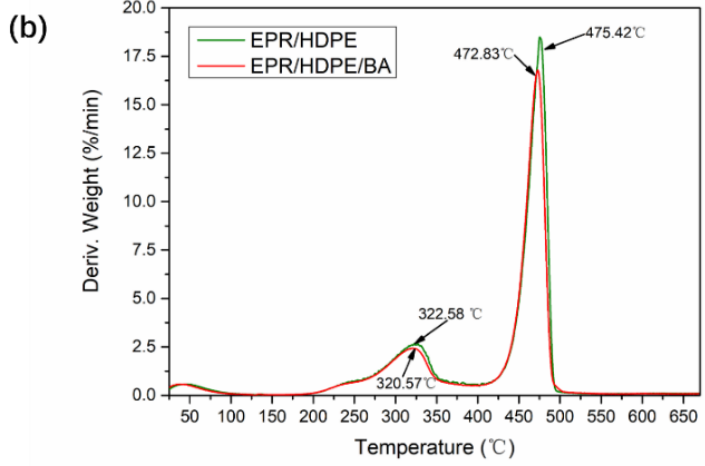


Fig. 3.5 TGA-DTG profiles of EPR and HDPE co-pyrolysis with and without BA.

The DTG curves of EPR/HDPE and EPR/HDPE/BA are presented in Fig. 3.5b. It can be observed that the DTG curve of EPR/HDPE is similar with the curve obtained in EPR/HDPE/BA. Compared with the non-catalytic pyrolysis, the peak temperature shifts to slightly lower temperature after adding BA. Moreover, the maximum degradation rate decreases when BA was added into the pyrolysis of EPR/HDPE. It has been reported that the maximum degradation rate is one of the most important factors for the reduction of the energy consumption in the pyrolysis process. Although these changes are relatively minor, they suggest that BA exerts a weak synergistic or catalytic effect during the co-pyrolysis process. The reduced peak temperature implies a marginal facilitation of the decomposition reactions, whereas the lower maximum degradation rate may reflect the heat absorption and diffusion effects of the mineral components in BA, which smooth the reaction rate profile. This observation is consistent with previous reports indicating that the maximum degradation rate

is a key parameter influencing the energy efficiency of the pyrolysis process [89]. Therefore, BA can be considered to have a slight promoting yet moderating influence on the thermal degradation behaviour of the EPR/HDPE blend.

# 3.3.3 Py-GC-MS analysis

Py-GC-MS analysis was carried out to investigate the pyrolysis products from EPR/HDPE blends and the effect of BA. The main compositions of the pyrolysis product can be classified into aromatics, ketone, furan, hydrocarbon, alcohols and other substances. The relative abundances of these compositions are shown in Fig 3.6, and the detailed products are listed in Table 3.6. There is no acetic acid in both catalytic and non-catalytic pyrolysis products, and the abundance of ketones are low. This phenomenon can be attributed to the low content of hemicellulose in EPR. It is demonstrated that acid is produced from the cracking of the acetyl group in hemicellulose, and ketones are also generated after hemicellulose degradation [211,212]. Alcohols are mainly produced from the decomposition of hemicellulose and cellulose [213]. Attributed to the abundant cellulose content in the EPR, the concentration of alcohols is relatively higher than other products. The highest content found in both the catalytic and non-catalytic pyrolysis samples is hydrocarbon, which is attributed to the decomposition of HDPE.

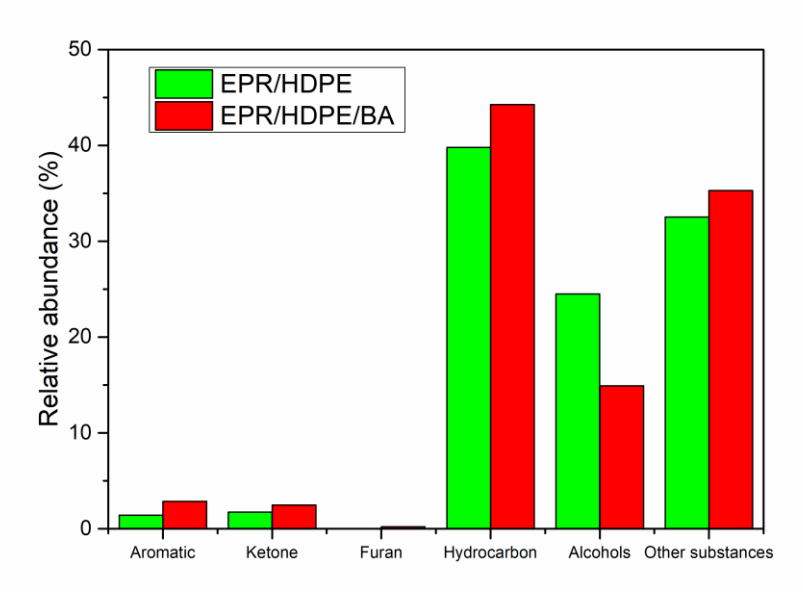


Fig 3.6 Pyrolysis products of EPR and HDPE co-pyrolysis with and without BA.

The aromatic hydrocarbons from catalytic pyrolysis are higher than that from non-catalytic pyrolysis, owing to the acidity and size selectivity of BA [214]. It also can be observed that the presence of BA enhanced the production of hydrocarbons. Hydrocarbons are often

regarded as valuable products from biomass pyrolysis. The enhancement of hydrocarbons production indicates that the BA facilitated the pyrolysis of biomass. Catalytic pyrolysis of biomass is usually carried out by breaking of C-CO(OH) and C-OH bonds in dehydration, decarbonylation and decarboxylation reactions [215]. After adding BA, the production of alcohols is decreased significantly (Fig 3.6). BA may deoxygenate the pyrolysis products in terms of lowering the yield of alcohols. All these points indicate that BA can be used as a catalyst in co-pyrolysis of EPR and HDPE.

Table 3.6 Pyrolytic products of EPR/HDPE blend and EPR/HDPE/BA blend

Cataga	Commovedo	EPR/HDPE/BA	EPR/HDPE	
Category	Compounds	Peak area(%)	Peak area(%)	
Hydrocarbons		44.25	39.79	
	2-Butene	1.13	4.38	
	1-Hexene	2.29	2.07	
	1-Heptene	1.81	1.39	
	1-Octene	1.03	0.81	
	Octane	0.3	0.22	
	1,8-Nonadiene	0.52	0.37	
	1-Nonene	1.29	1.03	
	Nonane	0.43	-	
	Cyclohexane, 2-propenyl-	0.18	0.18	
	1,9-Decadiene	0.52	0.42	
	1-Decene	2.34	1.98	
	Decane	0.29	0.27	
	1,10-Undecadiene	0.64	0.46	
	1-Tetradecene	2.32	1.95	
	Undecane	0.64	0.41	
	1,11-Dodecadiene	0.71	0.51	
	1-Dodecene	1.83	1.47	
	1,12-Tridecadiene	0.96	0.73	
	1-Tridecene	1.83	1.51	
	1,13-Tetradecadiene	0.96	0.73	
	1-Tetradecene	2.09	1.81	
	Tetradecane	0.42	0.34	
	Naphthalene, decahydro-2-methyl-	0.16	-	
	1,13-Tetradecadiene	1.05	0.79	
	Pentadecane	0.5	0.42	
	Cetene	1.8	1.52	

Substances		55.49	5 <b>2.</b> 57
Other		35.29	32.54
	Octacosanol	2.7	10.47
	1-Heptacosanol	2.97	3.69
	1-Hexacosanol	2.85	3.59
	n-Tetracosanol	2.77	2.36
	1,15-Pentadecanediol	1	1.29
	11-Hexadecen-1-ol	0.83	1.07
	n-Pentadecanol	1.65	1.95
1.0011010	2-Nonyn-1-ol	0.13	0.1
Alcohols	1,5 Systopenumentone	14.9	24.52
. wiwii	1,3-Cyclopentanedione	0.22	_
Furan		0.22	11.0
	E-14-Hexadecenal	1.76	1.46
	1,2-Cyclopentan edione, 3-methyl-	0.44	0.27
aldehydes	3-Cyclopentene-1-acetaldehyde,2-oxo-	0.27	_
Ketones and		2.47	1.73
	3',5'-Dimethoxyacetophenone	0.22	-
	Naphthalene, 1-(2-propenyl)-	-	0.11
	2-Methoxy-4-vinylphenol	0.75	0.76
	Benzofuran,2,3-dihydro-	1.77	-
	Phenol,2,5-dimethyl-	0.13	-
	p-Xylene	-	0.32
	Ethylbenzene	-	0.23
Aromatics		2.87	1.42
	Heptacos-1-ene	2.29	1.84
	1-Hexacosene	2.25	1.89
	1-Tetracosene	2.21	1.93
	1-Docosene	1.79	1.49
	1,19-Eicosadiene	1.27	0.99
	1-Nonadecene	1.86	1.57
	Octadecane	0.52	1.56
	1-Nonadecene	1.85	0.96
	Heptadecane	0.47	0.39
	1,15-Hexadecadiene	1.16	0.91
	Hexadecane	0.54	

# 3.3.4 Kinetic analysis

Compared to model-fitting methods, model-free methods are more accurate for non-linear reaction mechanism study [216]. Hence, KAS and FWO methods were chosen to calculate the activation energy. Because of the unstable decomposition reaction at the start and end of pyrolysis process, the conversion rate ( $\alpha$ ) from 0.1 to 0.9 is selected [208]. The kinetic parameters including apparent activation energy  $(E_a)$  and the coefficients of determination  $(R^2)$ are shown in Table 3.7. The  $E_a$  values are distinct between different conversion rates due to the various energy requirements of the reactions occurring during the pyrolysis process [217]. Based on the KAS method, the linear model of non-catalytic and catalytic co-pyrolysis of EPR and HDPE is determined by plotting  $\frac{1}{T}$  versus  $ln\left(\frac{\beta}{T^2}\right)$  (Fig 3.7a and 3.7b). All the points fitted well with  $R^2$  ranging from 0.971 to 1.000 (Table 3.7). Therefore, the first order reaction mechanism was suitable for both non-catalytic and catalytic EPR/HDPE pyrolysis. The average  $E_a$  value for non-catalytic pyrolysis of EPR/HDPE is 174.8 kJ/mol, which is higher than that of catalytic pyrolysis of EPR/HDPE using BA (171.3 kJ/mol). Activation energy is the minimum energy requirement for a reaction to start [86]. A reaction with a low  $E_a$  value can increase the reaction rate and energy efficiency [141]. Although the reduction in  $E_a$  is relatively minor, it still implies that the presence of BA exerts a weak but positive catalytic influence on the co-pyrolysis process. This subtle decrease can be attributed to the alkaline and alkalineearth metal oxides (e.g., CaO, MgO, and K<sub>2</sub>O) present in the bottom ash, which may promote the initial cracking and deoxygenation reactions of oxygenated intermediates by providing active basic sites. However, since BA is a heterogeneous and relatively inert solid, its catalytic activity is limited, resulting in only a modest reduction in the overall energy barrier. Therefore, BA primarily acts as a mild catalyst and heat carrier, facilitating heat transfer and local radical stabilization rather than significantly altering the reaction pathway.

To ensure the reliability of the kinetic parameters, another model-free method, the FWO kinetic method is adopted. The linear relationships for the given conversion rate are determined by the plots of  $\frac{1}{T}$  versus  $ln(\beta)$  (Fig 3.7c and 3.7d). As shown in Table 3.7, the  $E_a$  values estimated by FWO method are slightly higher than that of KAS method. The  $R^2$  values in FWO method are all greater than 0.97, which is similar with the results obtained by KAS method. The results reaffirm the first-order reaction mechanism fitted well with both non-catalytic pyrolysis of EPR/HDPE and catalytic pyrolysis of EPR/HDPE using BA. By the catalysis of BA, the  $E_a$  value decreased from 177.3 kJ /mol to 174.0 kJ /mol. The results are in good agreement with KAS method. In both KAS and FWO method, the average  $E_a$  value decreased

with the presence of BA as catalyst. This phenomenon can be attributed to the suitable porous structure and the chemical composition of BA (Fig 3.7 and Table 3.7). Additionally, the metal oxides and char component in BA would further boost the decomposition reaction [86]. Overall, the  $E_a$  values estimated by KAS and FWO methods are similar, which demonstrate the reliability of the experimental data. Therefore, the addition of BA in EPR/HDPE blends could reduce the  $E_a$  value of the co-pyrolysis process.

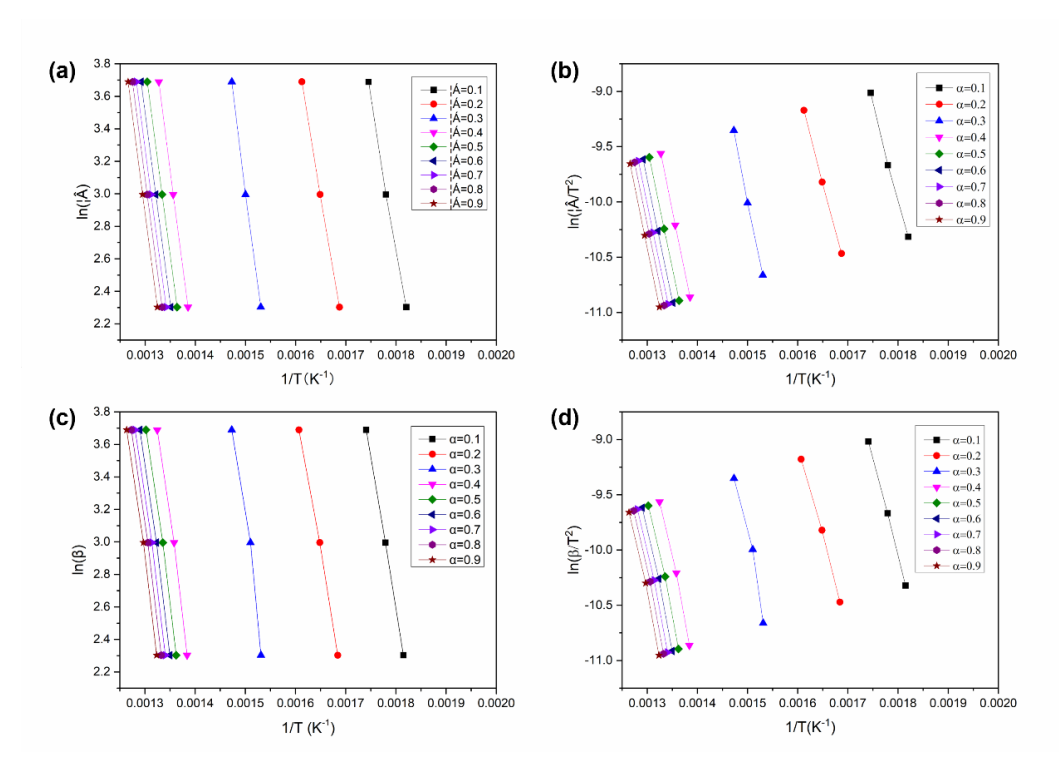


Fig 3.7 Linear correlation of co-pyrolysis of EPR and HDPE by FWO and KAS methods. (a) EPR/HDPE (KAS); (b) EPR/HDPE/BA (KAS); (c) EPR/HDPE (FWO); (d) EPR/HDPE/BA (FWO).

Table 3  $E_{\alpha}$  and  $R^2$  values corresponding to  $\alpha$  for EPR/HDPE co-pyrolysis

	Non-catalyti	c co-pyr	olysis of EPR	/HDPE	Catalytic co-pyrolysis of EPR/HDPE			
α	KAS		FWO		KAS		FWO	
	$\boldsymbol{E_a}$ (J/mol)	$R^2$	$\boldsymbol{E_a}$ (J/mol)	$R^2$	$\boldsymbol{E_a}$ (J/mol)	$R^2$	$\boldsymbol{E_a}$ (J /mol)	$R^2$
0.1	143.7	0.999	145.5	0.999	146.2	0.997	147.9	0.998
0.2	143.6	0.997	146.1	0.998	138.9	1.000	141.7	0.999
0.3	188.0	0.971	189.3	0.974	181.3	0.999	182.9	0.999
0.4	185.8	0.994	188.3	0.994	180.4	1.000	182.9	1.000
0.5	181.6	0.995	184.4	0.995	178.5	1.000	181.6	1.000
0.6	181.7	0.995	184.7	0.996	178.9	0.999	182.0	0.999

0.7	181.0	0.995	184.1	0.996	178.4	1.000	181.7	1.000
0.8	182.8	0.996	185.9	0.996	180.2	1.000	183.5	1.000
0.9	184.7	0.995	187.8	0.996	178.8	1.000	182.1	1.000
Average	174.8	-	177.3	-	171.3	-	174.0	-

### 3.4 Conclusion

The thermal characteristics, product distribution, and kinetic behavior of the co-pyrolysis of EPR and HDPE using recycled BA as a catalyst were systematically investigated. The TGA results revealed that the incorporation of BA caused a slight decrease in the peak temperature and maximum degradation rate, indicating a moderate influence on the decomposition process. Correspondingly, the average activation energy values decreased from 174.8 kJ/mol (KAS) and 177.3 kJ/mol (FWO) for the non-catalytic co-pyrolysis to 171.3 kJ/mol (KAS) and 174.0 kJ/mol (FWO) for the catalytic system. Although the reduction in  $E_a$  was relatively minor, it still suggests that BA exerts a weak but positive catalytic effect, facilitating the decomposition of EPR and HDPE by enhancing heat transfer and providing mineral-derived active sites. Overall, the use of recycled BA as a low-cost catalyst offers a sustainable approach for valorising ethanol-processing residue through co-pyrolysis with waste plastics. This process contributes to the energy recovery and solid waste minimization goals of biorefinery systems, supporting the development of eco-efficient and circular bioenergy production routes.

# **Chapter 4**

Pyrolysis behaviour and kinetic analysis of waste polylactic acid composite reinforced with reed straw processing residue

# 4. Pyrolysis behaviour and kinetic analysis of waste polylactic acid composite reinforced with reed straw processing residue

This chapter explores the thermochemical behaviour and valorisation potential of polylactic acid (PLA)-based composites reinforced with biorefinery residues. Unlike traditional composites using raw lignocellulosic biomass, this study utilizes reed straw processing residue (RSPR), a byproduct of biorefinery operations, as a sustainable filler in PLA composites. The integration of such residues not only enhances waste management efficiency but also adds economic value to bioplastic recycling. To assess the thermal decomposition behaviour, pyrolysis kinetics were investigated using multiple model-free methods (FWO, KAS, and Friedman) along with the model-fitting master-plot approach. Additionally, TG-FTIR analysis was employed to identify the evolved gaseous products. The findings contribute to a deeper understanding of the pyrolytic conversion of PLA composites and support the development of circular strategies for bioplastic waste and biorefinery byproducts.

### 4.1 Introduction

PLA is a kind of fully degradable polymer with good mechanical properties [218], which has been widely used in packaging, medical application and other consumer products [219]. Nevertheless, owing to the obstacle of its brittleness, poor gas and water barriers, and low heat distortion temperature, pure PLA is seldom directly used as a functional material to replace the commonly used petroleum-based plastics, such as PE and PP [220,221]. A well-proven route to solve the above barriers is adding a reinforcement phase such as rice straw, coconut coir fibre, and rice husk to produce composite materials [222–224]. In addition, to endow better mechanical and physical properties, it was also indicated that the phenolic groups in the natural fibre reinforcement phase could obviously enhance the ductility, UV light barrier and thermal resistance of PLA [225].

Although lignocellulose/PLA composites are fully biodegradable materials, it always requires a long time to realize harmless disposal [226,227]. A pitfall of the rapidly growing PLA market is the potential environment pollution once the amount of waste PLA-based composite exceeds the maximum capacity of municipal composting facilities [101]. In fact, the discarded PLA-based composites are a good carbon resource to create additional values, rather than directly degrading in municipal composting facilities [228]. Compared to composting, which is less efficient and less economically valuable, one of the most practical strategies is to

convert waste lignocellulose/PLA composites into more valuable chemicals such as bio-oil, pyrolytic gas and carbons by pyrolysis [101,229,230].

The pyrolysis mechanisms of the pure PLA have been investigated in previous research. Sun *et al.* [231] pointed out transesterification and radical reactions are two major pathways involved in the PLA pyrolysis process. The transesterification reactions occurr at relatively lower temperatures. During the process, CO, acetaldehyde, D,L-lactide and the cyclic polymers that are similar to lactide, are generated by the back-biting reaction of carboxyl groups or hydroxyl groups on the PLA molecular chains [232]. When the pyrolysis temperature exceeds 300 °C, a series of free radical reactions occur, in which process the carbon free radicals and oxygen free radicals are generated from the cleavage of PLA molecular chains [233]. Since the stereoisomerism formed on carbon radicals, the PLA moiety is racemized, and further generate the meso-lactide, which product is the indicator that distinguish whether free radical reactions occur or not during the pyrolysis [229]. Zhang et al. (2022) studied the pyrolysis characteristics of 3D printed polylactic acid waste (3DP-PLAW) using TG-FTIR and Py-GC/MS. They found that the main pyrolysis products of 3DP-PLAW consists of CO, CO<sub>2</sub>, CH<sub>4</sub>, acetaldehyde, esters (meso-lactide and D, L lactide), and other carbon-based compounds. Furthermore, the high volatile matter in 3DP-PLAW contributes to a more efficient thermochemical conversion.

Many studies suggest the co-pyrolysis of plastics and lignocelluloses could facilitate the pyrolysis reaction and reduce the energy consumption, which is attributed to the synergistic effect between these two distinct types of feedstocks [139,190,218]. Compared to pyrolysis, co-pyrolysis always generates homogenous stable products with low oxygen content and high caloric value [234]. Sun et al. [101] suggested there are synergistic effects between wood flour and PLA during the co-pyrolysis process, in which process the free radical reaction of PLA can be promoted due to the presence of wood flour. In other research, Qi et al. [235] explored the generation of aromatic hydrocarbons through the co-pyrolysis of microalgae and polypropylene (PP). The co-pyrolysis of microalgae and PP exhibits a synergistic effect, leading to a more significant production of aromatic hydrocarbons in comparison to the individual pyrolysis of microalgae and PP. For the pyrolytic recycling of the lignocelluloses/plastic composite materials, the abovementioned statements regarding the positive effect of the natural fibres as reinforcement on the pyrolysis behaviour of composites are generally applicable. For instance, Lin et al. [94] evaluated the products distribution and synergy during the catalytic pyrolysis of wood-plastic composite (WPC). The results suggest that there were strong synergistic interactions between poplar and PP in the process of WPC pyrolysis, which promote the yield of alkenes. In addition, Sun et al. [129] investigated the products' distribution during the pyrolysis of wood-plastic composites (WPC) using pyrolysis-gas chromatography/mass spectrometry (Py-GC/MS) and reported poplar wood provided radicals to promote the breaking of polymer chains, resulting in the formation of lighter paraffins. Nonetheless, the pyrolysis behaviours of the lignocelluloses/PLA composite are rarely studied.

To gain deeper insights into the thermal properties and pyrolysis kinetics of solid materials, thermogravimetric analysis (TGA) is a widely employed method with high accuracy [236]. In the case of studying the pyrolytic kinetics of PLA-based composites, model-free methods are reliable methods which can be used for the calculation of various thermodynamic parameters, including activation energy, pre-exponential factor, and order of reaction [237]. Commonly utilized methods in previous research include the Flynn-Wall-Ozawa (FWO) method, the Starink method, and the Kissinger–Akahira–Sunose (KAS) method. [163,198,238]

Fig 4.1 showed the graphic abstract of this section. Compared to directly employing lignocellulosic biomass as reinforcement in PLA composite production, using the solid residue from biorefinery plant can markedly enhance the economic feasibility and streamline the management of solid waste in subsequent stages [11,220]. The pyrolysis behaviour of the blend of PLA and wood flour has been well studied in previous works [101,190,218] and limited research investigated the pyrolysis behaviour of PLA composite [239]. However, no investigation has been done on the pyrolysis behaviour of biorefinery residue reinforced PLA composites. In this section, the pyrolysis kinetics of reed straw processing residual (RSPR) reinforced polylactic acid (PLA) composite was investigated by the Flynn-Wall-Ozawa (FWO) method, the Kissinger–Akahira–Sunose (KAS) method, the Friedman method and master-plot method. During the pyrolysis of RSPR/PLA composites, the evolved gaseous products were monitored and analyzed using TG-FTIR. The primary objective of this study is to maximize the value of waste PLA-based composites in the energy area and provide basic understanding of thermo-chemical conversion to support the rapid growth of the PLA industry.

# **Novelty statement**

This chapter expands pyrolysis research beyond raw or residue feedstocks to the lignocellulose-reinforced composite level, focusing on RSPR/PLA composites—a representative bio-based 3D printing material. It provides the first detailed kinetic and mechanistic analysis of RSPR-assisted PLA decomposition, demonstrating the synergistic radical interactions between lignocellulose and PLA that significantly lower activation energy and modify gas-evolution profiles. The study identifies the one-dimensional diffusion (D1)

mechanism as the dominant reaction mechanism and establishes a foundation for thermochemical upgrading of discarded bio-composites.

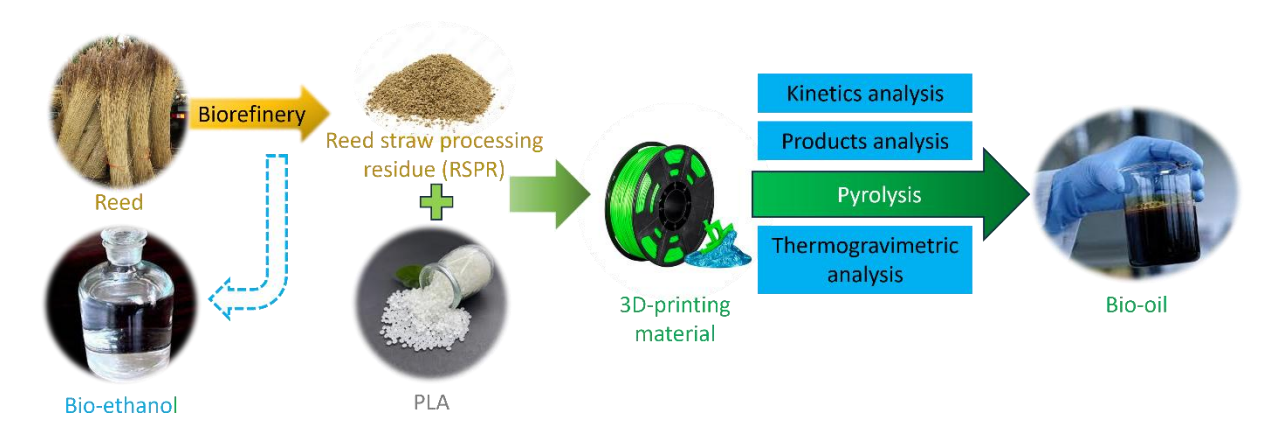


Fig 4.1 The graphic abstract of this section

# 4.2 Materials and methods

This section outlines the experimental procedures, materials, and analytical techniques employed in this study.

# 4.2.1 Materials and preparation of RSPR/PLA composite

The reed straw (RS) was harvested in Changping district, Beijing, China. After drying out and milling into ~60 meshes, the RS powder was pre-treated by dilute NaOH aqueous solution, followed by collection and hydrolysis by cellulase. Then, the solid residual that was defined as the RSPR collected and dried at 105 °C for 24 h. After milling, the RSPR was used as the reinforcement phase for the RSPR/PLA composite. The chemical constituents (cellulose, hemicellulose, lignin) of the RSPR were determined by the standard of National Renewable Energy Laboratory of USA (detailed method in Appendix 3) [240], and the results showed the chemical constituents of RSPR are 39.15±1.2 wt% of cellulose, 22.5±0.9 wt% of hemicellulose, 19.6±0.4 wt% of lignin and 18.75±0.4 wt% of other substances, respectively. The PLA (4032D) was purchased from Natureworks LLC, USA.

A COPERION ZSK series twin-screw extruder (Werner & Pfleiderer, Germany) was used for the preparation of RSPR/PLA composites. A mixture of PLA (70 wt%), RSPR (20 wt%), and coupling agent (3 wt% synthesis of plant ester, 3 wt % PEG600 and 4 wt % KH550) was extruded under the heating zone temperatures of 145-170 °C with screw speed of 60 rpm. The injection of the standard specimen was prepared at 145-160 °C and 50 MPa by an injection

moulding machine (HTF 120 X2, Haitian, China). The RSPR/PLA composite was first dried at 105 °C for 24 h, followed by milling into particles with average size of less than 20 µm.

# 4.2.2 Characteristics of RSPR/PLA composite

The proximate analysis and the ultimate analysis were performed based on the methods in Appendix 1 and 2 to determine the elemental composition and the moisture, volatile, fixed carbon and ash content. The results were listed in Table 4.1. According to the proximate analysis results, the volatiles in RSPR (73.13±0.75 wt%), PLA (99.88±0.08 wt%) and RSPR/PLA composite (95.25±0.66 wt%) was the predominated fraction, which inferred low solid products yield in the pyrolysis process [198,238]. Meanwhile, according to the ultimate analysis results, carbon and oxygen were the main elements in all the tested specimens (93.69 wt% for RSPR, 94.22 wt% for PLA and 93.4 wt% for RSPR/PLA composite). The N element (0.40.4±0.09 wt%) in RSPR could be assigned to the remaining proteins during the fermentation process. While the N elements in the RSPR/PLA composite could be attributed to the introduction of couple agent in the preparation process.

Table 4.1 Ultimate analysis and proximate analysis results of the specimens

Samples	Ultimate analysis <sup>a</sup> (wt%)				Proximate analysis <sup>b</sup> (wt%)			
•	С	Н	N	O *	Moisture	Volatile	Ash	Fixed
								carbon
RSPR	44.72±	5.91±0.0	$0.4 \pm 0.09$	48.97±0.53	5.3±0.15	73.13±0.75	6.07±0.11	14.5±0.1
	0.45	9						5
PLA	$49.94 \pm$	$5.76\pm0.1$	$0.02 \pm 0.001$	$44.28 \pm 0.35$	0	$99.88 \pm 0.08$	$0.09 \pm 0.02$	$0.03 \pm 0.0$
	0.26	2						01
RSPR/PLA	51.96±	$6.3 \pm 0.14$	$0.3 \pm 0.01$	41.44±0.15	$0.76 \pm 0.0$	$95.25 \pm 0.66$	1.55±0.02	$2.44 \pm 0.0$
composite	0.23				2			7

<sup>&</sup>lt;sup>a</sup> On dry and ash-free basis (wt%), <sup>b</sup> On dry mass fraction basis (wt%), \* Calculated by difference.

### 4.2.3 Thermogravimetric and pyrolysis products analysis

Thermal decomposition behaviour of RSPR, PLA and RSPR/PLA composite were characterized using TGA/DSC3+ (Mettler, Switzerland). The experiments were conducted from 30 °C to 700 °C at different heating rates (5 °C/min, 10 °C/min and 20 °C/min) in nitrogen atmosphere. The TGA experiment was conducted three times to ensure the reproducibility and trustworthiness of the data.

The gaseous products were analysed by TG-FTIR. In this process, the RSPR, PLA and RSPR/PLA composite specimens were heating from 30 °C to 800 °C, with a heating rate of 10 °C/min, within a purity nitrogen atmosphere flowing at a rate of 50 mL/min by using a TG 209F1 Libra thermal analyser (NETZSCH, Germany). The temperature of the transfer line connecting to the TG-FTIR apparatus was maintained at 250 °C. The identification of functional groups in the gas products was carried out using an FTIR spectrometer (Nicolet 6700, Thermo Fisher, USA) with a spectral resolution of 4 cm<sup>-1</sup> in the spectral region from 4500 cm<sup>-1</sup> to 500 cm<sup>-1</sup>.

The pyrolysis products were analysed by Py-GC/MS to identify and characterise the volatile compounds generated during thermal decomposition. The analyses were conducted using a CDS 5000 pyrolyser (Chemical Data Systems, USA) coupled to a GC/MS system (Thermo Fisher TRACE 1310 GC and ISQ LT MS, USA). Approximately  $0.80 \pm 0.10$  mg of finely ground and oven-dried sample (< 0.20 mm) was placed in a deactivated stainless-steel sample cup and introduced into the microfurnace of the pyrolyser. The initial furnace temperature was set at 300 °C, then increased to 600 °C at a heating rate of 1 °C/ms, and held for 20 s to ensure complete volatilisation of the organic components. The interface and transfer line temperatures between the pyrolyser and the GC/MS were maintained at 300 °C to prevent condensation of pyrolysates. Chromatographic separation of the evolved volatiles was achieved using a VF-17MS capillary column (30 m  $\times$  0.25 mm i.d.  $\times$  0.25  $\mu$ m film thickness). The injector temperature was maintained at 300 °C with a split ratio of 80:1, and helium (99.999 %) was used as the carrier gas at a constant flow rate of 1 mL min<sup>-1</sup>. The column temperature program was as follows: the initial oven temperature was held at 40 °C for 12 s, ramped to 200 °C at 5 °C min<sup>-1</sup>, then to 300 °C at 20 °C min<sup>-1</sup>, and maintained at the final temperature for 5 min. The mass spectrometer was operated in electron ionisation (EI) mode at an energy of 70 eV, scanning over a mass-to-charge (m/z) range of 35–500 u. The ion source and quadrupole were maintained at 230 °C and 150 °C, respectively. Compound identification was performed by matching the acquired spectra with the NIST 17 mass spectral library, applying a minimum match quality threshold of 800. Semi-quantitative analysis of the pyrolysis products was carried out based on the relative peak areas in the total ion chromatogram (TIC), assuming equal response factors for all detected compounds.

# 4.2.4 Kinetics analysis

To better understand the pyrolysis characteristics of the RSPR/PLA composite, a kinetic analysis was conducted to determine the pyrolysis kinetics. The basic kinetic theory was previously discussed in the previous section.

### 4.2.4.1 Model-free methods

Model-free methods do not require the knowledge of the reaction mechanism, which helps avoid errors in estimating  $E_a$ . KAS and FWO which are two integral model-free methods were employed to analyse the pyrolytic kinetics analysis of RSPR, PLA and RSPR/PLA composite. In additional, Friedman method, a differential model-free method, has been adopted to calculate the E value to reduce the error in results. The equations for these three model-free methods can be expressed as follows:

KAS: 
$$ln\left(\frac{\beta}{T^2}\right) = ln\frac{AR}{E_a g(\alpha)} - \frac{E_a}{RT}$$
 (4.1)

FWO: 
$$ln(\beta) = ln \frac{0.0048AE}{Rg(\alpha)} - \frac{1.0516E_a}{RT}$$
 (4.2)

Friedman: 
$$ln\left(\frac{d\alpha}{dt}\right) = ln\left[Af(\alpha)\right] - \frac{E_a}{RT}$$
 (4.3)

The activation energy  $E_a$  can be estimated by the slopes of the  $\frac{1}{T}$  versus  $ln\left(\frac{\beta}{T^2}\right)$  plots (KAS), the  $\frac{1}{T}$  versus  $ln(\beta)$  plots (FWO) and  $ln\left(\frac{d\alpha}{dt}\right)$  versus  $\frac{1}{T}$  plots (Friedman) [162–164,241].

### 4.2.4.2 Master-plot method

The Master-plot method was employed to determine the most suitable reaction mechanism model for the pyrolysis process. The relative equation and calculation have been presented in Chapter 2.

# 4.2.4.3 Thermodynamic parameters

The kinetic parameters and reaction mechanism model obtained from the model-free methods and master-plot method were utilized to compute the thermodynamic parameters of RSPR/PLA composite, including the pre-exponential factor A (s<sup>-1</sup>) [242], enthalpy change  $\Delta H$  (kJ/mol), Gibbs free energy  $\Delta G$  (kJ/mol), and changes in entropy  $\Delta S$  (kJ/mol·K). The relative explanation and calculations were presented in Chapter 3.

### 4.3 Results and discussion

# 4.3.1 Thermogravimetric analysis

Fig 4.2 showed the TGA and DTG curves of RSPR, PLA and RSPR/PLA composite at heating rate of 10 °C/min. The thermal decomposition curves of RSPR could be divided into three stages. The initial stage, occurring below 200 °C, was attributed to the evaporation of the moisture and small molecule volatile substance compounds in RSPR [243]. The second stage around 200-350 °C was caused by the depolymerization of hemicellulose and cellulose. Because of the relatively loose structure and poor thermal stability, the temperature for hemicelluloses depolymerization (200-300 °C) was lower than that of the crystalline regions containing cellulose (240-350 °C) [63,139,244]. The third stage is the decomposition of lignin, it lasted until the end of pyrolysis. Since the structure of lignin is very stable and rich in aromatic subunits, the decomposition of lignin exists almost throughout the whole pyrolysis process [208].

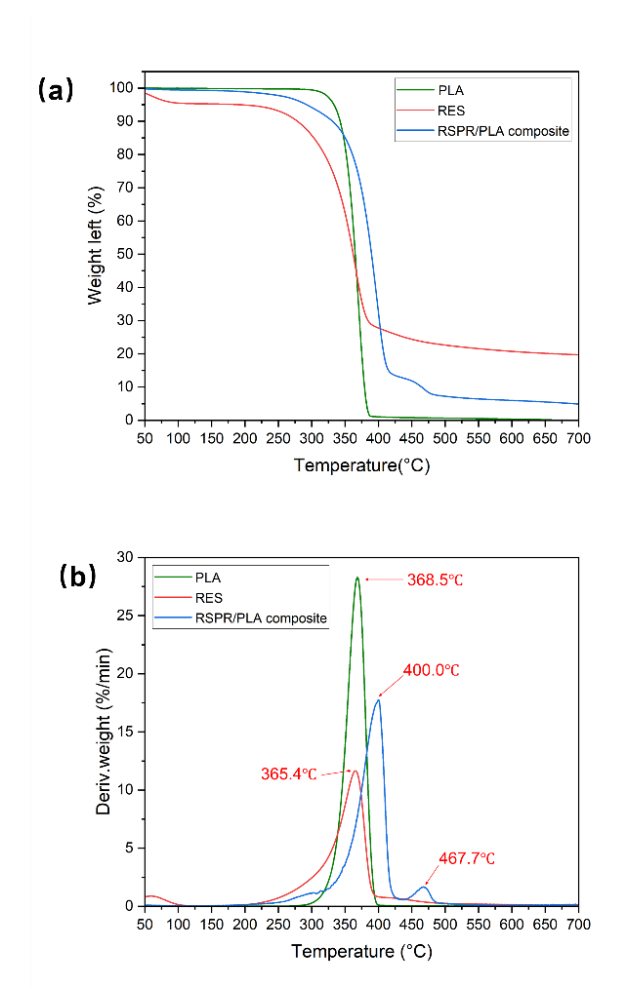


Fig 4.2 (a) TGA and (b) DTG curves of RSPR, PLA and RSPR/PLA composite at heating rate of 10 °C/min.

The decomposition of the pure PLA was completed in a single stage (300-398 °C). The orderly and repetitive molecular chains within PLA resulted in a concentrated pyrolysis temperature range, leading to a narrow DTG peak [218]. By contrast, the decomposition of RSPR/PLA composites can be divided into three stages. Similar with the phenomenon of the RPSR pyrolysis, the initial stage ranges from 200 °C to 330 °C was caused by the decomposition of hemicellulose and part of cellulose, while the second stage, occurring within the range of 330 °C to 440 °C, was associated with the pyrolysis of PLA and the remaining highly crystalline cellulose. The third stage (> 440 °C) was attributed to the pyrolysis of lignin and coupling agents in RSPR/PLA composites.

In comparison to the pyrolysis of RSPR and pure PLA, the DTG peak of the RSPR/PLA composites shifted to higher temperature. This phenomenon can be explained as follow: after alkali pre-treatment and enzymatic hydrolysis, the hydrogen bonds in the initial RSPS fibre was interrupted, thereby increased the roughness of the RSPR surface. Consequentially, the increased hydroxyl groups on the surface of the RSPR improved the adhesion of the reinforcement phase to the polymer matrix [245]. Furthermore, the addition of coupling agents including the synthetic plant ester, PEG600 and KH550 could also positively affect the thermal stability of the composite. With the increase of the heating rate, the peaks in all the DTG curves of the tested specimens shifted to higher temperatures, owing to the increase of the thermal hysteresis (Fig 4.3-4.5) [246].

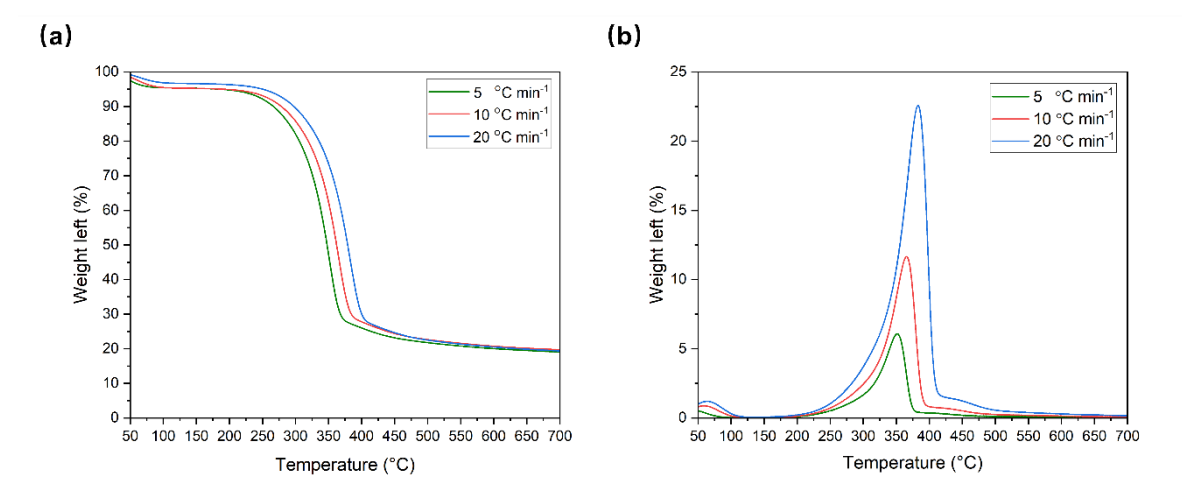


Fig 4.3 TGA and DTG curves of RSPR at different heating rates (5 °C /min, 10 °C /min and 20 °C /min).

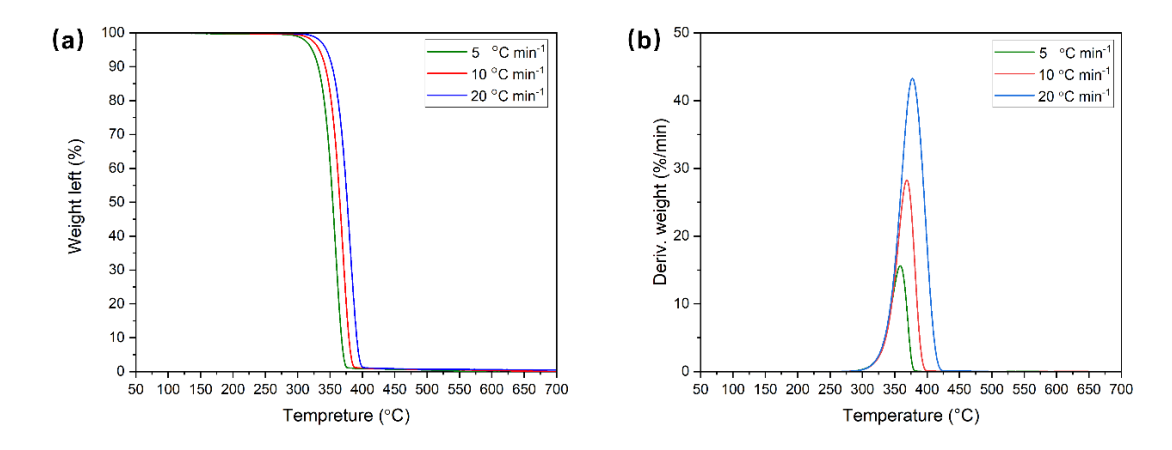


Fig 4.4 TGA and DTG curves of PLA at different heating rates (5 °C /min, 10 °C /min and 20 °C /min).

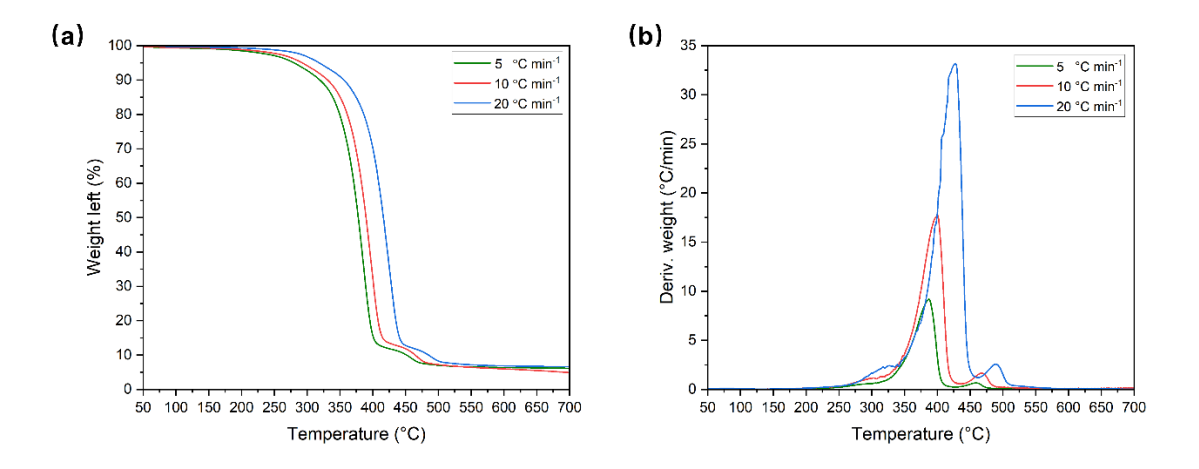


Fig 4.5 TGA and DTG curves of RSPR-reinforced PLA composite at different heating rates (5 °C /min, 10 °C /min and 20 °C /min).

# 4.3.2 Volatile products analysis by TG-FTIR and Py-GC/MS

The characterization and comparison of volatile products generated during the pyrolysis of RSPR, PLA, and RSPR/PLA composite were conducted. Fig 4.6(a), (c), (e) illustrated the 3D FTIR spectra of the gaseous products for RSPR, PLA, and the RSPR/PLA composite during the pyrolysis. According to the Beer-Lambert law, the absorbance of the gaseous pyrolysis products should be proportional to the concentration [247]. Therefore, the temperature range corresponding to peak absorption in the FTIR spectra indicates the stage during which the majority of pyrolysis products are generated. Specifically, the highest absorption peaks for RSPR occurred within the temperature range of 320-350 °C, whereas for PLA, they were in the range of 380-420 °C. In contrast, the RSPR/PLA composite exhibited its maximum

absorption peaks in the temperature range of 390-430 °C. Thus, compared to pyrolysis of RSPR and the pure PLA, the predominated pyrolysis products range shifted to higher temperatures in the group of RSPR/PLA composite. This may be due to the improved adhesion between RSPR and PLA matrix caused by the presence of coupling agents in the composite material [220].

Fig 4.6(b), (d), (f) showed the FTIR spectrums of RSPR, PLA and RSPR/PLA composite at different pyrolysis temperature. For the FTIR spectra of RSPR/PLA composite, the bands located in the range of 4000-3500 cm<sup>-1</sup> corresponded to the water released by dehydration and evaporation [248]. The peaks at the range of 3100-2640 cm<sup>-1</sup> can be assigned to the stretching vibration of C-H bonds, inferring the existence of hydrocarbon [249]. Specially, the peaks located in the range of 2800-2640 cm<sup>-1</sup> in FTIR spectra was the stretching vibration peak of the O=C-H group [250], which suggested the existence of aldehydes. The peaks within the range of 2400-2250 cm<sup>-1</sup> were associated with the C=O stretching vibration, specifically related to CO<sub>2</sub>, which was generated from the cracking and reforming of carbonyl and carboxyl during the pyrolysis [248]. The absorption at the range of 2240-2000 cm<sup>-1</sup> was related to CO. The strong peaks located at the ranged of 1850-1600 cm<sup>-1</sup> was attributed to the stretching vibration of C=O, indicating the generation of carbonyl compounds such as ester, ketone, acid, etc. [218]. The peaks in the range of 1400-1000 cm<sup>-1</sup> were the stretching vibration of C-O(H), which suggests the existence of alcohols, phenols and ethers [101]. The absorption peaks of the RSPR/PLA composite were mainly located at the range of 3100-2640 cm<sup>-1</sup> and 1850-1600 cm<sup>-2</sup> <sup>1</sup>, indicating the generation of hydrocarbons and carbonyl compounds. Therefore, the decomposition of RSPR/PLA composite mainly occurred at the methyl and ester bonds [101]. The main absorption peaks of RSPR located at the range of 4000-3500 cm<sup>-1</sup>, 3100-2640 cm<sup>-1</sup>, 2400-2250 cm<sup>-1</sup>, 2240-2000 cm<sup>-1</sup>, 1850-1600 cm<sup>-1</sup> and 1400-1000 cm<sup>-1</sup> corresponded to the existence of water, hydrocarbon, aldehydes, carbon dioxide, carbon monoxide, carbonyl compounds and alcohols, phenols, respectively [248]. The mainly gaseous products of PLA were located at the range of 3100-2640 cm<sup>-1</sup>, which were related to the presence of hydrocarbon and aldehydes.

Compared with the FTIR spectra of the gaseous products of PLA and RSPR, no additional absorption peak occurred in the spectra of RSPR/PLA composite, indicating there was no new product during the pyrolysis process. The largest change in FTIR spectra peaks of RSPR/PLA composite was C=O bond compared with that of PLA. This could be attributed to the presence of RSPR in composite promotes the free radical reaction of PLA, leading to the increase production of ester groups [229]. Furthermore, in comparison with the FTIR spectra of RSPR, the CO group nearly vanished, and the CO<sub>2</sub> group was also significantly weakened in the FTIR

spectra of RSPR/PLA composite. It has been reported that CO and CO<sub>2</sub> were the transesterification products of PLA pyrolysis [190]. The reduction of CO and CO<sub>2</sub> group in the FTIR spectra of RSPR/PLA composite demonstrated the presence of RSPR in composite promoted the reaction mechanism of PLA pyrolysis from the transesterification reaction to the free radical reaction.

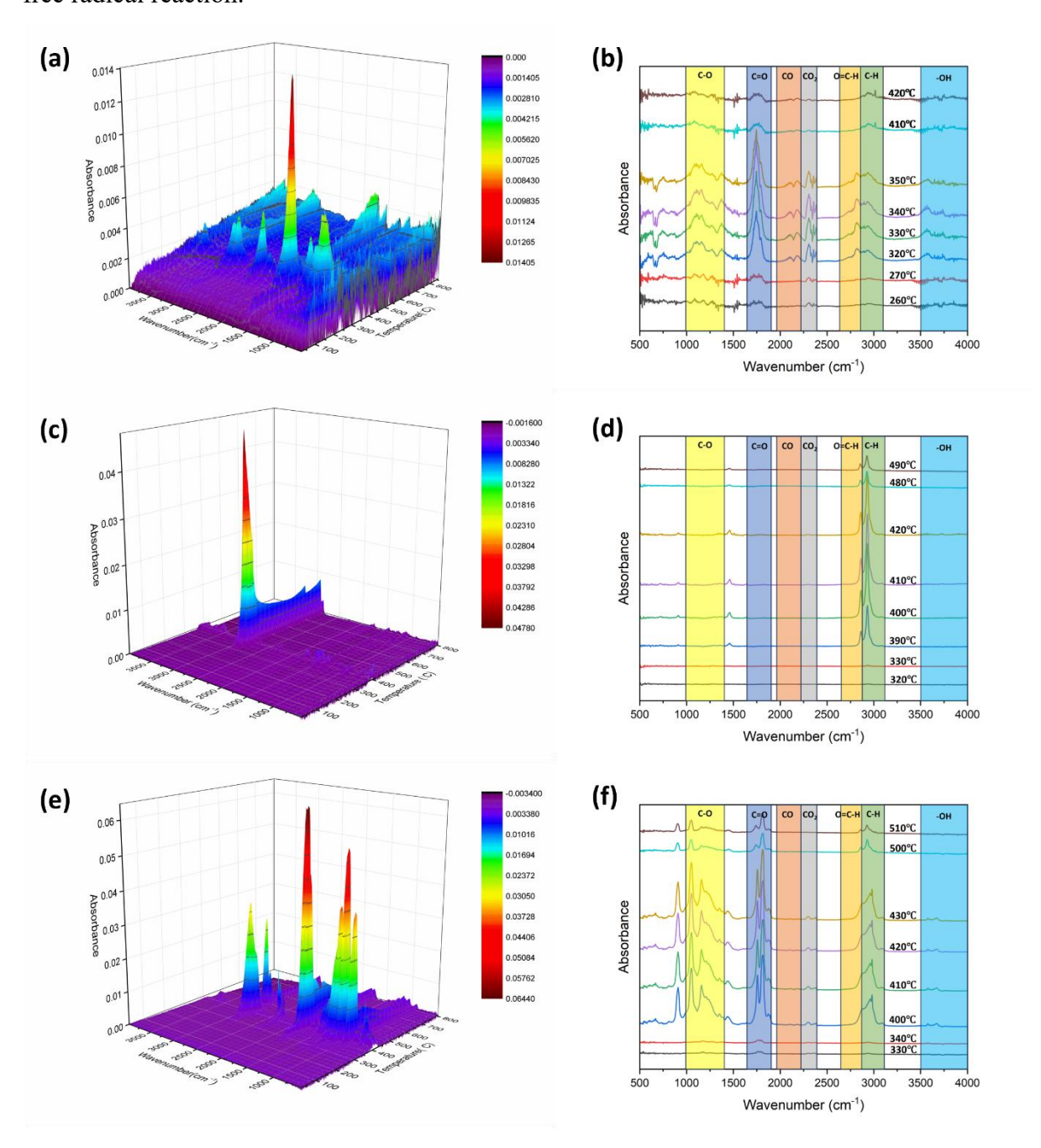


Fig 4.6 3D FTIR spectrums of (a) RSPR, (c) PLA and (e) RSPR/PLA composite; FTIR spectrum of (b) RSPR, (d) PLA and (f) RSPR/PLA composite during pyrolysis at different temperatures with heating rate of 10 °C/min.

To further investigate the composition of pyrolysis volatiles, Py-GC/MS analysis was conducted. Fig 4.7 illustrated the total ion chromatogram of the product of RSPR,PLA and RSPR/PLA composite after pyrolysis. Table 4.2 listed the main products generated during the pyrolysis of RSPR fibre, PLA and RSPR/PLA composite.

The types of the products obtained from Py-GC/MS were basically the same as that obtained from TG-FTIR, which were mainly olefins, esters, ketones, alcohols. The primary pyrolysis products of RSPR were ester, ketone, alcohol, which are mainly oxygen-containing compounds. As can be seen from Table 4.2, the ester products take a large proportion of the pyrolysis products of RSPR. This can be attributed to the pyrolysis of hemicellulose and cellulose, which are major components of RSPR fibre. During pyrolysis, these polysaccharides decompose, producing various intermediates and final products, including carboxylic acids such as acetic acid and formic acid. These acids can further react with alcohols present in the biomass or formed during pyrolysis, leading to the formation of esters. In addition, the pyrolysis of lignin generates a wide range of aromatic and aliphatic compounds, including phenols, alcohols, and carboxylic acids. The carboxylic acids formed during lignin pyrolysis can esterify with available alcohols to form esters. The pyrolysis products of PLA are mainly alkene and alcohol, which are formed due to the structure of PLA and the thermal degradation mechanisms that involve the breaking of ester bonds, depolymerization, and secondary reactions. These processes lead to the generation of unsaturated and alcoholic compounds, which dominate the pyrolysis product spectrum of PLA. As it illustrated in Table 4.2, the pyrolysis products of RSPR/PLA composite are not the simple combination of the pyrolysis products of solo RSPR and PLA. There are a lot of new species of compounds generated during the pyrolysis process, which indicated the interactions effect between RSPR fibres and PLA. Furthermore, some compounds such as Diethyl maleate, are probably generated from the pyrolysis of the couple agent. Over all, the results of TG-FTIR and Py-GC/MS both confirmed the synergistic effect of RSPR fibre and PLA.

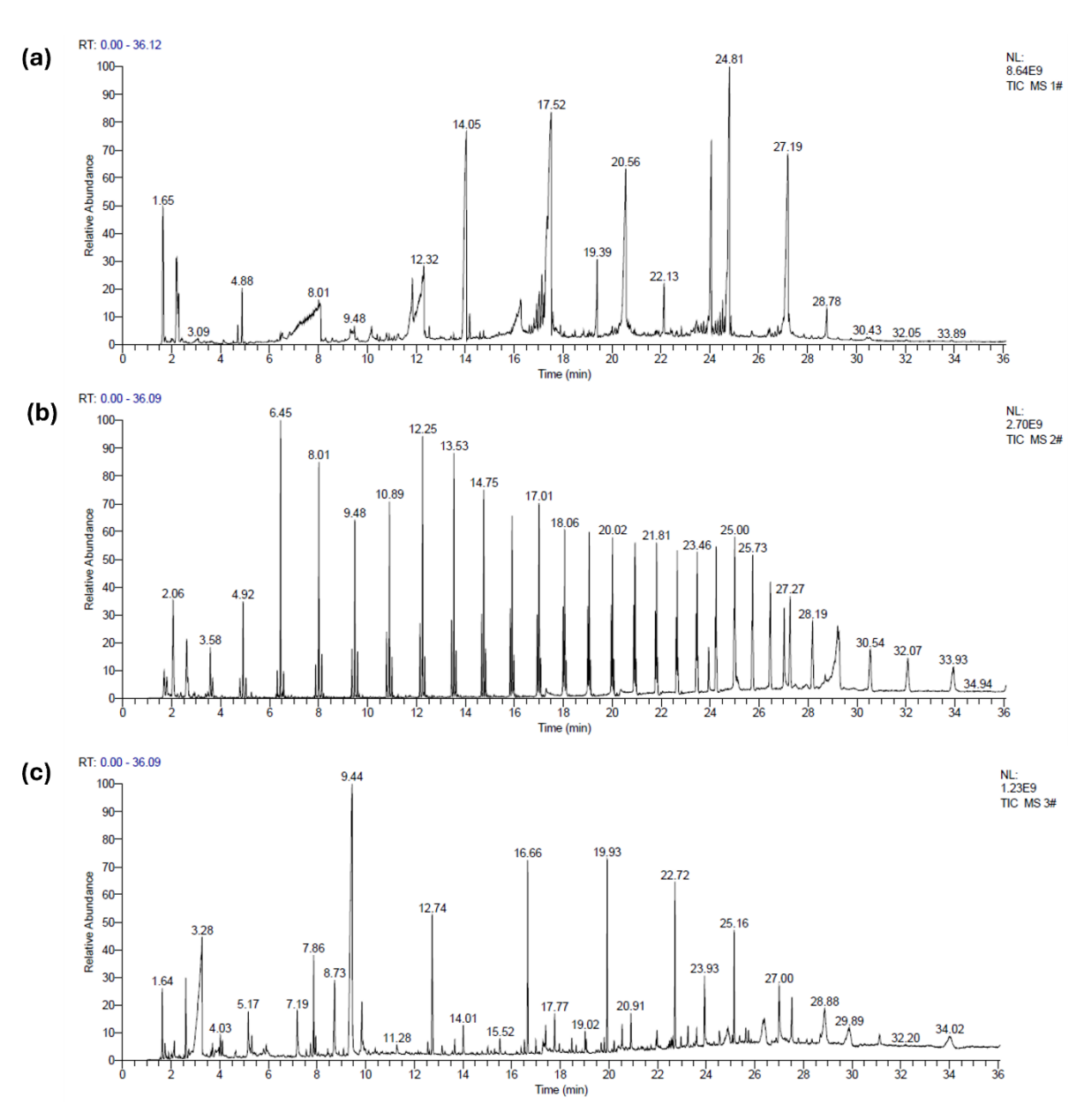


Fig 4.7 The total ion chromatogram of the product of RSPR,PLA and RSPR/PLA composite after pyrolysis.

Table 4.2 The main products generated during the pyrolysis process

			Area Pct(%)			
R.T. (min)	Compounds	Formula	RSPR	PLA	RSPR/PLA composite	Туре
1.64	1,3-Butadiene	C <sub>4</sub> H <sub>6</sub>	3.89		1.31	Alkene
2.06	1-Hexene	$C_6H_{12}$		2.34		Alkene
3.26	2-Propenoic acid	$C_3H_4O_2$			8.01	Acid

3.58	1-Octene	C <sub>8</sub> H <sub>16</sub>		0.84		Alkene
4.88	3-Buten-1-ol, propanoate	C <sub>7</sub> H <sub>12</sub> O <sub>2</sub>	0.86			Alcohol
4.92	1-Nonene	$C_9H_{18}$		1.28		Alkene
5.17	Cyclopentanone, 2,2,5-trimethyl-				1.53	Ketone
6.45	1-Decene	$C_{12}H_{20}$		3.27		Alkene
7.19	2,5-Furandione, 3,4-dimethyl-	C <sub>6</sub> H <sub>6</sub> O		3.27	1.68	Ketone
7.86	2-Propenoic acid, (1-propionato)ethyl easter	$C_8H_{12}O_4$			2.05	Ester
8.01	1-Dodecene	$C_{12}H_{24}$		2.63		Alkene
9.43	N-Acetyl-L- glutamine	$C_7H_{12}N_2O_4$			16.53	N containing substance
9.48	1-Dodecene	$C_{12}H_{24}$		2.03		Alkene
9.48	Propanoic acid, hexyl ester	C <sub>9</sub> H <sub>18</sub> O <sub>2</sub>	0.39			Ester
10.89	1-Tridecene	$C_{13}H_{26}$		2.17		Alkene
11.28					0.34	
12.24	1-Tetradecene	$C_{14}H_{28}$		3.00		Alkene
12.31	3-Methyl- butyrolactone	$C_5H_8O_2$	4.81			Ester
12.74	Diethyl maleate	$C_8H_{12}O_4$			3.37	Ester
13.53	1-Pentadencene	$C_{15}H_{30}$		2.81		Alkene
14.03	Succinic acid, di(but-3-en-1-yl) ester	$C_{12}H_{18}O_4$	10.53			Ester
14.75	1-Hexadeconol	$C_{16}H_{34}O$		2.41		Alcohol
15.52	Diethyleneglycol diacrylate	$C_{10}H_{14}O_5$			0.46	Ester
16.66	3,7,11-Trioxo-4,8,12-trioxa-1-hexadecene	$C_{13}H_{20}O_6$			3.82	Ketone/Ether
17.01	E-15-Heptadecenal	$C_{17}H_{32}O$		2.46		Aldehyde
17.51	Succinic acid, di(2-methylally1) ester	$C_{12}H_{18}O_4$	9.75			Ester
18.06	1-Nonadecene	$C_{19}H_{38}$		2.63		Alkene
19.03	3,7,11-Trioxo-4,8,12-trioxa-1-hexadecene	$C_{13}H_{20}O_6$			0.44	Ketone/Ether
19.39	2-t-Butyl-5-propyl- [1,3]dioxolan-4-one	$C_{10}H_{18}O_3$	1.81			Ketone

20.02	1-Docosene	C <sub>22</sub> H <sub>44</sub>		2.20		Alkene
20.56	1,3-Dioxepane, 2-pentadecyl-	$C_{20}H_{40}O_2$	6.85			Ether
21.81	1-Nonadecene	$C_{19}H_{38}$		3.19		Alkene
22.13	2-t-Butyl-5-propyl- [1,3]dioxolan-4-one	$C_{10}H_{18}O_3$	1.40			Ketone
22.72	1,1,2,2- Ethanetetracarboxylic acid, tetraethyl ester	$C_{14}H_{22}O_8$		3.27		Ester
23.46	n-Tetracosanol-1	$C_{24}H_{50}O$		3.13		Alcohol
24.80	Succinic acid, di(but-3-en-1-yl) ester	$C_{12}H_{18}O_4$	11.61		1.78	Ester
25.00	1-Heptacosanol	$C_{27}H_{56}O$		4.03		Alcohol
	1,1,2,2-					
25.16	Ethanetetracarboxylic	$C_{14}H_{22}O_{8}$			2.29	Ester
	acid, tetraethyl ester					
25.73	Octacosanol	$C_{28}H_{58}O$		3.06		Alcohol
27.19	Succinic acid, di(2-methylally1) ester	$C_{12}H_{18}O_4$	7.30		2.33	Ester
27.27	Octacosanol	$C_{28}H_{58}O$		2.52		Alcohol
28.19	Octacosanol	$C_{28}H_{58}O$		2.16		Alcohol
	Succinic acid, 2-					
28.78	ethylhexyl but-3-en-	$C_{16}H_{28}O_4$	0.93		2.17	Ester
	1-yl ester					
30.54	Octacosanol	$C_{28}H_{58}O$		1.63	1.43	Alcohol
32.07	17-Pentatriacontene	$C_{35}H_{70}$		1.38		Alkene
33.93	17-Pentatriacontene	$C_{35}H_{70}$		1.09		Alkene
34.02	Octacosanol				1.17	Alcohol

#### 4.3.3 Kinetic analysis

# 4.3.3.1 Activation energy calculation

The pyrolysis kinetics were studied by three model-free methods. Fig 4.8 shows the linear relationship between  $\frac{1}{T}$  and  $\ln\left(\frac{\beta}{T^2}\right)$  (KAS),  $\frac{1}{T}$  and  $\ln(\beta)$  (FWO) and  $\ln\left(\frac{d\alpha}{dt}\right)$  and  $\frac{1}{T}$  (Friedman) at different heating rates. The activation energy ( $E_a$ ) and linear correlation coefficients ( $R^2$ ) of RSPR, PLA and RSPR/PLA composite at different conversion rates were calculated by KAS, FWO and Friedman methods (Table 4.3). The  $R^2$  values of different specimens and kinetic methods were between 0.95 and 1, suggesting the kinetic methods was conformed with the

reaction mechanism of feedstocks' pyrolysis. The  $E_a$  values of three models at different conversion rates were generally similar, indicating the models were suitable for analysing the kinetics of the RSPR/PLA composite pyrolysis. Meanwhile, FWO exhibited a better performance in calculating  $E_a$  than KAS and Friedman method according to the  $R^2$  values. Table 4.3 shows the  $E_a$  value calculated by FWO method were always higher than those by KAS methods, which ascribed to the difference in the derivation process and error range of different models [179].

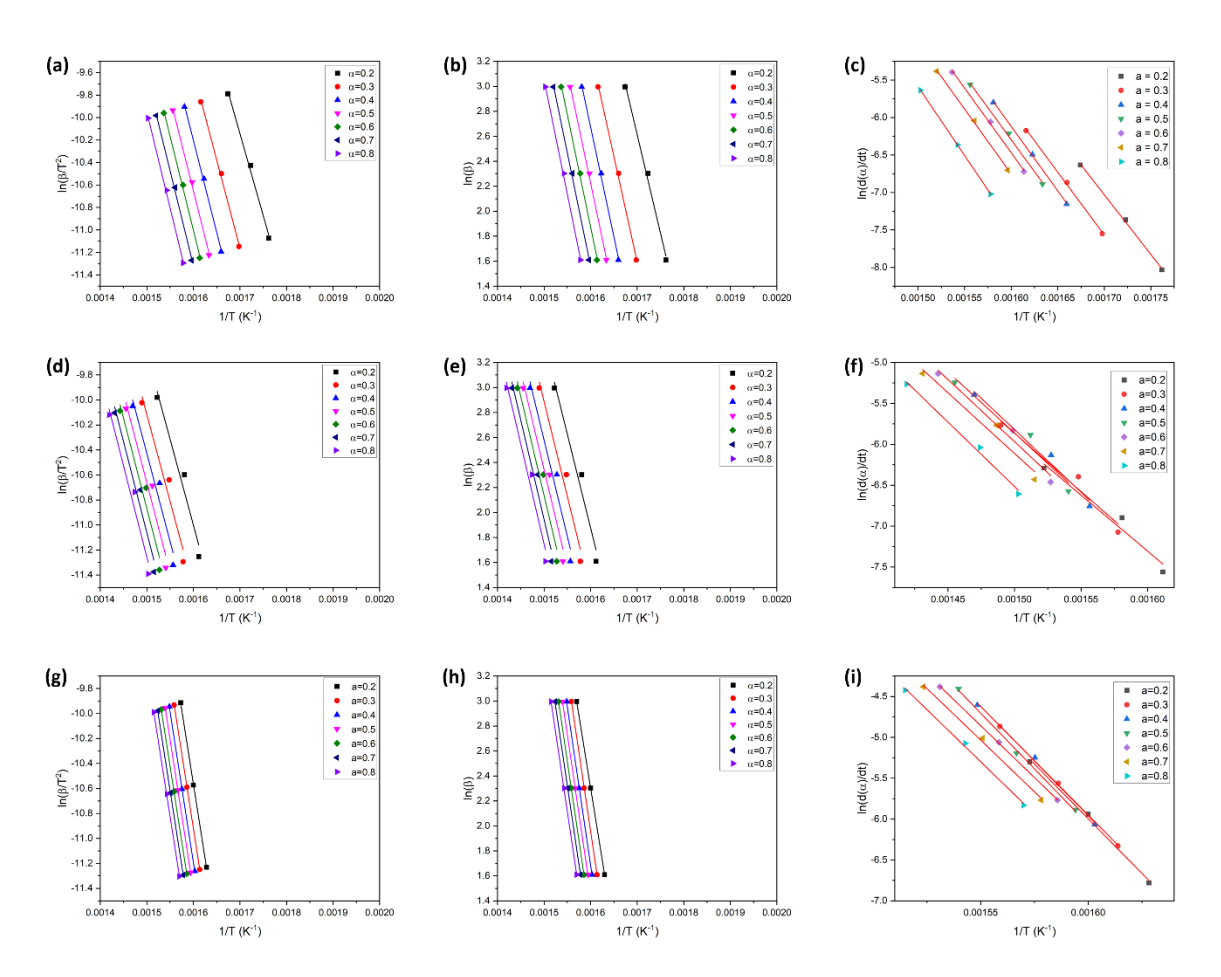


Fig 4.8 Linear plots for activation energy determination by FWO method of (a) RSPR, (d) PLA, (g) RSPR/PLA composite; KAS method of (b) RSPR, (e) PLA, (h) RSPR/PLA composite; Friedman method of (c) RSPR, (f) PLA, (i) RSPR/PLA composite.

Table 4.3 The activation energy and linear correlation coefficients of the pyrolysis of RSPR, PLA and RSPR/PLA at different conversion rates calculated by FWO, KAS and Friedman method.

	RSPR						PLA					RSPR/PLA composite						
a	FWO		KAS		Friedma	n	FWO		KAS		Friedma	n	FWO		KAS		Friedma	ın
α	$E_a$ (kJ	$R^2$	Ea (kJ	$R^2$	Ea (kJ	$R^2$	Ea (kJ	$R^2$	Ea (kJ	$R^2$	Ea (kJ	$R^2$	Ea (kJ	$R^2$	Ea (kJ	$R^2$	Ea (kJ	$R^2$
	/mol)	Λ	/mol)	Λ	/mol)	Λ	/mol)	Λ	/mol)	Λ	/mol)	Λ	/mol)	Λ	/mol)	Λ	/mol)	Λ
0.2	124.6	0.996	121.3	0.995	132.2	0.998	197.6	1.0	197.3	1.0	220.2	0.991	118.7	0.97	114.2	0.96	113.7	0.959
0.3	133.7	0.998	130.6	0.998	139.6	0.998	199.5	1.0	199.4	1.0	221.1	0.999	120.2	0.97	115.6	0.96	118.5	0.958
0.4	138.9	0.998	135.8	0.998	140.1	0.999	200.7	1.0	200.5	1.0	222.2	0.993	121.8	0.96	117.1	0.96	120.2	0.98
0.5	140.8	0.998	137.6	0.998	141.7	0.999	201.4	1.0	201.2	1.0	226	0.996	123.8	0.96	119.1	0.96	124.2	0.949
0.6	142.2	0.998	139.0	0.998	143.1	0.998	200.6	1.0	200.3	1.0	211	0.999	125.0	0.97	120.3	0.96	126.4	0.974
0.7	143.4	0.998	140.2	0.998	143.7	0.998	199.6	1.0	199.3	1.0	209.9	0.994	125.8	0.97	121.1	0.96	128.2	0.962
0.8	145.3	0.998	142.0	0.999	152.8	1	198.9	1.0	198.4	1.0	209.1	0.994	126.4	0.97	121.6	0.96	130.8	0.992
Average	138.4	-	135.2	-	141.9	-	199.8	-	199.5	-	217.1	-	123.1	-	118.4	-	123.1	-

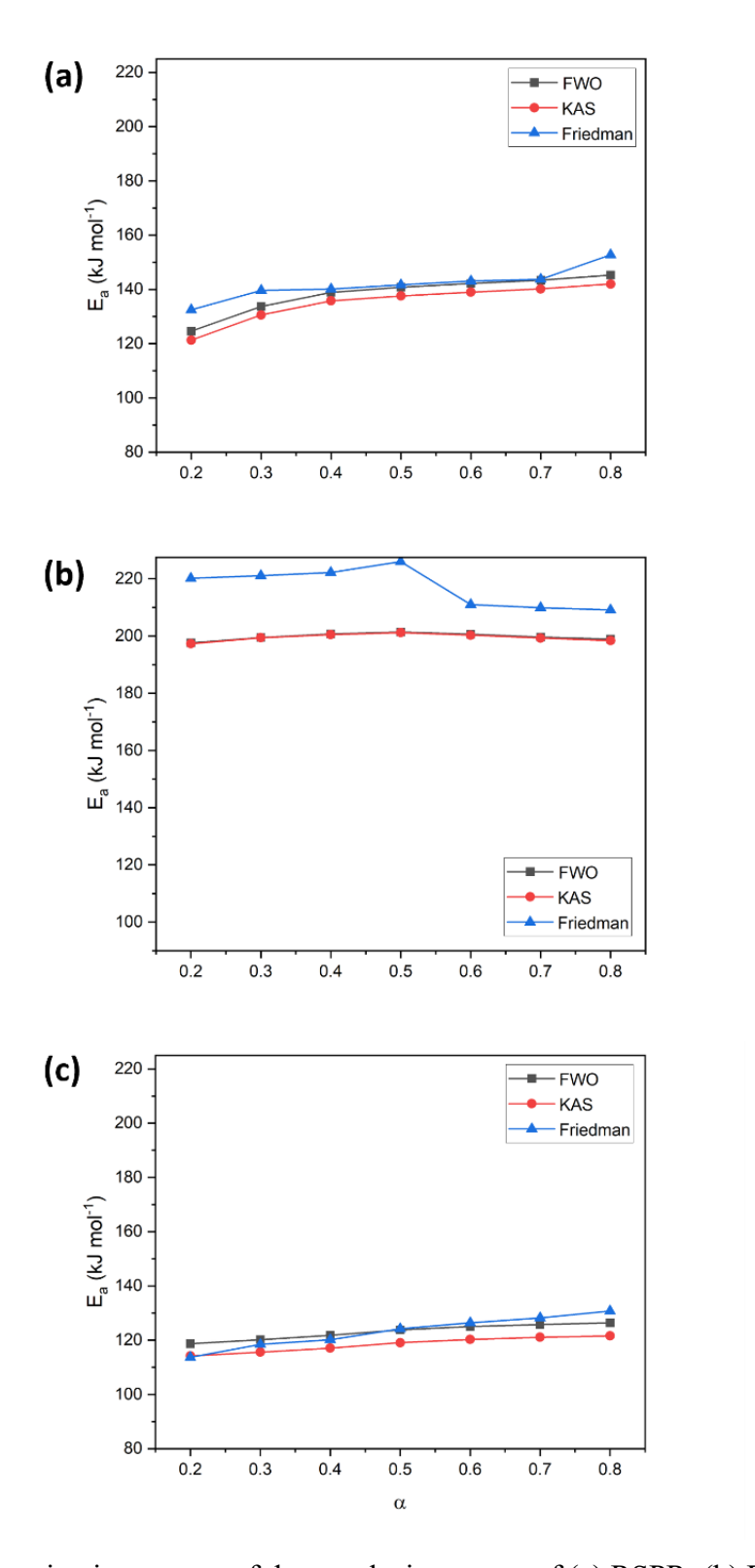


Fig 4.9 The activation energy of the pyrolysis process of (a) RSPR, (b) PLA, and (c) RSPR/PLA composite at different conversion rates.

 $E_a$  is the minimum energy required for a chemical reaction to occur [251]. A higher  $E_a$  value signifies a greater amount of energy, or an extended reaction time was required in the pyrolysis process. For the RSPR pyrolysis, the  $E_a$  increased with an increase in conversion rate (Fig 4.9). The initial  $E_a$  was lower than that of PLA because the volatiles and small molecule substances from RSPR were eliminated at this stage [252]. Then, the  $E_a$  was increased at  $\alpha$ =0.3. The large increase of  $E_a$  at  $\alpha$ =0.3 could be attributed to the onset of decomposition of the hemicellulose and cellulose in RSPR. The steady increase of  $E_a$  after  $\alpha$ =0.3 inferred the breakdown of strong chemical bonds (e.g., benzene ring in lignin), which required an increasing amount of energy and initiates at higher temperatures [253]. At the end of the pyrolysis progress, the remained ash would hinder the diffusion of volatiles. Thus, the  $E_a$  reached its highest value at  $\alpha$ =0.8 [179].

For pure PLA pyrolysis, the average  $E_a$  values were 197.0 kJ/mol, 196.6 kJ/mol and 217.1 kJ/mol by FWO, KAS and Friedman methods, respectively. It can be observed that with the increase of the conversion rate,  $E_a$  first increased, followed by a stable stage, and then it slightly dropped after  $\alpha$ =0.5. The PLA pyrolysis process can be divided into two reactions: transesterification and free radical reaction, transesterification reaction takes place at the beginning of PLA pyrolysis while the free radical reaction happens above 300 °C [254]. Because of the cleavage of covalent bonds, free radical reaction requires more energy when compared to the transesterification reaction [218]. So, with the increase of conversion rate, the  $E_a$  value increased. Compared to the  $E_a$  value of RSPR, the  $E_a$  value of PLA is higher and more stable throughout the entire pyrolysis process. The lower  $E_a$  value of RSPR could be ascribed to the relatively high content of hemicellulose in RSPR fibre, which has a loose structure and requires less energy to decompose [63]. In addition, due to the neat and repeated structure of PLA, the  $E_a$  value of PLA is more stable than that of RSPR.

For the pyrolysis of RSPR/PLA composite, the average  $E_a$  value (121.5 kJ/mol) was lower than that of RSPR (138.5 kJ/mol) and the pure PLA (205.5 kJ/mol) groups. Therefore, the RSPR as the reinforcement phase in the composite material could significantly reduce  $E_a$ . The  $E_a$  value during the whole pyrolysis progress of the composite was lower than the other two groups. At the physical level, energy conversion during co-pyrolysis cannot be lower than that the lowest  $E_a$  value when pyrolyzing the individual material separately. Therefore, the reason for reduction of the  $E_a$  was ascribed to the synergetic effects between RSPR reinforcement and PLA matrix [190], and the promotion of the free radical reactions of PLA by the free radical released from lignin in RSPR [255].

Meanwhile, the  $E_a$  curve of RSPR/PLA composite was similar to that of RSPR. At the first stage, owing to the transformation of the dominant reaction from the transesterification to the free radical reaction, the energy required was higher, which further led to the increase of  $E_a$ . Then, as the temperature reached the threshold for the initiation of the free radical reaction of PLA, the energy consumption was stable. However, because the cellulose, hemicellulose and lignin in RSPR started to decompose during this period ( $\alpha$ =0.2-0.8), the  $E_a$  was further slowly increased.

#### 4.3.3.2 Kinetics model determination by master plot method

The master plot method was further adopted to determine the reaction model for RSPR/PLA composite. It was crucial to determine the reaction model to guide the selection or designation of the pyrolysis reactor [107]. The curves of  $\alpha$  versus  $P(u)/P(u_{0.5})$  obtained from TGA of the pure PLA and RSPR at 5 °C /min, 10 °C /min, and 20 °C /min are shown in Fig 4.10(a) and (b). The  $P(u)/P(u_{0.5})$  curves of the above two specimens were generally similar, which suggested the pyrolysis of the pure PLA and RSPR followed the single kinetic model [256]. Fig 4.10(c) and (d) shows the comparison of the curves of  $\alpha$  versus  $G(\alpha)/G(0.5)$  plotted by various theoretical kinetic functions and experimental master-plots  $P(u)/P(u_{0.5})$  of PLA at heating rate of 10 °C /min. The experimental master-plots of PLA were consistent with the contracting cylinder model (R2), which coincided with the results in previous research [190]. Similarly as most petroleum-based plastics, the pyrolysis mechanism of PLA belongs to the geometrical contraction model [257], which indicates the pyrolysis occurred rapidly on the surface of PLA crystal and the degradation rate was controlled by bounded centre-oriented reaction [258]. As compared to RSPR/PLA composite, the reaction mechanism for the pyrolysis of RSPR/PLA composite can be divided into two parts. No matching reaction model can be found in the range of conversation rate from 0.2-0.4. In the range of 0.4-0.8, the experimental master-plot curve matched the diffusion model (D1) (Fig 4.10 (e) and (f)). Therefore, one-dimensional (D1) diffusion model was dominated to the pyrolysis process of RSPR/PLA composite. In addition, D1 model suggested the conversion rate was proportional to the thickness of the product barrier layer but did not consider the shape factors [259].

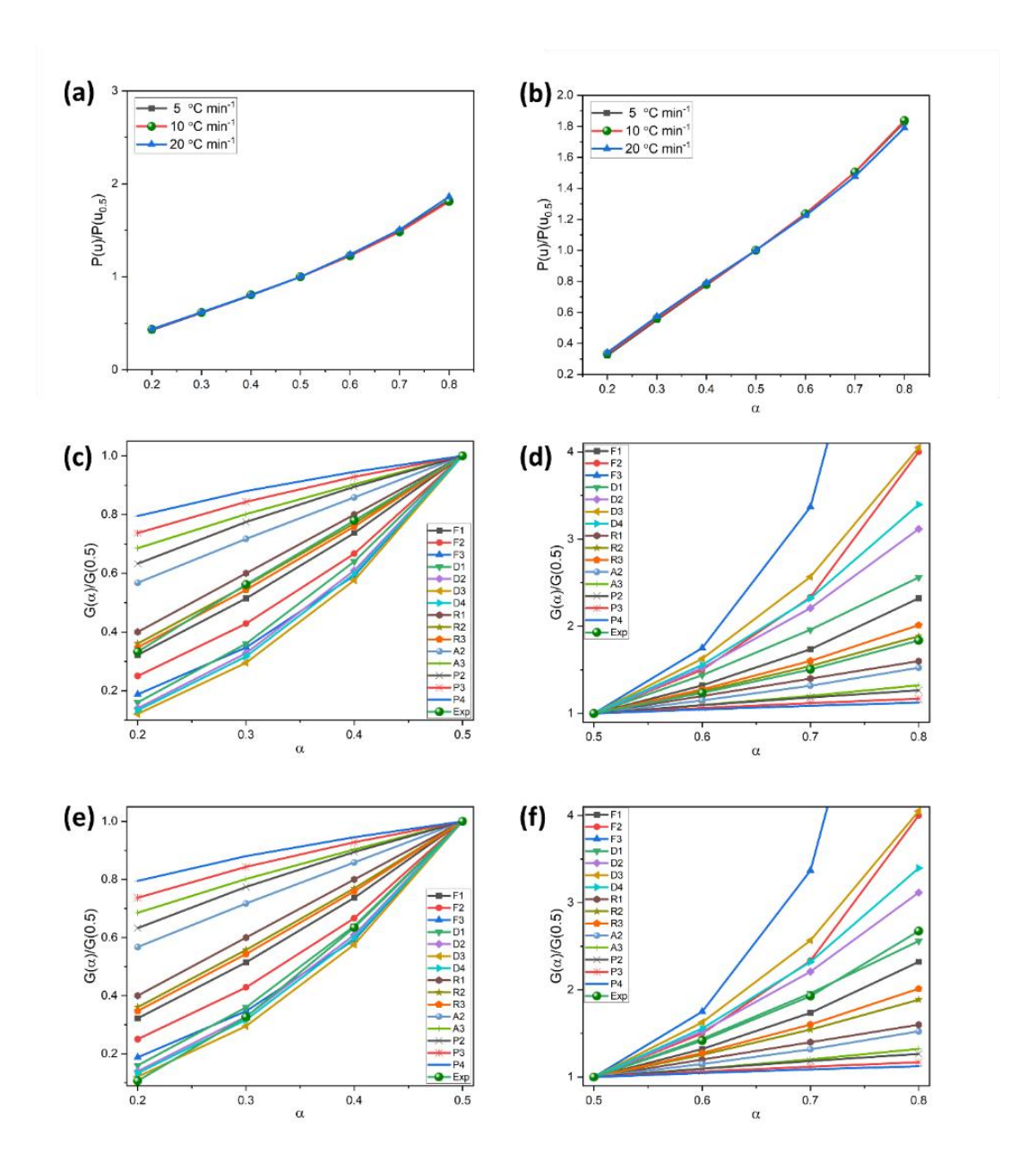


Fig 4.10 The curves of α versus P(u)/P(u<sub>0.5</sub>) obtained from TG results of (a) PLA; (b) RSPR/PLA composite at 5 °C/min, 10 °C /min and 20 °C/min; the comparison of the experimental and theoretical master plots of PLA (c, d) and RSRP/PLA composite (e, f) at heating rate of 10 °C/min.

#### 4.3.3.3 The evaluation of thermodynamic parameters

The thermodynamic parameters are crucial to optimize the pyrolysis reactor [99]. The thermodynamic parameters calculated by Eq. 4.5-Eq. 4.8 using the different  $E_a$  obtained from FWO, KAS and Friedman methods were listed in Table 4.4. The  $\Delta H$  refers to the energy consumption of breaking chemical bonds of material and forming new chemical bonds [179]. As can be seen, the  $\Delta H$  of RSPR/PLA composite were positive, which indicated the pyrolysis

of RSPR/PLA composite were endothermic.  $\Delta G$  represents the whole energy changes of the pyrolysis system for the activated complex formation [190]. So, a lower value of  $\Delta G$  is more favourable for a reaction to take place. The average  $\Delta G$  of RSPR/PLA composite by FWO, KAS and Friedman methods were 175.7 kJ/mol, 180.6 kJ/mol and 175.7 kJ/mol, respectively.  $\Delta S$  reflects on the randomness or disorder degree of the pyrolysis system. Typically, a negative value of  $\Delta S$  illustrates the reactivity of the material was low, which leads to a longer time for the formation of the activated complex, which has a higher degree of arrangement [260]. In the pyrolysis process of RSPR/PLA composite, all the  $\Delta S$  values were negative, inferring the pyrolytic conversion of PLA composite forms an activated complex with a more organized structure than that of the initial material.

Table 4.4 Thermodynamic parameters of RSPR/PLA composite calculated by FWO, KAS and Friedman method at heating rate of 10 °C /min.

	A	$\Delta H$	$\Delta G$	$\Delta S$	A	$\Delta H$	$\Delta G$	$\Delta S$	A	$\Delta H$	$\Delta G$	$\Delta S$		
α	$(s^{-1})$	(kJ/mol)	(kJ/mol)	$(J/mol \cdot K)$	$(s^{-1})$	(kJ/mol)	(kJ/mol)	$(J/mol \cdot K)$	$(s^{-1})$	(kJ/mol)	(kJ/mol)	$(J/mol \cdot K)$		
FWO						KAS				Friedman				
0.2	5.16×10 <sup>8</sup>	113.4	170.7	-85.1	2.22×10 <sup>8</sup>	108.9	175.6	-99.1	2.02×10 <sup>8</sup>	108.4	176.1	-100.6		
0.3	$6.83 \times 10^{8}$	114.8	174.1	-88.1	$2.89 \times 10^{8}$	110.2	178.9	-102.0	4.97×10 <sup>8</sup>	113.1	175.9	-93.3		
0.4	$9.21 \times 10^{8}$	116.4	174.1	-85.7	$3.82 \times 10^{8}$	111.7	179.0	-100.0	6.83×10 <sup>8</sup>	114.8	175.8	-90.6		
0.5	$1.34 \times 10^{9}$	118.3	176.0	-85.7	$5.56 \times 10^{8}$	113.6	180.9	-100.0	$1.44 \times 10^9$	118.7	175.6	-84.5		
0.6	$1.67 \times 10^{9}$	119.5	177.0	-85.4	$6.96 \times 10^{8}$	114.8	181.9	-99.7	2.17×10 <sup>9</sup>	120.9	175.5	-81.1		
0.7	$1.94 \times 10^{9}$	120.2	177.9	-85.7	$8.08 \times 10^{8}$	115.5	182.8	-100.0	$3.04 \times 10^9$	122.6	175.4	-78.4		
0.8	$2.17 \times 10^{9}$	120.8	179.9	-87.8	$8.87E \times 10^{8}$	116.0	184.9	-102.3	4.94×10 <sup>9</sup>	125.2	175.3	-74.4		
Average	$1.32 \times 10^{09}$	117.6	175.7	-86.2	5.49×10 <sup>8</sup>	113.0	180.6	-100.4	1.85×10 <sup>9</sup>	117.7	175.7	-86.1		

#### 4.4 Conclusion

In this chapter, to improve the economic feasibility of discarded PLA-based composite disposal, the pyrolysis behaviour and kinetics of RSPR/PLA composite as the model were investigated. The TG-FTIR results demonstrated the presence of RSPR as the reinforcement phase could facilitate the free radical reaction of PLA during the pyrolysis process, leading to the reduction of CO and CO<sub>2</sub> groups in the pyrolysis of REPR/PLA composite. Compared with the pyrolysis of the pure PLA (205.5 kJ/mol) and RSPR (136.5 kJ/mol) in control groups, lower activation energy ( $E_a$ ) was realized in the group of RSPR/PLA composite (121.5 kJ/mol), confirming the synergistic interactions between RSPR and PLA in the composite material. Besides, the results of master-plots method show one-dimensional (D1) diffusion model dominated the RSPR/PLA composite pyrolysis process. This study provides valuable insights regarding the thermal behaviours and kinetics of the pyrolysis of lignocellulose/PLA composites, which not only enhance the economic value of discarded lignocellulose/PLA composites but also provide a solution for the potential waste lignocellulose/PLA composites pollution.

# **Chapter 5**

Pyrolytic valorisation of post-consumed wood-plastic composites: emphasis on the weathering as a variable to the thermal behaviour, kinetics and pyrolytic products distribution

# 5. Pyrolytic valorisation of post-consumed wood-plastic composites: emphasis on the weathering as a variable to the thermal behaviour, kinetics and pyrolytic products distribution

In this chapter, post-consumer wood-plastic composites (WPCs) were utilized as feedstock to investigate their pyrolysis behaviour. This study not only explores the thermal degradation characteristics of aged WPC materials but also provides insights into their end-of-life valorisation potential. By examining the decomposition kinetics and product distribution, the findings contribute to a deeper understanding of the recyclability and energy recovery potential of WPCs, thereby highlighting their broader practical implications in sustainable waste management and circular material design.

#### 5.1 Introduction

In the last chapter, the pyrolysis behaviour, kinetics and pyrolysis products distribution of reed straw processing residue/PLA composites has been studied. Most existing studies have used brand-new WPCs as feedstocks in WPCs pyrolysis study, which does not meet the realistic demand of upcycling post-consumer weathered WPCs that cannot be reprocessed. Aging can cause significant changes in the structure of WPCs, such as increased crystallinity, oxidation of the polymer matrix, and deterioration of lignocellulosic fibres [261,262]. These structural changes can profoundly influence pyrolysis behaviour. For instance, increased crystallinity in aged WPCs can enhance thermal stability but may also slow down the pyrolysis rate due to reduced polymer chain mobility [263]. The breaking of chemical bonds in the lignocellulosic fibre, particularly in lignin and cellulose, makes the fibres structure more loose and unstable, further decreasing the pyrolysis activation energy [264]. Additionally, the deterioration of lignocellulosic fibres can alter the interaction between the polymer matrix and the fibres, influencing the overall pyrolysis kinetics and the distribution of volatile products [265]. Hence, it is crucial to take a deeper insight into the differences in the pyrolysis behaviours between the pristine and aged WPCs.

Fig 5.1 shows the graphical abstract of this section. In this section, in facing the actual demanded for the pyrolytic waste WPCs valorisation, xenon lamp weathering was conducted to allow rapid aging of the WPC composed of high-density polyethylene (HDPE) as the continuous matrix and the lignocellulosic ethanol processing residual (EPR) as the reinforcement phase. The differences between the pyrolysis performances of weathered and the

brand-new WPCs were studied. In the first part of the current work, the impact of weathering time on the surface characterization and properties of the WPCs were investigated, followed by investigating the decomposition behaviour via thermogravimetry analysis (TGA) and kinetics by the model free and master-plot methods. In the second part, the effect of WPC weathering on liquid and gaseous product distribution was highlighted. The information obtained in the current work lay the foundation for future work on catalysts and process improvements towards the weathered WPCs.

# **Novelty statement**

This chapter introduces aging and environmental exposure as a new dimension in pyrolysis research by investigating weathered WPCs derived from EPR and HDPE. It systematically links artificial weathering effects—including oxidation, crystallinity change, and volatile loss—to variations in pyrolysis kinetics, product composition, and reaction order. This approach closes a critical gap in previous studies that treated feedstocks as pristine materials. By coupling TGA, TG–FTIR, and Py–GC/MS, the chapter provides the first integrated view of how environmental aging alters pyrolytic behaviour, guiding more realistic end-of-life management and lifecycle modelling of WPCs.

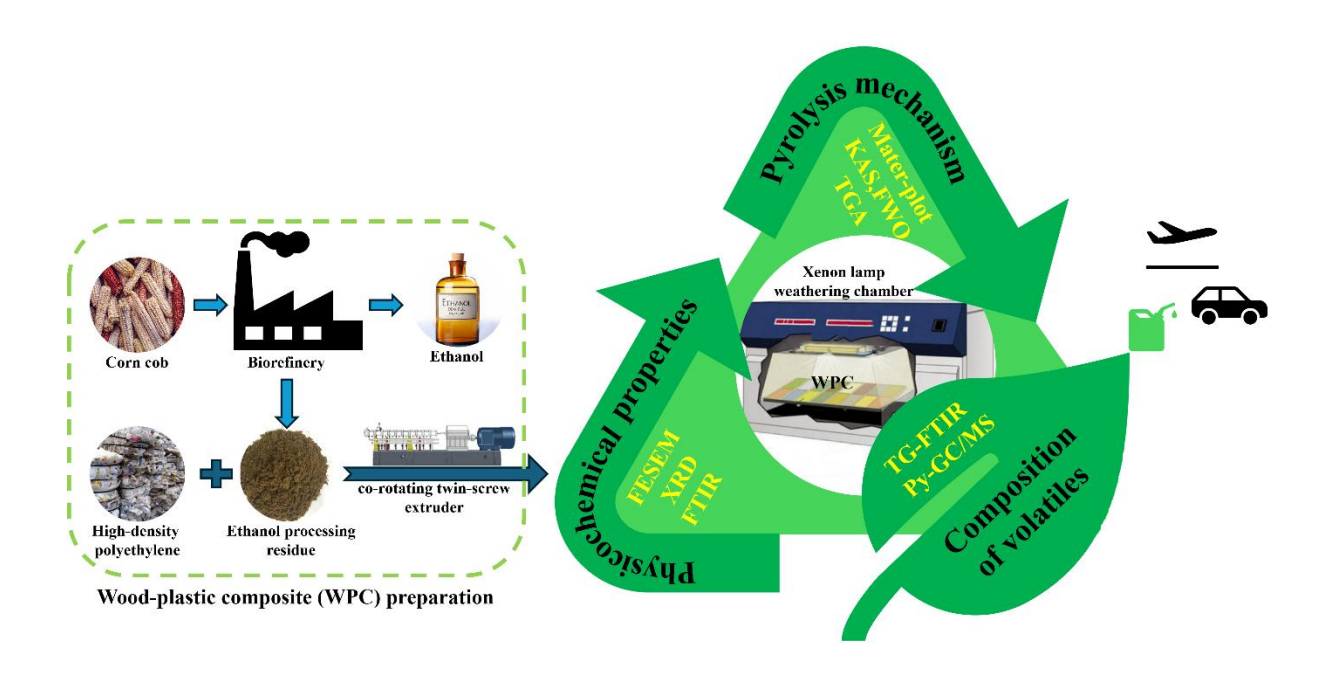


Fig 5.1 The graphical abstract

#### 5.2 Materials and methods

#### 5.2.1 Materials

The ethanol processing residue (EPR) used in current work was provided by Longlive Biotechnology Co., Ltd., Yucheng, Shandong, China. Before milling into ~60 meshes, the crude EPR was dried for 24h at 105 °C. The chemical composition of the EPR, as tested in previous study [11], is 58.8±2.3% cellulose, 5.4±0.1% hemicellulose, 22.5±0.9% lignin, 5.1±0.2% soluble substances, and 8.2±0.1% ash content. HDPE 600 was purchased from Jinma Plastic Co., Ltd., Beijing, China. The maleic anhydride grafted HDPE (MA-HDPE) that was used as the compatibilizer was purchased from Nantong Rizhisheng Polymer Technology Co., Ltd.,

Jiangsu, China.

#### 5.2.2 Preparation of wood-plastic composite and Xenon lamp weathering

The detailed preparation process of WPCs was described in Section 4.2.2, using a corotating twin-screw extruder (Coperion ZSK, Werner & Pfleiderer, Germany). The chemical compositions of WPCs were: EPR powder (50 wt%), HDPE (40 wt%), MA-HDPE (3 wt%), stearic acid (4 wt%) and polyethylene (3 wt%).

Xenon lamp weathering was conducted based on GB/T 24508-2009 [266]. The test was carried out in a closed-loop xenon-arc chamber equipped with automatic control of irradiance, humidity, and black-panel temperature. The irradiance intensity was set at 550 W/m<sup>2</sup> within the wavelength range of 290-800 nm, simulating natural solar radiation. During exposure, the black panel temperature and relative humidity inside the chamber were maintained at  $65 \pm 5$  °C and  $50 \pm 5$  %, respectively. Specimens were pre-conditioned at  $23 \pm 2$  °C and  $50 \pm 10$  % RH for at least 24 h before testing to equilibrate moisture content. The samples were mounted on the specimen rack with the exposed surface facing the light source, ensuring uniform illumination and no mutual shading. The weathering process was conducted under continuous irradiation without dark or spray cycles. Irradiance, temperature, and humidity were recorded at 10 min intervals to ensure that all parameters remained within the specified tolerances. A set of unexposed specimens was retained as a control for comparison. WPC specimens were withdrawn after 500 h, 1000 h, and 2000 h of exposure, corresponding to cumulative radiant doses of approximately 990, 1980, and 3960 MJ/m<sup>2</sup>, respectively. Each set of samples was cooled to room temperature under laboratory atmosphere immediately after removal, sealed in polyethylene bags, and stored in a desiccator prior to subsequent analyses.

#### 5.2.3 Characterization of wood-plastic composite

In order to understand the physical and chemical changes of WPCs after weathering, the proximate analysis was done to determine the moisture, volatiles, fixed carbon and ash content, while ultimate analysis was employed to analyse the chemical composition changes of WPCs (detailed description is in Appendix 1 and 2). Field emission scanning electron microscopy (FESEM) (SU8000, Hitachi, Japan) was used to observe the morphological change of WPCs before and after weathering. Changes in functional groups of WPCs after weathering were monitored by FTIR (Nicolet 6700, Thermo Fisher, USA). The IR spectra were obtained in the spectral range from 400-4000 cm<sup>-1</sup> at a resolution of 4 cm<sup>-1</sup>. An XRD (D 8, Bruker, Germany) was used to analyse the crystallinity change of WPC specimens. The test was conducted at the step size of 0.02°, and a speed of 1°/min between 15° and 30°.

# 5.2.4 Pyrolysis of the weathered wood-plastic composites

TGA was carried out to study the thermal behaviour of the weathered WPCs. The experiment was conducted using TGA/DSC3+ (Mettler, Switzerland) from room temperature (~25 °C) to 850 °C with different heating rates (5, 10, 20, 30 °C/min).

TG analyser (TG 209F1, NETZSCH, Germany) was coupled to the FTIR spectrometer (Nicolet 6700, Thermo Fisher, USA) system to detect the gaseous products from pyrolysis of the weathered WPCs. 10 mg of WPCs specimens were heated from 30 °C to 700 °C at 10 °C /min under nitrogen (>99.999 %) flowing at a rate of 50 mL/min. The temperature of the transfer line between the TG analyser and FTIR spectrometer apparatus was maintained at 250 °C to avoid condensation of the gases. The functional groups in the gas products was determined by FTIR in the range of 500-4000 cm<sup>-1</sup>.

The volatile products from pyrolysis of WPCs under different weathering times were identified by Py-GC/MS (Frontier-EGA/PY3030D-JP, Thermo Fisher-TRACE1310-USA, Thermo ISQLT-USA). The rapid pyrolysis was performed at 600 °C with a heating rate of 20 °C ms<sup>-1</sup> and a retention time of 20 s with a purified He atmosphere of 1.2 mL/min. The transfer pipe was maintained at 300 °C. The GC/MS injector temperature was 290 °C, with a split ratio of 1:100. The pyrolysis products were analysed according to the National Institute of Standards and Technology (NIST) mass spectrometry database and relevant literature. Other information for Py-GC/MS test can be found in previous research [11].

#### 5.2.5 Kinetics analysis

WPC specimens undergo typical solid-state decomposition reactions, converting the initial materials into gases, volatiles, and solid fractions [144]. This process involves a series of complex reactions, making it challenging to develop a precise kinetic model to fully understand the mechanisms [104]. Therefore, some assumptions are made to simplify the kinetic model [162]. The relative formulas and equations for estimating kinetics according to TG data were detailed described in previous sections. Most of the kinetics methods are based on Eq. (1):

$$g(\alpha) = \int_0^\alpha \frac{d\alpha}{f(\alpha)} = \frac{A}{\beta} \int_{T_0}^T exp\left(-\frac{E}{RT}\right) dT \approx \frac{A}{\beta} \int_0^T exp\left(-\frac{E}{RT}\right) dT$$
 (1)

#### 5.2.5.1 Iso-conversional method

The iso-conversional method is a typical technique to estimate the apparent activation energy regardless of the reaction mechanism. Two kinds of iso-conversional methods, KAS and FWO, are applied to evaluate the activation energy in this work. The relative equation and assumption has been discussed in Chapter 2.

#### 5.2.5.2 Master-plot method

To better understand the reaction mechanism of the weathered WPCs pyrolysis, masterplot method was adopted to determine the reaction model. The relative equation and assumption has also been discussed in Chapter 2.

### 5.3 Results and discussions

#### 5.3.1 Physicochemical and surface properties of the weathered wood-plastic composites

To clarify the effect of WPC weathering on pyrolysis performance, it is crucial to thoroughly characterize the surface properties of WPC specimens after different durations of xenon lamp irradiation. Table 5.1 presents the results of proximate and ultimate analyses of the WPC specimens. Generally, there were no significant differences between the samples in these analyses, indicating that the weathering process had minimal influence on the chemical and physical compositions of WPCs. Additionally, negligible sulfur content was detected in all WPC specimens, suggesting lower SOx emissions and environmental benignity in the pyrolytic valorization process [267].

Table 5.1 Physicochemical properties of the weathered WPCs.

Specim	Pr	oximate and	alysis (wt%	(o) <sup>b</sup>	Ultimate analysis (wt%) <sup>a</sup>							
ens	M	V	A	FC	С	Н	O*	N	S			
0 h	2.10±0.	81.11±0.	8.21±0.	8.59±0.	64.99±0	9.63±0.	13.90±0	0.76±0.	0.41±0.0			
	08	95	22	58	.95	22	.22	03	7			
500 h	1.69±0.	81.09±1	8.46±0.	8.76±0.	65.58±1	9.89±0.	14.21±0	0.75±0.	0.42±0.1			
	10	.02	36	36	.02	35	.30	01	1			
1000 h	1.83±0.	81.54±1	8.11±0.	8.51±0.	64.83±1	9.84±0.	14.25±0	0.76±0.	$0.38\pm0.0$			
	09	.35	45	15	.03	10	.30	02	8			
2000 h	1.96±0.	81.51±1	8.22±0.	8.32±0.	64.97±1	9.83±0.	13.86±0	0.76±0.	$0.40\pm0.0$			
	12	.20	11	95	.80	15	.33	05	.09			

M: moisture; V: volatiles; A: ash; FC: fixed carbon;

Fig 5.2 shows the visual appearance of the weathered WPCs. It was obvious that the accelerated (xenon lamp) weathered WPCs were gradually whitened and presented a clearer powdered surface with the increase of exposure time. The bleaching of weathered WPCs was caused by the degradation of both the plastic matrix and the reinforcement phase (EPR) [268,269]. During the accelerated weathering, the plastic matrix (HDPE) lost the translucency and further caused the colour change of WPCs [268]. In addition, the lignin fractions in lignocellulosic fibres can be particularly susceptible to UV-induced photodegradation [262]. Previous studies indicated the exposing of lignin under UV light could initiate photochemical reactions, leading to the formation of aromatic and other free radicals, which causes the degradation of lignin structure and the photo-oxidation of cellulose and hemicelluloses, and effectively causing the discoloration [270].

Fig 5.3 presents the SEM micrographs of the weathered WPCs. The surface of unweathered WPC (0 h) was fairly smooth and unwrinkled. However, after xenon lamp weathering, obvious morphological alteration appeared, resulting in a crumbled surface. The crazing of WPCs may be caused by polymer chain scission, leading to highly crystallized polymer zones that crack and/or contract differently between the surface and interior sections during the weathering process [264]. More specifically, clear EPR particles were still discernible in the matrix after 500 hours of weathering. However, after 2000 hours of xenon lamp weathering, both the HDPE and EPR were co-degraded.

<sup>&</sup>lt;sup>a</sup> On dry and ash-free basis (wt%), <sup>b</sup> On dry mass fraction basis (wt%), \* Calculated by difference.



Fig 5.2 Photographs of WPCs after different weathering time.

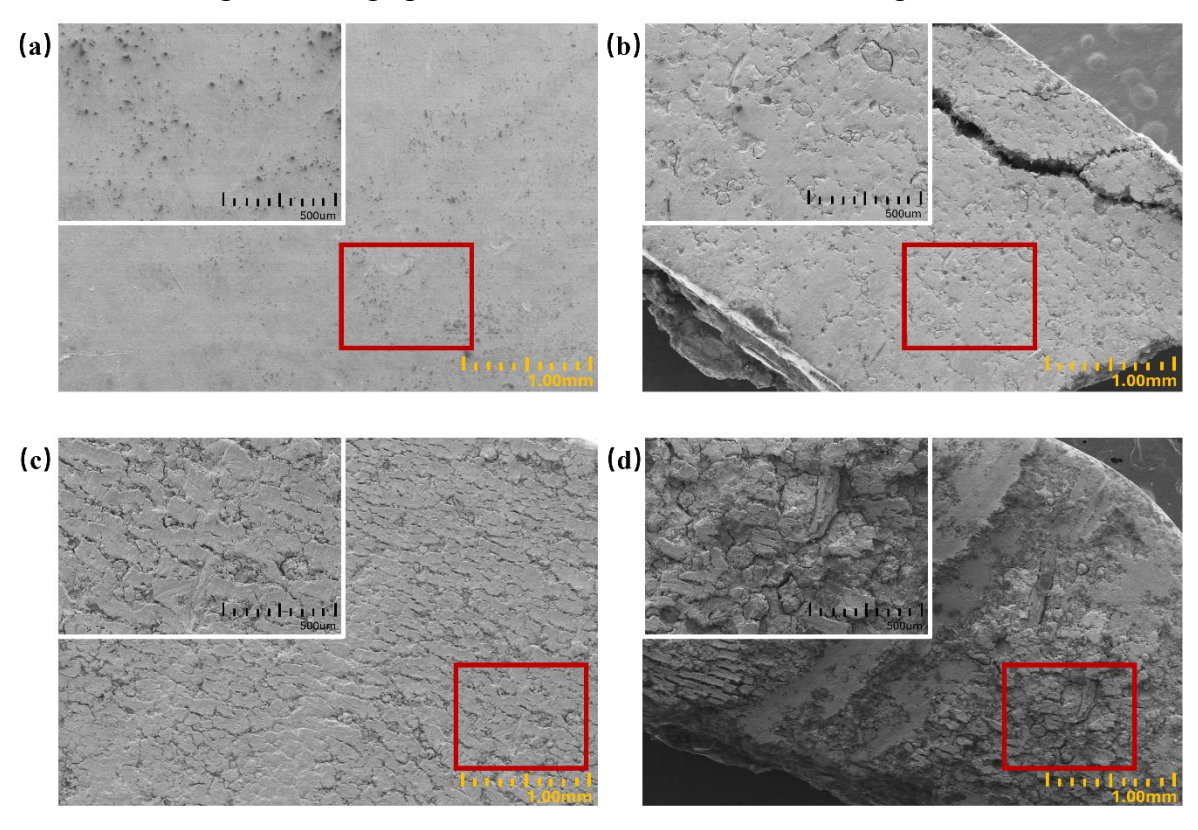


Fig 5.3 SEM images of the weathered WPCs. Specimens obtained after (a) 0 h, (b) 500 h, (c) 1000h, and (d) 1000 h of xenon lamp weathering (Scale:1.00 mm)

FT-IR spectroscopy was further conducted to investigate the changes of chemical functional groups of WPCs after weathering (Fig 5.4). As expected, the results confirmed that the degradation was ascribed to a series of reactions occurring on the surface of weathered WPCs. The peaks' intensity of typical functional groups assigned to EPR (C-O stretching and

C-O-C asymmetric vibration at 1035-1105 cm<sup>-1</sup>, and O-H stretching at 3300 to 3400 cm<sup>-1</sup>) obviously decreased [271,272]. Additionally, the peak at 1511 cm<sup>-1</sup>, assigned to lignin, also sharply reduced after weathering [273], illustrating the relatively quick degradation of lignocellulosic fractions in WPCs. Moreover, the intensity of carbonyl functional groups located at 1715 cm<sup>-1</sup> increased with weathering progress, further confirming the photodegradation of EPR and HDPE [274].

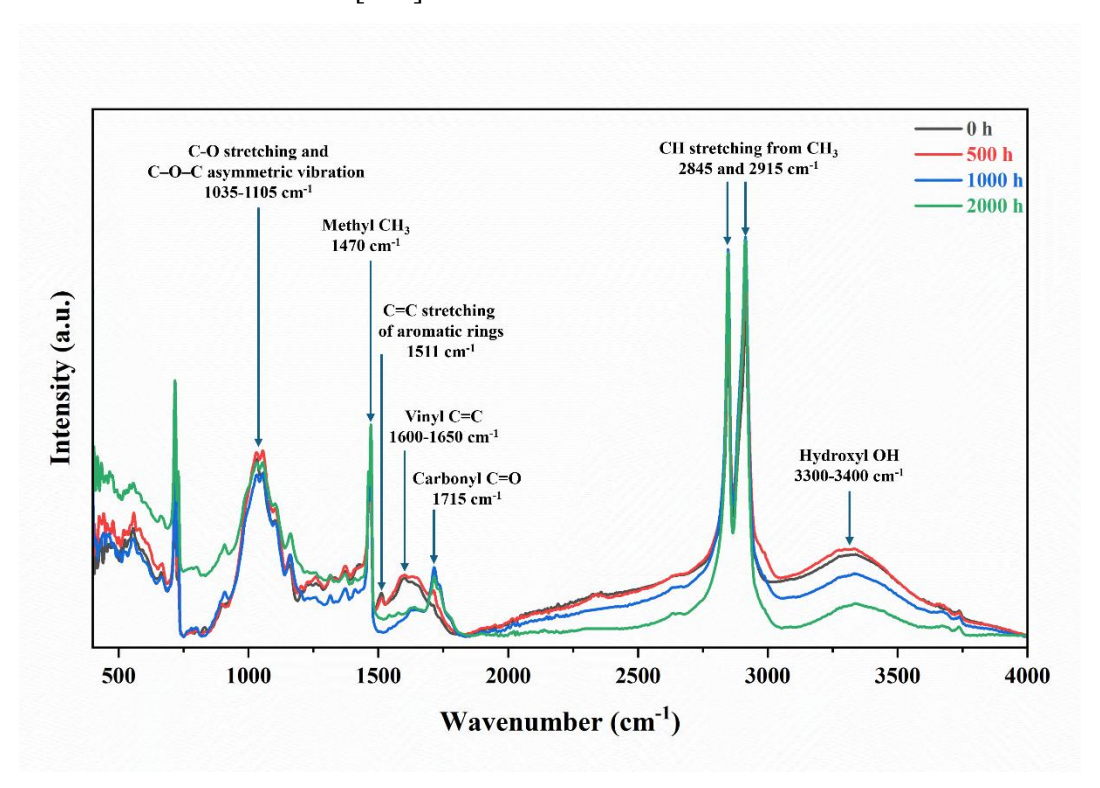


Fig 5.4 FTIR spectra of the weathered WPCs.

XRD was further adopted to determine the crystallinity change of the weathered WPCs (Fig 5.5). The strong peaks at 21.38 ° and 23.68 ° in the XRD pattern of unweathered WPC were from the (110) lattice plane and (200) lattice plane of HDPE crystals, respectively [275]. After weathering, the peaks were shifted to higher angles, suggesting the decrease of interlayer distance of HDPE [276]. In addition, the cellulose fractions in EPR should have a crystalline region. However, the corresponded peak that was located at 22 ° was overlapped by the HDPE [70]. More importantly, the intensity of the diffraction peaks increased sharply upon weathering, inferring the increase of crystallinity of the WPC specimens. The increase in crystallinity was attributed to PE chain scission reactions, initiated by free radicals and shorter chain molecules generated during the xenon lamp weathering process. Chain scission via the Norrish I and II reactions reduces the density of entanglements in the amorphous phase, thereby allowing lower molecular weight PE molecules to more freely crystallize due to their enhanced mobility [261].

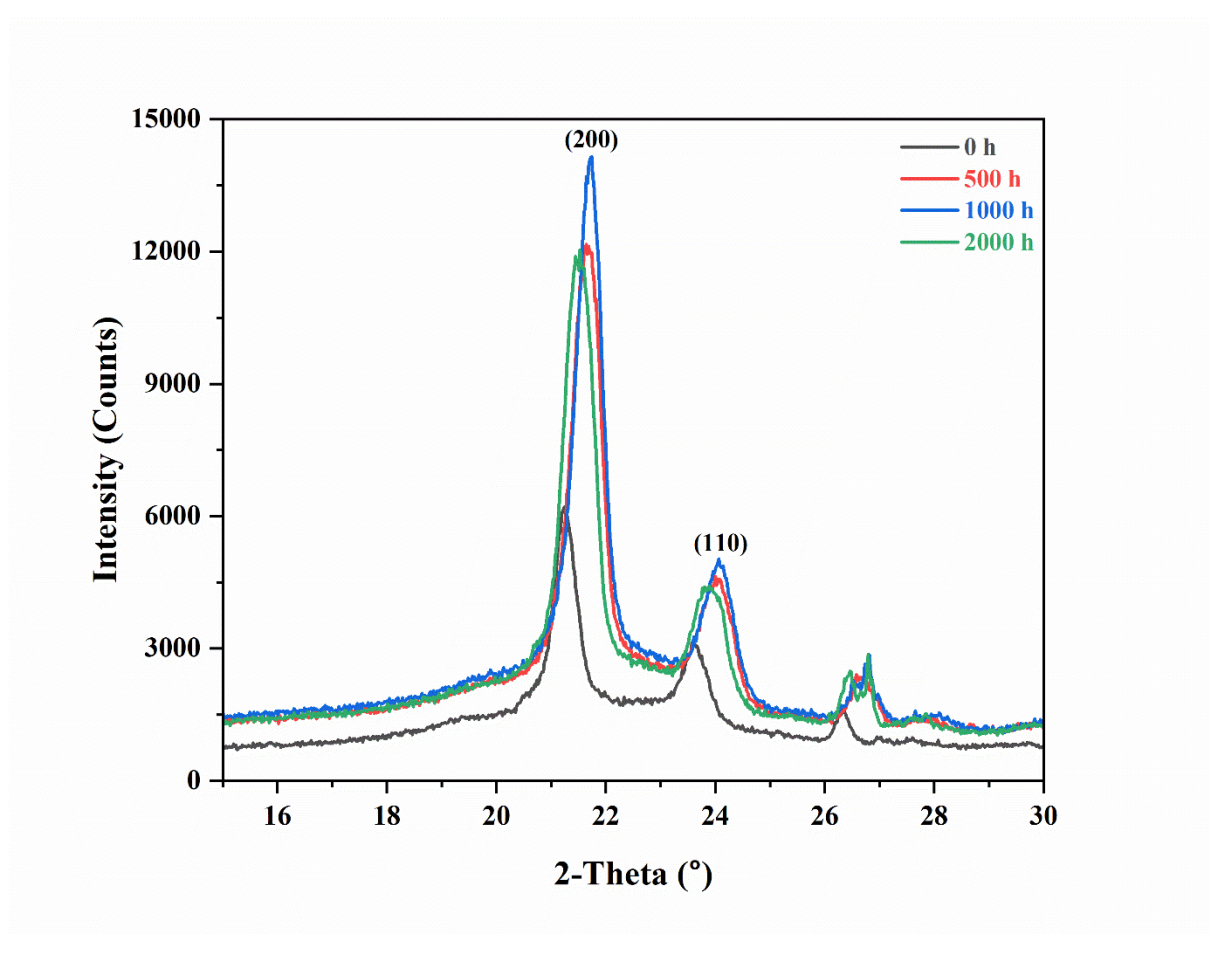


Fig 5.5 XRD patterns of weathered WPCs.

# 5.3.2 Thermogravimetric analysis of the weathered wood-plastic composites

The obvious changes of the surface characterizations of the WPCs after weathering under xenon lamp irradiation motivated further investigation into the differences in pyrolysis performances. Fig 5.6 illustrates the TG and DTG curves of the weathered WPCs. In general, the thermal decomposition of all the WPC specimens can be divided into three stages no matter the weathering durations. The first stage, occurring below 150 °C, involves the evaporation of moisture and unstable small molecule volatiles in WPCs [277]. The second stage was the main decomposition of lignocellulosic fractions in WPCs (range from 180 °C to 400 °C). The decomposition temperature of hemicellulose, lignin and cellulose, which were the primary composition of EPR, were 180–350 °C, 250–500 °C and 275–350 °C, respectively [63]. Because of the unstable structure of hemicellulose, the decomposition temperature of hemicellulose was lower than that of cellulose and lignin [278]. Consequently, a small leaning peak in the DTG curves of all the test WPC specimens were observed at around 250 °C. Because the lignin structure is rich in more stable aromatic subunits, its decomposition is

slower than that of the carbohydrates in EPR and spans almost the entire pyrolysis process. Consequently, the decomposition peak of lignin overlaps with that of cellulose. The third stage, ranging from 440 °C to 525 °C, involved the decomposition of HDPE, which appeared as a sharp and narrow peak in the DTG curves. The breaking of long-chain structures of HDPE occurred in this stage. Due to the neat and repetitive structure of HDPE, its decomposition is nearly completed in one step [279]. The slight weight loss of WPCs after 550 °C is attributed to the coupling agent and residual lignin [63].

Compared with the unweathered WPC specimen, the DTG peak temperatures of the weathered WPC specimens almost unchanged. However, the decomposition rates of WPCs decreased with the increase of weathering time. This indicated WPCs became more stable with the increase of weathering time. It could be attributed to the increased crystallinity of HDPE in WPCs with increased of weathering time [263]. Moreover, the DTG curves also illustrated that the residual solid after pyrolysis gradually increased with the lengthening of weathering time. This can be assigned to the loss of microplastics and EPR during accelerated weathering progress [263,280]. Continuous xenon lamp weathering could cause photooxidative degradation of both lignocellulosic fibres in EPR and the HDPE, and generated volatile oxidation by-products that can be escaped from the WPC and causing weight reductions [281]. Moreover, the elevated temperatures and moisture in the xenon lamp aging chamber accelerate the thermal and hydrolytic degradation of both the EPR and HDPE in WPCs. Consequently, the polymer chains in weathered WPCs broke into smaller and soluble pieces that may volatilize and leach out, contributing to the overall weight loss [280]. For instance, the photodegradation of lignin generated low molar mass water-soluble products containing carbonyl-conjugated phenolic hydroxyl groups, which can leach out in humid environments [282]. Due to the loss of volatiles, it was also observed that the residual mass after WPC pyrolysis increased with the duration of weathering.

To understand the effect of heating rate on the thermal behaviour of WPCs, the TGA and DTG curves of the weathering WPC specimens at heating rates of 5, 10, 20 and 30 °C/min was further discussed. Regardless of the heating rates, the TG and DTG curves had similar trends with the same weathering conditions. With the increase of heating rate, the peaks of DTG curves shifted to higher temperature and became wider in all of the groups. This phenomenon became more pronounced with an increase in the heating rate. A higher heating rate made it more difficult for heat to penetrate the boundary layer and reach the surface of the reacting solid, while a lower heating rate allowed for a slower, more complete pyrolysis [267,283].

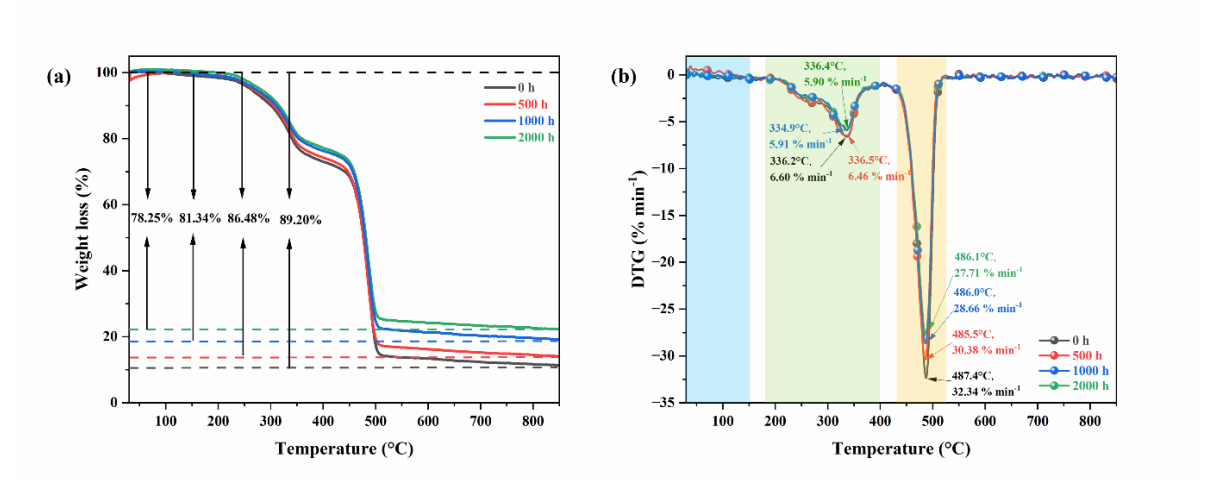


Fig 5.6 The TG (a) and DTG (b) curves of weathered WPCs at heating rate of 20 °C/min.

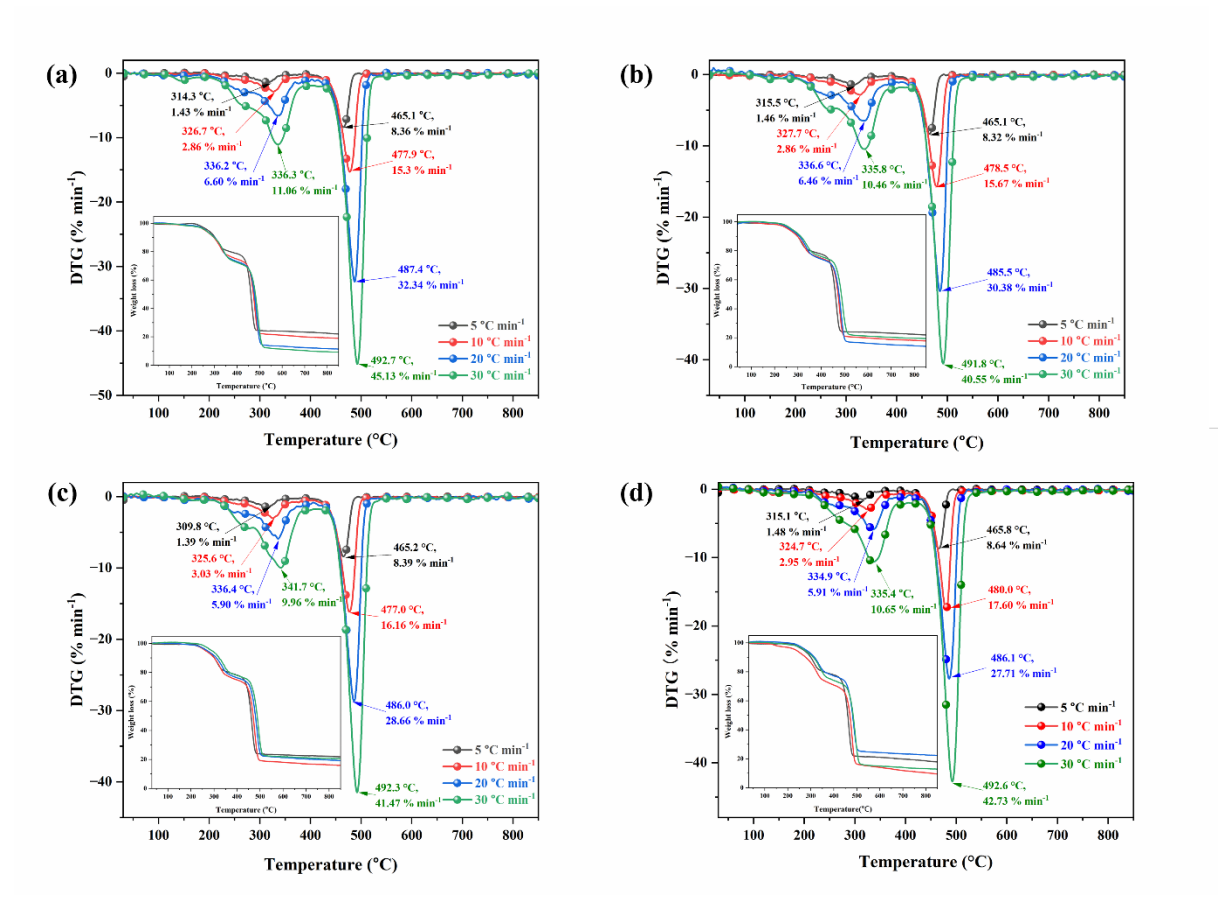


Fig 5.7 The TGA and DTG curves of weathered WPCs. (a) 0 h, (b) 500 h, (c) 1000 h, and (d) 2000 h of xenon lamp irradiation.

# 5.3.3 Pyrolysis kinetics of the weathered wood-plastic composites

Activation energy ( $E_a$ ) is the minimum energy required for transforming a chemical molecule from normal state to an activated state [267]. Compared to the model-fitting methods, model-free methods are more accurate for the non-linear reaction mechanism, and they were

satisfied with the case of WPC pyrolysis [216]. Hence, two model free methods (KAS and FWO) were employed to determine the  $E_a$  value of the weathered WPCs pyrolysis. Because of the unstable decomposition reaction at the start and end of the pyrolysis process, the conversion rate ( $\alpha$ ) from 0.2 to 0.8 is selected to identify the changes of  $E_a$  for different conversion rates. Fig 5.8 shows the kinetic diagrams of weathered WPCs, while Table 5.2 lists  $E_a$  values and correlation coefficient ( $R^2$ ) obtained by KAS and FWO methods at different conversion rates.  $R^2$  values in all groups varied between 0.87-0.99, indicating the reliability of the estimated results. Fig.6 shows the change in trend of the  $E_a$  values of WPCs upon different weathering conditions and different conversion rates.

According to Table 5.2, the  $E_a$  values calculated by KAS methods were higher than that calculated by FWO, which the difference ascribed to the derivation process and error range of the different models [179]. In addition, EPR and HDPE in WPCs leads to the changes of  $E_a$ during pyrolysis. At the initial stage of WPCs pyrolysis ( $\alpha$ =0.2-0.4), the decomposition of hemicellulose, cellulose, and lignin in EPR was prominent. During this stage, the  $E_a$  increased sharply. This increase was attributed to the sequential decomposition of the lignocellulosic components. In accordance with the aforementioned TGA results, hemicellulose comprises various types of saccharides (amorphous structure and high branching) which were easy to decompose to volatiles at low temperature [127,185]. Cellulose and lignin decompose at higher energies because cellulose has a stable structure of crystalline regions and long polymer chains of glucose without branches, and lignin contains strong chemical bonds, such as benzene rings, which necessitate higher energy to initiate the decomposition reaction [253]. The second stage ( $\alpha$ =0.4-0.8) was the decomposition of HDPE. The  $E_a$  value decreased at this stage in all of the test groups. This was ascribed to the synergistic effect between lignocelluloses in EPR and HDPE during pyrolysis, which increases the reactivity of the weathered WPCs and further lowers  $E_a$  [284].

The average  $E_a$  values of unweathered WPC were 326.88 kJ/mol (FWO) and 332.03 kJ/mol (KAS), which was higher than that of the 500 h xenon lamp weathering specimen (319.35 kJ/mol (FWO) and 324.07 kJ/mol (KAS)). With the prolonged weathering time, the average  $E_a$  decreased, in which the average  $E_a$  values of 1000 h weathering WPC were 305.69 kJ/mol (FWO) and 309.74 kJ/mol (KAS), and the average  $E_a$  values of 2000 h weathering WPC were 288.83 kJ/mol (FWO) and 291.25 kJ/mol (KAS), respectively. The decrease of  $E_a$  upon weathering could be attributed to the photodegradation of WPCs.

At the initial stage of pyrolysis ( $\alpha$ =0.2-0.4), with the decomposition of lignocellulose fractions in WPCs, the  $E_a$  values decreased upon weathering time. During xenon lamp

irradiation, ultraviolet and visible light caused the breaking of chemical bonds in the EPR, particularly in lignin and cellulose fractions (it has been proved by Fig 5.4) [264]. This made the lignocellulosic structure of EPR looser and more unstable. In addition, the weathering of WPC leads to photo-oxidation reactions of cellulose and hemicellulose, forming more carbonyl and carboxyl groups [285]. The presence of the oxidation products makes the EPR easier to decompose during pyrolysis, thus lowering the activation energy. Furthermore, the increased surface roughness and porosity upon weathering also could facilitate the pyrolysis reactions, thereby lowering the activation energy.

The second stage of pyrolysis ( $\alpha$ =0.4-0.8) is mainly attributed to the decomposition of HDPE, the  $E_a$  values of unweathered WPC was close or slightly lower than that of weathered WPCs. It has been reported the degradation of HDPE was caused by chain scission via Norrish Type I and II reactions, and resulted in shorter polymer chains [261]. However, the increased crystallinity of HDPE upon weathering made HDPE more stable, suggesting more energy was required to trigger decomposition of HDPE.

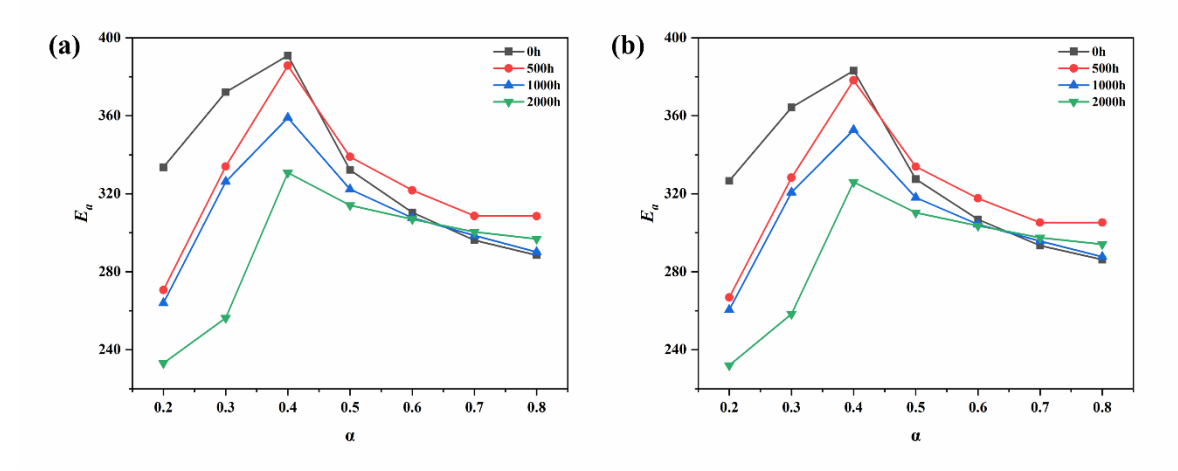


Fig 5.9 Changes of  $E_a$  values at different conversion rate upon different weathering condition according to (a) KAS and (b) FWO.

Understanding the reaction model of pyrolysis is crucial to optimize the pyrolysis process and reactor design [127]. Hence, the Master-plot method was adopted to determine the reaction model for the pyrolysis of weathered WPCs. Fig 5.10 presents P(u)/P(u0.5) as a function of the  $\alpha$  value for different heating rates. The curves of P(u)/P(u0.5) versus  $\alpha$  remained similar regardless of the heating rates in all of the testing groups, indicating the reaction model of WPCs pyrolysis did not depend on the heating rate. Therefore, the curves of P(u)/P(u0.5)

versus  $\alpha$  at a heating rate of 20 °C/min were used to determine the reaction models for all groups.

As shown in Fig 5.11, the reaction model for WPCs upon different weathering time was determined by comparing the theoretical and experimental master diagrams. There was no matching reaction model for the  $\alpha$ =0.2-0.4 in all groups, indicating the pyrolysis reaction was complex during this stage. This stage corresponded to the main decomposition stage of lignocellulose in the EPR. Because of the complex interior structure and composition of lignocellulose matrix, the pyrolysis reaction did not follow a single reaction model [187]. Within  $\alpha$ =0.4-0.8, the pyrolysis of unweathered WPC followed the reaction model of R0.7 ( $\alpha$ =0.4-0.5) and P2.5 ( $\alpha$ =0.5-0.8). Besides, 500 h weathered WPC followed the reaction model of R2 ( $\alpha$ =0.4-0.5) and P2.9 ( $\alpha$ =0.5-0.8), 1000 h weathered WPC followed the reaction model of P1.7 ( $\alpha$ =0.4-0.5) and P3.3 ( $\alpha$ =0.5-0.8), and 2000 h weathered WPC followed P3.3 ( $\alpha$ =0.4-0.5) and P5.5 ( $\alpha$ =0.5-0.8). These results suggest that the pyrolysis reaction of weathered WPCs at high conversion rate ( $\alpha$ =0.5-0.8) was P (phase interface) reaction, the volatile contents were released from the solid surface [106]. In addition, the results demonstrated that the reaction model moved to higher reaction order upon weathering time, which can be attributed to the increased crystallinity of HDPE upon weathering.

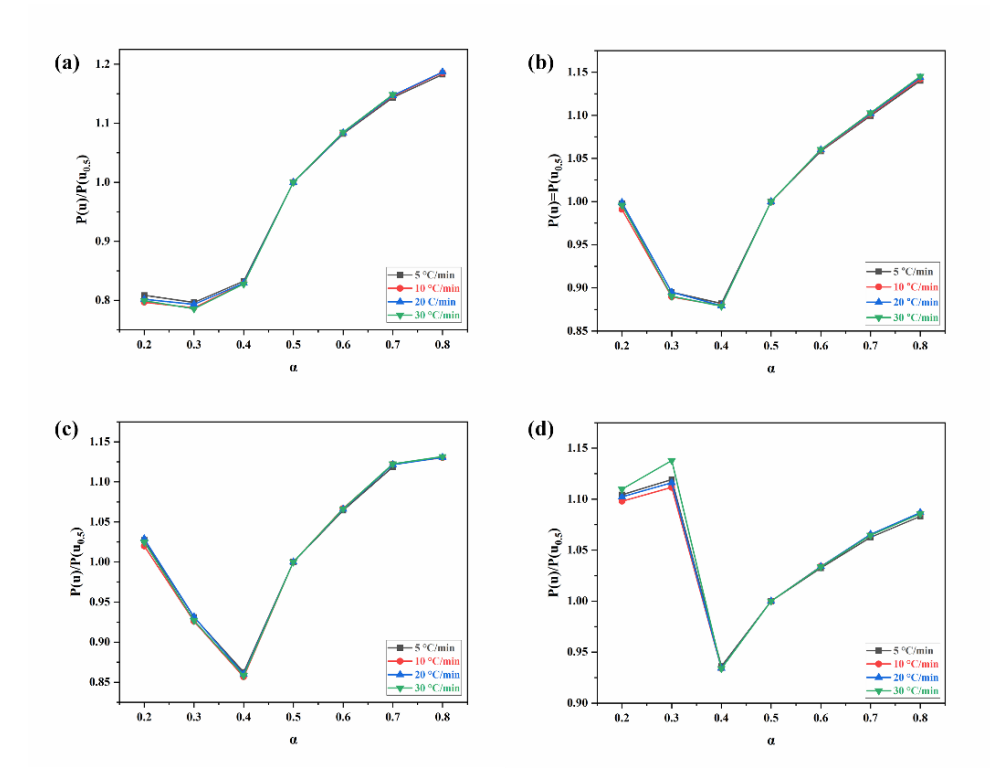


Fig 5.10 The curves of  $\alpha$  versus P(u)/P(u<sub>0.5</sub>). (a) 0 h, (b) 500 h, (c) 1000 h, and (d) 2000 h of xenon lamp irradiation.

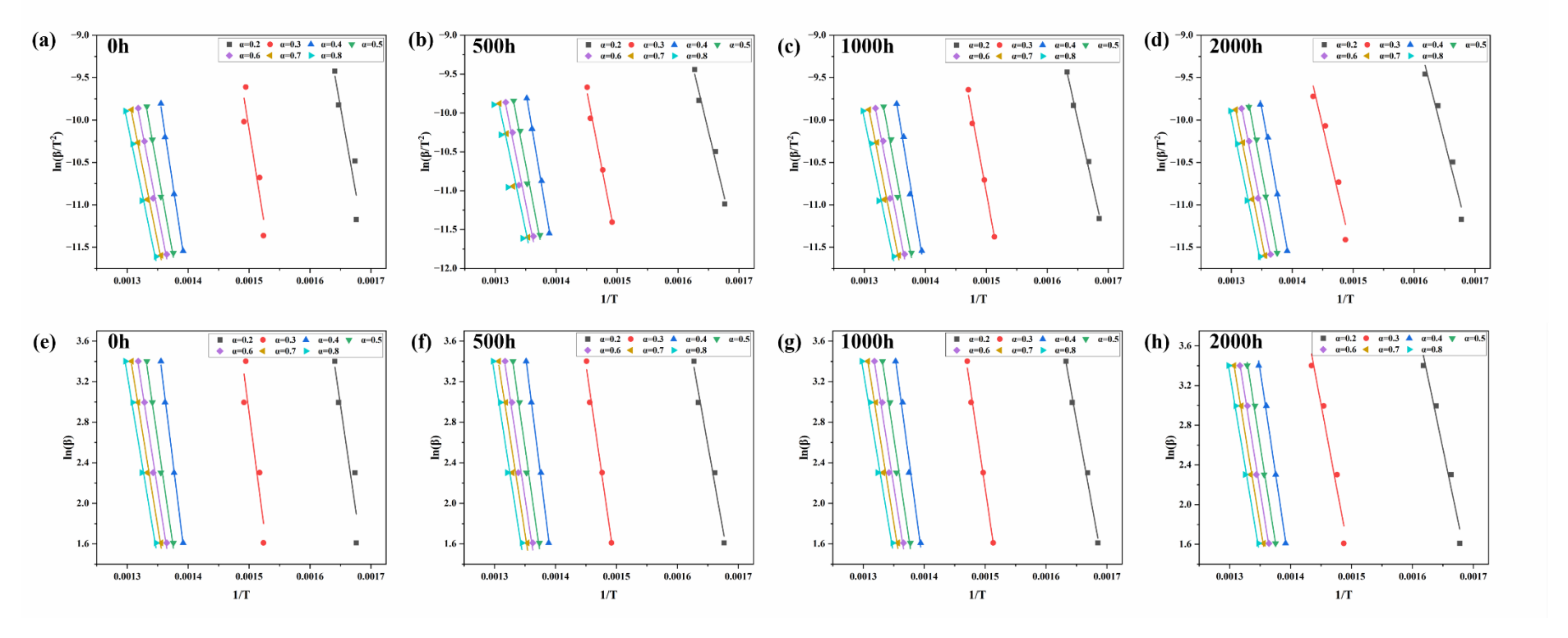


Fig 5.8 Kinetic diagram of the weathered WPCs according to (a-d) KAS and (e-h) FWO.

Table 5.2 The  $E_a$  value and  $R^2$  of the weathered WPCs under different conditions

	FWO								KAS							
Aging time	0 h		500 h		1000 h		2000 h		0 h		500 h		1000 h		2000 h	
α	E <sub>a</sub> (kJ/mol)	$R^2$														
0.2	326.67	0.89	266.85	0.98	260.48	0.99	231.95	0.97	333.63	0.88	270.66	0.98	264.00	0.99	233.14	0.96
0.3	364.27	0.88	328.27	0.98	320.70	0.99	258.35	0.95	372.18	0.87	334.04	0.99	326.24	0.99	256.37	0.94
0.4	383.12	0.99	378.22	0.99	352.82	0.99	325.97	0.99	390.94	0.99	385.76	0.99	359.07	0.98	330.78	0.99
0.5	327.53	0.99	333.92	0.98	318.11	0.98	310.29	0.99	332.28	0.99	338.99	0.98	322.39	0.98	314.13	0.99
0.6	306.88	0.99	317.68	0.97	304.27	0.98	303.61	0.99	310.45	0.99	321.81	0.97	307.71	0.98	306.99	0.99
0.7	293.44	0.99	305.28	0.97	295.73	0.98	297.52	0.99	296.21	0.99	308.66	0.98	298.63	0.98	300.50	0.99
0.8	286.24	0.99	305.25	0.98	287.73	0.98	294.12	0.99	288.55	0.99	308.55	0.97	290.13	0.98	296.84	0.99
Average	326.88	-	319.35	-	305.69	-	288.83	-	332.03	-	324.07	-	309.74	-	291.25	-

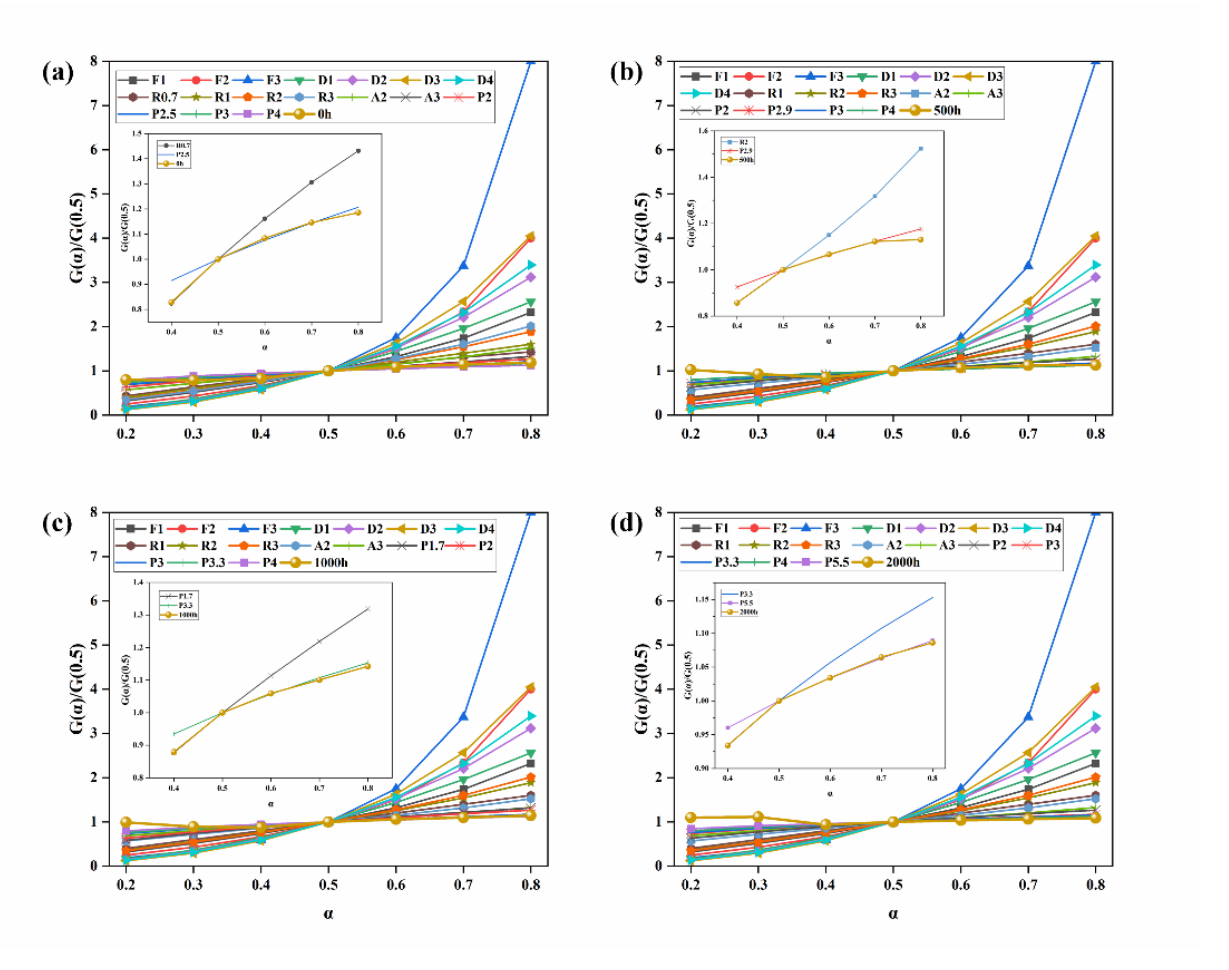


Fig 5.11  $G(\alpha)/G(0.5)$  versus  $\alpha$  for the reaction models and the (a) 0 h, (b) 500 h, (c) 1000, and (d) 2000 h weathered WPCs at 20 °C/min.

# 5.3.4 Valorisation products from the pyrolysis of the weathered wood-plastic composites

After investigation of the pyrolysis behaviour and kinetics of the weathered WPCs, the volatiles products of typical pyrolysis targeted to waste-to-wealth valorisation of the post-consumed WPCs was further investigated. TG-FTIR was conducted to analysis the functional groups of the gaseous products during the slow pyrolysis of weathered WPCs (Fig 5.12), which indicated the pyrolysis process can be divided into 2 stages. Fig 5.12e illustrated the FTIR spectra of the WPCs pyrolysis in stage I, which is assigned to the decomposition of EPR in WPCs. The peaks located between 3800-3500 cm<sup>-1</sup> were related to the stretching vibration of -OH, which indicated the presence of H<sub>2</sub>O, alcohol and phenol [267]. The absorption peaks in the range of 2960-2850 cm<sup>-1</sup> were attributed to the stretching vibration of methylene (-CH<sub>2</sub>-). The two strong peaks between 2400–2240 cm<sup>-1</sup> proved the presence of CO<sub>2</sub>. The strong peaks of CO<sub>2</sub> may be due to the high content of oxygen-containing groups in lignocellulose fractions

in EPR [286]. The peaks between 1810 and 1680 cm<sup>-1</sup> were assigned to the stretching vibration of C=O, which suggested the generation of aldehyde. The two peaks located between 2240 and 2060 cm<sup>-1</sup> proved the presence of CO, which was generated by the decarbonylation of aldehydes [267]. The weak peaks in the range of 1325–1000 cm<sup>-1</sup> can be ascribed to the stretching vibrations of C–O and O–H, indicative of the formations of phenols, alcohols, and ethers [287]. As aforementioned in section 5.3.2, the lignocellulose fractions in the WPC was partially lost upon the weathering process due the photodegradation of the main constituents including cellulose, hemicellulose, and lignin. According to the Lambert-Beer law, there was a positive correlation between the gaseous product concentration and the absorption peak intensity [247]. Therefore, the intensity of all the functional groups decreased upon weathering.

Fig 5.12f presented the FTIR spectra of the weathered WPCs pyrolysis in stage II, which was mainly attributed to the decomposition of HDPE. The strong peaks between 2960 cm<sup>-1</sup> and 2850 cm<sup>-1</sup> were C-H stretching vibration in methylene [288]. The characteristic absorption peaks in the ranges of 3080–3000 cm<sup>-1</sup> and 1700–1610 cm<sup>-1</sup> were associated with the =C-H and C=C stretching vibrations, respectively, indicative of the alkenes' formation. The appearance of the R-CH=CH<sub>2</sub> bending vibration in the range of 1040–1370 cm<sup>-1</sup> showed the existence of alkenes [180]. The absorption peak in the range of 1455–1370 cm<sup>-1</sup> was associated with the -CH<sub>3</sub> bending vibration, indicative of the formation of alkanes, in particular, CH<sub>4</sub> [287]. The irregular chain break occurred with the pyrolysis of HDPE. Alkanes and alkenes were the main gas products of the HDPE pyrolysis [153]. Similar with Stage I, the intensity of all the functional groups decreased upon weathering. These observations agreed well with the results in Section 5.3.2. During the xenon lamp weathering process, the photooxidative, thermal and hydrolytic degradation of plastic matrix generated volatile and soluble by-products which can escape or leach out from the solid phase, thereby causing a reduction in pyrolysis products.

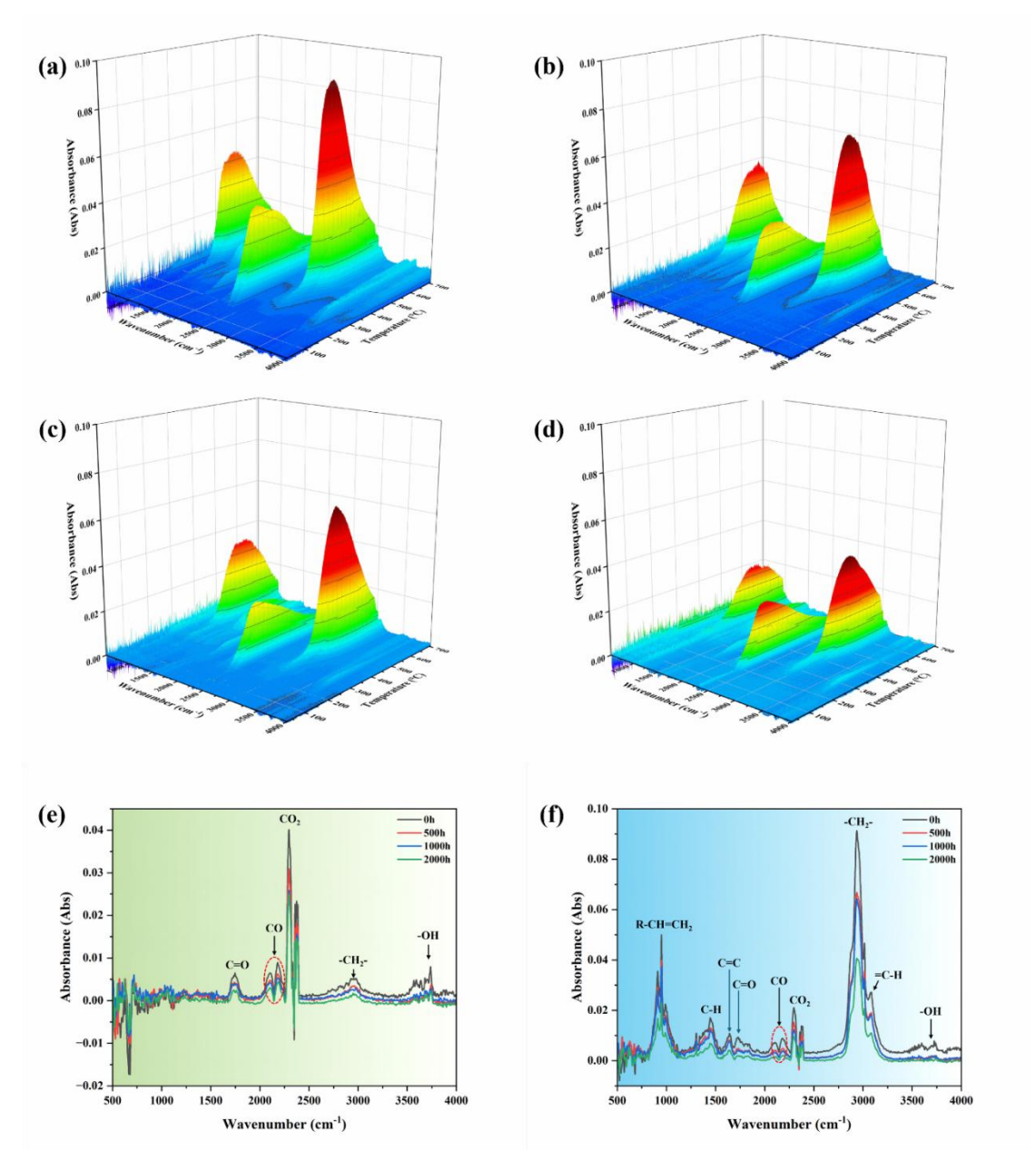


Fig 5.12 The pyrolysis products of weathered WPCs at heating rate of 10 °C /min. (a-e) 3D FTIR diagram and (e-f) 2D FTIR diagram of pyrolysis products at the temperature of maximum mass loss peaks of (e) stage I and (f) stage II.

Py-GC/MS analysis was conducted to analyse the gaseous products generated by the rapid pyrolysis of the weathered WPCs. All the weathered WPCs specimens were almost completely decomposed before 600 °C. Therefore, the rapid pyrolysis temperature was set at 600 °C. The main gaseous products from rapid pyrolysis of the WPCs upon different aging time are listed in Table 5.3, and the products distribution is shown in Fig 5.13. Generally, the complex gaseous products was obtained from the pyrolysis of WPC specimens, including the products originating from HDPE, EPR, as well as the "cross-products" [84]. The main products generated from pyrolysis of WPCs were belonging to hydrocarbons, oxygen-containing

compounds, and nitrogen-containing compounds. The hydrocarbons such as liner and isohydrocarbons (paraffin and olefins) were mainly from the decomposition of HDPE, which have a wide carbon chain length ranging from C<sub>3</sub>-C<sub>44</sub> [85]. Similar to the pure lignocellulose pyrolysis, the pyrolysis of the lignocellulosic reinforcement phase in weathered WPCs mainly produced oxygen-containing compounds such as aldehyde, alcohol, ester, and phenol [84,289].

It has been reported that exposure to ultraviolet light can break the chemical bonds within a polymer, leading to chain scission and the formation of free radicals [288]. Subsequently, βscission propagation and radical reactions occurred, resulted in the fragmentation of the primary polymer chains into smaller straight chains [290]. As Fig 5.13 showed, the C<sub>1</sub>-C<sub>10</sub> hydrocarbon content in pyrolysis products increased upon the weathering time, and new molecules such as propene (C<sub>3</sub>H<sub>6</sub>), 1-pentene (C<sub>5</sub>H<sub>10</sub>) and 1-decene (C<sub>10</sub>H<sub>20</sub>) were formatted in the pyrolysis products of 1000 h and 2000 h weathered WPCs. With the increase of exposure time, the initial cracking of the long hydrocarbon chain in HDPE was further promoted, leading to the formation of smaller olefins and more thermal decomposition sites [288]. Subsequently, the smaller olefins and thermal decomposition sites facilitated the formation of short hydrocarbons during pyrolysis [288]. In addition, small molecular weight oxygen-containing compounds such as methoxy-acetaldehyde (C<sub>3</sub>H<sub>6</sub>O<sub>2</sub>) was also detected in 1000 h and 2000 h weathered groups. This can be ascribed to the high oxidation degree and significant chain scissions. Moreover, a series of *n*-alkanes with different carbon numbers, such as pentadecane (C<sub>15</sub>H<sub>32</sub>), hexadecane (C<sub>16</sub>H<sub>34</sub>) and heptadecane (C<sub>17</sub>H<sub>36</sub>), were detected, which agreed-well with a previous study [291]. Compared to the pyrolysis products of unweathered WPC, the content of oxygen-containing compounds, such as alcohol, ester and phenol, were decreased in the pyrolysis products of weathered WPCs, which coincided with the results of the TG-FTIR (Fig 5.12). The oxygen-containing compounds were mainly produced by the decomposition of lignocellulosic fractions in WPCs. Fabiyi et al. (2008) reported that the wood content decreased from 60 % to 21% on the WPC surface after 400 h xenon-arc for PP/pine WPC [264]. Therefore, the loss of biomass content would decrease the content of oxygen-containing compounds in the pyrolysis products. Over all, the prolonged weathering time increased the loss of lignocellulose fractions in WPCs, leading to the decrease of oxygen-containing compounds in pyrolysis products, while the formation of value-added short chain hydrocarbons was favoured.

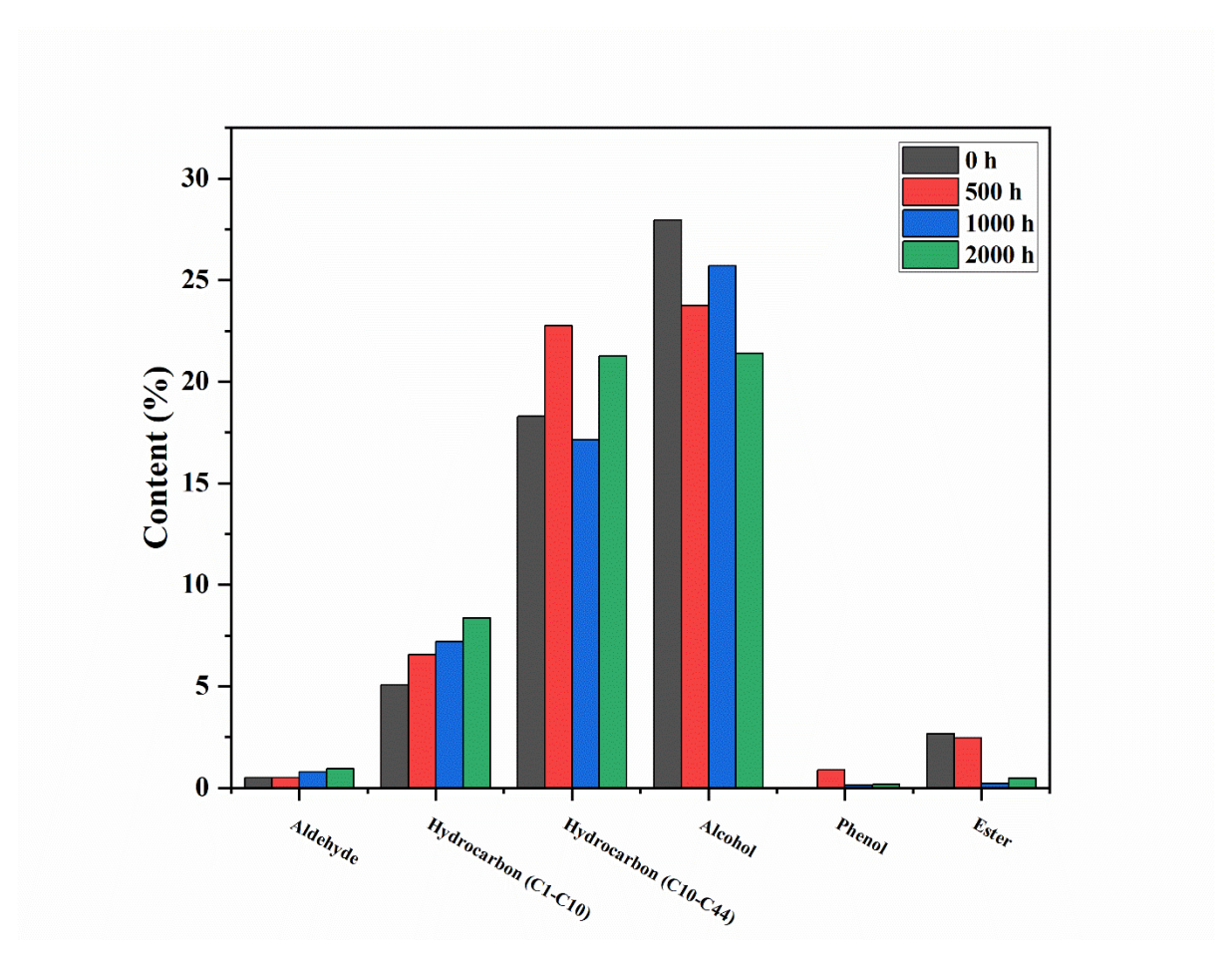


Fig 5.13 The products distribution of weathered WPCs pyrolysis.

Table 5.3 The main gaseous products from rapid pyrolysis of unweathered, 500h, 1000h, and 2000h weathered WPCs at  $600~^{\circ}$ C for 20~s

R.T.	Compounds	Formula		Area	Pct (%)		Туре
(min)	Compounds	Torriura	0h	500h	1000h	2000h	Турс
1.560	Acetaldehyde, methoxy-	C <sub>3</sub> H <sub>6</sub> O <sub>2</sub>	N.D.	N.D.	0.56	0.67	Aldehyde
1.625	Propene	$C_3H_6$	N.D.	N.D.	1.05	1.24	Alkene
1.688	Pentanenitrile	$C_5H_9N$	N.D.	N.D.	0.77	0.96	Others
	Formic acid, 2-						
1.729	methylpropyl	$C_5H_{10}O_2$	2.2	2.18	N.D.	N.D.	Ester
	ester						
1.845	1-Pentene	$C_5H_{10}$	N.D.	N.D.	1.04	1.04	Alkene
1.881	1-Pentanol	$C_5H_{12}O$	1.6	1.24	N.D.	N.D.	Alcohol
2.291	1-Hexene	$C_6H_{12}$	2.2	1.90	1.54	1.87	Alkene
3.190	1-Heptene	$C_7H_{14}$	1.22	1.06	1.11	1.31	Alkene
3.270	3-Hexanone	$C_6H_{12}O$	N.D.	0.49	N.D.	N.D.	Ketone
3.283	1-Heptane	C <sub>7</sub> H <sub>16</sub>	0.54	N.D.	N.D.	N.D.	Alkane

4.894	1-Octene	$C_8H_{16}$	0.86	0.70	0.49	0.58	Alkene
5.057	1-Octane	$C_8H_{18}$	0.50	0.41	0.27	0.34	Alkane
7.412	1-Nonene	$C_9H_{18}$	0.94	0.75	0.53	0.62	Alkene
7.610	1-Nonane	$C_9H_{20}$	0.31	0.25	0.17	0.20	Alkane
10.153	1-Decene	$C_{10}H_{20}$	N.D.	N.D.	1.01	1.17	Alkene
10.212	1-Undecene	$C_{11}H_{22}$	1.72	1.48	0.9	1.04	Alkene
10.352	Undecane	$C_{11}H_{24}$	0.86	0.76	0.56	0.40	Alkane
12.104	1-Tridecene	$C_{13}H_{26}$	1.52	1.32	1.49	1.68	Alkene
12.247	Phenol, 2- methoxy-	$C_7H_8O_2$	0.15	N.D.	N.D.	N.D.	Phenol
12.403	Phenol, 3-methyl-	$C_7H_8O$	0.27	N.D.	N.D.	N.D.	Phenol
13.508	1-Tetradecene	$C_{14}H_{28}$	1.20	1.05	N.D.	N.D.	Alkene
13.589	Dodecane	$C_{12}H_{26}$	0.54	0.50	0.28	0.30	Alkane
14.321	Benzaldehyde, 3- methyl-	$C_8H_8O$	0.51	0.50	0.24	0.28	Aromatics/Aldehyde
14.573	8-Dodecen-1-ol, (Z)-	C <sub>12</sub> H <sub>24</sub> O	0.54	N.D.	0.26	N.D.	Alcohol
14.666	1-Tetradecene	$C_{14}H_{28}$	2.82	2.56	2.07	3.39	Alkene
14.731	Tetradecane	$C_{14}H_{30}$	1.43	0.98	0.28	0.57	Alkane
15.108	2-Methoxy-4- vinylphenol	$C_9H_{10}O_2$	0.29	N.D.	0.14	0.17	Phenol
15.494	Phenol, 2,6-dimethoxy-	$C_8H_{10}O_3$	0.18	N.D.	N.D.	N.D.	Phenol
15.588	1,13- Tetradecadiene	$C_{14}H_{26}$	1.17	3.36	1.01	1.57	Alkene
15.600	Cyclododecene, (Z)-	$C_{12}H_{22}$	2.95	1.22	N.D.	N.D.	Alkene
16.584	n-Pentadecanol	$C_{15}H_{32}O$	5.32	6.57	N.D.	1.09	Alcohol
16.629	Eicosane	$C_{20}H_{42}$	1.75	2.66	N.D.	N.D.	Alkane
16.631	Pentadecane	$C_{15}H_{32}$	N.D.	N.D.	0.37	0.36	Alkane
17.469	Hexadecane	$C_{16}H_{34}$	N.D.	N.D.	0.39	0.38	Alkane
18.160	1,15- Hexadecadiene	$C_{16}H_{30}$	N.D.	N.D.	3.07	3.06	Alkene
18.258	Heptadecane	$C_{17}H_{36}$	N.D.	N.D.	1.41	2.23	Alkane
19.637	5-Cyclohexyl-1- pentene	$C_{11}H_{20}$	N.D.	1.30	N.D.	N.D.	Alkene
19.673	1-Nonadecene	$C_{19}H_{38}$	5.42	N.D.	N.D.	N.D.	Alkene
19.776	1,19-Eicosadiene	$C_{20}H_{38}$	0.79	N.D.	0.62	0.40	Alkene
20.386	Heneicosane	$C_{21}H_{44}$	N.D.	N.D.	0.99	0.77	Alkane

20.637	17- Pentatriacontene	C <sub>35</sub> H <sub>70</sub>	N.D.	1.11	2.90	3.57	Alkene
20.990	n-Tetracosanol-1	$C_{24}H_{50}O$	7.29	7.17	3.53	3.07	Alcohol
21.207	Methyl stearate	$C_{19}H_{38}O_2$	0.27	0.49	0.22	0.49	Ester
21.402	n-Heptadecanol-1	$C_{17}H_{36}O$	0.67	0.17	1.42	1.28	Alcohol
22.070	1-Heneicosanol	$C_{21}H_{44}O$	3.92	1.14	N.D.	N.D.	Alcohol
22.124	Tetracosane	$C_{24}H_{50}$	N.D.	N.D.	0.79	N.D.	Alkane
22.432	Henicos-1-ene	$C_{21}H_{42}$	0.60	N.D.	N.D.	N.D.	Alkene
22.573	n-Nonadecanol-1	$C_{19}H_{40}O$	0.75	3.42	3.11	3.49	Alcohol
23.447	1-Heptacosanol	$C_{21}H_{44}O$	N.D.	3.06	7.52	1.04	Alcohol
30.640	2- Methylhexacosane	C <sub>27</sub> H <sub>56</sub>	N.D.	N.D.	N.D.	0.82	Alkane
31.578	Tetratetracontane	$C_{44}H_{90}$	N.D.	0.82	N.D.	0.74	Alkane
32.324	1- Hentetracontanol	C <sub>41</sub> H <sub>84</sub> O	3.66	5.20	9.64	10.95	Alcohol

#### 5.4 Conclusion

This section demonstrates that the pyrolysis behaviour and product distribution of woodplastic composites (WPCs) changed after weathering. The xenon lamp-induced weathering increases the crystallinity of high-density polyethylene (HDPE) in the WPCs, resulting in enhanced thermal stability and reduced decomposition rates. FT-IR and XRD analyses confirm the degradation of lignocellulosic fractions and the increased crystallinity of HDPE. Additionally, the increased residue content after weathering illustrated the loss of volatile content of plastic and lignocellulosic fiber during weathering. The kinetic results showed that the average activation energy  $(E_a)$  of WPCs pyrolysis decreased, while the  $E_a$  of HDPE fraction in WPCs decomposition increased after weathering, aligning well with the TGA analysis results. The master plots indicated that the pyrolysis reaction moved to a higher order with increased weathering time. TG-FTIR results showed that the intensity of absorption peaks for all functional groups decreased with increased weathering time. Py-GC/MS results demonstrated that weathering altered the pyrolysis product distribution, forming short-chain hydrocarbons such as Propene (C<sub>3</sub>H<sub>6</sub>), 1-Pentene (C<sub>5</sub>H<sub>10</sub>) and 1-Decene (C<sub>10</sub>H<sub>20</sub>) with prolonged weathering, while the content of oxygen-containing compounds such as alcohols, esters, and phenols decreased in the pyrolysis products of weathered WPCs, which reveals a shift in pyrolysis products towards valuable short-chain hydrocarbons with prolonged weathering. These findings provide actionable insights for optimizing the pyrolytic valorization of post-consumer

WPCs, emphasizing the potential for producing biofuels and chemicals from weathered composites.

# Chapter 6

Conclusion and future work

#### 6. Conclusion and future work

#### 6.1 Conclusion

This dissertation presents a sequential and integrated investigation into the thermal valorisation of corn stalk biomass, biorefinery residues, and lignocellulose-based composites, establishing a quantitative and mechanistic understanding of waste-to-energy conversion within a circular bioeconomy framework. Table 6.1 illustrates the sequential and integrated research framework from the thermal conversion of corn stalk biomass to the valorisation of industrial residues, biocomposites, and weathered WPC, supported by multi-scale characterization and AI-assisted modelling.

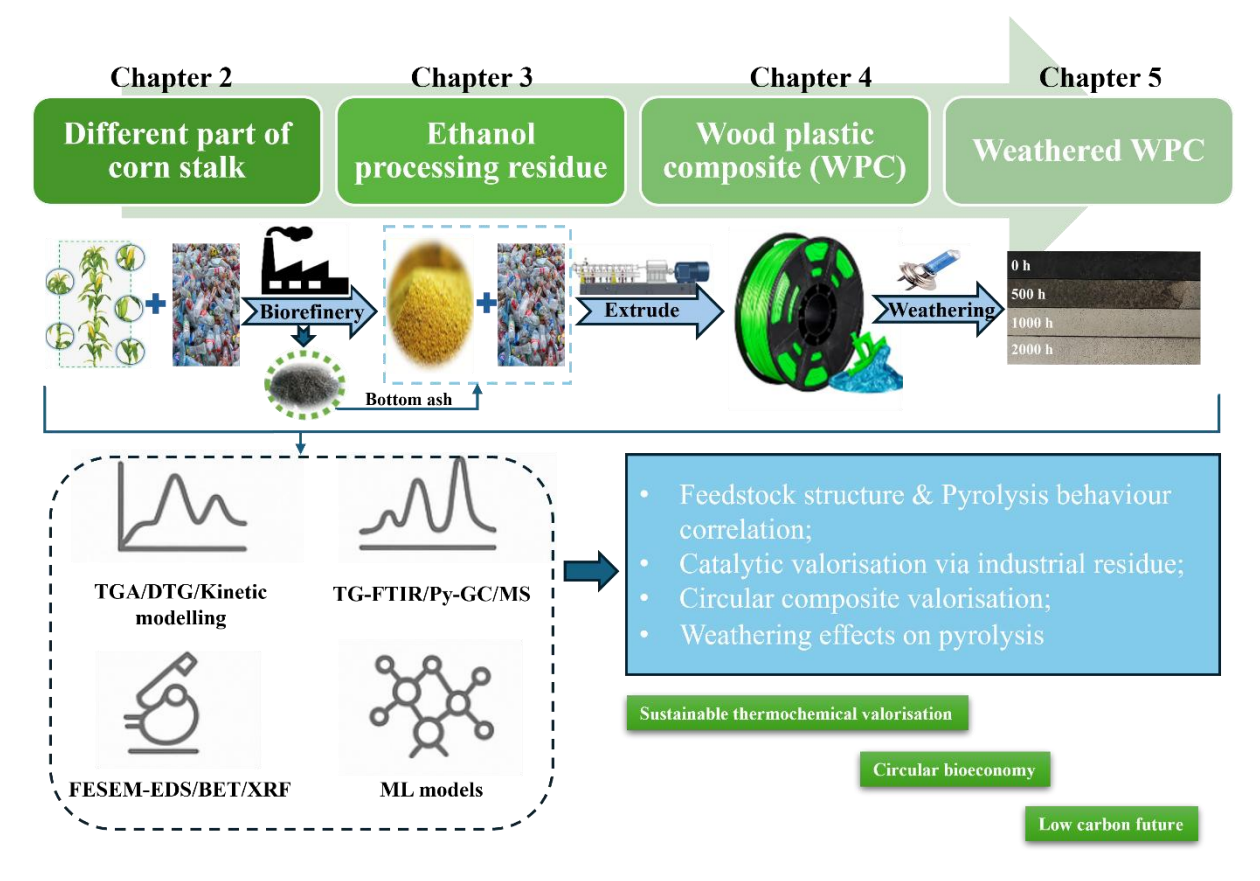


Table 6.1 Graphical summary of the thesis

# 1. Feedstock structural dependence and co-pyrolysis synergy

The systematic comparison of different corn stalk tissues revealed that feedstock microstructure and composition strongly dictate pyrolytic behaviour. Among all tissues, the corn cob/HDPE blend exhibited the lowest activation energy (149.3 kJ/mol) and the highest yield of aromatic hydrocarbons and furans, indicating the most energy-efficient decomposition

and greatest potential for biofuel production. The observed 20-30 °C reduction in DTG peak temperature across all corn stalk/HDPE blends further confirmed synergistic interactions between lignocellulose and polymer radicals, underscoring the importance of feedstock-specific pre-management in optimizing co-pyrolysis efficiency.

### 2. Catalytic valorisation using industrial byproducts

Transitioning from raw biomass to EPR, the introduction of BA as a low-cost catalyst led to measurable but moderate kinetic enhancement. The average activation energy decreased from 174.8 to 171.3 kJ/mol (KAS method) and from 177.3 to 174.0 kJ/mol (FWO method), demonstrating that BA's catalytic role—though limited—reduces the energetic barrier through mineral-mediated reactions and improved heat transfer. The catalytic EPR/HDPE system yielded a 5-8 % higher proportion of aromatic hydrocarbons, supporting the concept of industrial symbiosis, where waste-derived BA facilitates the valorisation of bioethanol residues.

# 3. Composite and residue integration in circular design

Expanding to processed materials, the pyrolysis of RSPR/PLA composites demonstrated clear evidence of interphase synergy. The composite exhibited a lower activation energy (121.5 kJ/mol) compared to the pure PLA (205.5 kJ/mol) and RSPR (136.5 kJ/mol), confirming mutual radical interactions that promote decomposition and suppress CO/CO<sub>2</sub> emissions observed in TG-FTIR spectra. These results demonstrate that discarded lignocellulose/PLA composites retain recoverable thermal value, enabling eco-efficient end-of-life management for bioplastic-based materials.

#### 4. Weathering-induced evolution of WPC pyrolysis

The artificial weathering experiments (0–2000 h xenon exposure) showed that aging alters both thermal and chemical degradation pathways in WPCs composed of EPR and HDPE. The residue content increased by 10.6 %, while the average activation energy decreased from 326.9 to 288.8 kJ/mol. During weathering, the fibre structure becomes increasingly loosened due to photodegradation and moisture-induced swelling, which weakens interfacial bonding and facilitates thermal scission. This structural relaxation lowers the energy barrier for pyrolysis, resulting in a reduced activation energy. Py-GC/MS analysis revealed a shift toward short-chain hydrocarbons (C<sub>3</sub>–C<sub>10</sub>) and a reduction in oxygenated species such as alcohols. These results provide a practical understanding of how environmental exposure modifies polymer–biomass interfaces and influence pyrolytic valorisation outcomes in post-consumer composites.

#### 5. Data-driven prediction and process generalisation

Machine learning models were successfully applied to predict mass loss during copyrolysis, achieving R<sup>2</sup> > 0.98 for both Random Forest (RF) and Gradient Boosting Regression Tree (GBRT) models. These predictive frameworks validated experimental kinetics and offer a scalable digital tool for real-time process optimisation, bridging experimental thermochemical analysis with AI-driven pyrolysis design.

#### 6. Overall contribution and implications

Collectively, this work establishes a hierarchical and interconnected understanding of biomass–plastic–residue pyrolysis across four complexity levels:

- (1) tissue-scale interactions,
- (2) catalytic upgrading of industrial residues,
- (3) valorisation of composite waste, and
- (4) environmental durability of WPCs.

By quantifying the structural, catalytic, and aging influences on activation energy, reaction rate, and product selectivity, this study provides design-oriented insights for developing low-cost, low-emission, and circular pyrolysis systems. The integrated dataset and kinetic framework support future reactor design, process modelling, and techno-economic analyses for bioenergy recovery from mixed lignocellulose—plastic waste streams. Ultimately, this dissertation contributes a quantitative and mechanism-informed foundation for the sustainable thermochemical valorisation of hybrid biopolymers—advancing both the scientific understanding and engineering practice of circular waste-to-energy systems.

#### **6.2** Future perspectives and outlook

The thermal processing of agricultural waste and WPCs, such as corn stalk, biorefinery residues, biorefinery residue-reinforced WPCs and weathered WPCs, holds immense potential for advancing sustainability in fuel production and materials management. Looking ahead, several key perspectives and future directions can be identified:

#### • Innovative feedstock utilization

Emerging feedstocks provide opportunities for diversifying the range of sustainable fuels and value-added products. Biomass and biorefinery residues represent renewable and carbonneutral resources that can be harnessed for bio-oils, syngas, and biochar through thermal processes like pyrolysis and gasification. Furthermore, the inclusion of composite materials such as biorefinery residue-reinforced WPCs and weathered WPCs expands the scope of feedstocks suitable for thermal processing, particularly by addressing end-of-life challenges for composite materials.

### • Advanced thermal processing technologies

Continued advancements in thermal processing technologies are critical to enhancing the efficiency and economic viability of these processes. Innovations in reactor design, such as fluidized beds and microwave-assisted pyrolysis, could improve the scalability and energy efficiency of converting these complex feedstocks. Integration of catalytic processes within thermal systems also offers opportunities to tailor the product slate towards high-value fuels and chemicals.

### • Integrated biorefinery approaches

The concept of integrated biorefineries can be extended to include thermal processing as a key component, enabling a circular economy approach. For instance, biorefinery residues can serve as inputs for thermal processing, while the derived biochar and syngas can be utilized within the biorefinery itself, minimizing waste and maximizing resource utilization. Similarly, weathered WPCs can be thermally converted to recover energy and materials, offsetting the environmental footprint of composite materials.

# Environmental and economic sustainability

Life cycle assessment (LCA) and techno-economic analysis (TEA) will play crucial roles in evaluating the sustainability of thermal processing pathways for these feedstocks. Improvements in processing efficiency, reduction in greenhouse gas emissions, and valorization of by-products will be essential to ensure these processes contribute positively to global sustainability goals. Additionally, policy frameworks and incentives promoting the use of renewable feedstocks and sustainable fuel production could accelerate the adoption of these technologies.

#### Challenges and research directions

Key challenges include the heterogeneity of feedstocks, process optimization for mixedmaterial systems, and handling of contaminants. Research should focus on developing robust pre-treatment technologies, optimizing process parameters, and exploring hybrid thermalchemical methods for improved product quality and yield. Additionally, studies on the longterm stability and performance of catalysts, especially in the presence of feedstock impurities, will be critical.

Another critical research direction involves examining the impact of varying wood filler, additive, and plastic ratios on balancing the mechanical properties of WPCs with their recyclability through pyrolysis. Current knowledge on the optimal composition of WPCs for both performance in use and efficiency in recycling is limited. Deepening our understanding in this area could lead to the formulation of WPCs designed with their end-of-life disposal and recycling in mind, promoting a circular economy approach.

The logistical aspects of applying pyrolysis to WPC waste, including the spatial and operational disconnect between WPC usage scenarios and recycling facilities, also necessitate a comprehensive techno-economic evaluation. This analysis should consider the costs associated with collecting, transporting, and storing WPC waste, as well as the economic feasibility of integrating catalysts into the WPC manufacturing process to enhance pyrolysis outcomes. Such catalysts could potentially lower the activation energy required for pyrolysis, making the process more energy-efficient and economically viable.

Advancements in the upgrading of pyrolysis products—transforming bio-oil into more refined fuels and chemicals, improving the quality of syngas, and finding valuable applications for the char—remain pivotal. Future research should explore the multi-phase upgrading processes for the liquid, gaseous, and solid products of pyrolysis. Investigating these pathways can lead to more sustainable and profitable recycling methods, contributing to the reduction of waste and the creation of value-added products.

The application of artificial intelligence (AI) and machine learning (ML) in predicting the outcomes of co-pyrolysis processes, including those involving different feedstocks, offers exciting possibilities. While AI has shown potential in optimizing pyrolysis conditions and predicting product yields for various feedstocks, its applicability to the unique context of different feedstocks requires thorough investigation. Research should focus on adapting AI models to account for the complexities of pyrolysis, such as WPC pyrolysis, including the effects of additives, the impact of WPC aging, and the optimal feedstock composition for recycling.

### Market development and industry adoption

The market for fuels and materials derived from these emerging feedstocks is likely to expand as industries seek sustainable alternatives. Collaboration among stakeholders, including feedstock suppliers, technology developers, and policymakers, will be vital to establish reliable supply chains and promote market confidence. Demonstration projects showcasing the feasibility and benefits of these technologies can further drive industry adoption.

# Societal and policy implications

The thermal processing of these feedstocks aligns with broader societal goals, such as waste reduction, renewable energy generation, and climate change mitigation. Policies supporting the circular economy, waste-to-energy initiatives, and renewable fuel standards can create an enabling environment for these technologies. Public awareness and acceptance of products derived from such processes will also be key to their success.

### 6.3 Implications of the current work

While this dissertation provides a comprehensive investigation into the pyrolytic valorisation of corn stalk biomass, biorefinery residues, and lignocellulose-based composites, several key implications arising from the current research should be highlighted to inform and guide future studies.

#### (1) Experimental constraints and scalability

The pyrolysis and co-pyrolysis experiments were conducted at laboratory scale using batch systems and limited sample quantities. Although this allowed for precise kinetic and mechanistic interpretation, scale-up effects such as heat and mass transfer limitations, secondary cracking, and gas-phase residence times were not captured. Future work should incorporate pilot-scale continuous reactors (e.g., fluidized-bed, auger, or microwave-assisted systems) to validate the observed kinetic trends under practical conditions and to assess process scalability and energy integration.

### (2) Simplified reaction environments

The co-pyrolysis systems studied here were nitrogen-purged and isolated, excluding the influence of reactive gases (e.g., steam, CO<sub>2</sub>) or catalytic bed effects. This simplification limits

direct extrapolation to industrial thermochemical systems. Future investigations could employ reactive atmospheres or co-feeding strategies (e.g., steam-assisted or CO<sub>2</sub>-assisted pyrolysis) to better simulate real reactor environments and enhance gas-phase reforming and tar conversion.

### (3) Limited catalyst characterization and optimization

Although the catalytic role of BA was demonstrated, its surface chemistry, mineral phase evolution, and recyclability were not exhaustively examined. The catalytic effect was found to be relatively weak ( $\Delta E \approx 3-5$  kJ/mol). Further studies should include systematic modification of BA, such as acid/base treatment or metal impregnation, and in situ spectroscopic analysis (e.g., XPS, TPR, DRIFTS) to elucidate the reaction pathways and identify active sites. Catalyst regeneration and deactivation behaviour under cyclic operation should also be explored.

#### (4) Feedstock variability and representativeness

The feedstocks (corn stalk tissues, EPR, RSPR) were collected from specific sources, and their composition may vary with harvest season, location, and industrial pretreatment. Such variability can affect reproducibility and comparability. Future research should employ multisource and statistically representative sampling, coupled with machine-learning-assisted compositional mapping, to develop more generalizable kinetic models across biomass-plastic matrices.

#### (5) Simplified product quantification

The Py-GC/MS analysis provided detailed qualitative identification of volatile species, but quantitative mass balance for gas, liquid, and solid fractions was not established. This limits insight into carbon conversion efficiency and product yield optimization. Future work should integrate online micro-GC and GC×GC–TOF–MS techniques or semi-continuous condensation systems to obtain complete yield distributions and correlate them with kinetic modelling.

#### (6) Machine learning model interpretability

Although RF and GBRT algorithms achieved high predictive accuracy ( $R^2 > 0.98$ ), these models function as black boxes, offering limited physical interpretability. Future studies should focus on physics-informed machine learning or hybrid data–kinetic modelling frameworks,

enabling interpretable feature analysis that links compositional variables and temperatureprogrammed reactivity to pyrolytic outcomes.

#### (7) Environmental durability and lifecycle implications

The weathering experiments provided valuable insights into aging effects on WPC pyrolysis; however, only accelerated laboratory weathering (xenon exposure) was conducted. Real environmental conditions involving UV—moisture—temperature cycling and microbial degradation are more complex. Long-term outdoor exposure tests and comparative life-cycle assessment (LCA) should be performed to evaluate the environmental resilience and end-of-life performance of WPCs more comprehensively.

### (8) Techno-economic and policy integration

The study primarily focused on the thermochemical and mechanistic aspects of copyrolysis. For practical deployment, techno-economic analysis (TEA), supply-chain modelling, and policy alignment with renewable energy frameworks are necessary. Integrating these with environmental metrics (carbon footprint, emission offset potential) will provide a holistic assessment of feasibility and sustainability.

Addressing these limitations through multi-scale experimentation, advanced characterization, and integrative modelling will refine the understanding of biomass—plastic—residue interactions and accelerate the design of efficient, scalable, and sustainable pyrolysis systems. Future research should emphasize reactor-level optimization, data-driven process control, and circular-economy integration, ensuring that the scientific advances achieved in this work are translated into practical and impactful applications.

This work has addressed a series of fundamental and applied challenges in the pyrolytic valorisation of agricultural biomass, biorefinery residues, and lignocellulose-based composites, establishing a coherent framework that bridges material characterisation, reaction mechanisms, catalytic pathways, and process optimisation. Collectively, the outcomes not only deepen our understanding of thermochemical conversion behaviours, but also open new avenues for designing carbon-neutral, resource-efficient, and industrially scalable pyrolysis strategies. By demonstrating how integrated experimentation, modelling, and mechanistic insights can drive innovation, this dissertation lays a solid foundation for future research and technological deployment in sustainable materials management and renewable energy production. The

findings presented here therefore represent a meaningful step towards advancing circular bioeconomy pathways and inspiring continued progress in the field.

### **Appendix 1. Proximate Analysis**

The proximate analysis of the samples was performed to determine the moisture, ash, volatile matter, and fixed carbon contents following standard procedures. The samples used for the analysis were ground to a particle size below 0.2 mm.

#### (1) Moisture Content Determination

Approximately  $1.0 \pm 0.1$  g of sample (< 0.2 mm) was accurately weighed (to  $\pm$  0.0002 g) into a pre-dried and pre-weighed weighing bottle. The sample was evenly spread inside the bottle and placed, with the lid removed, in a forced-air drying oven preheated to 105-110 °C. Drying was maintained for 2 h.

After drying, the bottle was immediately covered, transferred to a desiccator, cooled to room temperature, and reweighed. The moisture content  $(M_{ad}, \%)$  was calculated from the loss in mass according to:

$$M_{ad} = \frac{m_1 - m_2}{m_1} \times 100$$

Where  $m_1$  is the mass of sample before drying (g) and  $m_2$  is the mass of sample after drying (g).

# (2) Ash Content Determination

Approximately  $1.0 \pm 0.1$  g of the sample (< 0.2 mm, weighed to  $\pm$  0.0002 g) was placed evenly in a pre-ignited crucible such that the mass did not exceed 0.15 g/cm<sup>-2</sup>. The crucible was placed in a muffle furnace maintained below 100 °C and heated gradually to 500 °C over at least 30 min with the furnace door slightly open (~15 mm gap). The temperature was then raised to (815  $\pm$  10) °C and maintained for 1 h.

After ashing, the crucible was removed, cooled on a heat-resistant or asbestos board in air for about 5 min, transferred to a desiccator, cooled to room temperature, and reweighed. The ash content  $(A_{ad}, \%)$  was calculated from the mass of the residue relative to the original sample:

$$A_{ad} = \frac{m_3}{m_1} \times 100$$

Where  $m_3$  is the mass of ash residue (g).

#### (3) Volatile Matter Determination

Approximately  $1.0 \pm 0.01$  g of the sample (< 0.2 mm) was accurately weighed (to  $\pm$  0.0002 g) into a covered porcelain crucible that had been previously ignited to constant weight at 900 °C. The sample was lightly tapped to form an even layer, covered with the lid, and placed on a crucible stand. The stand was then quickly introduced into the isothermal zone of a

preheated muffle furnace at 920 °C. The furnace door was immediately closed and heating continued for exactly 7 min. The furnace temperature was required to return to  $(900 \pm 10)$  °C within 3 min of sample insertion and remain within this range for the remainder of the heating period; otherwise, the test was considered invalid.

After 7 min, the crucible was removed, cooled in air for 5 min, then transferred to a desiccator and weighed after reaching room temperature. The volatile matter content ( $V_{ad}$ , %) was calculated as the mass loss (excluding moisture) relative to the air-dried sample:

$$V_{ad} = \left(\frac{m_1 - m_4}{m_1}\right) \times 100 - M_{ad}$$

Where m<sub>4</sub> is the mass of sample after heating (g).

# (4) Fixed Carbon Calculation

The fixed carbon content of the sample on an air-dried basis (FC<sub>ad</sub>, %) was obtained by mass balance according to Equation below:

$$FC_{ad} = 100 - (M_{ad} + V_{ad} + A_{ad})$$

#### Appendix 2. Ultimate analysis

The elemental composition of the samples, including C, H, O, N and S was determined using an elemental analyser (Elementar Vario EL, Germany) based on the high-temperature combustion method. This technique quantifies the major organic elements by complete oxidation, gas separation, and thermal conductivity detection. Each analysis required approximately 9 minutes per sample.

# (1) Principle of measurement

In the CHNS mode, the sample is completely combusted at 1150 °C in an oxidation tube under a pure oxygen atmosphere, generating gaseous products including CO<sub>2</sub>, H<sub>2</sub>O, NO<sub>X</sub>, SO<sub>2</sub>, and SO<sub>3</sub>. These gases then pass through a reduction tube maintained at 850 °C containing reduced copper, where nitrogen oxides are reduced to N<sub>2</sub> and sulfur oxides to SO<sub>2</sub>. The resulting mixture of CO<sub>2</sub>, H<sub>2</sub>O, N<sub>2</sub>, and SO<sub>2</sub> is subsequently separated by a temperature-programmed desorption (TPD) adsorption column and detected using a thermal conductivity detector (TCD), yielding the elemental contents of C, H, N, and S.

# (2) TPD and Detection sequence

During the TPD process, at near-ambient temperature, CO<sub>2</sub>, H<sub>2</sub>O, and SO<sub>2</sub> are adsorbed on the column material, while N<sub>2</sub> passes directly through to the TCD and is detected first as the nitrogen peak. As the column temperature increases, the adsorbed gases are sequentially desorbed and detected: H<sub>2</sub>O at approximately 60 °C, CO<sub>2</sub> at approximately 140 °C, and SO<sub>2</sub> at approximately 220 °C. Each desorbed component produces a characteristic TCD signal corresponding to H, C, and S contents, respectively. The integrated peak areas are automatically converted into mass percentages via the instrument's calibration curves.

# (3) Determination of Oxygen Content

The oxygen content (O, %) was calculated by difference according to the following relationship:

$$0 = 100 - (C + H + N + S)$$

That is, the analyser operated in CHNS mode, and oxygen was obtained by subtraction of the measured C, H, N, and S percentages from 100%. This indirect approach provides reliable results for solid organic materials where direct oxygen determination (O-mode) is unnecessary or less accurate.

#### Appendix 3. Biochemical analyses

The biochemical composition—cellulose, hemicellulose, and lignin—was determined following the National Renewable Energy Laboratory (NREL) protocol [161]. Samples are (i) solvent-extracted to remove extractives, (ii) depolymerised by two-step acid hydrolysis (72% H, then 4% H<sub>2</sub>SO<sub>4</sub>) to release monosugars quantified by HPLC, while acid-insoluble lignin is obtained gravimetrically with ash correction.

# (1) Reagents, Standards, and Equipment:

Acids/alkali: 72% H<sub>2</sub>SO<sub>4</sub> and 4% H<sub>2</sub>SO<sub>4</sub>; NaOH for neutralisation.

Sugars: glucose, xylose, arabinose; cellobiose may be used where needed for system checks.

HPLC: Aminex HPX-87H column with guard, RI detector, 0.005 mol/L H<sub>2</sub>SO<sub>4</sub> mobile phase, 0.6 mL/min, 65 °C, injection 20 μL.

Autoclave: 121 °C for dilute-acid stage.

Certified monosugar standards; preparation of sugar-recovery solutions for correction during 4% acid/121 °C treatment.

### (2) Sample Preparation:

Air-dry, mill, and sieve to 40–60 mesh; dry at 105 °C before analysis. Typical test portion  $\sim 0.5$  g (robust window 0.3–0.7 g).

### (3) Procedure:

- 1. Removal of extractives (Soxhlet): extract  $\sim$ 0.5 g sample with ethanol at  $\sim$ 95 °C to remove lipids/pigments; air-dry. This step reduces matrix effects and protects the HPLC column.
- 2. Concentrated-acid hydrolysis (72% H<sub>2</sub>SO<sub>4</sub>): add 3.00 mL 72% H<sub>2</sub>SO<sub>4</sub> to the sample (~0.5 g) in a tube, mix, and incubate 30 °C for 1 h to depolymerise cellulose/hemicellulose to oligomers/monosugars.
- 3. Dilute-acid hydrolysis (4%  $H_2SO_4$ ): quantitatively transfer to a flask and dilute to 4%  $H_2SO_4$  (total water  $\approx$ 84 mL); autoclave 121 °C for 45 min to convert oligomers to monosugars. Run a sugar-recovery standard in parallel to correct degradation during this stage.
- 4. Neutralisation and HPLC analysis: adjust an aliquot to pH  $\approx$ 2 with 8% NaOH, dilute to volume, and analyse by HPLC under the conditions above. Use recovery-corrected peak areas for quantitation of glucose (cellulose proxy) and xylose + arabinose (hemicellulose proxy).
- 5. Acid-insoluble lignin and ash correction: filter the hydrolysis solids, wash to neutral, dry at 105 °C and weigh; ash at 550 °C and reweigh. Acid-insoluble lignin = (dry residue ash).
- 6. Acid-soluble lignin: quantify UV absorbance of the filtrate and add to total lignin.

#### (4) Calculations

Let  $m_0$  be the initial test mass, V the analysis volume, and apply recovery-corrected sugar concentrations.

Cellulose (wt%) = 
$$0.90 \times \frac{\text{[Glucose]} \times V}{m_0} \times 100$$

Hemicellulose (wt%) =  $0.88 \times \frac{([\text{Xylose}] + [\text{Arabinose}]) \times V}{m_0} \times 100$  (stoichiometric factors convert monosugars to anhydrous polymer basis).

Acid-insoluble lignin (wt%) = 
$$\frac{m_{\text{dry residue}} - m_{\text{ash}}}{m_0} \times 100$$

Appendix 4. The pyrolytic products from the co-pyrolysis of corn stalk tissues and HDPE. (Chapter 2)

Table S1 The pyrolytic products from the co-pyrolysis of corn stalk tissues and HDPE.

	Compounds	Formula	Area Pct (%					
R.T. (min)			Leaf/HDP E	Cob/HDPE	Ear/HDPE	Husk/HDPE	Stem/HDPE	Туре
0.321	Pyrazole, 1,4-dimethyl-	$C_5H_8N_2$	0.4872	N.D.	N.D.	N.D.	N.D.	Others
0.6572	2-Butanone	$C_4H_8O$	0.1007	N.D.	N.D.	N.D.	N.D.	Ketone
0.7661	2-Propanone, 1-(acetyloxy)-	$C_5H_8O_3$	0.568	N.D.	N.D.	0.4785	N.D.	Ketone
1.1032	Bicyclo[4.2.0]°Cta-1,3,5-triene	$C_8H_8$	0.3198	N.D.	N.D.	N.D.	N.D.	Alkene
1.1367	1,3-Butadiene	$C_4H_6$	19.9765	15.7914	18.01	20.3274	15.4042	Alkene
1.1405	Methylenecyclopropane	$C_4H_6$	N.D.	N.D.	N.D.	6.0147	7.5048	Alkane
1.2709	Acetic acid	$C_2H_4O_2$	N.D.	N.D.	5.3332	2.0089	N.D.	Acid
1.2759	Cyclohexan-1,4,5-triol-3-one-1-carboxylic acid	$C_7H_{10}O_3$	2.6474	N.D.	N.D.	N.D.	4.5796	Acid
1.3464	Tetrahydrofuran	$C_4H_8O$	N.D.	4.9983	3.4643	2.4762	6.1607	Furan
1.4541	Benzene	$C_6H_6$	N.D.	12.0869	5.9388	4.4168	6.715	Benzene
1.5437	1,3,6-Triox°Cane	$C_5H_{10}O_3$	N.D.	N.D.	N.D.	0.5791	N.D.	Oxygenates
1.5805	2H-Pyran, 3,4-dihydro-	$C_5H_8O$	0.1286	N.D.	N.D.	N.D.	N.D.	Oxygenates
1.7127	2-Cyclopenten-1-one, 2-hydroxy-	$C_5H_6O_2$	0.4406	N.D.	N.D.	N.D.	N.D.	Ketone
1.7611	1-Butanamine, N-methyl-N-nitroso-	$C_5H_{12}N_2O$	N.D.	N.D.	1.9102	0.5076	N.D.	others
1.8029	O-Methylisourea	$C_2H_6N_2O$	N.D.	N.D.	N.D.	N.D.	1.2936	Acid
1.8428	Propanoic acid, 2-oxo-, methyl ester	$C_4H_6O_3$	N.D.	N.D.	N.D.	1.4998	N.D.	Ester
1.8518	3-Amino-2-oxazolidinone	$C_3H_6N_2O_2$	N.D.	N.D.	3.0231	N.D.	N.D.	Ketone
1.8396	Succindialdehyde	$C_4H_6O_2$	N.D.	3.0027	N.D.	N.D.	N.D.	Aldehyde

2.1642	3-Furaldehyde	C <sub>5</sub> H <sub>4</sub> O <sub>2</sub>	N.D.	N.D.	N.D.	0.5029	N.D.	Aldehyde
2.172	Pyrazole, 1,4-dimethyl-	$C_5H_8N_2$	N.D.	0.8645	N.D.	N.D.	N.D.	others
2.1825	1H-Pyrazole, 1,3-dimethyl-	$C_5H_8N_2$	N.D.	N.D.	1.0589	N.D.	N.D.	others
2.3386	2,3-Epoxybutane	$C_4H_8O$	N.D.	0.9422	N.D.	N.D.	N.D.	Oxygenates
2.3493	3-Aminopyrrolidine	$C_4 H_{10} N_2$	N.D.	N.D.	1.177	0.3133	N.D.	others
2.4877	7-Oxabicyclo [4.1.0] heptane, 3-methyl-	$C_7H_{12}O$	0.1927	N.D.	N.D.	N.D.	N.D.	Oxygenates
2.5476	Methyl[2-(1-methylpyrazol-4-yl)ethyl]amine	$C_4H_7N_3$	N.D.	N.D.	0.6996	N.D.	N.D.	Others
2.5495	Cathinone	$C_9H_{10}NO$	N.D.	0.3719	N.D.	N.D.	N.D.	Others
2.5539	Benzonitrile	$C_7H_5N$	0.7752	N.D.	N.D.	N.D.	N.D.	Others
2.7061	Phenol	$C_6H_6O$	1.1993	0.7637	N.D.	N.D.	N.D.	Phenol
2.8637	Cyclohexanone	$C_6H_{10}O$	N.D.	N.D.	2.1198	0.746	N.D.	Ketone
3.1039	Urea, N,N'-bis(1-methylethyl)	$C_7H_{16}N_2O$	N.D.	N.D.	0.3069	N.D.	N.D.	Others
3.1853	Benzaldehyde	$C_7H_6O$	0.7353	0.5607	0.9131	0.4989	N.D.	Aldehyde
3.3059	7-Oxabicyclo [4.1.0] heptane, 2-methylene-	$C_7H_{12}O_2$	0.106	N.D.	N.D.	N.D.	N.D.	Oxygenates
3.3703	Benzaldehyde, 2-hydroxy-	$C_7H_6O_2$	0.1268	N.D.	N.D.	N.D.	N.D.	Aldehyde
3.5204	N,N-Diamylmethylamine	$C_{11}H_{25}N$	N.D.	N.D.	N.D.	0.5669	N.D.	Others
3.5416	Sydnone, 3,4-dimethyl-	$C_8H_{12}N_2O_2$	N.D.	N.D.	1.3031	N.D.	N.D.	Others
3.704	Acetophenone	$C_8H_8O$	0.311	0.3943	0.5816	0.2924	N.D.	Ketone
3.8295	1,2-Cyclopentanedione, 3-methyl-	$C_6H_8O_2$	0.2835	0.1919	N.D.	0.1631	N.D.	Ketone
3.8449	2-Cyclopenten-1-one, 2-hydroxy-3-methyl-	$C_6H_8O_2$	N.D.	N.D.	0.8647	N.D.	N.D.	Ketone
3.8907	Amphetamine	$C_9H_{13}N$	N.D.	0.2028	N.D.	N.D.	N.D.	Others
3.8935	1-Undecene	$C_{11}H_{22}$	0.2128	N.D.	N.D.	N.D.	N.D.	Alkene
4.2029	3-Ethoxyamphetamine	$C_{11}H_{17}NO$	0.3424	N.D.	N.D.	0.1967	N.D.	Others
4.4635	Benzoic acid, methyl ester	$C_8H_8O_2$	1.2251	0.6672	0.9218	0.5394	N.D.	Ester
4.5912	2-Heptanamine, 5-methyl-	$C_8H_{19}N$	N.D.	N.D.	0.5471	N.D.	N.D.	Others
5.1672	Cyclododecane	$C_{12}H_{24}$	0.3062	N.D.	N.D.	N.D.	N.D.	Alkane

5.5865	Benzoic acid	$C_7H_6O_2$	24.5539	14.8395	10.3465	20.1597	18.14	Acid
5.9432	Benzofuran, 2,3-dihydro-	$C_8H_8O$	N.D.	1.3456	3.8404	N.D.	N.D.	Furan
6.0422	N-Methyl-N-benzyl-4-oxo-4-phenyl-	C <sub>14</sub> H <sub>15</sub> NO	N.D.	N.D.	N.D.	N.D.	2.0834	Others
0.0422	butyramide	C141115110	N.D.	N.D.	N.D.	N.D.	2.0054	Onicis
6.1363	Cathinone	$C_9H_{10}NO$	N.D.	1.0195	N.D.	N.D.	N.D.	Others
6.2834	Tenamfetamine	$C_{10}H_{13}NO_2\\$	N.D.	0.3896	N.D.	0.1381	N.D.	Others
6.3117	1-Tridecene	$C_{13}H_{26}$	0.3561	N.D.	N.D.	N.D.	N.D.	Alkene
6.4121	Benzeneethanamine4-methoxyalphamethyl-	$C_{10}H_{15}NO\\$	N.D.	0.2389	N.D.	N.D.	N.D.	Others
6.4136	Phenylephrine	$C_9H_{13}NO_2$	N.D.	N.D.	0.4364	N.D.	0.7953	Others
6.5408	3-Hydroxy-N-methylphenethylamine	$C_9H_{14}NO$	N.D.	0.3162	N.D.	N.D.	N.D.	Others
6.7216	2-Methoxy-4-vinylphenol	$C_9H_{10}O_2$	1.5161	1.6707	3.0895	1.0631	0.9502	Phenol
7.0979	Benzoic acid, phenyl ester	$C_{13}H_{10}O_2$	2.5893	N.D.	N.D.	N.D.	N.D.	ester
7.1375	Crotonic acid, 2-benzamido-, methyl ester	$C_{13}H_{15}NO_4\\$	N.D.	N.D.	1.2829	N.D.	N.D.	Others
7.1446	N-Methylbenzamide, N-pentafluoropropionyl-	$C_{14}H_{11}N_3O$	N.D.	N.D.	N.D.	2.9546	2.283	Others
7.1440	N-Methyloenzamide, N-pentandoropropionyi-	2	N.D.	N.D.	N.D.	2.9540	2.203	Others
7.2199	Phenol, 2,6-dimethoxy-	$C_8H_{10}O_3$	N.D.	N.D.	0.6713	N.D.	N.D.	Phenol
7.2888	Butyl benzoate	$C_{11}H_{14}O_2$	0.6473	0.4847	N.D.	0.1981	N.D.	Ester
7.3288	2-Amino-1-(o-methoxyphenyl)propane	$C_{10}H_{15}NO$	N.D.	N.D.	0.2541	0.3065	N.D.	Others
7.3895	Biphenyl	$C_{12}H_{10}$	1.7802	1.594	0.9359	0.7537	0.6059	Benzene
7.7932	Vanillin	$C_8H_8O_3$	0.3952	N.D.	N.D.	N.D.	N.D.	Aldehyde
7.91	Diphenylmethane	$C_{13}H_{12}$	0.5275	0.2134	N.D.	0.4008	N.D.	Alkane
7.9521	3,5-Dimethoxyamphetamine	$C_{11}H_{17}NO_2\\$	N.D.	N.D.	0.7787	N.D.	N.D.	Others
8.158	Benzoic acid, hydrazide	$C_7H_8N_2O$	1.0998	0.2805	N.D.	0.3626	N.D.	Others
8.1869	2,4-Dimethylamphetamine	$C_{11}H_{17}N$	N.D.	N.D.	0.6051	N.D.	N.D.	Others
8.3232	p-Toluic acid, allyl ester	$C_{11}H_{12}O_2$	N.D.	N.D.	N.D.	0.1523	N.D.	ester
8.3613	1-Pentadecene	$C_{15}H_{30}$	0.2531	N.D.	N.D.	N.D.	N.D.	Alkene

8.5291	1,1'-Biphenyl, 4-methyl-	$C_{13}H_{12}$	0.2676	N.D.	N.D.	N.D.	N.D.	Benzene
8.6057	1,4-Benzenedicarboxylic acid, dimethyl ester	$C_{10}H_{10}O_4$	5.1725	N.D.	0.4356	0.8795	N.D.	Ester
8.7901	Dibenzofuran	$C_{12}H_8O$	0.3468	N.D.	N.D.	N.D.	N.D.	Furan
8.9628	1H-Pyrrole, 2-ethyl-3,4,5-trimethyl-	$C_9H_{15}N$	0.7029	N.D.	N.D.	N.D.	N.D.	Others
9.0322	2-n-Propyladamantane	$C_{13}H_{22}$	N.D.	N.D.	N.D.	0.1543	N.D.	Alkane
9.2326	Phenol, 4-ethenyl-2,6-dimethoxy-	$C_{10}H_{14}O_3$	1.1592	N.D.	0.5748	N.D.	N.D.	Phenol
9.2717	2,5-Dimethoxy-4-ethylamphetamine	$C_{13}H_{21}NO_2\\$	N.D.	0.3251	N.D.	N.D.	N.D.	Others
9.4107	4-Vinylbenzoic acid	$C_9H_8O_2$	0.2675	N.D.	N.D.	N.D.	N.D.	Acid
9.4519	Benzene, 1,1'-(diazomethylene)bis-	$C_{13}H_{10}N_2$	N.D.	N.D.	N.D.	0.1641	N.D.	Others
9.6019	T°Cainide	$C_{10}H_{14}N_2O$	N.D.	N.D.	0.2313	N.D.	N.D.	Others
9.7257	2-Acetylbenzoic acid	$C_9H_8O_3$	N.D.	N.D.	N.D.	0.3085	N.D.	Acid
9.7506	1-Hexadecanamine, N-methyl-	$C_{17}H_{37}N$	N.D.	0.1961	N.D.	N.D.	N.D.	Others
9.8138	Benzophenone	$C_{13}H_{10}O$	1.2813	0.5767	0.3488	0.6182	N.D.	Ketone
9.9502	n-Propyl benzoate	$C_{10}H_{12}O_2$	N.D.	N.D.	N.D.	0.2004	N.D.	Ester
9.9565	3-Methoxyamphetamine	$C_{10}H_{15}NO$	N.D.	0.1945	N.D.	N.D.	N.D.	others
10.2103	Benzoic acid, pent-2-yl ester	$C_{17}H_{26}O_2$	1.068	N.D.	N.D.	N.D.	N.D.	Ester
10.2758	n-Propyl benzoate	$C_{10}H_{12}O_2$	N.D.	N.D.	N.D.	0.4793	N.D.	Ester
10.325	Bicyclohexyl	$C_{12}H_{22}$	0.5111	N.D.	N.D.	N.D.	N.D.	Alkane
10.4392	(E)-2,6-Dimethoxy-4-(prop-1-en-1-yl)phenol	$C_{11}H_{14}O_3$	N.D.	N.D.	0.633	0.1016	N.D.	Phenol
10.452	2(1H)-Naphthalenone, 3,4,4a,5,6,7-hexahydro- 4a-[(methylamino)methyl]-, ethylene acetal	C <sub>15</sub> H <sub>22</sub> O	N.D.	0.2672	N.D.	N.D.	N.D.	Ketone
10.4991	1-Tetradecene	$C_{14}H_{28}$	0.8762	N.D.	N.D.	N.D.	N.D.	Alkene
10.573	Butyrophenone, 2',3,4',6'-tetramethyl-	$C_{13}H_{18}O$	0.3246	N.D.	N.D.	N.D.	N.D.	Ketone
10.5741	Acetic acid, (1-methyl-1H-indol-3-yl) ester	$C_{11}H_{11}NO_2$	N.D.	N.D.	N.D.	0.1537	N.D.	Others
10.5892	4-Methoxyamphetamine, N-acetyl	$C_{12}H_{17}NO_2$	N.D.	0.1602	N.D.	N.D.	N.D.	Others

10.6498	Propylparaben	$C_{10}H_{12}O_3$	0.3288	N.D.	N.D.	N.D.	N.D.	Ester
10.7182	Mesitylglyoxylic acid	$C_{11}H_{12}O_3$	0.4692	N.D.	N.D.	N.D.	N.D.	Acid
10.7229	N-[(2-Phenyl-1,3-dioxolan-2-yl)methylidene]hydroxylamine	C <sub>23</sub> H <sub>25</sub> NO <sub>3</sub>	N.D.	N.D.	N.D.	0.1486	N.D.	Others
10.8153	3,4-Pyridinedicarboxylic anhydride	$C_7H_3NO_3$	N.D.	0.1446	N.D.	N.D.	N.D.	Others
10.8266	2-Amino-1-(o-hydroxyphenyl)propane	$C_9H_{13}NO$	N.D.	N.D.	0.106	N.D.	N.D.	Others
10.84	9H-Fluoren-9-one	$C_{13}H_8O$	0.8318	N.D.	N.D.	N.D.	N.D.	Ketone
10.9051	Terephthalic acid, isobutyl methyl ester	$C_{13}H_{16}O_4$	N.D.	0.9353	N.D.	0.7443	N.D.	ester
11.0714	N-methylalpha.methyl-3,4- methylenedioxyphenethylamine	C <sub>9</sub> H <sub>11</sub> NO <sub>2</sub>	N.D.	N.D.	0.1734	0.3254	N.D.	others
11.0946	Benzenebutanenitrile, 4-ethoxy gamma oxo-	$C_{13}H_{16}O_3$	0.7057	N.D.	N.D.	0.1998	N.D.	oxygenates
11.1461	2-Hydroxy-1-isoindolinone	$C_{12}H_{15}NO_2$	0.3698	N.D.	N.D.	N.D.	N.D.	Ketone
11.1515	1,2-Benzenedicarboxylic acid, 2-butoxyethyl butyl ester	$C_{20}H_{30}O_{6}$	N.D.	N.D.	N.D.	0.1212	N.D.	Ester
11.2286	4-(3-Aminobutyl)-2-methoxyphenol	$C_{11}H_{17}NO_2$	N.D.	N.D.	0.1931	N.D.	N.D.	others
11.3899	1,2-Benzenediol, 4-[2-(methylamino)ethyl]-	$C_9H_{13}NO_2$	N.D.	N.D.	0.0716	N.D.	0.484	Others
11.394	Neophytadiene	$C_{20}H_{38}$	0.5224	N.D.	N.D.	N.D.	N.D.	Alkene
11.44	Isophthalic acid	$C_8H_6O_4$	N.D.	N.D.	N.D.	0.2747	N.D.	Acid
11.4615	2-Pentadecanone, 6,10,14-trimethyl-	$C_{18}H_{36}O$	0.504	N.D.	N.D.	N.D.	N.D.	Ketone
11.5496	Diamyl phthalate	$C_{18}H_{26}O_4$	N.D.	N.D.	N.D.	N.D.	12.7186	Ester
11.5606	Phthalic acid, 2-ethylbutyl propyl ester	$C_{20}H_{30}O_4$	N.D.	N.D.	6.0776	N.D.	N.D.	Ester
11.5974	1,2-Benzenedicarboxylic acid, diheptyl ester	$C_{22}H_{34}O_4$	N.D.	0.836	N.D.	N.D.	N.D.	Ester
11.9565	Acetamide, N-methyl-N- [methyl(isopropyl)phosphinatomethyl]-		N.D.	0.2311	N.D.	N.D.	N.D.	Acid
12.416	1,2-Benzenedicarboxylic acid, monobutyl ester	$C_{12}H_{14}O_4$	0.3884	N.D.	N.D.	0.5155	N.D.	Ester

12.4985	°Ctodrine	$C_8H_{19}N$	N.D.	0.1497	N.D.	N.D.	N.D.	Others
12.5588	n-Hexadecanoic acid	$C_{16}H_{32}O_2$	2.7255	0.5119	1.377	2.1425	1.6589	Acid
12.6379	1,2-Benzenedicarboxylic acid, monobutyl ester	$C_{12}H_{14}O_4$	1.1686	N.D.	N.D.	N.D.	N.D.	Ester
12.7928	Terephthalic acid, di(but-3-enyl) ester	$C_{16}H_{18}O_4$	N.D.	N.D.	N.D.	N.D.	4.7448	Ester
12.8228	Terephthalic acid, dicyclobutyl ester	$C_{17}H_{20}O_4$	N.D.	N.D.	N.D.	3.8835	N.D.	Ester
12.8478	Terephthalic acid, di(but-2-enyl) ester	$C_{16}H_{18}O_4$	3.2316	7.9128	4.006	3.9629	5.3901	Ester
12.9861	Isophthalic acid, di(2-methylprop-2-en-1-yl) ester	$C_{16}H_{18}O_4$	3.2427	N.D.	N.D.	N.D.	N.D.	Ester
13.0765	Isophthalic acid, butyl 4-formylphenyl ester	$C_{21}H_{27}NO_6$	N.D.	N.D.	N.D.	N.D.	0.3825	Others
13.0798	Butanedinitrile, 2,3-dimethyl-	$C_6H_8N_2$	N.D.	N.D.	0.1922	N.D.	N.D.	Others
13.0822	Isophthalic acid, 2-formylphenyl isobutyl ester	$C_{19}H_{18}O$	N.D.	0.335	N.D.	N.D.	N.D.	Ester
13.0908	Terephthalic acid, isobutyl phenyl ester	$C_{18}H_{18}O_3$	N.D.	N.D.	N.D.	0.4328	N.D.	Ester
13.2966	Phthalic acid, isoporpyl propyl ester	$C_{14}H_{18}O_4$	N.D.	N.D.	N.D.	0.1147	N.D.	ester
13.2992	4-Acetylbenzoic acid	$C_9H_8O_3$	1.1795	N.D.	N.D.	0.3375	N.D.	Acid
13.5045	1,2-Benzenedicarboxylic acid, bis(1-methylethyl) ester	$C_{13}H_{16}O_4$	N.D.	N.D.	N.D.	0.25	N.D.	Ester
13.5195	dl-Alanyl-dl-phenylalanine	$C_{12}H_{16}N_2O$	N.D.	0.1669	N.D.	N.D.	N.D.	Acid
13.5477	Diethyl Phthalate	$C_{12}H_{14}O_4$	0.5081	N.D.	N.D.	0.0957	N.D.	Ester
13.6603	Isophthalic acid, heptyl 2-methylprop-2-en-1-yl ester	C <sub>20</sub> H <sub>28</sub> O <sub>4</sub>	N.D.	0.2782	N.D.	N.D.	N.D.	ester
13.686	Pterin-6-carboxylic acid	$C_7H_5N_5O_3$	N.D.	N.D.	N.D.	0.3842	N.D.	others
13.7644	Diethyl Phthalate	$C_{12}H_{14}O_4$	1.1012	N.D.	N.D.	0.0827	N.D.	ester
13.8306	N-Methyl-3-(2-methylphenoxy)-3- phenylpropan-1-amine	C <sub>17</sub> H <sub>21</sub> NO	N.D.	N.D.	0.326	N.D.	N.D.	others
13.8602	9H-Fluorene, 9-phenyl-	$C_{19}H_{14}$	N.D.	0.6975	N.D.	N.D.	N.D.	Hydr°Carbon

13.8913	°Ctadecanoic acid	$C_{18}H_{36}O_2$	1.4275	N.D.	N.D.	1.3159	N.D.	Acid
140510	Propenone, 1-(adamantan-1-yl)-3-(1,5-	$C_{18}$	0.2500	N.D.	N.D.	N.D.	N.D.	0.1
14.0518	dimethyl-1H-pyrazol-4-yl)-	$H_{24}N_2O$	0.2708	N.D.	N.D.	N.D.	N.D.	Others
14.1854	p-Terphenyl	$C_{18}H_{14}$	0.5885	N.D.	N.D.	0.1524	N.D.	Benzene
14.4216	Terephthalic monohydroxamic acid	$C_8H_7O_3N$	0.173	N.D.	N.D.	1.2008	N.D.	Others
14.6583	3',4'-Formoxylidide	$C_9H_{11}NO$	0.3116	N.D.	N.D.	N.D.	N.D.	Others
14.9444	1H-1,2,3-Triazole-5-methanol, 1-(4-amino-1,2,5-oxadiazol-3-yl)-	$C_5H_6N_6O_2$	N.D.	N.D.	N.D.	N.D.	0.9045	others
14.9449	3-Oxabicyclo[3.2.0]heptane-2,4-dione, cis-	$C_6H_{10}O_3$	N.D.	0.7264	N.D.	0.4023	0.9486	Ketone
14.9451	Benzoic acid, 2-(1-oxopropyl)-	$C_{10}H_9O_3$	N.D.	N.D.	0.2324	N.D.	N.D.	Acid
14.9625	Cyclobutanecarbonitrile	$C_5H_7N$	0.7532	N.D.	N.D.	N.D.	N.D.	others
15.2718	Ethaneperoxoic acid, 1-cyano-1-[2-(2-phenyl-1,3-dioxolan-2-yl)ethyl]pentyl ester	C <sub>19</sub> H <sub>25</sub> NO <sub>5</sub>	N.D.	N.D.	N.D.	0.6454	N.D.	Others
15.2906	Di-sec-butyl phthalate	$C_{16}H_{22}O_4$	0.5423	N.D.	N.D.	N.D.	N.D.	Ester
15.325	2-((Pent-4-enyloxy)carbonyl)benzoic acid	$C_{13}H_{14}O_4$	N.D.	0.665	N.D.	N.D.	N.D.	Acid
15.4393	Diethyl Phthalate	$C_{12}H_{14}O_4$	0.2876	N.D.	0.325	0.1698	N.D.	Ester
15.5236	Indole, 3-benzoyl-	$C_{15}H_{11}NO$	N.D.	0.5091	N.D.	N.D.	N.D.	Others
15.5355	2-Acetylbenzoic acid	$C_9H_8O_3$	0.2117	N.D.	N.D.	0.311	N.D.	Acid
15.5957	1,4-Butanediol, dibenzoate	$C_{18}H_{18}O_4$	N.D.	1.3495	N.D.	2.3965	N.D.	Ester
15.598	.betaBenzilmonoxime	$C_{14}H_{11}NO_2\\$	N.D.	N.D.	0.3311	N.D.	0.7204	Others
15.6139	N-Benzoyl betaalanine	$C_{10}H_{12}N_2O$	0.4262	N.D.	N.D.	N.D.	N.D.	Others
15.9006	Phenylpropanamide	$C_9H_{11}NO$	0.1491	N.D.	N.D.	N.D.	N.D.	Others
15.9522	Benzoic acid, 2-(3-nitrophenyl)ethyl ester	$C_{18}H_{18}NO_3\\$	N.D.	N.D.	N.D.	0.1998	N.D.	Others
16.0416	Benzoic acid, 4-(1-azepinyl)azo-, ethyl ester	$C_{15}H_{21}N_3O$	0.0579	N.D.	N.D.	0.1789	N.D.	Others

16.5228	2H-1,4-Benzoxazin-3(4H)-one, 4-hydroxy-2,6-dimethyl-	C <sub>10</sub> H <sub>11</sub> NO <sub>3</sub>	N.D.	0.1336	N.D.	N.D.	N.D.	Others
16.538	Benzaldehyde, 4-(dimethylamino)-	C <sub>9</sub> H <sub>11</sub> NO	0.1105	N.D.	N.D.	0.2095	N.D.	Others
17.3584	MDMA methylene homolog	$C_{12}H_{17}NO_2$	N.D.	0.1115	0.0494	N.D.	N.D.	Others
17.876	2-((But-3-enyloxy)carbonyl)benzoic acid	$C_{13}H_{16}O_4$	N.D.	N.D.	1.7677	0.3182	N.D.	Acid
17.9005	cis,trans-5,9-Cyclododecadiene-cis-1,2-diol	$C_{12}H_{20}O_2$	N.D.	1.4748	N.D.	N.D.	N.D.	Alcohol
17.9921	3-(Cyclohex-3-enyl)prop-2-enoic acid	$C_9H_{14}O_2$	N.D.	N.D.	2.795	N.D.	N.D.	Acid
17.9965	But-3-enyl isobutyl carbonate	$C_{13}H_{25}O_3$	N.D.	N.D.	N.D.	0.4017	N.D.	ester
18.4311	Phthalic acid, 3-methylbenzyl ethyl ester	$C_{14}H_{18}O_6$	N.D.	N.D.	1.3407	N.D.	N.D.	ester
18.4749	Phthalic acid, decyl 2,7-dimethyl°Ct-7-en-5-yn-4-yl ester	C <sub>28</sub> H <sub>41</sub> O <sub>4</sub>	N.D.	0.6151	N.D.	N.D.	N.D.	Ester
18.6803	1-Methyl-3-ethyladamantane	$C_{13}H_{22}$	N.D.	N.D.	0.937	1.0145	N.D.	Alkane
18.6985	1H-Pyrrolo[2,3-b]pyridine-1-propionitrile, 2-phenyl-	$C_{16}H_{13}\;N_2$	N.D.	0.2532	N.D.	N.D.	N.D.	Others
19.0192	2-Hydroxy-1-isoindolinone	$C_8H_{10}O_2N$	0.1533	N.D.	N.D.	0.2518	N.D.	Ketone
19.324	Phthalic acid, monoamide, N-ethyl-N-phenyl-, butyl ester	C <sub>20</sub> H <sub>20</sub> O4	N.D.	N.D.	N.D.	N.D.	1.0237	Ester
19.3306	[1,3,4]Thiadiazole-2-carbodithioic acid, 5-(4-methoxyphenylcarbamoyl)-, methyl ester	$C_9H_7N_3O_2$ S	N.D.	N.D.	0.8125	N.D.	N.D.	Ester
19.3311	4-Methyl-6,6-diphenyl-2-(N-phenylcarbamoyl)-2-azatricyclo[5.2.2.0(1,5)]undeca-4,8,10-trien-3-one	$C_{30}H_{24}N_2O$	N.D.	1.5834	N.D.	1.5261	N.D.	Ketone
19.34	2-((4aS,8R,8aR)-4a,8-Dimethyl-3,4,4a,5,6,7,8,8a-°Ctahydronaphthalen-2-yl)propan-2-ol	C <sub>15</sub> H <sub>26</sub> O	0.1837	N.D.	N.D.	0.3544	N.D.	Alcohol

19.65	1,6-Heptadiene	C <sub>7</sub> H <sub>12</sub>	0.117	N.D.	N.D.	N.D.	N.D.	Alkene
19.9092	(2-°Cten-1-yl)succinic anhydride	$C_{12}H_{18}O_3$	N.D. N.D.	0.1388	N.D.	N.D.	N.D.	Acid

#### Reference

- [1] Papari S, Hawboldt K. A review on the pyrolysis of woody biomass to bio-oil: Focus on kinetic models. Renewable and Sustainable Energy Reviews 2015;52. https://doi.org/10.1016/j.rser.2015.07.191.
- [2] Hoffert MI, Caldeira K, Jain AK, Haites EF, Harvey LDD, Potter SD, et al. Energy implications of future stabilization of atmospheric CO2 content. Nature 1998;395. https://doi.org/10.1038/27638.
- [3] Li P, Cai D, Luo Z, Qin P, Chen C, Wang Y, et al. Effect of acid pretreatment on different parts of corn stalk for second generation ethanol production. Bioresour Technol 2016;206. https://doi.org/10.1016/j.biortech.2016.01.077.
- [4] Jiang L, Shen Y, Jiang Y, Mei W, Wei L, Feng J, et al. Amino acid metabolism and MAP kinase signaling pathway play opposite roles in the regulation of ethanol production during fermentation of sugarcane molasses in budding yeast. Genomics 2024;116. https://doi.org/10.1016/j.ygeno.2024.110811.
- [5] Phichitsurathaworn N, Simasatitkul L, Amornraksa S, Anantpinijwatna A, Charoensuppanimit P, Assabumrungrat S. Techno-economic analysis of co-production of bio-hydrogenated diesel from palm oil and methanol. Energy Convers Manag 2021;244. https://doi.org/10.1016/j.enconman.2021.114464.
- [6] Koberg M, Abu-Much R, Gedanken A. Optimization of bio-diesel production from soybean and wastes of cooked oil: Combining dielectric microwave irradiation and a SrO catalyst. Bioresour Technol 2011;102. https://doi.org/10.1016/j.biortech.2010.08.055.
- [7] Singh SK, Chauhan A, Sarkar B. Resilience of sustainability for a smart production system to produce biodiesel from waste animal fat. J Clean Prod 2024:142047. https://doi.org/10.1016/J.JCLEPRO.2024.142047.
- [8] Özsin G, Pütün AE, Pütün E. Investigating the interactions between lignocellulosic biomass and synthetic polymers during co-pyrolysis by simultaneous thermal and spectroscopic methods. Biomass Convers Biorefin 2019;9. https://doi.org/10.1007/s13399-019-00390-9.
- [9] McKendry P. Energy production from biomass (part 1): Overview of biomass. Bioresour Technol 2002;83. https://doi.org/10.1016/S0960-8524(01)00118-3.
- [10] McKendry P. Energy production from biomass (part 2): Conversion technologies. Bioresour Technol 2002;83. https://doi.org/10.1016/S0960-8524(01)00119-5.
- [11] Chen B, Yao Z, Zhang C, Cheng S, Zhu M, Wang Y, et al. Catalytic co-pyrolysis of cellulosic ethanol—processing residue with high-density polyethylene over biomass bottom ash catalyst. Biomass Convers Biorefin 2023. https://doi.org/10.1007/s13399-023-03915-5.
- [12] Yang Z, Kumar A, Apblett AW, Moneeb AM. Co-Pyrolysis of torrefied biomass and methane over molybdenum modified bimetallic HZSM-5 catalyst for hydrocarbons production. Green Chemistry 2017;19. https://doi.org/10.1039/c6gc02497a.
- [13] Ahmed MHM, Batalha N, Mahmudul HMD, Perkins G, Konarova M. A review on advanced catalytic co-pyrolysis of biomass and hydrogen-rich feedstock: Insights into synergistic effect, catalyst development and reaction mechanism. Bioresour Technol 2020;310:123457. https://doi.org/https://doi.org/10.1016/j.biortech.2020.123457.
- [14] Chen WH, Naveen C, Ghodke PK, Sharma AK, Bobde P. Co-pyrolysis of lignocellulosic biomass with other carbonaceous materials: A review on advance technologies, synergistic effect, and future prospectus. Fuel 2023;345. https://doi.org/10.1016/j.fuel.2023.128177.

- [15] Keleş S, Kar T, Akgün M, Kaygusuz K. Catalytic fast pyrolysis of hazelnut cupula: Characterization of bio-oil. Energy Sources, Part A: Recovery, Utilization and Environmental Effects 2017;39. https://doi.org/10.1080/15567036.2017.1403511.
- [16] Lou R, Wu S Bin, Lv GJ. Effect of conditions on fast pyrolysis of bamboo lignin. J Anal Appl Pyrolysis 2010;89. https://doi.org/10.1016/j.jaap.2010.08.007.
- [17] Wang S, Dai G, Yang H, Luo Z. Lignocellulosic biomass pyrolysis mechanism: A state-of-the-art review. Prog Energy Combust Sci 2017;62. https://doi.org/10.1016/j.pecs.2017.05.004.
- [18] Jahirul MI, Rasul MG, Chowdhury AA, Ashwath N. Biofuels production through biomass pyrolysis- A technological review. Energies (Basel) 2012;5. https://doi.org/10.3390/en5124952.
- [19] Wu M, Zhao M, Chang G, Hu X, Guo Q. A composite obtained from waste automotive plastics and sugarcane skin flour: Mechanical properties and thermo-chemical analysis. Powder Technol 2019;347. https://doi.org/10.1016/j.powtec.2019.02.039.
- [20] Lin X, Zhang Z, Wang Q, Sun J. Interactions between biomass-derived components and polypropylene during wood–plastic composite pyrolysis. Biomass Convers Biorefin 2022;12. https://doi.org/10.1007/s13399-020-00861-4.
- [21] Kan T, Strezov V, Evans TJ. Lignocellulosic biomass pyrolysis: A review of product properties and effects of pyrolysis parameters. Renewable and Sustainable Energy Reviews 2016;57. https://doi.org/10.1016/j.rser.2015.12.185.
- [22] Foong SY, Chan YH, Cheah WY, Kamaludin NH, Tengku Ibrahim TNB, Sonne C, et al. Progress in waste valorization using advanced pyrolysis techniques for hydrogen and gaseous fuel production. Bioresour Technol 2021;320. https://doi.org/10.1016/j.biortech.2020.124299.
- [23] Seo J, Kim H, Jeon S, Valizadeh S, Khani Y, Jeon BH, et al. Thermocatalytic conversion of wood-plastic composite over HZSM-5 catalysts. Bioresour Technol 2023;373. https://doi.org/10.1016/j.biortech.2023.128702.
- [24] Pio DT, Tarelho LAC, Pinto PCR. Gasification-based biorefinery integration in the pulp and paper industry: A critical review. Renewable and Sustainable Energy Reviews 2020;133. https://doi.org/10.1016/j.rser.2020.110210.
- [25] Mah AXY, Ho WS, Bong CPC, Hassim MH, Liew PY, Asli UA, et al. Review of hydrogen economy in Malaysia and its way forward. Int J Hydrogen Energy 2019;44. https://doi.org/10.1016/j.ijhydene.2019.01.077.
- [26] Hameed Z, Aslam M, Khan Z, Maqsood K, Atabani AE, Ghauri M, et al. Gasification of municipal solid waste blends with biomass for energy production and resources recovery: Current status, hybrid technologies and innovative prospects. Renewable and Sustainable Energy Reviews 2021;136. https://doi.org/10.1016/j.rser.2020.110375.
- [27] Thomson R, Kwong P, Ahmad E, Nigam KDP. Clean syngas from small commercial biomass gasifiers; a review of gasifier development, recent advances and performance evaluation. Int J Hydrogen Energy 2020;45. https://doi.org/10.1016/j.ijhydene.2020.05.160.
- [28] Li J, Burra KRG, Wang Z, Liu X, Gupta AK. Co-gasification of high-density polyethylene and pretreated pine wood. Appl Energy 2021;285. https://doi.org/10.1016/j.apenergy.2021.116472.
- [29] Samadi SH, Ghobadian B, Nosrati M. Prediction and estimation of biomass energy from agricultural residues using air gasification technology in Iran. Renew Energy 2020;149. https://doi.org/10.1016/j.renene.2019.10.109.
- [30] Salbidegoitia JA, Fuentes-Ordóñez EG, González-Marcos MP, González-Velasco JR, Bhaskar T, Kamo T. Steam gasification of printed circuit board from e-waste: Effect of

- coexisting nickel to hydrogen production. Fuel Processing Technology 2015;133. https://doi.org/10.1016/j.fuproc.2015.01.006.
- [31] Mah AXY, Ho WS, Bong CPC, Hassim MH, Liew PY, Asli UA, et al. Review of hydrogen economy in Malaysia and its way forward. Int J Hydrogen Energy 2019;44. https://doi.org/10.1016/j.ijhydene.2019.01.077.
- [32] Jeon S, Farooq A, Lee IH, Lee D, Seo MW, Jung SC, et al. Green conversion of wood plastic composites: A study on gasification with an activated bio-char catalyst. Int J Hydrogen Energy 2024;54. https://doi.org/10.1016/j.ijhydene.2023.05.127.
- [33] Wang D, Jin L, Li Y, Wei B, Yao D, Hu H. Effect of reducibility of transition metal oxides on in-situ oxidative catalytic cracking of tar. Energy Convers Manag 2019;197. https://doi.org/10.1016/j.enconman.2019.111871.
- [34] Gollakota ARK, Kishore N, Gu S. A review on hydrothermal liquefaction of biomass. Renewable and Sustainable Energy Reviews 2018;81. https://doi.org/10.1016/j.rser.2017.05.178.
- [35] Vardon DR, Sharma BK, Scott J, Yu G, Wang Z, Schideman L, et al. Chemical properties of biocrude oil from the hydrothermal liquefaction of Spirulina algae, swine manure, and digested anaerobic sludge. Bioresour Technol 2011;102. https://doi.org/10.1016/j.biortech.2011.06.041.
- [36] Siwal SS, Sheoran K, Saini AK, Vo DVN, Wang Q, Thakur VK. Advanced thermochemical conversion technologies used for energy generation: Advancement and prospects. Fuel 2022;321. https://doi.org/10.1016/j.fuel.2022.124107.
- [37] Mohammed IY, Abakr YA, Xing Hui JN, Alaba PA, Morris KI, Ibrahim MD. Recovery of clean energy precursors from Bambara groundnut waste via pyrolysis: Kinetics, products distribution and optimisation using response surface methodology. J Clean Prod 2017;164. https://doi.org/10.1016/j.jclepro.2017.07.068.
- [38] Biswas B, Sahoo D, Sukumaran RK, Krishna BB, Kumar J, Reddy YS, et al. Cohydrothermal liquefaction of phumdi and paragrass an aquatic biomass: Characterization of bio-oil, aqueous fraction and solid residue. Journal of the Energy Institute 2022;102. https://doi.org/10.1016/j.joei.2022.03.013.
- [39] Wang J, Wang S, Lu J, Yang M, Wu Y. Improved Bio-Oil Quality from Pyrolysis of Pine Biomass in Pressurized Hydrogen. Applied Sciences (Switzerland) 2022;12. https://doi.org/10.3390/app12010046.
- [40] Tian H, Zhu R, Chen L, Wang J, Cheng Y. Aromatic hydrocarbons rich bio-oil production from Miscanthus pyrolysis by coupling torrefaction and MoO3/ZSM-5 dual catalysis process. Ind Crops Prod 2023;204. https://doi.org/10.1016/j.indcrop.2023.117314.
- [41] Nie N, Wang Y, Yellezuome D, Liu X, Wang P, Wang X, et al. Exploring kinetic and thermodynamic mechanisms of switchgrass pyrolysis using iterative linear integral isoconversional method and master plots approach. Fuel 2023;338. https://doi.org/10.1016/j.fuel.2022.127266.
- [42] Sun J, Norouzi O, Mašek O. A state-of-the-art review on algae pyrolysis for bioenergy and biochar production. Bioresour Technol 2022;346. https://doi.org/10.1016/j.biortech.2021.126258.
- [43] Zeb W, Roosen M, Knockaert P, Janssens S, Withoeck D, Kusenberg M, et al. Purification and characterisation of post-consumer plastic pyrolysis oil fractionated by vacuum distillation. J Clean Prod 2023;416. https://doi.org/10.1016/j.jclepro.2023.137881.
- [44] Armenise S, SyieLuing W, Ramírez-Velásquez JM, Launay F, Wuebben D, Ngadi N, et al. Plastic waste recycling via pyrolysis: A bibliometric survey and literature review. J Anal Appl Pyrolysis 2021;158. https://doi.org/10.1016/j.jaap.2021.105265.

- [45] Adelodun AA. Plastic Recovery and Utilization: From Ocean Pollution to Green Economy. Front Environ Sci 2021;9. https://doi.org/10.3389/fenvs.2021.683403.
- [46] Nanda S, Berruti F. Municipal solid waste management and landfilling technologies: a review. Environ Chem Lett 2021;19. https://doi.org/10.1007/s10311-020-01100-y.
- [47] Vamvuka D, Esser K, Marinakis D, Kalantzakis G. Evaluation of Pyrolysis Products of Industrial Wastes as Potential Feedstocks for Bioenergy and Biofuels. Advances in Environmental and Engineering Research 2023;04. https://doi.org/10.21926/aeer.2301005.
- [48] Han W, Han D, Chen H. Pyrolysis of Waste Tires: A Review. Polymers (Basel) 2023;15. https://doi.org/10.3390/polym15071604.
- [49] Fonts I, Gea G, Azuara M, Ábrego J, Arauzo J. Sewage sludge pyrolysis for liquid production: A review. Renewable and Sustainable Energy Reviews 2012;16. https://doi.org/10.1016/j.rser.2012.02.070.
- [50] Elkhalifa S, Al-Ansari T, Mackey HR, McKay G. Food waste to biochars through pyrolysis: A review. Resour Conserv Recycl 2019;144. https://doi.org/10.1016/j.resconrec.2019.01.024.
- [51] Kim S, Lee Y, Andrew Lin KY, Hong E, Kwon EE, Lee J. The valorization of food waste via pyrolysis. J Clean Prod 2020;259. https://doi.org/10.1016/j.jclepro.2020.120816.
- [52] Li H, Xu J, Mbugua Nyambura S, Wang J, Li C, Zhu X, et al. Food waste pyrolysis by traditional heating and microwave heating: A review. Fuel 2022;324. https://doi.org/10.1016/j.fuel.2022.124574.
- [53] Panthapulakkal S, Zereshkian A, Sain M. Preparation and characterization of wheat straw fibers for reinforcing application in injection molded thermoplastic composites. Bioresour Technol 2006;97. https://doi.org/10.1016/j.biortech.2005.02.043.
- [54] Ashori A. Wood-plastic composites as promising green-composites for automotive industries! Bioresour Technol 2008;99. https://doi.org/10.1016/j.biortech.2007.09.043.
- [55] Clemons C. Wood-plastic composites in the United States: The interfacing of two industries. For Prod J 2002;52.
- [56] Grand View Research I. Wood Plastic Composites Market Size, Share & Trends Analysis Report By Product (Polyethylene, Polypropylene), By Application (Automotive Components), By Region, And Segment Forecasts, 2023 2030 2023:0–198.
- [57] Teuber L, Osburg VS, Toporowski W, Militz H, Krause A. Wood polymer composites and their contribution to cascading utilisation. J Clean Prod 2016;110. https://doi.org/10.1016/j.jclepro.2015.04.009.
- [58] Qi X, Shang Y, Ding Z, Wei W. Particularities and research progress of the cutting machinability of wood-plastic composites. Mater Today Commun 2023;37:106924. https://doi.org/10.1016/J.MTCOMM.2023.106924.
- [59] Michaud F, Castéera P, Fernandez C, Ndiaye A. Meta-heuristic methods applied to the design of woodĝ€" plastic composites, with some attention to environmental aspects. J Compos Mater 2009;43. https://doi.org/10.1177/0021998308097681.
- [60] Adhikary KB, Pang S, Staiger MP. Dimensional stability and mechanical behaviour of wood-plastic composites based on recycled and virgin high-density polyethylene (HDPE). Compos B Eng 2008;39. https://doi.org/10.1016/j.compositesb.2007.10.005.
- [61] Haque MMU, Goda K, Ogoe S, Sunaga Y. Fatigue analysis and fatigue reliability of polypropylene/wood flour composites. Advanced Industrial and Engineering Polymer Research 2019;2. https://doi.org/10.1016/j.aiepr.2019.07.001.

- [62] Qiang T, Yu D, Zhang A, Gao H, Li Z, Liu Z, et al. Life cycle assessment on polylactide-based wood plastic composites toughened with polyhydroxyalkanoates. J Clean Prod 2014;66. https://doi.org/10.1016/j.jclepro.2013.11.074.
- [63] Chen B, Cai D, Luo ZF, Chen CJ, Zhang CW, Qin PY, et al. Corncob residual reinforced polyethylene composites considering the biorefinery process and the enhancement of performance. J Clean Prod 2018;198:452–62.
- [64] Benoit N, Rodrigue D. Mechanical properties of foamed and unfoamed wood/plastic composites produced by extrusion-calendering. Annual Technical Conference ANTEC, Conference Proceedings, vol. 2, 2013.
- [65] Friedrich D. Post-process hot-pressing of wood-polymer composites: Effects on physical properties. Journal of Building Engineering 2022;46. https://doi.org/10.1016/j.jobe.2021.103818.
- [66] Fletes RCV, López EOC, Sánchez FJM, Mendizábal E, Núñez RG, Rodrigue D, et al. Morphological and mechanical properties of bilayers wood-plastic composites and foams obtained by rotational molding. Polymers (Basel) 2020;12. https://doi.org/10.3390/polym12030503.
- [67] Kamdem DP, Jiang H, Cui W, Freed J, Matuana LM. Properties of wood plastic composites made of recycled HDPE and wood flour from CCA-treated wood removed from service. Compos Part A Appl Sci Manuf, vol. 35, 2004. https://doi.org/10.1016/j.compositesa.2003.09.013.
- [68] Gardner DJ, Han Y, Wang L. Wood–Plastic composite technology. Current Forestry Reports 2015;1. https://doi.org/10.1007/s40725-015-0016-6.
- [69] Lopez G, Artetxe M, Amutio M, Alvarez J, Bilbao J, Olazar M. Recent advances in the gasification of waste plastics. A critical overview. Renewable and Sustainable Energy Reviews 2018;82. https://doi.org/10.1016/j.rser.2017.09.032.
- [70] Chen B, Luo Z, Chen H, Chen C, Cai D, Qin P, et al. Wood Plastic Composites from the Waste Lignocellulosic Biomass Fibers of Bio-Fuels Processes: A Comparative Study on Mechanical Properties and Weathering Effects. Waste Biomass Valorization 2020;11. https://doi.org/10.1007/s12649-018-0413-8.
- [71] Beg MDH, Pickering KL. Reprocessing of wood fibre reinforced polypropylene composites. Part I: Effects on physical and mechanical properties. Compos Part A Appl Sci Manuf 2008;39. https://doi.org/10.1016/j.compositesa.2008.04.013.
- [72] Englund K, Villechevrolle V. Flexure and water sorption properties of wood thermoplastic composites made with polymer blends. J Appl Polym Sci 2011;120. https://doi.org/10.1002/app.33237.
- [73] Jin QM, Wang XB, Li SS, Mikulcic H, Besenic T, Deng SH, et al. Synergistic effects during co-pyrolysis of biomass and plastic: Gas, tar, soot, char products and thermogravimetric study. Journal of the Energy Institute 2019;92:108–17.
- [74] Ghorbannezhad P, Park S, Onwudili JA. Co-pyrolysis of biomass and plastic waste over zeolite- and sodium-based catalysts for enhanced yields of hydrocarbon products. Waste Management 2020;102. https://doi.org/10.1016/j.wasman.2019.12.006.
- [75] Venderbosch RH, Prins W. Fast pyrolysis technology development. Biofuels, Bioproducts and Biorefining 2010;4. https://doi.org/10.1002/bbb.205.
- [76] Álvarez-Chávez BJ, Godbout S, Le Roux É, Palacios JH, Raghavan V. Bio-oil yield and quality enhancement through fast pyrolysis and fractional condensation concepts. Biofuel Research Journal 2019;6. https://doi.org/10.18331/BRJ2019.6.4.2.
- [77] Bridgwater A V. Review of fast pyrolysis of biomass and product upgrading. Biomass Bioenergy 2012;38. https://doi.org/10.1016/j.biombioe.2011.01.048.

- [78] Kim YM, Jeong J, Ryu S, Lee HW, Jung JS, Siddiqui MZ, et al. Catalytic pyrolysis of wood polymer composites over hierarchical mesoporous zeolites. Energy Convers Manag 2019;195. https://doi.org/10.1016/j.enconman.2019.05.034.
- [79] Anuar Sharuddin SD, Abnisa F, Wan Daud WMA, Aroua MK. A review on pyrolysis of plastic wastes. Energy Convers Manag 2016;115. https://doi.org/10.1016/j.enconman.2016.02.037.
- [80] Aguado J, Serrano DP, Escola JM. Catalytic Upgrading of Plastic Wastes. Feedstock Recycling and Pyrolysis of Waste Plastics: Converting Waste Plastics into Diesel and Other Fuels, 2006. https://doi.org/10.1002/0470021543.ch3.
- [81] Zhang H, Samsudin I bin, Jaenicke S, Chuah GK. Zeolites in catalysis: sustainable synthesis and its impact on properties and applications. Catal Sci Technol 2022;12. https://doi.org/10.1039/d2cy01325h.
- [82] Park YK, Jung JS, Jae J, Hong SB, Watanabe A, Kim YM. Catalytic fast pyrolysis of wood plastic composite over microporous zeolites. Chemical Engineering Journal 2019;377.
- [83] Sun JP, Sui SJ, Zhang ZJ, Tan S, Wang QW. Catalytic upgrading of wood-plastic composite fast pyrolysis vapors with USY/ HUSY catalysts. ICMREE 2013 Proceedings: 2013 International Conference on Materials for Renewable Energy and Environment, vol. 1, 2013. https://doi.org/10.1109/ICMREE.2013.6893660.
- [84] Lin X, Zhang Z, Zhang Z, Sun J, Wang Q, Pittman CU. Catalytic fast pyrolysis of a wood-plastic composite with metal oxides as catalysts. Waste Management 2018;79. https://doi.org/10.1016/j.wasman.2018.07.021.
- [85] Heo HS, Pyo S, Kang BS, Jung JS, Rhee GH, Kim YM, et al. Synthesis of biofuel via catalytic fast pyrolysis of wood-plastic composite over low-cost catalysts. Sustainable Energy Technologies and Assessments 2023;56. https://doi.org/10.1016/j.seta.2023.103051.
- [86] Loy ACM, Gan DKW, Yusup S, Chin BLF, Lam MK, Shahbaz M, et al. Thermogravimetric kinetic modelling of in-situ catalytic pyrolytic conversion of rice husk to bioenergy using rice hull ash catalyst. Bioresour Technol 2018;261:213–22.
- [87] Herman AP, Yusup S, Shahbaz M, Patrick DO. Bottom Ash Characterization and its Catalytic Potential in Biomass Gasification. Procedia Eng, vol. 148, 2016. https://doi.org/10.1016/j.proeng.2016.06.447.
- [88] Prasara-A J, Gheewala SH. Sustainable utilization of rice husk ash from power plants: A review. J Clean Prod 2017;167:1020–8. https://doi.org/https://doi.org/10.1016/j.jclepro.2016.11.042.
- [89] Loy ACM, Yusup S, Lam MK, Chin BLF, Shahbaz M, Yamamoto A, et al. The effect of industrial waste coal bottom ash as catalyst in catalytic pyrolysis of rice husk for syngas production. Energy Convers Manag 2018;165:541–54.
- [90] Wu W, Zhang R, Wang Z, Li J, Cui X, Zhong L, et al. Catalytic pyrolysis of biogas residues with incineration bottom ash by TG-MS: Kinetics analysis and biochar stability. Fuel 2022;322:124253. https://doi.org/https://doi.org/10.1016/j.fuel.2022.124253.
- [91] Sutrisno B, Hidayat A. Upgrading of bio-oil from the pyrolysis of biomass over the rice husk ash catalysts. IOP Conf Ser Mater Sci Eng 2016;162:12014. https://doi.org/10.1088/1757-899x/162/1/012014.
- [92] Zhang D, Lin X, Zhang Q, Ren X, Yu W, Cai H. Catalytic pyrolysis of wood-plastic composite waste over activated carbon catalyst for aromatics production: Effect of preparation process of activated carbon. Energy 2020;212. https://doi.org/10.1016/j.energy.2020.118983.

- [93] Lin X, Zhang Z, Sun J, Guo W, Wang Q. Effects of phosphorus-modified HZSM-5 on distribution of hydrocarbon compounds from wood-plastic composite pyrolysis using Py-GC/MS. J Anal Appl Pyrolysis 2015;116. https://doi.org/10.1016/j.jaap.2015.09.007.
- [94] Lin X, Zhang Z, Wang Q. Evaluation of zeolite catalysts on product distribution and synergy during wood-plastic composite catalytic pyrolysis. Energy 2019;189. https://doi.org/10.1016/j.energy.2019.116174.
- [95] Gan LH, Goldfarb JL. Solid waste to biofuels and heterogeneous sorbents via pyrolysis of wheat straw in the presence of fly ash as an in situ catalyst. J Anal Appl Pyrolysis 2019;137:96–105.
- [96] Tan S, Zhang Z, Sun J, Wang Q. Recent progress of catalytic pyrolysis of biomass by HZSM-5. Cuihua Xuebao/Chinese Journal of Catalysis 2013;34. https://doi.org/10.1016/s1872-2067(12)60531-2.
- [97] Yildiz G, Ronsse F, Duren R Van, Prins W. Challenges in the design and operation of processes for catalytic fast pyrolysis of woody biomass. Renewable and Sustainable Energy Reviews 2016;57. https://doi.org/10.1016/j.rser.2015.12.202.
- [98] Paasikallio V, Lindfors C, Kuoppala E, Solantausta Y, Oasmaa A, Lehto J, et al. Product quality and catalyst deactivation in a four day catalytic fast pyrolysis production run. Green Chemistry 2014;16. https://doi.org/10.1039/c4gc00571f.
- [99] Lee BH, Thieu Trinh V, Moon H Bin, Lee JH, Kim HT, Lee JW, et al. Physicochemical properties and pyrolysis behavior of petcoke with artificial neural network modeling. Fuel 2023;331. https://doi.org/10.1016/j.fuel.2022.125735.
- [100] Gai C, Dong Y, Zhang T. The kinetic analysis of the pyrolysis of agricultural residue under non-isothermal conditions. Bioresour Technol 2013;127. https://doi.org/10.1016/j.biortech.2012.09.089.
- [101] Sun C, Li C, Tan H, Zhang Y. Synergistic effects of wood fiber and polylactic acid during co-pyrolysis using TG-FTIR-MS and Py-GC/MS. Energy Convers Manag 2019;202:112212. https://doi.org/10.1016/J.ENCONMAN.2019.112212.
- [102] Zhang X, Huang R. Thermal decomposition kinetics of basalt fiber-reinforced wood polymer composites. Polymers (Basel) 2020;12. https://doi.org/10.3390/polym12102283.
- [103] Chrysafi I, Ainali NM, Xanthopoulou E, Zamboulis A, Bikiaris DN. Thermal Degradation Mechanism and Decomposition Kinetic Studies of Poly(Ethylene Succinate)/Hemp Fiber Composites. Journal of Composites Science 2023;7. https://doi.org/10.3390/jcs7060216.
- [104] Choudhary M, Singh D, Jain SK, Singh D, Devnani GL, Singh S, et al. Thermal and mechanical investigation of chemically treated hybrid biomass epoxy bio-composite: An approach of pyrolysis kinetics. Bioresour Technol Rep 2023;23. https://doi.org/10.1016/j.biteb.2023.101589.
- [105] Sonobe T, Worasuwannarak N. Kinetic analyses of biomass pyrolysis using the distributed activation energy model. Fuel 2008;87. https://doi.org/10.1016/j.fuel.2007.05.004.
- [106] Liu H, Xu G, Li G. Pyrolysis characteristic and kinetic analysis of sewage sludge using model-free and master plots methods. Process Safety and Environmental Protection 2021;149. https://doi.org/10.1016/j.psep.2020.10.044.
- [107] Gözke G. Kinetic and thermodynamic analyses based on thermogravimetric pyrolysis of watermelon seed by isoconversional and master plots methods. Renew Energy 2022;201:916–27. https://doi.org/10.1016/J.RENENE.2022.10.100.
- [108] Vamvuka D. Bio-oil, solid and gaseous biofuels from biomass pyrolysis processes-An overview. Int J Energy Res 2011;35. https://doi.org/10.1002/er.1804.

- [109] White JE, Catallo WJ, Legendre BL. Biomass pyrolysis kinetics: A comparative critical review with relevant agricultural residue case studies. J Anal Appl Pyrolysis 2011;91. https://doi.org/10.1016/j.jaap.2011.01.004.
- [110] Mulligan CJ, Strezov L, Strezov V. Thermal decomposition of wheat straw and mallee residue under pyrolysis conditions. Energy and Fuels, vol. 24, 2010. https://doi.org/10.1021/ef9004797.
- [111] Wang S, Guo X, Wang K, Luo Z. Influence of the interaction of components on the pyrolysis behavior of biomass. J Anal Appl Pyrolysis 2011;91. https://doi.org/10.1016/j.jaap.2011.02.006.
- [112] Cepeliogullar O, E. Putun A. Utilization of Two Different Types of Plastic Wastes from Daily and Industrial Life. Journal of Selcuk University Natural and Applied Science 2000.
- [113] Ratanawilai T, Taneerat K. Alternative polymeric matrices for wood-plastic composites: Effects on mechanical properties and resistance to natural weathering. Constr Build Mater 2018;172. https://doi.org/10.1016/j.conbuildmat.2018.03.266.
- [114] Czernik S, Bridgwater A V. Overview of applications of biomass fast pyrolysis oil. Energy and Fuels 2004;18. https://doi.org/10.1021/ef034067u.
- [115] Zhang Y, Chen P, Lou H. In situ catalytic conversion of biomass fast pyrolysis vapors on HZSM-5. Journal of Energy Chemistry 2016;25. https://doi.org/10.1016/j.jechem.2016.03.014.
- [116] Abnisa F, Wan Daud WMA. A review on co-pyrolysis of biomass: An optional technique to obtain a high-grade pyrolysis oil. Energy Convers Manag 2014;87. https://doi.org/10.1016/j.enconman.2014.07.007.
- [117] Yuan H, Fan H, Shan R, He M, Gu J, Chen Y. Study of synergistic effects during copyrolysis of cellulose and high-density polyethylene at various ratios. Energy Convers Manag 2018;157. https://doi.org/10.1016/j.enconman.2017.12.038.
- [118] Chen W, Shi S, Zhang J, Chen M, Zhou X. Co-pyrolysis of waste newspaper with high-density polyethylene: Synergistic effect and oil characterization. Energy Convers Manag 2016;112. https://doi.org/10.1016/j.enconman.2016.01.005.
- [119] Ephraim A, Pham Minh D, Lebonnois D, Peregrina C, Sharrock P, Nzihou A. Copyrolysis of wood and plastics: Influence of plastic type and content on product yield, gas composition and quality. Fuel 2018;231. https://doi.org/10.1016/j.fuel.2018.04.140.
- [120] Ojha DK, Vinu R. Fast co-pyrolysis of cellulose and polypropylene using Py-GC/MS and Py-FT-IR. RSC Adv 2015;5. https://doi.org/10.1039/c5ra10820a.
- [121] Dorado C, Mullen CA, Boateng AA. H-ZSM5 catalyzed co-pyrolysis of biomass and plastics. ACS Sustain Chem Eng 2014;2. https://doi.org/10.1021/sc400354g.
- [122] Sun L, Wu Q, Xie Y, Cueto R, Lee S, Wang Q. Thermal degradation and flammability behavior of fire-retarded wood flour/polypropylene composites. J Fire Sci 2016;34. https://doi.org/10.1177/0734904116637632.
- [123] Das SK, Ghosh GK, Avasthe R. Application of biochar in agriculture and environment, and its safety issues. Biomass Convers Biorefin 2023;13. https://doi.org/10.1007/s13399-020-01013-4.
- [124] Seo J, Kim H, Jeon S, Valizadeh S, Khani Y, Jeon BH, et al. Thermocatalytic conversion of wood-plastic composite over HZSM-5 catalysts. Bioresour Technol 2023;373. https://doi.org/10.1016/j.biortech.2023.128702.
- [125] Al-Rumaihi A, Shahbaz M, Mckay G, Mackey H, Al-Ansari T. A review of pyrolysis technologies and feedstock: A blending approach for plastic and biomass towards optimum biochar yield. Renewable and Sustainable Energy Reviews 2022;167. https://doi.org/10.1016/j.rser.2022.112715.

- [126] Jeong CS, Park SH, Lee IG, Ryu C, Jung SC, Ko CH, et al. Influence of reaction parameters on pyrolysis of waste wood polymer composite. J Biobased Mater Bioenergy 2014;8. https://doi.org/10.1166/jbmb.2014.1434.
- [127] Chen B, Ma S, Kumar S, Yao Z, Feng W, Zhao J, et al. Pyrolysis behaviour and kinetic analysis of waste polylactic acid composite reinforced with reed straw processing residue. Carbon Resources Conversion 2024;7:100226. https://doi.org/10.1016/J.CRCON.2024.100226.
- [128] Collard FX, Blin J. A review on pyrolysis of biomass constituents: Mechanisms and composition of the products obtained from the conversion of cellulose, hemicelluloses and lignin. Renewable and Sustainable Energy Reviews 2014;38. https://doi.org/10.1016/j.rser.2014.06.013.
- [129] Sun JP, Sui SJ, Zhang ZJ, Tan S, Wang QW. Study on the pyrolytic behavior of woodplastic composites using Py-GC/MS. Bioresources 2013;8. https://doi.org/10.15376/biores.8.4.6196-6210.
- [130] Jakab E, Várhegyi G, Faix O. Thermal decomposition of polypropylene in the presence of wood-derived materials. J Anal Appl Pyrolysis 2000;56. https://doi.org/10.1016/S0165-2370(00)00101-7.
- [131] Kumagai S, Fujita K, Kameda T, Yoshioka T. Interactions of beech wood–polyethylene mixtures during co-pyrolysis. J Anal Appl Pyrolysis 2016;122. https://doi.org/10.1016/j.jaap.2016.08.012.
- [132] Wang S, Ru B, Dai G, Sun W, Qiu K, Zhou J. Pyrolysis mechanism study of minimally damaged hemicellulose polymers isolated from agricultural waste straw samples. Bioresour Technol 2015;190. https://doi.org/10.1016/j.biortech.2015.04.098.
- [133] Gu J, Fan H, Wang Y, Zhang Y, Yuan H, Chen Y. Co-pyrolysis of xylan and high-density polyethylene: Product distribution and synergistic effects. Fuel 2020;267. https://doi.org/10.1016/j.fuel.2019.116896.
- [134] Brebu M, Spiridon I. Co-pyrolysis of LignoBoost® lignin with synthetic polymers. Polym Degrad Stab 2012;97. https://doi.org/10.1016/j.polymdegradstab.2012.08.024.
- [135] Menares T, Herrera J, Romero R, Osorio P, Arteaga-Pérez LE. Waste tires pyrolysis kinetics and reaction mechanisms explained by TGA and Py-GC/MS under kinetically-controlled regime. Waste Management 2020;102:21–9. https://doi.org/https://doi.org/10.1016/j.wasman.2019.10.027.
- [136] Mishra RK, Mohanty K, Wang X. Pyrolysis kinetic behavior and Py-GC–MS analysis of waste dahlia flowers into renewable fuel and value-added chemicals. Fuel 2020;260:116338. https://doi.org/https://doi.org/10.1016/j.fuel.2019.116338.
- [137] Luo ZF, Li P, Cai D, Chen QC, Qin PY, Tan TW, et al. Comparison of performances of corn fiber plastic composites made from different parts of corn stalk. Ind Crops Prod 2017;95:521–7.
- [138] Duan P, Jin B, Xu Y, Wang F. Co-pyrolysis of microalgae and waste rubber tire in supercritical ethanol. Chemical Engineering Journal 2015;269. https://doi.org/10.1016/j.cej.2015.01.108.
- [139] Gou X, Zhao X, Singh S, Qiao D. Tri-pyrolysis: A thermo-kinetic characterisation of polyethylene, cornstalk, and anthracite coal using TGA-FTIR analysis. Fuel 2019;252. https://doi.org/10.1016/j.fuel.2019.03.143.
- [140] Wang WL, Sun K, Ali M, Liu XJ, Huang QX. Copyrolysis Behavior of Xylan and Polyvinyl Chloride Plastic. Energy & Fuels 2019;33:8727–34.
- [141] Ozsin G, Putun AE. Insights into pyrolysis and co-pyrolysis of biomass and polystyrene: Thermochemical behaviors, kinetics and evolved gas analysis. Energy Convers Manag 2017;149:675–85.

- [142] Azizi K, Keshavarz Moraveji M, Abedini Najafabadi H. Simultaneous pyrolysis of microalgae C. vulgaris, wood and polymer: The effect of third component addition. Bioresour Technol 2018;247. https://doi.org/10.1016/j.biortech.2017.09.059.
- [143] Yao Z, Cai D, Chen X, Sun Y, Jin M, Qi W, et al. Thermal behavior and kinetic study on the co-pyrolysis of biomass with polymer waste. Biomass Convers Biorefin 2022. https://doi.org/10.1007/s13399-022-02480-7.
- [144] Sarkar JK, Wang Q. Characterization of pyrolysis products and kinetic analysis of waste jute stick biomass. Processes 2020;8. https://doi.org/10.3390/pr8070837.
- [145] Singh SK, Prakash H, Akhtar MJ, Kar KK. Lightweight and High-Performance Microwave Absorbing Heteroatom-Doped Carbon Derived from Chicken Feather Fibers. ACS Sustain Chem Eng 2018;6. https://doi.org/10.1021/acssuschemeng.8b00183.
- [146] Fang S, Yu Z, Lin Y, Hu S, Liao Y, Ma X. Thermogravimetric analysis of the copyrolysis of paper sludge and municipal solid waste. Energy Convers Manag 2015;101. https://doi.org/10.1016/j.enconman.2015.06.026.
- [147] Xiang Z, Liang J, Morgan HM, Liu Y, Mao H, Bu Q. Thermal behavior and kinetic study for co-pyrolysis of lignocellulosic biomass with polyethylene over Cobalt modified ZSM-5 catalyst by thermogravimetric analysis. Bioresour Technol 2018;247. https://doi.org/10.1016/j.biortech.2017.09.178.
- [148] Aboulkas A, El Harfi K, El Bouadili A. Non-isothermal kinetic studies on co-processing of olive residue and polypropylene. Energy Convers Manag 2008;49. https://doi.org/10.1016/j.enconman.2008.06.029.
- [149] Biswas B, Pandey N, Bisht Y, Singh R, Kumar J, Bhaskar T. Pyrolysis of agricultural biomass residues: Comparative study of corn cob, wheat straw, rice straw and rice husk. Bioresour Technol 2017;237. https://doi.org/10.1016/j.biortech.2017.02.046.
- [150] Çepelioğullar Ö, Pütün AE. Thermal and kinetic behaviors of biomass and plastic wastes in co-pyrolysis. Energy Convers Manag 2013;75. https://doi.org/10.1016/j.enconman.2013.06.036.
- [151] Zhou S, Xue Y, Sharma A, Bai X. Lignin Valorization through Thermochemical Conversion: Comparison of Hardwood, Softwood and Herbaceous Lignin. ACS Sustain Chem Eng 2016;4. https://doi.org/10.1021/acssuschemeng.6b01488.
- [152] Wu XY, Wu YL, Wu KJ, Chen Y, Hu HS, Yang MD. Study on pyrolytic kinetics and behavior: The co-pyrolysis of microalgae and polypropylene. Bioresour Technol 2015;192:522–8.
- [153] Kai X, Yang T, Shen S, Li R. TG-FTIR-MS study of synergistic effects during copyrolysis of corn stalk and high-density polyethylene (HDPE). Energy Convers Manag 2019;181:202–13. https://doi.org/10.1016/J.ENCONMAN.2018.11.065.
- [154] Cai D, Li P, Chen C, Wang Y, Hu S, Cui C, et al. Effect of chemical pretreatments on corn stalk bagasse as immobilizing carrier of Clostridium acetobutylicum in the performance of a fermentation-pervaporation coupled system. Bioresour Technol 2016;220. https://doi.org/10.1016/j.biortech.2016.08.049.
- [155] Quan S, Liu Z, Shi L, Liu Q. Volatiles reaction during pyrolysis of corn stalk Its influence on bio-oil composition and coking behavior of volatiles. Fuel 2019;246. https://doi.org/10.1016/j.fuel.2019.02.069.
- [156] Cen K, Chen D, Wang J, Cai Y, Wang L. Effects of Water Washing and Torrefaction Pretreatments on Corn Stalk Pyrolysis: Combined Study Using TG-FTIR and a Fixed Bed Reactor. Energy and Fuels 2016;30. https://doi.org/10.1021/acs.energyfuels.6b02813.

- [157] Zeng Y, Zhao S, Yang S, Ding SY. Lignin plays a negative role in the biochemical process for producing lignocellulosic biofuels. Curr Opin Biotechnol 2014;27. https://doi.org/10.1016/j.copbio.2013.09.008.
- [158] Cai D, Li P, Luo Z, Qin P, Chen C, Wang Y, et al. Effect of dilute alkaline pretreatment on the conversion of different parts of corn stalk to fermentable sugars and its application in acetone-butanol-ethanol fermentation. Bioresour Technol 2016;211. https://doi.org/10.1016/j.biortech.2016.03.076.
- [159] Wang T, Yin J, Liu Y, Lu Q, Zheng Z. Effects of chemical inhomogeneity on pyrolysis behaviors of corn stalk fractions. Fuel 2014;129. https://doi.org/10.1016/j.fuel.2014.03.061.
- [160] Shuping Z, Yulong W, Mingde Y, Chun L, Junmao T. Pyrolysis characteristics and kinetics of the marine microalgae Dunaliella tertiolecta using thermogravimetric analyzer. Bioresour Technol 2010;101. https://doi.org/10.1016/j.biortech.2009.08.020.
- [161] Sluiter A, Hames B, Ruiz R, Scarlata C, Sluiter J, Templeton D, et al. Determination of Structural Carbohydrates and Lignin in Biomass, Laboratory Analytical Procedure (LAP), Technical Report NREL/TP-510-42618. National Renewable Energy Laboratory (NREL), U.S. Dept. of Energy. 2011 2011.
- [162] Starink MJ. The determination of activation energy from linear heating rate experiments: a comparison of the accuracy of isoconversion methods. Thermochim Acta 2003;404:163–76.
- [163] Kissinger HE. Reaction Kinetics in Differential Thermal Analysis. Anal Chem 1957;29:1702–6. https://doi.org/10.1021/ac60131a045.
- [164] Doyle CD. Estimating isothermal life from thermogravimetric data. J Appl Polym Sci 1962;6:639–42. https://doi.org/10.1002/app.1962.070062406.
- [165] Gotor FJ, José, Criado M, Malek J, Koga N. Kinetic analysis of solid-state reactions: The universality of master plots for analyzing isothermal and nonisothermal experiments. Journal of Physical Chemistry A 2000;104. https://doi.org/10.1021/jp0022205.
- [166] Schonlau M, Zou RY. The random forest algorithm for statistical learning. Stata Journal 2020;20. https://doi.org/10.1177/1536867X20909688.
- [167] Yang F, Wang D, Xu F, Huang Z, Tsui KL. Lifespan prediction of lithium-ion batteries based on various extracted features and gradient boosting regression tree model. J Power Sources 2020;476. https://doi.org/10.1016/j.jpowsour.2020.228654.
- [168] Zhang G, Sun Y, Shi Y, Jia Y, Xu Y, Zhao P, et al. Characteristic and kinetics of corn stalk pyrolysis in a high pressure reactor and steam gasification of its char. J Anal Appl Pyrolysis 2016;122. https://doi.org/10.1016/j.jaap.2016.09.017.
- [169] Liu X, Zhang Y, Li Z, Feng R, Zhang Y. Characterization of corncob-derived biochar and pyrolysis kinetics in comparison with corn stalk and sawdust. Bioresour Technol 2014;170. https://doi.org/10.1016/j.biortech.2014.07.077.
- [170] Tranvan L, Legrand V, Jacquemin F. Thermal decomposition kinetics of balsa wood: Kinetics and degradation mechanisms comparison between dry and moisturized materials. Polym Degrad Stab 2014;110. https://doi.org/10.1016/j.polymdegradstab.2014.09.004.
- [171] Azizi K, Keshavarz Moraveji M, Abedini Najafabadi H. Characteristics and kinetics study of simultaneous pyrolysis of microalgae Chlorella vulgaris, wood and polypropylene through TGA. Bioresour Technol 2017;243. https://doi.org/10.1016/j.biortech.2017.06.155.
- [172] Burra KG, Gupta AK. Kinetics of synergistic effects in co-pyrolysis of biomass with plastic wastes. Appl Energy 2018;220:408–18.

- [173] Maiti S, Purakayastha S, Ghosh B. Thermal characterization of mustard straw and stalk in nitrogen at different heating rates. Fuel 2007;86. https://doi.org/10.1016/j.fuel.2006.11.016.
- [174] Jin SH, Lee HW, Ryu C, Jeon JK, Park YK. Catalytic fast pyrolysis of Geodae-Uksae 1 over zeolites. Energy 2015;81. https://doi.org/10.1016/j.energy.2014.10.059.
- [175] Hassan H, Hameed BH, Lim JK. Co-pyrolysis of sugarcane bagasse and waste high-density polyethylene: Synergistic effect and product distributions. Energy 2020;191. https://doi.org/10.1016/j.energy.2019.116545.
- [176] Mohan D, Pittman CU, Steele PH. Pyrolysis of wood/biomass for bio-oil: A critical review. Energy and Fuels 2006;20. https://doi.org/10.1021/ef0502397.
- [177] Iliopoulou EF, Stefanidis SD, Kalogiannis KG, Delimitis A, Lappas AA, Triantafyllidis KS. Catalytic upgrading of biomass pyrolysis vapors using transition metal-modified ZSM-5 zeolite. Appl Catal B 2012;127. https://doi.org/10.1016/j.apcatb.2012.08.030.
- [178] Lin X, Kong L, Ren X, Zhang D, Cai H, Lei H. Catalytic co-pyrolysis of torrefied poplar wood and high-density polyethylene over hierarchical HZSM-5 for monoaromatics production. Renew Energy 2021;164. https://doi.org/10.1016/j.renene.2020.09.071.
- [179] Liu Y, Song Y, Fu J, Ao W, Ali Siyal A, Zhou C, et al. Co-pyrolysis of sewage sludge and lignocellulosic biomass: Synergistic effects on products characteristics and kinetics. Energy Convers Manag 2022;268:116061. https://doi.org/10.1016/J.ENCONMAN.2022.116061.
- [180] Li J, Yao X, Chen S, Xu K, Fan B, Yang D, et al. Investigation on the co-pyrolysis of agricultural waste and high-density polyethylene using TG-FTIR and artificial neural network modelling. Process Safety and Environmental Protection 2022;160. https://doi.org/10.1016/j.psep.2022.02.033.
- [181] Wu Y, Gui Q, Zhang H, Li H, Li B, Liu M, et al. Effect of biomass components' interaction on the pyrolysis reaction kinetics and small-molecule product release characteristics. J Anal Appl Pyrolysis 2023;173. https://doi.org/10.1016/j.jaap.2023.106039.
- [182] Tao L, Ma X, Ye L, Jia J, Wang L, Ma P, et al. Interactions of lignin and LDPE during catalytic co-pyrolysis: Thermal behavior and kinetics study by TG-FTIR. J Anal Appl Pyrolysis 2021;158. https://doi.org/10.1016/j.jaap.2021.105267.
- [183] Yang K, Wu K, Li F, Jia L, Wang S, Zhang H. Investigation on the co-pyrolysis of bamboo sawdust and low-density polyethylene via online photoionization mass spectrometry and machine learning methods. Fuel Processing Technology 2023;240. https://doi.org/10.1016/j.fuproc.2022.107579.
- [184] Abdullahi Shagali A, Hu S, Li H, He L, Han H, Chi H, et al. Synergistic interactions and co-pyrolysis characteristics of lignocellulosic biomass components and plastic using a fast heating concentrating photothermal TGA system. Renew Energy 2023;215. https://doi.org/10.1016/j.renene.2023.118936.
- [185] Singh S, Patil T, Tekade SP, Gawande MB, Sawarkar AN. Studies on individual pyrolysis and co-pyrolysis of corn cob and polyethylene: Thermal degradation behavior, possible synergism, kinetics, and thermodynamic analysis. Science of the Total Environment 2021;783. https://doi.org/10.1016/j.scitotenv.2021.147004.
- [186] Raveendran K, Ganesh A, Khilar KC. Pyrolysis characteristics of biomass and biomass components. Fuel 1996;75. https://doi.org/10.1016/0016-2361(96)00030-0.
- [187] Mishra A, Nanda S, Ranjan Parida M, Jena PK, Dwibedi SK, Manjari Samantaray S, et al. A comparative study on pyrolysis kinetics and thermodynamic parameters of little millet and sunflower stems biomass using thermogravimetric analysis. Bioresour Technol 2023;367. https://doi.org/10.1016/j.biortech.2022.128231.

- [188] Muigai HH, Choudhury BJ, Kalita P, Moholkar VS. Co–pyrolysis of biomass blends: Characterization, kinetic and thermodynamic analysis. Biomass Bioenergy 2020;143. https://doi.org/10.1016/j.biombioe.2020.105839.
- [189] Xie T, Zhao L, Yao Z, Kang K, Jia J, Hu T, et al. Co-pyrolysis of biomass and polyethylene: Insights into characteristics, kinetic and evolution paths of the reaction process. Science of the Total Environment 2023;897. https://doi.org/10.1016/j.scitotenv.2023.165443.
- [190] Sun C, Chen X, Zheng D, Yao W, Tan H, Zhang Y, et al. Exploring the synergetic effects of the major components of biomass additives in the pyrolysis of polylactic acid. Green Chemistry 2021;23. https://doi.org/10.1039/d1gc03002g.
- [191] Xu Y, Chen B. Investigation of thermodynamic parameters in the pyrolysis conversion of biomass and manure to biochars using thermogravimetric analysis. Bioresour Technol 2013;146:485–93. https://doi.org/10.1016/j.biortech.2013.07.086.
- [192] Ni Z, Bi H, Jiang C, Wang C, Tian J, Zhou W, et al. Investigation of the co-pyrolysis of coal slime and coffee industry residue based on machine learning methods and TG-FTIR: Synergistic effect, kinetics and thermodynamic. Fuel 2021;305. https://doi.org/10.1016/j.fuel.2021.121527.
- [193] Zhang Y, Raashid M, Shen X, Waqas Iqbal M, Ali I, Ahmad MS, et al. Investigation of the evolved pyrolytic products and energy potential of Bagasse: experimental, kinetic, thermodynamic and boosted regression trees analysis. Bioresour Technol 2024;394:130295. https://doi.org/10.1016/J.BIORTECH.2023.130295.
- [194] Virmond E, de Sena RF, Albrecht W, Althoff CA, Moreira RFPM, José HJ. Characterisation of agroindustrial solid residues as biofuels and potential application in thermochemical processes. Waste Management 2012;32:1952–61. https://doi.org/https://doi.org/10.1016/j.wasman.2012.05.014.
- [195] Cristóbal J, Caldeira C, Corrado S, Sala S. Techno-economic and profitability analysis of food waste biorefineries at European level. Bioresour Technol 2018;259:244–52. https://doi.org/https://doi.org/10.1016/j.biortech.2018.03.016.
- [196] Kim YM, Jae J, Kim BS, Hong Y, Jung SC, Park YK. Catalytic co-pyrolysis of torrefied yellow poplar and high-density polyethylene using microporous HZSM-5 and mesoporous Al-MCM-41 catalysts. Energy Convers Manag 2017;149:966–73.
- [197] Zhang XS, Lei HW, Zhu L, Zhu XL, Qian M, Yadavalli G, et al. Thermal behavior and kinetic study for catalytic co-pyrolysis of biomass with plastics. Bioresour Technol 2016;220:233–8.
- [198] Balasundram V, Ibrahim N, Kasmani RM, Abd Hamid MK, Isha R, Hasbullah H, et al. Thermogravimetric catalytic pyrolysis and kinetic studies of coconut copra and rice husk for possible maximum production of pyrolysis oil. J Clean Prod 2017;167:218–28.
- [199] Mishra RK, Mohanty K. Pyrolysis of Manilkara zapota seeds over ZSM-5 to produce high-quality bio-oil and chemicals. Fuel 2020;280. https://doi.org/10.1016/j.fuel.2020.118594.
- [200] Wang P, Shen Y. Catalytic pyrolysis of cellulose and chitin with calcined dolomite Pyrolysis kinetics and products analysis. Fuel 2022;312. https://doi.org/10.1016/j.fuel.2021.122875.
- [201] Deng Z, Syed-Hassan SSA, Chen Y, Jiang L, Xu J, Hu S, et al. Effect of Ni/Al2O3 mixing on the coking behavior of bio-oil during its pyrolysis: Further understanding based on the interaction between its components. Fuel 2022;315. https://doi.org/10.1016/j.fuel.2022.123136.
- [202] Liew JX, Loy ACM, Chin BLF, AlNouss A, Shahbaz M, Al-Ansari T, et al. Synergistic effects of catalytic co-pyrolysis of corn cob and HDPE waste mixtures using weight

- average global process model. Renew Energy 2021;170. https://doi.org/10.1016/j.renene.2021.02.053.
- [203] Ghetti P, Ricca L, Angelini L. Thermal analysis of biomass and corresponding pyrolysis products. Fuel 1996;75:565–73.
- [204] Nadlene R, Sapuan SM, Jawaid M, Ishak MR, Yusriah L. The effects of chemical treatment on the structural and thermal, physical, and mechanical and morphological properties of roselle fiber-reinforced vinyl ester composites. Polym Compos 2018;39:274–87. https://doi.org/https://doi.org/10.1002/pc.23927.
- [205] Liu R, Peng Y, Cao J, Chen Y. Comparison on properties of lignocellulosic flour/polymer composites by using wood, cellulose, and lignin flours as fillers. Compos Sci Technol 2014;103:1–7. https://doi.org/https://doi.org/10.1016/j.compscitech.2014.08.005.
- [206] Sahraei OAZ, Larachi F, Abatzoglou N, Iliuta MC. Hydrogen production by glycerol steam reforming catalyzed by Ni-promoted Fe/Mg-bearing metallurgical wastes. Applied Catalysis B-Environmental 2017;219:183–93.
- [207] Khan Z, Yusup S, Ahmad MM. Performance Study of Ni Catalyst with Quicklime (CaO) as CO2 Adsorbent in Palm Kernel Shell Steam Gasification for Hydrogen Production. Proceedings of the International Conference on Process Engineering and Advanced Materials 2012-Icpeam 2012 2014;917:283–91. https://doi.org/10.4028/www.scientific.net/AMR.917.283.
- [208] Cai H, Liu J, Xie W, Kuo J, Buyukada M, Evrendilek F. Pyrolytic kinetics, reaction mechanisms and products of waste tea via TG-FTIR and Py-GC/MS. Energy Convers Manag 2019;184:436–47. https://doi.org/https://doi.org/10.1016/j.enconman.2019.01.031.
- [209] Gu X, Ma X, Li L, Liu C, Cheng K, Li Z. Pyrolysis of poplar wood sawdust by TG-FTIR and Py–GC/MS. J Anal Appl Pyrolysis 2013;102:16–23. https://doi.org/https://doi.org/10.1016/j.jaap.2013.04.009.
- [210] Yang HP, Yan R, Chen HP, Lee DH, Zheng CG. Characteristics of hemicellulose, cellulose and lignin pyrolysis. Fuel 2007;86:1781–8.
- [211] Huber GW, Iborra S, Corma A. Synthesis of Transportation Fuels from Biomass: Chemistry, Catalysts, and Engineering. Chem Rev 2006;106:4044–98. https://doi.org/10.1021/cr068360d.
- [212] Chen W-H, Wang C-W, Kumar G, Rousset P, Hsieh T-H. Effect of torrefaction pretreatment on the pyrolysis of rubber wood sawdust analyzed by Py-GC/MS. Bioresour Technol 2018;259:469–73. https://doi.org/https://doi.org/10.1016/j.biortech.2018.03.033.
- [213] Chen H, Xie Y, Chen W, Xia M, Li K, Chen Z, et al. Investigation on co-pyrolysis of lignocellulosic biomass and amino acids using TG-FTIR and Py-GC/MS. Energy Convers Manag 2019;196:320–9. https://doi.org/https://doi.org/10.1016/j.enconman.2019.06.010.
- [214] Pattiya A, Titiloye JO, Bridgwater A v. Fast pyrolysis of cassava rhizome in the presence of catalysts. J Anal Appl Pyrolysis 2008;81:72–9. https://doi.org/https://doi.org/10.1016/j.jaap.2007.09.002.
- [215] Lin Y-C, Huber GW. The critical role of heterogeneous catalysis in lignocellulosic biomass conversion. Energy Environ Sci 2009;2:68–80. https://doi.org/10.1039/B814955K.
- [216] Yap TL, Loy ACM, Chin BLF, Lim JY, Alhamzi H, Chai YH, et al. Synergistic effects of catalytic co-pyrolysis Chlorella vulgaris and polyethylene mixtures using artificial neuron network: Thermodynamic and empirical kinetic analyses. J Environ Chem Eng 2022;10. https://doi.org/10.1016/j.jece.2022.107391.

- [217] Aslan DI, Ozogul B, Ceylan S, Geyikci F. Thermokinetic analysis and product characterization of Medium Density Fiberboard pyrolysis. Bioresour Technol 2018:258:105–10.
- [218] Sun C, Li W, Chen X, Li C, Tan H, Zhang Y. Synergistic interactions for saving energy and promoting the co-pyrolysis of polylactic acid and wood flour. Renew Energy 2021;171. https://doi.org/10.1016/j.renene.2021.02.099.
- [219] Swetha TA, Ananthi V, Bora A, Sengottuvelan N, Ponnuchamy K, Muthusamy G, et al. A review on biodegradable polylactic acid (PLA) production from fermentative food waste Its applications and degradation. Int J Biol Macromol 2023;234. https://doi.org/10.1016/j.ijbiomac.2023.123703.
- [220] Ma S, Yang X, Guo Z, Zhang X, Tan T. Co-production of additive manufacturing composites with solid residue from enzymatic hydrolysis of reed. J Clean Prod 2020;249. https://doi.org/10.1016/j.jclepro.2019.119421.
- [221] Jem KJ, Tan B. The development and challenges of poly (lactic acid) and poly (glycolic acid). Advanced Industrial and Engineering Polymer Research 2020;3. https://doi.org/10.1016/j.aiepr.2020.01.002.
- [222] Kumar S, Varadarajan YS, Shamprasad MS. Three-body abrasive wear behavior of rice straw fibers reinforced PLA composites. Mater Today Proc 2023. https://doi.org/10.1016/J.MATPR.2023.05.009.
- [223] Hamdan MHM, Siregar JP, Rejab MRM, Bachtiar D, Jamiluddin J, Tezara C. Effect of Maleated Anhydride on Mechanical Properties of Rice Husk Filler Reinforced PLA Matrix Polymer Composite. International Journal of Precision Engineering and Manufacturing - Green Technology 2019;6. https://doi.org/10.1007/s40684-019-00017-4.
- [224] Kumar S, Shamprasad MS, Varadarajan YS, Sangamesha MA. Coconut coir fiber reinforced polypropylene composites: Investigation on fracture toughness and mechanical properties. Mater Today Proc, vol. 46, 2021. https://doi.org/10.1016/j.matpr.2021.01.402.
- [225] Gordobil O, Delucis R, Egüés I, Labidi J. Kraft lignin as filler in PLA to improve ductility and thermal properties. Ind Crops Prod 2015;72. https://doi.org/10.1016/j.indcrop.2015.01.055.
- [226] Thompson AA, Samuelson MB, Kadoma I, Soto-Cantu E, Drijber R, Wortman SE. Degradation Rate of Bio-based Agricultural Mulch is Influenced by Mulch Composition and Biostimulant Application. J Polym Environ 2019;27. https://doi.org/10.1007/s10924-019-01371-9.
- [227] Li C, Liu Q, Gong W, Zhou Z, Yao Z, Meng X. Study on the atomic scale of thermal and thermo-oxidative degradation of polylactic acid via reactive molecular dynamics simulation. Thermochim Acta 2022;709. https://doi.org/10.1016/j.tca.2021.179144.
- [228] Wang S, Sun Y, Shan R, Gu J, Huhe T, Ling X, et al. Polypropylene pyrolysis and steam reforming over Fe-based catalyst supported on activated carbon for the production of hydrogen-rich syngas. Carbon Resources Conversion 2023;6. https://doi.org/10.1016/j.crcon.2023.02.004.
- [229] Nishida H, Mori T, Hoshihara S, Fan Y, Shirai Y, Endo T. Effect of tin on poly(L-lactic acid) pyrolysis. Polym Degrad Stab 2003;81. https://doi.org/10.1016/S0141-3910(03)00152-6.
- [230] Zhang F, Sun Y, Li J, Su H, Zhu Z, Yan B, et al. Pyrolysis of 3D printed polylactic acid waste: A kinetic study via TG-FTIR/GC-MS analysis. J Anal Appl Pyrolysis 2022;166. https://doi.org/10.1016/j.jaap.2022.105631.

- [231] Sun C, Wei S, Tan H, Huang Y, Zhang Y. Progress in upcycling polylactic acid waste as an alternative carbon source: A review. Chemical Engineering Journal 2022;446. https://doi.org/10.1016/j.cej.2022.136881.
- [232] McNeill IC, Leiper HA. Degradation studies of some polyesters and polycarbonates-2. Polylactide: Degradation under isothermal conditions, thermal degradation mechanism and photolysis of the polymer. Polym Degrad Stab 1985;11. https://doi.org/10.1016/0141-3910(85)90035-7.
- [233] Sivalingam G, Madras G. Thermal degradation of binary physical mixtures and copolymers of poly(ε-caprolactone), poly(D, L-lactide), poly(glycolide). Polym Degrad Stab 2004;84. https://doi.org/10.1016/j.polymdegradstab.2003.12.008.
- [234] Chew KW, Chia SR, Chia WY, Cheah WY, Munawaroh HSH, Ong WJ. Abatement of hazardous materials and biomass waste via pyrolysis and co-pyrolysis for environmental sustainability and circular economy. Environmental Pollution 2021;278. https://doi.org/10.1016/j.envpol.2021.116836.
- [235] Qi PY, Chang GZ, Wang HC, Zhang XL, Guo QJ. Production of aromatic hydrocarbons by catalytic co-pyrolysis of microalgae and polypropylene using HZSM-5. J Anal Appl Pyrolysis 2018;136:178–85.
- [236] Liu J, Jiang X, Cai H, Gao F. Study of Combustion Characteristics and Kinetics of Agriculture Briquette Using Thermogravimetric Analysis. ACS Omega 2021;6. https://doi.org/10.1021/acsomega.1c01249.
- [237] Liu J, Luo L, Zhang Z, Hu Y, Wang F, Li X, et al. A combined kinetic study on the pyrolysis of chrome shavings by thermogravimetry. Carbon Resources Conversion 2020;3. https://doi.org/10.1016/j.crcon.2020.11.003.
- [238] Patnaik S, Panda AK, Kumar S. Thermal degradation of corn starch based biodegradable plastic plates and determination of kinetic parameters by isoconversional methods using thermogravimetric analyzer. Journal of the Energy Institute 2020;93. https://doi.org/10.1016/j.joei.2020.01.007.
- [239] Yiga VA, Lubwama M, Olupot PW. Pyrolysis, kinetics and thermodynamic analyses of rice husks/clay fiber-reinforced polylactic acid composites using thermogravimetric analysis. J Therm Anal Calorim 2023;148. https://doi.org/10.1007/s10973-022-11927-y.
- [240] Sluiter A, Hames B, Ruiz R, Scarlata C, Sluiter J, Templeton D, et al. Determination of structural carbohydrates and lignin in biomass. Laboratory Analytical Procedure 2008;1617:1–16.
- [241] Friedman HL. Kinetics of thermal degradation of char-forming plastics from thermogravimetry. Application to a phenolic plastic. Journal of Polymer Science Part C: Polymer Symposia 1964;6. https://doi.org/10.1002/polc.5070060121.
- [242] Ali I. Misuse of pre-exponential factor in the kinetic and thermodynamic studies using thermogravimetric analysis and its implications. Bioresour Technol Rep 2018;2. https://doi.org/10.1016/j.biteb.2018.04.011.
- [243] Ali I, Seyfeli RC, Tahir MH, Ceylan S. Pyrolytic conversion of waste hemp: Kinetics, product characterization, and boosted regression tree modeling. J Anal Appl Pyrolysis 2023;175. https://doi.org/10.1016/j.jaap.2023.106165.
- [244] Ma Z, Chen D, Gu J, Bao B, Zhang Q. Determination of pyrolysis characteristics and kinetics of palm kernel shell using TGA-FTIR and model-free integral methods. Energy Convers Manag 2015;89. https://doi.org/10.1016/j.enconman.2014.09.074.
- [245] Setswalo K, Oladijo OP, Namoshe M, Akinlabi ET, Sanjay MR. The mechanical properties of alkali and laccase treated pterocarpus angolensis (mukwa)-polylactic acid (PLA) composites. Int J Biol Macromol 2022;217:398–406. https://doi.org/10.1016/j.ijbiomac.2022.07.075.

- [246] Ordonez-Loza J, Chejne F, Jameel AGA, Telalovic S, Arrieta AA, Sarathy SM. An investigation into the pyrolysis and oxidation of bio-oil from sugarcane bagasse: Kinetics and evolved gases using TGA-FTIR. J Environ Chem Eng 2021;9. https://doi.org/10.1016/j.jece.2021.106144.
- [247] Tahir MH, Ali I, Kaya EY, Ceylan S. Thermal conversion of waste furniture board under pyrolytic conditions: Kinetic analysis and product characterization. Fuel 2023;348. https://doi.org/10.1016/j.fuel.2023.128638.
- [248] Lv S, Zhang Y, Tan H. Thermal and thermo-oxidative degradation kinetics and characteristics of poly (lactic acid) and its composites. Waste Management 2019;87. https://doi.org/10.1016/j.wasman.2019.02.027.
- [249] Mumbach GD, Alves JLF, da Silva JCG, Domenico M Di, Marangoni C, Machado RAF, et al. Investigation on prospective bioenergy from pyrolysis of butia seed waste using TGA-FTIR: Assessment of kinetic triplet, thermodynamic parameters and evolved volatiles. Renew Energy 2022;191. https://doi.org/10.1016/j.renene.2022.03.159.
- [250] Özsin G, Pütün AE. TGA/MS/FT-IR study for kinetic evaluation and evolved gas analysis of a biomass/PVC co-pyrolysis process. Energy Convers Manag 2019;182. https://doi.org/10.1016/j.enconman.2018.12.060.
- [251] Nowakowski DJ, Jones JM, Brydson RMD, Ross AB. Potassium catalysis in the pyrolysis behaviour of short rotation willow coppice. Fuel 2007;86:2389–402. https://doi.org/10.1016/J.FUEL.2007.01.026.
- [252] Gašparoviè L, Labovský J, Markoš J, Jelemenský L. Calculation of kinetic parameters of the thermal decomposition of wood by distributed activation energy model (DAEM). Chem Biochem Eng Q 2012;26.
- [253] Maia AAD, de Morais LC. Kinetic parameters of red pepper waste as biomass to solid biofuel. Bioresour Technol 2016;204. https://doi.org/10.1016/j.biortech.2015.12.055.
- [254] Musioł M, Sikorska W, Adamus G, Janeczek H, Richert J, Malinowski R, et al. Forensic engineering of advanced polymeric materials. Part III Biodegradation of thermoformed rigid PLA packaging under industrial composting conditions. Waste Management 2016;52. https://doi.org/10.1016/j.wasman.2016.04.016.
- [255] Wang Z, Liu G, Shen D, Wu C, Gu S. Co-pyrolysis of lignin and polyethylene with the addition of transition metals Part I: Thermal behavior and kinetics analysis. Journal of the Energy Institute 2020;93. https://doi.org/10.1016/j.joei.2019.03.003.
- [256] Qu Y, Li A, Wang D, Zhang L, Ji G. Kinetic study of the effect of in-situ mineral solids on pyrolysis process of oil sludge. Chemical Engineering Journal 2019;374. https://doi.org/10.1016/j.cej.2019.05.183.
- [257] Carstensen JT. Stability of solids and solid dosage forms. J Pharm Sci 1974;63. https://doi.org/10.1002/jps.2600630103.
- [258] Khawam A, Flanagan DR. Solid-state kinetic models: Basics and mathematical fundamentals. Journal of Physical Chemistry B 2006;110. https://doi.org/10.1021/jp062746a.
- [259] He Q, Ding L, Gong Y, Li W, Wei J, Yu G. Effect of torrefaction on pinewood pyrolysis kinetics and thermal behavior using thermogravimetric analysis. Bioresour Technol 2019;280. https://doi.org/10.1016/j.biortech.2019.01.138.
- [260] Xu Y, Chen B. Investigation of thermodynamic parameters in the pyrolysis conversion of biomass and manure to biochars using thermogravimetric analysis. Bioresour Technol 2013;146. https://doi.org/10.1016/j.biortech.2013.07.086.
- [261] Jabarin SA, Lofgren EA. Photooxidative effects on properties and structure of high-density polyethylene. J Appl Polym Sci 1994;53. https://doi.org/10.1002/app.1994.070530404.

- [262] Pandey KK, Vuorinen T. Comparative study of photodegradation of wood by a UV laser and a xenon light source. Polym Degrad Stab 2008;93. https://doi.org/10.1016/j.polymdegradstab.2008.08.013.
- [263] Stark NM, Matuana LM. Characterization of weathered wood-plastic composite surfaces using FTIR spectroscopy, contact angle, and XPS. Polym Degrad Stab 2007;92. https://doi.org/10.1016/j.polymdegradstab.2007.06.017.
- [264] Fabiyi JS, McDonald AG, Wolcott MP, Griffiths PR. Wood plastic composites weathering: Visual appearance and chemical changes. Polym Degrad Stab 2008;93. https://doi.org/10.1016/j.polymdegradstab.2008.05.024.
- [265] Friedrich D. Comparative study on artificial and natural weathering of wood-polymer compounds: A comprehensive literature review. Case Studies in Construction Materials 2018;9. https://doi.org/10.1016/j.cscm.2018.e00196.
- [266] Wang H, Li D, Wang Y, Lin D. Cross-sectional stiffness analysis and support span calculation of WPC decking. Applied Mechanics and Materials, vol. 170–173, 2012. https://doi.org/10.4028/www.scientific.net/AMM.170-173.3175.
- [267] Lin Z, Liu J, Cai H, Evrendilek F, Zhu C, Liang F, et al. Actionable insights into hazard mitigation of typical 3D printing waste via pyrolysis. J Hazard Mater 2023;460. https://doi.org/10.1016/j.jhazmat.2023.132414.
- [268] Soccalingame L, Perrin D, Bénézet JC, Mani S, Coiffier F, Richaud E, et al. Reprocessing of artificial UV-weathered wood flour reinforced polypropylene composites. Polym Degrad Stab 2015;120. https://doi.org/10.1016/j.polymdegradstab.2015.07.013.
- [269] Kuka E, Andersons B, Cirule D, Andersone I, Kajaks J, Militz H, et al. Weathering properties of wood-plastic composites based on heat-treated wood and polypropylene. Compos Part A Appl Sci Manuf 2020;139. https://doi.org/10.1016/j.compositesa.2020.106102.
- [270] Peng Y, Liu R, Cao J, Chen Y. Effects of UV weathering on surface properties of polypropylene composites reinforced with wood flour, lignin, and cellulose. Appl Surf Sci 2014;317. https://doi.org/10.1016/j.apsusc.2014.08.140.
- [271] Pandey KK, Pitman AJ. FTIR studies of the changes in wood chemistry following decay by brown-rot and white-rot fungi. Int Biodeterior Biodegradation 2003;52. https://doi.org/10.1016/S0964-8305(03)00052-0.
- [272] Faix O. Fourier Transform Infrared Spectroscopy BT Methods in Lignin Chemistry. 1992.
- [273] Butylina S, Hyvärinen M, Kärki T. A study of surface changes of wood-polypropylene composites as the result of exterior weathering. Polym Degrad Stab 2012;97. https://doi.org/10.1016/j.polymdegradstab.2011.12.014.
- [274] Mayo DW. Spectra of Carbonyl Compounds of All Kinds (Factors Affecting Carbonyl Group Frequencies). Course Notes on the Interpretation of Infrared and Raman Spectra, 2004. https://doi.org/10.1002/0471690082.ch7.
- [275] Lei Y, Wu Q, Clemons CM, Yao F, Xu Y. Influence of nanoclay on properties of HDPE/wood composites. J Appl Polym Sci 2007;106. https://doi.org/10.1002/app.27048.
- [276] Rasamani KD, Alimohammadi F, Sun Y. Interlayer-expanded MoS2. Materials Today 2017;20. https://doi.org/10.1016/j.mattod.2016.10.004.
- [277] Hong J, Wang Z, Li L, Guo C. Value-added utilization of corncob hydrolysis residues: Preparation of reinforced wood-plastic composite with highly water resistance and decay resistance. Ind Crops Prod 2023;195. https://doi.org/10.1016/j.indcrop.2023.116497.

- [278] Kim HS, Kim S, Kim HJ, Yang HS. Thermal properties of bio-flour-filled polyolefin composites with different compatibilizing agent type and content. Thermochim Acta 2006;451. https://doi.org/10.1016/j.tca.2006.09.013.
- [279] Chen B, Luo Z, Cai T, Cai D, Zhang C, Qin P, et al. The effect of corn varieties on the production of fiber-reinforced high-density polyethylene composites. Biomass Convers Biorefin 2018;8. https://doi.org/10.1007/s13399-018-0337-3.
- [280] Ghanadi M, Padhye LP. Revealing the long-term impact of photodegradation and fragmentation on HDPE in the marine environment: Origins of microplastics and dissolved organics. J Hazard Mater 2024;465. https://doi.org/10.1016/j.jhazmat.2024.133509.
- [281] Andrady AL, Lavender Law K, Donohue J, Koongolla B. Accelerated degradation of low-density polyethylene in air and in sea water. Science of the Total Environment 2022;811. https://doi.org/10.1016/j.scitotenv.2021.151368.
- [282] Hon DNS, Chang ST. SURFACE DEGRADATION OF WOOD BY ULTRAVIOLET LIGHT. J Polym Sci A1 1984;22. https://doi.org/10.1002/pol.1984.170220923.
- [283] Chen J, Mu L, Cai J, Yin H, Song X, Li A. Thermal characteristics and kinetics of refining and chemicals wastewater, lignite and their blends during combustion. Energy Convers Manag 2015;100. https://doi.org/10.1016/j.enconman.2015.05.016.
- [284] Zhou L, Wang Y, Huang Q, Cai J. Thermogravimetric characteristics and kinetic of plastic and biomass blends co-pyrolysis. Fuel Processing Technology 2006;87. https://doi.org/10.1016/j.fuproc.2006.07.002.
- [285] Peng Y, Liu R, Cao J. Characterization of surface chemistry and crystallization behavior of polypropylene composites reinforced with wood flour, cellulose, and lignin during accelerated weathering. Appl Surf Sci 2015;332. https://doi.org/10.1016/j.apsusc.2015.01.147.
- [286] Ding Z, Chen H, Liu J, Cai H, Evrendilek F, Buyukada M. Pyrolysis dynamics of two medical plastic wastes: Drivers, behaviors, evolved gases, reaction mechanisms, and pathways. J Hazard Mater 2021;402. https://doi.org/10.1016/j.jhazmat.2020.123472.
- [287] Kai X, Li R, Yang T, Shen S, Ji Q, Zhang T. Study on the co-pyrolysis of rice straw and high density polyethylene blends using TG-FTIR-MS. Energy Convers Manag 2017;146. https://doi.org/10.1016/j.enconman.2017.05.026.
- [288] Ainali NM, Bikiaris DN, Lambropoulou DA. Aging effects on low- and high-density polyethylene, polypropylene and polystyrene under UV irradiation: An insight into decomposition mechanism by Py-GC/MS for microplastic analysis. J Anal Appl Pyrolysis 2021;158. https://doi.org/10.1016/j.jaap.2021.105207.
- [289] Dong C, Yang Y, Jin B, Horio M. The pyrolysis of sawdust and polyethylene in TG and U-shape tube reactor. Waste Management 2007;27. https://doi.org/10.1016/j.wasman.2006.10.021.
- [290] Grigoriadou I, Pavlidou E, Paraskevopoulos KM, Terzopoulou Z, Bikiaris DN. Comparative study of the photochemical stability of HDPE/Ag composites. Polym Degrad Stab 2018;153. https://doi.org/10.1016/j.polymdegradstab.2018.04.016.
- [291] Yang R, Zhao J, Liu Y. Oxidative degradation products analysis of polymer materials by pyrolysis gas chromatography-mass spectrometry. Polym Degrad Stab, vol. 98, 2013. https://doi.org/10.1016/j.polymdegradstab.2013.05.018.